THESIS FOR THE DEGREE OF DOCTOR OF PHILOSOPHY
in
THERMO AND FLUID DYNAMICS

Turbulence Measurements in a Natural Convection Boundary Layer and a Swirling Jet

ABOLFAZL SHIRI

Division of Fluid Dynamics

Department of Applied Mechanics

CHALMERS UNIVERSITY OF TECHNOLOGY

Göteborg, Sweden, 2010

Turbulence Measurements in a Natural Convection Boundary Layer and a Swirling Jet
ABOLFAZL SHIRI

Doktorsavhandling vid Chalmers tekniska högskola
ISBN: 978-91-7385-367-5
ISSN: 0346-718X
Ny serie nr: 3048

Division of Fluid Dynamics
Department of Applied Mechanics
Chalmers University of Technology
SE-412 96 Göteborg
Sweden
Telephone +46 31 772 1000

This document was typeset using LaTeX.

Printed at Chalmers Reproservice
Göteborg, Sweden 2010

To **Maryam** and **Arvin**

Turbulence Measurements in a Natural Convection Boundary Layer and a Swirling Jet

by

Abolfazl Shiri
abolfazl@chalmers.se
Chalmers University of Technology
Department of Applied Mechanics, Division of Fluid Dynamics
SE-412 96 Göteborg, Sweden
Thesis supervisor: Professor William K. George

Abstract

Two sets of experimental measurement were carried out on an axisymmetric swirling jet flow and a natural convection boundary layer. In the first experiment, the far field of an incompressible swirling jet, discharged into a quiescent ambient has been studied using laser Doppler anemometry. The effect of low to moderate swirl (below vortex breakdown) was studied by measuring velocity profiles of the mean and fluctuating streamwise, radial and azimuthal velocity components at different streamwise locations up to 50 jet exit diameters. The scaled velocity and turbulence intensity profiles, centerline decay and growth rates for two swirling jets with the strength of ($S = 0.15$ and 0.25) have been compared to those obtained in the same facility without swirl ($S = 0$). Like the previous observations for the near jet, there was no observable effect on the properly scaled far jet for the $S = 0.15$ case. For the $S = 0.25$ case, the only statistically significant effect was a shift in the virtual origin. The results were in excellent agreement with the equilibrium similarity theory of Ewing [1999] in which the mean azimuthal component of velocity falls off as the inverse square of the downstream distance. By contrast, the mean streamwise velocity and turbulence intensities fall off with the inverse of the downstream distance. As a consequence, the mean azimuthal equation uncouples from the rest, so the asymptotic swirling jet behaves like the non-swirling jet. The swirl is also shown to have a negligible effect on the overall Reynolds normal and shear stress balances.

Measurements are also presented for the boundary layer flow of air along a heated vertical cylinder. The flow was entirely driven by natural convection: there was no co-flow. The cylinder was 4.5 m in height, had a diameter of 0.15 m, and was maintained at a temperature of $70°C$ (approximately $40°C$ above ambient). The cylinder was heated by water flowing through it, and mounted inside a 1.2 m in diameter cylindrical tunnel through which the ambient flow could be controlled. Detailed measurements of temperature and velocity statistics were taken at heights of 1.5 m, 3m , 4 m height, the latter corresponding to a Rayleigh number based on length, $Ra = g\beta\Delta T x^4/\alpha\nu \approx 1.7 \times 10^{11}$. Two-component burst-mode LDA was used for measuring the instantaneous velocity, while the fluctuating temperature was measured simultaneously using 1-micron platinum wire. Arrays of thermocouples were used to monitor the ambient and wall conditions, as well as the mean profile. Particular attention was given to the buoyancy and momentum differential and integral equations in order to evaluate the residual effects of stratification and co-flow. The strong temperature gradients and end conduction effects on the temperature probes adversely affected unsteady temperature results, as did the development with increasing height of the flow between the concentric cylinders.

Keywords: Jet, swirl, natural convection, turbulent boundary layers, vertical cylinder, high Rayleigh number, cold-wire thermometry, constant current bridge, laser Doppler anemometry.

Acknowledgments

First and foremost I would like to express my deepest gratitude to Professor William K. George. I feel myself lucky, not only to have him as a great supervisor but also privileged to be friend with him. His encouragement, enthusiasm and motivation along with extraordinary pedagogical skills are the source of inspiration for all of his students. When I started working with him, I did not expect the life as a Ph.D. student to be both fun and educational. The times spent with him, either traveling or working on my thesis on his boat, were unique experiences in my life. I also appreciate his effort at trying to provide the best environment for his students despite all the problems. It is a great feeling be a member of his TRL family.

I wish to thank my co-supervisor Professor Gunnar T. Johansson for all the helpful whiteboard discussions and criticism. His office door was always open (even in the latest time of the day) for an urgent rescue.

I would also like to thank Professor Jonathan Naughton for the help and guidance on the swirling jet project. His encouragement and inspiration was a valuable gift at the beginning of my study. I learnt a lot from him both in the subject of our research and his experience in life and work. I also appreciate his hospitality during the visit from university of Wyoming.

I enjoyed every moment of these years working amongst my close friends in the Turbulence Research Lab. group. Maja Wänström , Murat Tutkun, Carlos Arroyo, Clara Velte and Lars-Uno Axelsson, I thank you all for the great company and generous helps. I am also grateful for all the help and supports from Dr. Peter Johansson. His technical insight made working in the lab. much easier.

The natural convection project wouldn't have started without all the effort made by Professor Rolf Karlsson. I had just a brief chance to meet him but his legacy remained with us through out the work.

I loved the tradition of daily "fika" breaks, chatting with the nice people in the department and enjoying a piece of cake or two. Thanks to all my friends in the Department of Applied Mechanics, especially Mohammad and Pirouz for making the working environment more tolerable.

Special thanks to Lars Jernqvist for all the technical supports and last minute rescues. The project could not be progressive without his skilled provision and handiwork.

I would like to express my appreciation to Ulla Lindberg Thieme and Monica Vargman for helping me out with all sorts of paperwork and their supportive attitude.

I can not thank enough my wife, Maryam for her unconditional love and support through out all these years. I certainly could not be able to carry on with my goals and dreams without her patience and encouragement. I am also thankful to Arvin, my son, for all the joy and fun he has brought into our life. He made the final days of my Ph.D. less stressful with his rejoice.

Last but not least I am grateful to my parents who were my first teachers and without their love and encouragement I don't think I could have succeeded.

Feb. 19th, 2010
Göteborg, Sweden

Nomenclature

Upper-case Roman

A, B_u, C	growth rate constants for self-preserving axisymmetric jet
A_w	wire cross-sectional area
C_w	specific heat of wire material
C_p	specific heat of fluid at constant pressure
C_v	specific heat of fluid at constant volume
D	nozzle exit diameter
F_o	kinematic wall heat flux =$\frac{q_w}{\rho\, C_p}$
G_θ	axial component of angular momentum flux
L	axial length scale
M_x	axial momentum flux
N_{eff}	number of effectively independent samples
R	cylinder radius; gas constant
T	temperature
U, V, W	mean axial, radial and tangential velocity components in the flow, respectively
U_0	average exit axial velocity of jet
U^+	velocity inner variable =$\frac{U}{u_*}$

Lower-case Roman

c	speed of sound
d	wire diameter
e	internal energy
$\mathbf{f_i}$	vector of body force
g	gravitational acceleration
h	enthalpy; convection heat transfer coefficient
k	kinetic energy
m_x	mass flux of jet in axial direction
p	pressure
q_w	wall heat flux
t	time ; fluctuating temperature
u, v, w	fluctuating axial radial and azimuthal velocity component, respectively
u_*	friction velocity = $(\tau_w/\rho)^{0.5}$
x, r, θ	cylindrical coordinate system
x_o	virtual origin for self-preserving axisymmetric jet
y^+	inner variable =$\frac{y\, u_*}{\nu}$

Greek Symbols

α	thermal diffusivity $=\frac{\kappa}{\rho C_p}$
β	volumetric thermal expansion coefficient
$\delta_{1/2}$	jet half-width
δ_T	temperature boundary layer thickness
δ_U	velocity boundary layer thickness
δ_{ij}	Kronecker delta
ϵ	dissipation of turbulent kinetic energy
Φ	viscous dissipation function
$\epsilon^2_{\psi_N}$	relative statistical error of estimator ψ_N
ε_ν	viscous dissipation
η	normalized radial coordinate in the momentum integral
ℓ	wire length
κ	thermal conductivity
μ	viscosity
ν	kinematic viscosity $=\mu/\rho$
ρ	density
σ	Stefan-Boltzman constant
τ	temporal separation
τ_w	wall shear stress $=\mu\left(\frac{\partial U}{\partial y}\right)_{y=0}$

Dimensionless Parameters

Gr_x	Grashof number $=\frac{g\beta\Delta T x^3}{\nu^2}$
H_x	the H-number $=\frac{g\beta F_o x^4}{\alpha^3}$
M	Mach number $=\frac{U}{c}$
Nu_x	Nusselt number $=\frac{hx}{\kappa} = \frac{F_o x}{\Delta T \alpha}$
Pr	Prandtl number $=\frac{\nu}{\alpha}$
Re	Reynolds number $=\frac{Ux}{\nu}$
Ra	Rayleigh number $=Gr_x.Pr$
S	swirl number $=\frac{G_\theta}{M_x R}$

Subscripts

c	center line
i	quantities associated with the inner region
o	quantities associated with the outer region
o	jet, nozzle exit condition
w	evaluated at the wall
∞	free stream or ambient conditions
max	maximum value
rms	root mean square value
$*$	scaled property
$+$	normalized by inner variables

Symbols

$\langle \dots \rangle$	time averaged quantity

Abbreviations

CFD	Computational Fluid Dynamics
LDV	Laser Doppler Velocimetry
LES	Large Eddy Simulation
RANS	Reynolds Averaged Navier-Stokes

Contents

List of Figures

List of Tables

Chapter 1

Overview of the thesis

The goal of this thesis is to describe the experimental investigations which have been carried out on two interesting turbulent flow fields:

- Turbulent natural convection boundary layer next to a vertical heated cylinder,
- Incompressible swirling jets with low to moderate swirl number.

In both of these experiments, the burst-mode laser Doppler anemometer (LDA) was used as the velocity measurement technique. Also thermocouple and cold-wire were used, both separately and simultaneously with the LDA, to measure the mean and fluctuating temperature field in the natural convection experiment.

Part I describes a swirling jet experiment which was a part of a continuing study of free shear flows at the Turbulence Research Laboratory. It was not originally intended to be part of this dissertation, but the years long delays in establishing a place for and constructing the natural convection rig for the experiments described in Part II opened the opportunity for this work. The particular unique feature of the experiment reported herein was to investigate the far-field evolution of the jet with an initial azimuthal velocity. The natural convection experiment described in Part II continued a series of experiments that had been carried out at Vattenfall Utveckling, and moved to the Turbulence Research Laboratory at Chalmers with Professor Rolf Karlsson in fall of 2000.

1.1 Swirling Jet Experiment

Initial condition have been known to affect the similarity solutions of an axisymmetric jet since the theoretical work of George [1989]. Numerous experiments on jets since then have made it clear that, contrary to what was long believed, laboratory jets cannot be categorized as universal self-similar, point-source of momentum jets. A jet flow asymptotically approaches to its self-preserving state, but this state is determined by the conditions at the jet source. One of the indicators of this dependence is the jet spreading rate ($d\delta/dx$). Thus the spreading rate of the swirling jet is of particular interest. The experiments reported herein were initiated to study the influence of a mild tangential velocity component on the axisymmetric jet flow.

The near-field of jets and the mixing enhancement due to an initial swirl have been studied by several investigators (see Farokhi et al. [1989] and Gilchrist and Naughton [2005]). This study focusses on the far-field; and in particular, on ability of the jet flow to establish self-similar behavior in the presence of a tangential velocity component. The experimental facility

was a modification of the same rig used in Hussein et al. [1994] experiment, (see figure 1.1). Three different sets of screens and two contractions inside the facility generate a one inch axisymmetric jet without any significant disturbances from upstream at the discharge position. The tangential component of velocity was created by three pairs of nozzles which injected compressed air before the screens. The velocity of the blowers of the main flow and swirl flow were separately controlled by two frequency converters to generate a specific swirl number.

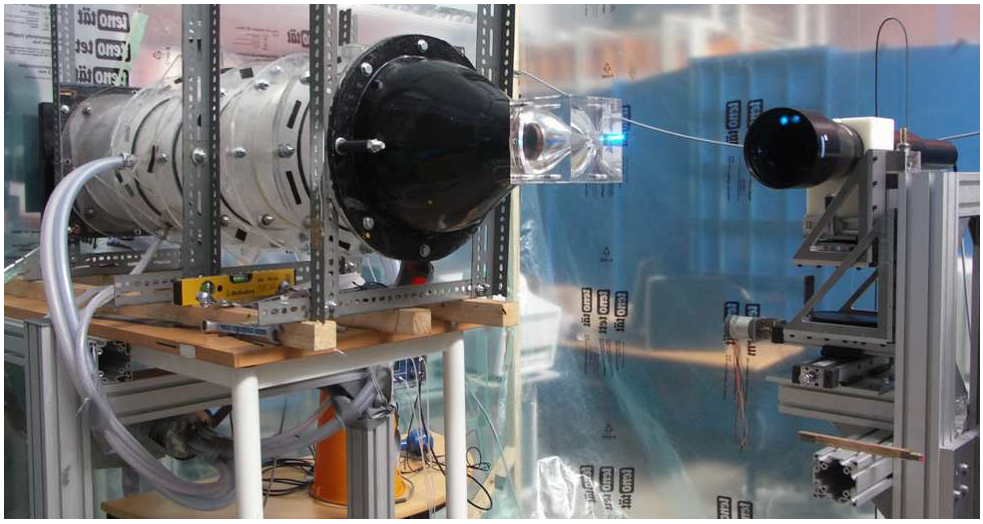

Figure 1.1: Swirling Jet Experimental Facility.

The experiment was performed using laser Doppler anemometry, both because of the relatively high turbulence intensities throughout the jet and to avoid any disturbances in the flow by a probe. The confinement around the flow was big enough ($3.5m \times 3.5m \times 10m$) to eliminate the effects of the walls on the entrainment using the criteria of Hussein et al. [1994]. The measurements were carried out at two different swirl numbers of $S = 0.15$ and $S = 0.25$, in addition to a non-swirling case. The far-field of the jet was measured at different distances downstream from the jet exit up to 50 diameters.

The first part of this thesis describes the study of the similarity region in swirling jet flows. Chapter 2 is a brief introduction of the flow characteristics and reviews the literatures in this field. In chapter 3 we look into the governing equations and similarity theories of the axisymmetric jets. A particularly novel feature of this chapter is the recognition of role of the rate of addition and conservation of angular momentum in determining the similarity scaling and flow development. The details of the experimental facility and measurement methods are discussed in chapter 4. And in the last two chapters of this part, the results of the experiment and a summary of the work are presented.

1.2 Natural Convection Experiment

This experiment was designed to improve understanding of the process of heat transfer from a surface with different temperature (in this case higher) than the quiescent surrounding fluid. Flows that are significantly influenced by gravity and density differences of a body from the ambient fluid are classified as *buoyancy-driven flows*. In the presence of a body force like gravity

or centripetal force, the change in the density due to the temperature difference creates a buoyancy force acting on the fluid which can cause motion. The moving fluid, together with the stagnant ambient, can create a free shear layer flow (e.g., like in a plume in an unconstrained environment). When it is constrained by a surface it creates a boundary layer flow along the surface (e.g., like the flow described below for which the surface was vertical so the flow rises along it).

In wall-bounded buoyancy-driven flow the laminar flow's stability is defined by a dimensionless number (called the *Grashof* number), which compares the amount of buoyancy force delivered into the flow relative to the viscous force damping the motion:

$$Gr_L = \frac{g\beta\ \Delta T L^3}{\nu^2} \sim \frac{\text{Buoyancy Force}}{\text{Viscous Force}} \tag{1.1}$$

where g is the gravitational acceleration, β is the coefficient of thermal expansion, ΔT is the temperature difference from some reference value (usually the free stream), ν is the kinematic viscosity, and L is an appropriate length scale (e.g., the distance from the leading edge of the surface). Another dimensionless parameter closely related to it is the *Rayleigh* number defined by:

$$Ra_L = \frac{g\beta\ \Delta T L^3}{\nu\alpha} \tag{1.2}$$

where α is the thermal diffusivity. It is easy to see that the *Rayleigh* number is just the *Grashof* number times the *Prandtl* number, $Pr = \nu/\alpha$. For air over the range of the experiments reported herein, the *Prandtl* number is nearly constant at 0.7. Note that for the case of a constant wall heat flux, so-called *flux Grashof and Rayleigh numbers* can be defined by using the wall heat flux, say q_w, instead of the temperature difference; i.e.,

$$Gr_* = \frac{g\beta q_w L^4}{\nu^3} \tag{1.3}$$

$$Ra_* = \frac{g\beta q_w L^4}{\nu^2\alpha} \tag{1.4}$$

The *Grashof* and *Rayleigh* numbers are typically many orders of magnitude higher than their counterparts for forced flow, the *Reynolds* number. This is because of their dependence on L^3 (or L^4) and inverse dependence on ν^2 (or $\alpha.\nu$). The *Reynolds* number, by contrast, is proportional to L/ν. Experiments and linear stability theory suggest that the critical value for *Grashof* number in air varies between 10^8 and 10^{10}. Incropera [2007] suggests $Ra \approx 10^9$ as the value for the critical *Grashof* number where the laminar flow becomes unstable. This critical value does not predict when the flow develops into a fully turbulent natural convection boundary layer. This is generally believed to occur much later at roughly $Gr > 10^{10}$ for air. The primary consideration in designing (actually modifying) the facility for this experiment was to insure a well-developed turbulent boundary layer. Of equal importance, however, was to insure that the boundary layer was of sufficient thickness and velocity that it could be measured with the available technology, especially the critical near wall region from which the wall shear stress and heat transfer rates can be determined.

The experimental facility used in this experiment was a modification of the rig used by Persson and Karlsson [1996]. A cylindrical surface was chosen in order to avoid the effect of side walls that could change the two-dimensional nature of the flow and add more complexity. On

Figure 1.2: Natural Convection Boundary Layer Experimental Facility.

the other hand the natural convective heat transfer from a cylindrical geometry is also appealing for industrial applications such as heat exchangers and reactors. In the original Vattenfall rig a length of $2\ m$ was used for a slender cylinder of $10cm$ in diameter to create a boundary layer with $Ra_L = 1.4 \times 10^{10}$. For this experiment the length of the cylinder was increased to $4.5\ m$ in order to give a Grashof number of $Ra_L = 1.7 \times 10^{11}$ at $4m$ height at a temperature difference of 40 degree Celsius.

For the rig shown in figure 1.2, the hot water circulates in a closed cycle through a water pump to keep the surface temperature of the cylinder constant. Air was used as the working fluid in the experiment, because the optical method of velocity measurement (LDA) has difficulties working in a fluid with high index of refraction such as water in the presence of a high temperature gradient (mirage effect). The entrance section of the rig from the bottom was also modified to let the air enter the rig in a uniform and symmetrical way. The cylinder is confined within a 1.2 m diameter fiberglass cylinder, and a collector at top of the tunnel diverts the hot air to an enclosure surrounding the rig where it is cooled down and small particles are added to the air for the LDA measurements. The entire system of air and water temperature is monitored by a set of thermocouples during the measurement, which typically takes several hours or more.

In Part II, chapter 7 of the thesis reviews the background, applications and previous attempts to study the natural convection flows. The equations and supporting theories of the fluid dynamics will be presented in chapter 8, and the details of the experimental facility will be discussed in chapter 10. The measurement methods, laser Doppler anemometry, resistance wire (cold-wire) and thermocouple thermometry, are described in chapter 11, and also deals

with the errors arising from the measurement methods. Finally in chapters 12 and 13, the results of the experiment along with discussion and a summary of the work are presented. Among the most significant findings are heat transfer results which call into question previous measurements of wall heat transfer in natural convection flows. Also the present results raise serious doubts about whether the previous measurements of natural convection wall-bounded flows were in flows which could in any sense be regarded as fully-developed. Questions are also raised about the methodologies of the present and previous experiments.

Part I

Incompressible Swirling Jets

Chapter 2

Introduction

This chapter introduces the concept of turbulent jet, and especially a jet with swirl. It also briefly reviews the literature and provides background for the theoretical and experimental presentations of the subsequent chapters.

2.1 What is a jet?

The jet flows are well-known because of their many engineering applications. But they also occur commonly in nature. Examples range from phenomena like the Mount St. Helens volcano to living creatures like a squid which propels itself by squirting water behind it. In fact, any stream of fluid that mixes with a surrounding medium moving more slowly can be called a jet flow. In this thesis the word *jet* will be used to refer only to a source of momentum exiting into a quiescent environment.

Figure 2.1: A jet flow visualization using a simple home humidifier.

For a fluid mechanician, jets represent a class of free shear flows which are inhomogeneous flows that evolve in the absence of walls. Wakes, plumes and shear layer flows are other classes of free shear flows. All undergo transition and transform from laminar into turbulent flow

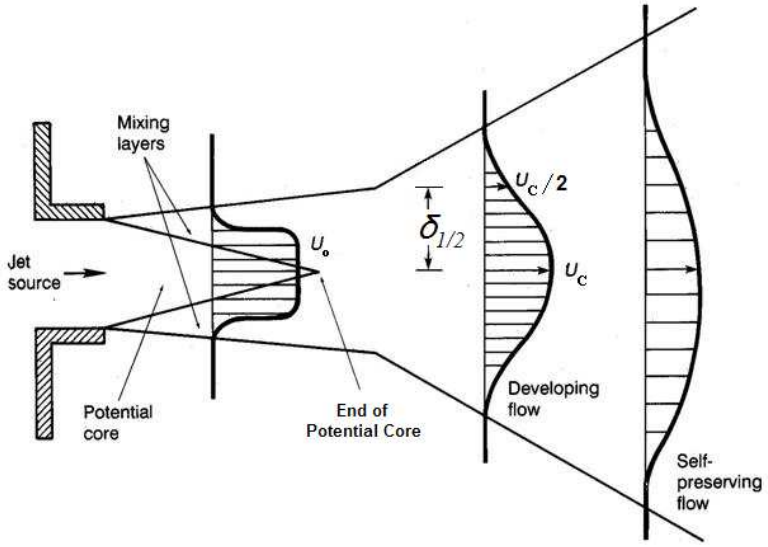

Figure 2.2: Schematic of the early development of a jet.

much more rapidly than wall bounded flows. In the absence of density differences, the mean velocity gradient (or mean shear) is the source of turbulence. More accurately, it is the Reynolds stresses working against this mean shear that accounts for all of the turbulence energy production. Underlying these 'averaged' measures of what is going on in a jet are an incredible array of vorticity interactions. The manner in which these vortices interact with each other and with the mean flow is for the most part poorly understood.

Both two-dimensional jets (flow discharged from a slot) and axisymmetric jets evolve in the surrounding ambient medium in the manner illustrated schematically in figure 2.2. A free shear layer is generated immediately after the laminar flow exiting the nozzle of jet meets the stationary fluid. This has its origins in the upstream boundary layers formed in the jet nozzle, so the nature of this boundary layer in the nozzle can very much influence the early transition process. But for even modest exit Reynolds numbers (a few thousand), the transition processes are dominated by the local shear instabilities and the shear layer rapidly becomes turbulent (usually within less than a diameter, sometimes much less). Eventually as the shear layers (or shear annulus) grows, the sides of the shear layer merge. But before they do there is a irrotational flow region inside called potential core which has not yet been entrained into the turbulent shear layer. This region has an approximately flat velocity profile in the middle is usually less than three nozzle diameters long. The next region is dominated still by the remnants of the mixing layer and the mass inflow from the nozzle. It is not until the fully developed region which evolves about 20 – 30 diameters downstream that the jet achieves a self-similar (or self-preserving) state. There are clearly two length scales here: the streamwise length scale which is the distance from nozzle and the jet half-width ($\delta_{1/2}$), that is the radial distance in each cross-section between the jet centerline and the position at which velocity reaches half of its maximum value.

The nature of turbulent free shear flows is also characterized by another important phenomenon; namely, entrainment in which turbulent (or vortical) fluid converts the surrounding (usually irrotational) flow into vortical fluid. Though this feature is not unique to turbulent

flows, it is substantially greater than in a laminar flow. In a turbulent flow, the large scale eddies engulf (or surround) parcels of irrotational fluid, which is then converted into vortical fluid by the 'nibbling' due to viscous diffusion of the small scale vorticity at the interface (sometimes called the 'Corrsin superlayer'). It is the efficiency of this process that explains the widespread application of jet flows in industry for mixing. The amount of the mass brought into the flow is overwhelmed by the entrained mass within 30 diameters from the exit plane (see figure 2.3).

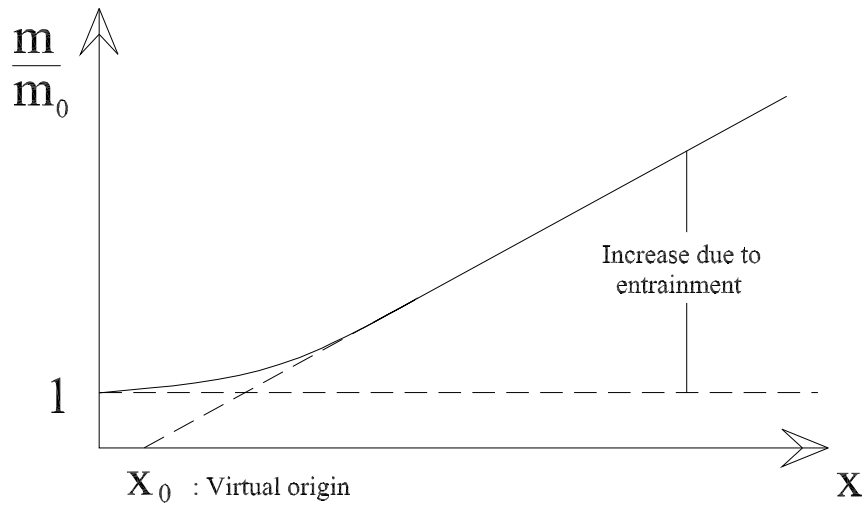

Figure 2.3: The entrainment of a jet flow overwhelms the initial mass flow and defines a virtual origin.

If a line tangent to the rate at which mass crosses any downstream section of the flow is extrapolated backwards, there is a location from which the jet source appears to emanate with no initial mass flow (see figure 2.3). This position is called the *virtual origin*, and is one of the parameters characterizing the initial conditions. The same virtual origin can be obtained by tracing lines tangent to the instantaneous interface between the jet and the ambient fluid (c.f., Cater and Soria [2002]), or by fitting a curve to a plot of the velocity profile half-widths as a function of downstream distance (c.f.,Hussein et al. [1994]).

Although the three-dimensional turbulent nature of the flow makes it difficult to model, the theoretical study is simplified by its symmetries. First it is a homogeneous flow in azimuthal direction (or homogeneous in the spanwise direction for the plain jets). This makes the spatial derivative of any averaged quantity with respect to the azimuthal angle, θ, identically zero. Second, the flow develops much more slowly in the streamwise direction than in the radial direction, so it can be treated to a first approximation as a thin shear layer using a boundary layer type approximation. The thin shear layer approximation considerably simplifies the averaged equations since the streamwise derivatives of the averaged flow are much smaller than spanwise ones (i.e., $\partial/\partial x \ll \partial/\partial r$).

Turbulent jets have continued to interest researchers for many years, both because of their numerous applications as well as their importance to our fundamental understanding of turbulence. Jet flows with swirl are of particular interest, especially in combustion; and many experimental and theoretical studies have tried to address the questions of the stability and

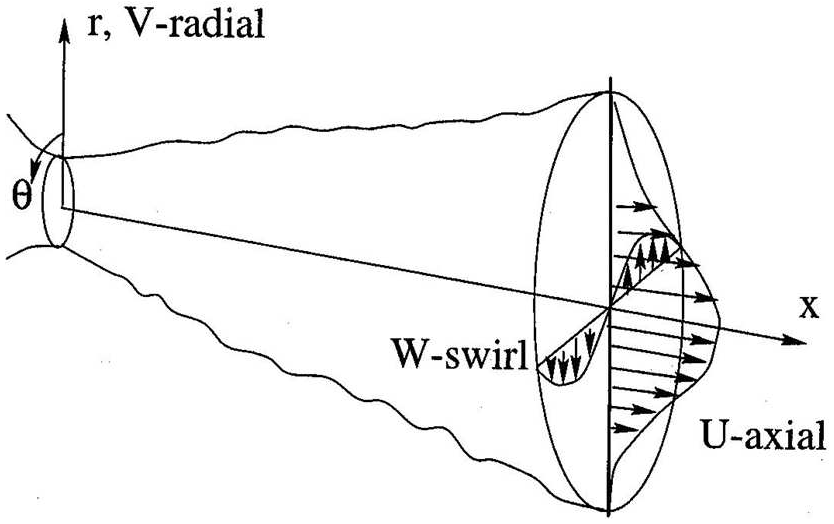

Figure 2.4: Swirling jet velocity components.

dependency on initial condition of jet flow. But even the non-swirling axisymmetric jet has proven a considerable challenge to researchers, and only recently have the role of upstream conditions and downstream similarity been fully recognized (George [1989], Cater and Soria [2002], Mi et al. [2001]). Only with this recognition has it become possible to sort out the apparently conflicting results for even the single point turbulence statistics (Hussein et al. [1994], Panchapakesan and Lumley [1993], Burattini et al. [2005]). This thesis extends the range of that understanding to include swirling jets, at least as far as the asymptotic flow is concerned.

2.2 Swirling Jets

Swirling jets add to the interest of this class of flows because swirl can be considered as a significant change in the jet flow's initial conditions. Farokhi et al. [1989] and Gilchrist and Naughton [2005] investigated the effect of swirl on the near-field flow of an axisymmetric jet and showed that moderate swirl (below vortex breakdown) enhances the growth rate and mixing compared to those of a non-swirling jet. The latter presented evidence that the enhanced growth rates persisted to 20 diameters downstream of the jet exit, even though the swirl had decayed to a point where it was barely detectable (Gilchrist and Naughton [2005]). Such changes in the flow characteristics in the near-field suggest that some turbulence structure of the swirling jet must persist far downstream.

An axisymmetric jet with an initial azimuthal velocity component is considered to be a swirling jet flow (see figure 2.4). When the azimuthal velocity strength exceeds the axial component strength of the flow (swirl number greater than unity), the flow behavior changes and the flow becomes unstable with recirculations. Investigations by Chigier and Chervinsky [1967] show even in swirl numbers lower than unity ($S \approx 0.6$), the reversed flow is observable. The present study was limited to low-to-moderate swirl ($S \leq 0.25$) below the vortex breakdown limit and for which the flow still behaves as a jet. How this change in the initial condition alters the flow far downstream in the similarity region is the question this study tried to answer.

While studies by Craya and Darrigol [1967] and Chigier and Chervinsky [1967] focused on the swirl strength and the flow behavior of different swirl degree, Gilchrist and Naughton

[2005] are also considered the effect of swirl generator's type on the growth rate of the jet. The azimuthal velocity component can be introduced to the axial flow in different ways. The so-called "q-vortex" type of swirl produced a higher peak in the exit velocity profile compared to the "solid-body" swirl type. The "radial-type" swirl generator used by Sheen et al. [1996] also produced the same range of swirl number with the variation in exit profile. In all these experiments, the shape of the jet source profile directly manipulated the behavior of near-near fields, in a similar manner to the investigations of as Mi et al. [2001] on non-swirling jets. The instabilities in swirling jets and the structures of the vortex break-down in high swirling number flows studied by Panda and McLaughlin [1994] and Shtern et al. [2000] indicate that the high swirl destabilizes the jet flow.

Although swirling jets in the near field have been studied for a long time, detailed measurements of the far-field flow under carefully controlled conditions are lacking. The objective of the present study is to make such measurements in the jet far field using laser Doppler anemometry (LDA) to complement our existing knowledge of these swirling flows. The LDA data acquired herein is used to assess the characteristics of the swirling jet in the far-field and compare these results with those in the near field. By contrast with the earlier studies of the near field, the present results for the far jet show a linear growth rate for the far field of swirling jet that is the same as for the non-swirling jet. Moreover, *if the statistical moments are properly scaled using the rates at which momentum and mass are added at the source*, there appears to be no effect of swirl in the far-field other than to move the virtual origin of the flow. The overall findings substantiate the theoretical analysis of Ewing [1999] who used equilibrium similarity considerations to argue that the effects of swirl on the asymptotic jet should be negligible.

In the following sections, the implications of the governing equations and the similarity results are reviewed. It is argued that the swirl introduces another length scale into the problem, with consequence that the swirl number is a ratio of length scales. Next the experimental facility and experiments are described and the data on the first and second moments is presented. Finally the implications of the similarity analysis on the results are considered.

Chapter 3

Theory of Axisymmetric Jets with Swirl

This chapter considers the consequences of swirl on the Reynolds-averaged Navier-Stokes equations. Of primary interest is the asymptotic development of the jet for large distances from the jet source. This work has previously been published as Shiri et al. [2008], and earlier versions appeared as Shiri [2006] and Shiri et al. [2006].

3.1 Introduction

For nearly half-a century, all jets were believed to evolve to be asymptotically independent of their initial conditions, and depend only on the rate at which momentum was added at the source and the distance downstream (c.f. Tennekes and Lumley [1974], Monin and Yaglom [1975]). While experiments never confirmed this, it was not until the analysis of George [1989] that an asymptotic dependence on initial conditions was shown to be consistent with similarity solutions to the RANS equations. The past two decades have seen numerous experiments confirming this asymptotic dependence for jets and other free shear flows (See George [2008] for a recent review).

By any measure, the addition of swirl at the jet source can be considered to be a significant change in the jet flow's initial conditions. As noted in the preceding chapter, numerous experimental and theoretical studies have tried to address the questions of the stability and dependency on initial condition of jet flow (e.g., Farokhi et al. [1989] and Gilchrist and Naughton [2005]). All have focused on the near-field flow of an axisymmetric jet, and showed enhanced growth rate and mixing compared to those of a non-swirling jet. This thesis is concerned with the asymptotic state of jets with moderate swirl and below vortex breakdown). Such jets evolve as statistically stationary flows for which the Reynolds-averaged Navier-Stokes equations apply. Stationarity assures that time-averaging and ensemble averages are the same, at least in the limit of an infinitely long record and an infinite number of members of the ensemble; i.e.,

$$\lim_{T\to\infty} \frac{1}{T} \int_0^T [quantity] dt = \langle [quantity] \rangle. \tag{3.1}$$

Note that this is not necessary true if the flow contains periodic components, which would probably be the case if it were unstable. This is not a problem for the swirl numbers under consideration herein, no matter whether the jet is swirling or not.

3.2 Basic equations for the swirling jet

3.2.1 Mass conservation

In the absence of sources of mass, the continuity equation is the same as for the non-swirling jet. For constant density flow, the Reynolds-averaged continuity equation is given by:

$$\frac{\partial U}{\partial x} + \frac{1}{r}\frac{\partial}{\partial r} rV + \frac{1}{r}\frac{\partial W}{\partial \theta} = 0 \tag{3.2}$$

With the assumption that the flow is axisymmetric in the mean, the last term is identically zero since the azimuthal derivative of any averaged quantity is zero; i.e., $\partial/\partial\theta = 0$. Thus the mean continuity equation reduces to:

$$\frac{\partial U}{\partial x} + \frac{1}{r}\frac{\partial}{\partial r} rV = 0 \tag{3.3}$$

Equation 3.3 can be integrated from the axis to any radial value r to obtain the following:

$$V(x, r, \theta) = -\frac{1}{r}\frac{d}{dx}\int_0^r U r' dr' \tag{3.4}$$

The entrainment rate per unit mass, say E, can be defined as:

$$E = \lim_{r\to\infty} \int_0^{2\pi} V r d\theta = 2\pi \lim_{r\to\infty} rV \tag{3.5}$$

Substituting equation 3.4 yields immediately:

$$E = 2\pi \lim_{r\to\infty} rV = 2\pi \frac{d}{dx}\int_0^\infty U r dr \tag{3.6}$$

For the asymptotic state, the last integral can be shown (see below) to be constant, which implies that $V \to 1/r$ for large values of r.

3.2.2 Momentum Conservation

The instantaneous Navier-Stokes equations in cylindrical coordinates for a constant density flow are given in Appendix B. Also in Appendix D the consequences of Reynolds-averaging of these equations are shown, and the order of magnitude analysis presented to identify the most important terms which form the basis of a similarity analysis. For high Reynolds number, the case of interest herein, the viscous terms can be neglected in the mean momentum equation. This can be verified *a posteriori* using the actual data.

Thus, ignoring the viscous terms and assuming azimuthal symmetry, the Reynolds-averaged Navier-Stokes equations in cylindrical coordinate can be shown to be given by:

$$U\frac{\partial U}{\partial x} + V\frac{\partial U}{\partial r} = -\frac{1}{\rho}\frac{\partial P}{\partial x} - \frac{\partial \overline{uv}}{\partial r} - \frac{\overline{uv}}{r} - \left\{\frac{\partial \overline{u^2}}{\partial x}\right\} \tag{3.7}$$

$$-\frac{W^2}{r} = -\frac{1}{\rho}\frac{\partial P}{\partial r} - \frac{\partial \overline{v^2}}{\partial r} + \frac{\overline{w^2} - \overline{v^2}}{r} - \left\{\frac{\partial \overline{uv}}{\partial x}\right\} \tag{3.8}$$

$$U\frac{\partial W}{\partial x} + V\frac{\partial W}{\partial r} + \frac{VW}{r} = -\frac{\partial \overline{vw}}{\partial r} - 2\frac{\overline{vw}}{r} - \left\{\frac{\partial \overline{uw}}{\partial x}\right\} \tag{3.9}$$

Note that the last term in brackets in each equation is usually neglected since they represent changes in the streamwise direction. The $\partial\overline{u^2}/\partial x$ term will be seen to make a second order contribution to the momentum integral, so will be retained for now; but the $\partial\overline{uv}/\partial x$ terms will be dropped since they are substantially smaller.

Equation 3.8 can be integrated from any radial value r to ∞ to obtain the pressure as:

$$\frac{1}{\rho}[P(x,r) - P(x,\infty)] = -\int_r^\infty \frac{W^2 + [\overline{w^2} - \overline{v^2}]}{r'}dr' - [\overline{v^2}] \tag{3.10}$$

where W and all turbulence quantities are assumed to vanish at infinite radius. Equation 3.10 can be differentiated with respect to x to obtain:

$$\frac{1}{\rho}\frac{\partial P(x,r)}{\partial x} = \rho\frac{dP_(x,\infty)}{dx} - \frac{\partial}{\partial x}\int_r^\infty \frac{W^2 + [\overline{w^2} - \overline{v^2}]}{r'}dr' - \frac{\partial\overline{v^2}}{\partial x} \tag{3.11}$$

If it is assumed that there is no external flow, then $dP(x,\infty)/dx = 0$. Assuming this and substituting equation 3.11 into equation 3.7 yields the streamwise momentum equation as:

$$U\frac{\partial U}{\partial x} + V\frac{\partial U}{\partial r} = -\frac{1}{r}\frac{\partial r\overline{uv}}{\partial r} + \frac{\partial}{\partial x}\left\{[\overline{v^2} - \overline{u^2}] + \int_r^\infty \frac{W^2 + [\overline{w^2} - \overline{v^2}]}{r'}dr'\right\} \tag{3.12}$$

The last term is almost always negligible compared to the others.

3.2.3 Integral equations for axial and angular momentum conservation

In order to compute the strength of the flow in streamwise and azimuthal directions, these equations can be integrated over a plane downstream of the jet to derive axial and angular integral momentum equations given below:

Conservation of axial momentum in axial direction:

First multiply the mean continuity equation 3.3 by U and add it to equation 3.12 to obtain:

$$\frac{\partial}{\partial x}U^2 + \frac{1}{r}\frac{\partial}{\partial r}rUV = -\frac{1}{r}\frac{\partial}{\partial r}r\overline{uv} + \frac{\partial}{\partial x}\left\{[\overline{v^2} - \overline{u^2}] + \int_r^\infty \frac{W^2 + [\overline{w^2} - \overline{v^2}]}{r'}dr'\right\} \tag{3.13}$$

Then multiply by r and integrate from $0 \le r < \infty$. If the swirl velocity and turbulence second-order moments are assumed to vanish at infinity, the result after integration by parts is:

$$\frac{d}{dx}\int_0^\infty \left[U^2 - \frac{W^2}{2} + \overline{u^2} - \left(\frac{\overline{w^2} + \overline{v^2}}{2}\right)\right] rdr = 0 \tag{3.14}$$

Integrating from the source to any streamwise value yields the following streamwise momentum integral constraint on the motion:

$$M_o = 2\pi\int_0^\infty \left[U^2 - \frac{W^2}{2} + \overline{u^2} - \left(\frac{\overline{w^2} + \overline{v^2}}{2}\right)\right] rdr \tag{3.15}$$

This clearly reduces to the integral equation of Hussein et al. [1994] (appendix) when $W = 0$ as it should. Note that $[\ U^2 + \overline{u^2}\ ]$ represents the flux of momentum per unit mass across

any plane perpendicular to the jet axis, while the remaining terms arise from the streamwise pressure gradient.

Conservation of angular momentum in axial direction:

The integral equation governing angular momentum can be derived in a similar manner. First multiply equation 3.3 by W and add it to equation 3.9 to obtain:

$$\frac{\partial}{\partial x}UW + \frac{\partial}{\partial x}\overline{uw} = -\frac{1}{r^2}\frac{\partial}{\partial r}(r^2 VW) - \frac{1}{r^2}\frac{\partial}{\partial r}(r^2 vw) \tag{3.16}$$

Then multiply to r^2; i.e.,

$$\frac{\partial}{\partial x}\left(r^2(UW + \overline{uw})\right) = -\frac{\partial}{\partial r}\left(r^2(VW + \overline{vw})\right)$$

The final angular momentum integral is obtained by integrating over r:

$$\frac{d}{dx}\left(\int_0^\infty 2\pi[UW + \overline{uw}]r^2 dr\right) = -\left[2\pi r^2(VW + \overline{vw})\right]_0^\infty$$

with boundary conditions,

$$\begin{aligned} \text{For} \quad r = 0 \quad &\longrightarrow \quad V = W = \overline{uv} = 0 \\ \text{For} \quad r = \infty \quad &\longrightarrow \quad U = W = \overline{uv} = \overline{vw} = 0 \end{aligned}$$

The right-hand side of the equation vanishes leaving:

$$-\left[2\pi r^2(VW + < vw >)\right]_0^\infty = 0.$$

So the left hand side of the equation yields immediately:

$$\frac{d}{dx}\int_0^\infty 2\pi[UW + \overline{uw}]r^2 dr = 0 \tag{3.17}$$

Again integrating from the source to any streamwise location yields the following angular momentum integral constraint:

$$G_o = 2\pi\int_0^\infty [UW + \overline{uw}]r^2 dr \tag{3.18}$$

3.3 Basic scaling parameters

3.3.1 Streamwise and angular momentum conservation

The basic equations have been carefully reconsidered recently by Ewing [1999] and Shiri et al. [2008]. Of primary concern were the two fundamental integrals of the RANS equations for the fully developed asymptotic turbulent swirling jet derived above. The first is M_x, which is the total rate of transfer of kinematic linear momentum across any downstream plane, say at location x. As shown above, at high Reynolds numbers and in the absence of an external flow, this reduces to:

$$M_x(x) = M_o = 2\pi\int_0^\infty \left[U^2 - \frac{W^2}{2} + \overline{u^2} - \frac{\overline{v^2} + \overline{w^2}}{2}\right] r dr \tag{3.19}$$

Moreover, since there are no net forces other than pressure (which is accounted for in 3.19) acting on any control volume containing this plane and the exit plane of the jet, M_x must remain equal to its source value M_o at all downstream positions x.

The second fundamental parameter $G_\theta(x)$ is the rate which kinematic angular momentum is swept across any downstream plane. From integration of the angular momentum equation with the same assumptions as above, this was shown above to reduce to:

$$G_\theta(x) = G_o = 2\pi \int_0^\infty [UW + \overline{uw}]r^2 dr. \tag{3.20}$$

Like the linear momentum, $G_\theta(x)$ should remain constant at its source value, G_o, since in an infinite environment there are no torques acting on any control volume containing the source plane nor any plane that cuts perpendicularly through the jet axis.

3.3.2 The effect of mass addition at the source

A third integral provides the rate at which volume (kinematic mass) is swept across any downstream plane:

$$m_x(x) = 2\pi \int_0^\infty U r dr. \tag{3.21}$$

Unlike M_x and G_θ, as noted above (and in the previous chapter), m_x is not constant at the rate at which kinematic mass is being added at the source, m_o, since mass is being continually entrained by the jet. Nonetheless, in non-swirling jets, m_o (together with M_o) sets the virtual origin of the jet (George [1989]), since it imposes a length scale, D_* , at the exit plane. D_* is the effective diameter defined by

$$D_* = \sqrt{\frac{m_o^2}{M_o}}. \tag{3.22}$$

In fact it is the ratio of the axial distance, x to this length scale that measures the evolution of the near jet into the far jet. In particular, it is only when $x >> D_*$ that the asymptotic free jet can be reached. Or said another way: only when the mass entrained by the turbulence overwhelms that added at the source close the jet is the asymptotic state attained. For top-hat jets of diameter D, this state seems to be achieved for $x/D > 30$.

Addition of mass at the source also introduces a velocity scale, U_*, into the problem. U_* is defined by

$$U_* = \frac{M_o}{m_o}. \tag{3.23}$$

Both D_* and U_* can be replaced by simply the exit diameter D and exit velocity U_o **if (and only if)** the exit profile has top-hat form (i.e., uniform velocity across the exit plane). This is easy to see since in the top-hat case

$$D_* = \frac{\sqrt{\pi}}{2} D, \tag{3.24}$$

$$U_* = U_0. \tag{3.25}$$

Much confusion in the history of the study of turbulent jets has resulted from the failure to recognize the importance of using D_* and U_* if the exit profile is not a top-hat. And often alleged effects of source conditions can be eliminated with proper scaling. As will be shown below, proper scaling becomes even more important when swirl is introduced, since the effect of G_o is to introduce yet another length scale into the problem.

3.3.3 The role of swirl

It is easy to show that addition of both linear and angular momentum imposes another length scale, L_*, onto the flow, even without mass addition at the source (i.e., point sources of linear and angular momentum). L_* can be defined as

$$L_* = \frac{G_o}{M_o}. \tag{3.26}$$

It is immediately obvious that, if mass is also added, then another length scale ratio, the so-called swirl number, can be defined

$$S_* = \frac{G_o}{M_o D_*}\sqrt{\pi}. \tag{3.27}$$

Note that the factor of $\sqrt{\pi}$ has been inserted into equation 3.27 to make it reduce to the usual definition for top-hat exit profiles (which seldom can be achieved when swirl is present); i.e.,

$$S = \frac{2G_o}{M_o D} = \frac{L_*}{D_*}\sqrt{\pi}. \tag{3.28}$$

Clearly we should expect L_* to replace D_* as the length scale governing downstream behavior only when the swirl number is large (in much the same manner that x replaces D_* for the far non-swirling jet). Since (as will be reviewed below) the effect of angular momentum on the flow diminishes as the flow evolves downstream, at low swirl numbers, L_* will provide an indication of a measure of at most a change in the virtual origin of the asymptotic swirling jet.

3.4 Equilibrium similarity implications for the far swirling jet

The similarity of the asymptotic swirling axisymmetric jet has recently been reconsidered by Ewing [1999], Shiri [2006], Shiri et al. [2008]. These theoretical results will prove to be crucial in interpreting the measurements presented later. The primary differences from the non-swirling axisymmetric jet are the need to consider the additional moments W, $\overline{uw}$, $\overline{vw}$, and the angular momentum integral constraint.

The most important results of the equilibrium similarity analysis of the swirling axisymmetric jet can be summarized as follows.

- The profiles of mean streamwise velocity and turbulence normal stresses can be described by single length and velocity scales. The convenient choices (and those used to scale the data in this paper) are U_c, the centerline velocity, and $\delta_{1/2}$, the velocity half-width (defined as the distance from the centerline to the point at which the mean velocity falls to half its centerline value). Thus the normalized radial coordinate is $\eta = r/\delta_{1/2}$, exactly like the non-swirling jet.

- The spreading rate of the asymptotic jet is linear; i.e.,

$$\delta_{1/2} = A(x - x_o), \tag{3.29}$$

  where x_o is a virtual origin which can depend on the Reynolds number and swirl number. The coefficient A (or $d\delta_{1/2}/dx$) can in principle at least depend on the jet exit conditions. Both sides can be normalized by D_*, but normalization by D introduces a dependence

on the exit profile (which can be non-uniform with swirl). Note that, if done rigorously, the result of equation 3.29 is not particularly straightforward to obtain, but follows from a detailed consideration of the Reynolds shear stress equations and the behavior of the dissipation George [1989], Hussein et al. [1994].

- The Reynolds shear stress, $\overline{uw}$, scales with $U_c^2 d\delta_{1/2}/dx$. The linear growth of the far jet implied by equation 3.29 means that the factor of $d\delta_{1/2}/dx$ is constant, so these moments scale the same as the turbulence intensities. However, it should be noted that the dependence of the coefficient on upstream conditions means that scaled profiles may differ from experiment to experiment.

- From the conservation of linear momentum, equation 3.19, it follows immediately that the mean centerline velocity falls asymptotically inversely with increasing $\delta_{1/2}$. Although this is well-known George [1989], Hussein et al. [1994] it is instructive to review briefly the reasons since similar considerations apply to the angular momentum considered below. First ignore for the moment the swirl and turbulence contributions and substitute the similarity profile for the mean velocity into equation 3.19 to obtain

$$M_x = [U_c^2 \delta_{1/2}^2]\ 2\pi \int_0^\infty f^2\ \eta d\eta, \tag{3.30}$$

where $\eta = r/\delta_{1/2}$ and $f = U/U_c$. Since the integrand depends only on the similarity variable η that is integrated over the entire domain, all of the x-dependence on the right-hand side is in the square-bracketed term. But the left-hand side is equal to a constant since $M_x = M_o$. Therefore, U_c must be inversely proportional to $\delta_{1/2}$; i.e.,

$$U_c \propto \delta_{1/2}^{-1}. \tag{3.31}$$

Inclusion of the turbulence terms only modifies the constant of proportionality, since they too can be shown to scale with U_c^2. The swirl contribution (from the radial pressure gradient), $W^2/2$ will be shown below to vanish downstream relative to the other terms, so the effect of its omission decreases with distance. Combining equations 3.30 and 3.31 with the linear growth rate of equation 3.29 implies that

$$U_c = B_u \frac{{M_o}^{1/2}}{(x - x_o)}, \tag{3.32}$$

where B_u is a constant. In fact B_u and A can not be independent, but must also be linked to each other and the shape of the profile through equation 3.19. Alternatively the centerline velocity can be normalized by U_*:

$$\frac{U_*}{U_c} = \frac{1}{B_u}\Big[\frac{x}{D_*} - \frac{x_0}{D_*}\Big]. \tag{3.33}$$

Note that U_o can be also used if the exit profile is top-hat; but if it is not, this introduces an artificial dependence on jet exit conditions.

- The mean azimuthal (or swirl) velocity component scales with its maximum value at any cross-section, W_{max}, **and falls off as the inverse square of $\delta_{1/2}$ (or $x - x_o$).** This is a surprising result (originally shown by Ewing [1999]), but can be seen immediately by

substituting similarity profiles for the mean velocity, say $U/U_c = f(\eta)$, $W/W_{max} = g(\eta)$, into the angular momentum integral of equation 3.20. Since $\overline{uw}$ is negligible, the result is:

$$G_x = [U_c\, W_{max}\, \delta_{1/2}^3\,]\; 2\pi \int_0^\infty f\; g\; \eta^2 d\eta. \tag{3.34}$$

The integral in similarity variables can at most depend on the exit conditions and is independent of x. Also the left-hand side is constant since conservation of angular momentum requires that $G_x = G_o$. Using equation 3.32 implies:

$$W_{max} \;\propto\; [U_c\, \delta_{1/2}^3\,]^{-1} \;\propto\; [\delta_{1/2}]^{-2} \tag{3.35}$$

It follows immediately from equation 3.29 that the swirl velocity, W_{max} falls off inversely with the square of the downstream distance. Combining equation 3.34 with 3.32 and 3.29 yields

$$W_{max} = C\frac{G_o}{{M_o}^{1/2}(x - x_o)^2} \tag{3.36}$$

where C is a constant (at most dependent on the jet exit conditions). Note that, just as A and B are linked by the linear momentum integral, C is linked to both by the angular momentum integral.

Since the mean velocity falls off only inversely with distance, but the swirl falls off as inversely with the square of distance, the swirl should appear to die off. This is exactly what was noted in the experiments of Gilchrist and Naughton [2005]: the swirl dies off downstream. Moreover, as first pointed out by Ewing [1999], this means the asymptotic swirling jet should behave exactly as a non-swirling jet, with at most different values of A, B and C that could in turn depend only on the jet exit conditions. A particular goal of the experiments described below was to test if and how these things happen.

Note the fact that the swirl appears to die out relative to the streamwise flow does not mean it is gone: angular momentum is still being conserved, it's just being spread over a larger area. As a consequence the swirl (or azimuthal mean equation) uncouples itself and plays no role in the evolution of the streamwise and radial equations which behave as though the jet were non-swirling.

Chapter 4

Jet Experimental Facility and Measurement Methods

This chapter describes the swirling jet facility and the velocity measurement methodology used in this experiment. Also the details of the measurement procedure and the boundary condition of the experiment will be discussed.

4.1 Experimental Setup

A two-component LDA (Laser Doppler Anemometer) was used to measure the instantaneous velocity field. Measurements were carried out in different cross-sections of the jet, starting from the jet nozzle up to 50 diameters from it. A traversing system was used for displacing the LDA probe in the three Cartesian coordinates. Two series of measurement were carried out. The first measured the streamwise and tangential velocities at $x/D = 5, 10, 20, 25, 30, 35, 40, 50$ by traversing the LDA lens horizontally. The second series of measurement was carried out at $x/D = 28, 30, 32$ by traversing the lens along radii both horizontally and vertically in order to obtain velocity statistics of all three velocity components: streamwise, radial and tangential. All the measurements were carried out for three different swirl conditions: $S = 0.25, 0.15$ and non-swirling.

4.1.1 Swirling Jet Facility

An existing facility, previously used by Hussein et al. [1994], was modified to produce both axial and tangential velocity components in an air jet flow. Two *fifth-order polynomial* contractions were used to accelerate the flow from the settling chamber into the jet exit, which was of diameter $D = 25.4mm$ (one inch), as shown in figure 4.1. The streamwise velocity of the jet exit for the non-swirling case was nearly a laminar top-hat profile flow (c.f. Shiri et al. [2008]). When swirl was added to the main flow, the tangential velocity component had an approximately solid-body distribution in the core region of the nozzle exit, but the streamwise profile was modified from a top-hat shape slightly as well. The exit profiles for all three swirl conditions are presented later with the experimental results.

One main centrifugal blower was used to supply axial flow, and six $15mm$ injectors connected to a second blower added the swirling component independently. These two fans were controlled by separate frequency converters so that the air speed and the strength of the swirl

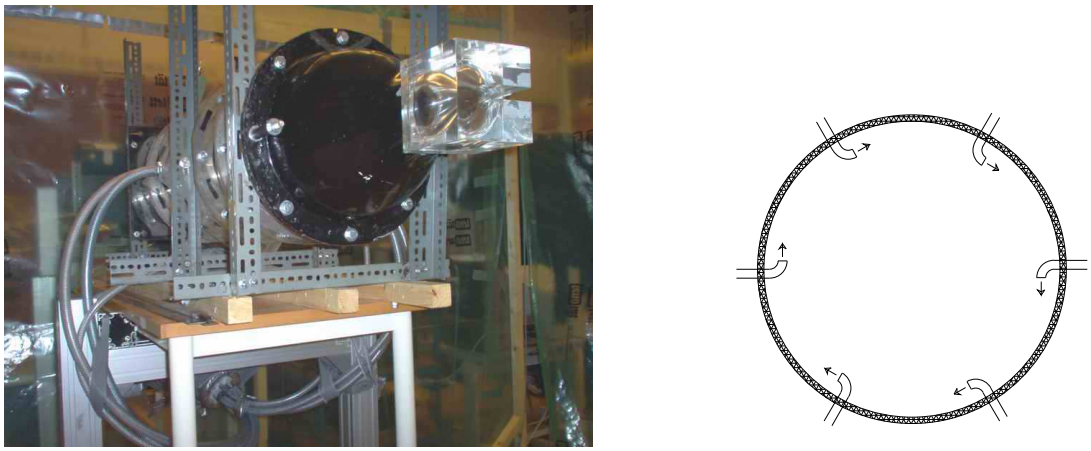

(a) (b)

Figure 4.1: (a) The swirling flow inside the tunnel converted into a $25.4\ mm$ (one inch) axisymmetric jet using two contractions; (b) The arrangement of the swirl nozzles.

could be adjusted by changing the rotational speeds of two blowers.

As shown in the schematic of the jet apparatus (figure 4.2), the main flow first exhausts into a diffuser, then passes through a pack of straws in order to eliminate all the large scale vortices generated by the blower and transferring pipes. In the next section the swirl flow is added at through 6 nozzles which were positioned tangentially in the inner circumference of the tunnel. The transferring pipes of the swirl nozzles were connected to a pressurized section, which can be seen in figure 4.1. Three sets of screens were positioned after the swirl injectors to dampen any large scale turbulence

The visualization of the jet from the side shown in Figure 4.3 was obtained by heavily seeding the jet flow. The potential core and developing region of the jet flow, as explained in chapter 3, are clearly visible.

The average streamwise velocity of the flow used in the experiment was $28\ m/s$, corresponding to a *Reynolds* number of $40,000$ with a turbulence intensity of 2%. The higher turbulence intensity of the flow produced compared to the original facility ($\sim 0.58\%$, reported by

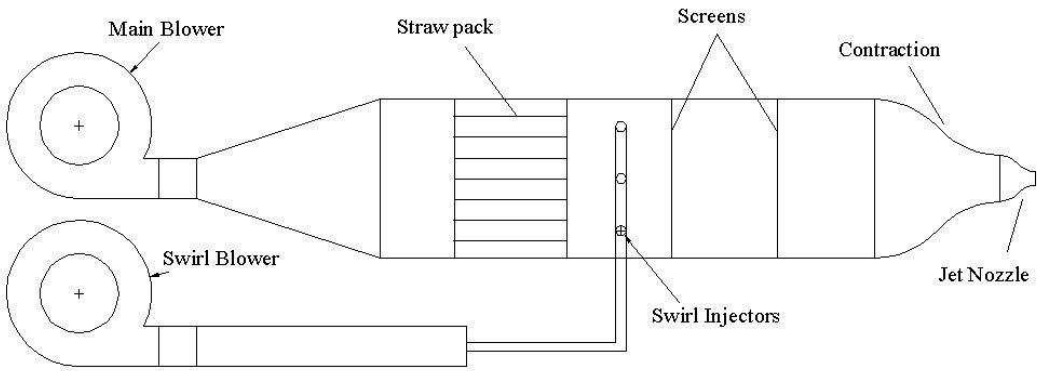

Figure 4.2: Schematic of the swirling jet facility.

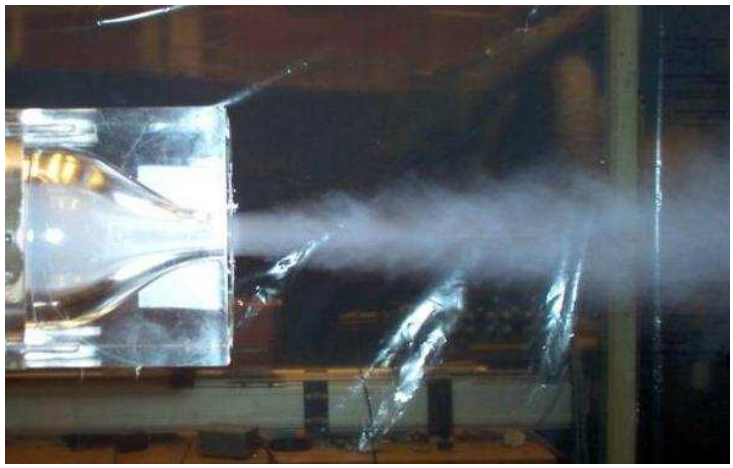

Figure 4.3: Smoke visualization of swirling jet used in experiments.

Hussein et al. [1994]) was due to the disturbances created by the swirl injectors. The exit velocity profile's shape changes with the strength of the swirl, therefore the *Reynolds* number at the exit varies slightly considering the effective diameter, D_* (see chapter 3). More details about the experimental facility can be found in Shiri [2006] and Hussein et al. [1994].

4.1.2 Boundary Conditions and Controlling the Experiment

As noted by Hussein et al. [1994] (see especially the appendix), there can be significant differences between a jet in a confined or semi-confined enclosure and one in an infinite environment because of the re-circulating flow entrained by the jet. The enclosure was needed to provide the approximately statistically uniform distribution of seeding particles necessary for the LDA measurement technique (c.f., Buchhave et al. [1979]). It also eliminated any disturbances from the working environment of the laboratory. A $10m \times 3.5m \times 3.5m$ size structure of plastic sheet was built around the jet facility. A closed loop circulation was achieved by placing the blower inlet inside the tent, but far upstream from the jet exit.

The jet was positioned along the centerline of the enclosure in order to be as far as possible from the side walls (and floor and ceiling). If the radial extension of the jet were too close to the surrounding walls, the entrainment would not appear to enter the jet from infinity in a radial direction. Instead it would be adversly influenced by the backward flow in the outer region which compensates for the entrainment from downstream. This reversed flow created by confinement progressively decreases the net momentum integral across the jet downstream. Hussein et al. [1994] suggested that the momentum loss due to confinement can be estimated as:

$$\frac{M_x}{M_o} = \left[1 + \frac{16}{\pi . B_u^2} \left(\frac{x}{D}\right)^2 \frac{A_o}{A_R}\right]^{-1} \tag{4.1}$$

where M_x is the momentum integral at the distance x from the jet exit with the diameter D and initial flow momentum of M_o. A_o/A_R is the ratio of the jet nozzle to the enclosure cross-sectional area, and B_u is defined as the velocity profile growth constant in chapter 3. From this experiment, $B_u = 6.87$; therefore at a distance of $x/D = 50$, the momentum loss can be estimated as $M/M_o \approx 0.99$. The estimated loss is below our ability to measure it, a fact

confirmed in the experiments by evaluating the momentum conservation along the jet axis as presented in chapter 5.

4.2 The Velocity Measurement in Turbulent Free Shear Flows

The main characteristic of free shear flows is their mixing ability. This arises from the high turbulence intensity of such flows, especially near their outer boundaries. Among all the methods used to measure instantaneous velocity and velocity correlations in high turbulence level shear flows like jets, laser Doppler anemometry is the most reliable.

The laser Doppler anemometer will be described in detail in chapter 11. The same laser and optics were used for both the swirling jet and natural convection boundary layer. The optical lens was set in back-scatter mode in both experiments and the same seeding generation method was used. The seeding was introduced into the jet through the main stream fan and allowed to run for a very long time before measurements were taken. This ensured that the flow was uniformly seeded, thereby avoiding any bias in velocity measurements in the outer intermittent region. The focal length of the lens was the same, but in the jet experiment the probe volume of the LDA created by the intersecting laser beams was made smaller ($< 50\ \mu m$) by using a different beam expander in order to have a better special resolution.

A two-component LDA system (Dantec) was used in a backscatter arrangement for the present study. The flow was seeded with an aerosol and bursts produced by particles passing through the control volume were analyzed by Dantec BSA burst processors. The sampling rate of the LDA system was not fixed, but rather a "burst" mode was used where all particles were sampled as they arrived. The particles were produced by SAFEX fog generator which generates a dense white fog by evaporation and condensation of a water-based fog liquid. The mean droplet size was around $1\mu m$ and a closed loop circulation of air kept the particle density constant during the measurement. The particle time constant was estimated to be approximately $2.5\ \mu s$ that can be compared to the smallest Kolmogorov microtime, ($\tau = (\nu/\epsilon)^{0.5}$) at $x/D = 30$, estimated using the results of the energy balance in chapter 5 as $450\ \mu s$.

The most notable effect of the additional swirl velocity component was a diminished particle concentration in the core of jet compared to non-swirling jet. Since this was also the region where the mean flow gradients were the smallest, it was believed to not adversely affect the results.

4.3 Statistical Uncertainty

All statistical moments were computed using the residence time weighting algorithms (Buchhave et al. [1979], George [1988]) as employed by Hussein et al. [1994]. For the measurements at $x/D = 30$, a fixed sampling period of 600 seconds was used. At most locations, the actual number of samples was at least 150,000 at each point in the high velocity regions, and more than 10,000 in regions where the velocity was less than one meter per second. The largest estimate of the integral time was 0.1 s., so the minimum number of effectively independent samples was 3000.

The relative statistical error can be estimated as George et al. [1978]

$$\epsilon^2_{\psi_N} = \frac{1}{N_{eff}} \frac{var(\psi_N - \langle\psi\rangle)}{\langle\psi\rangle^2}. \tag{4.2}$$

where ψ is the statistical quantity being estimated and ψ_N is the estimator using N independent estimates.

For the mean flow, $var(\psi_N - \langle\psi\rangle)/\langle\psi\rangle^2$ is just the turbulence intensity squared. For the second moments using Gaussian statistics it is 2, but it increases rapidly to 15 for fourth moments. Using these, the relative statistical error for the mean streamwise velocity U is estimated to be less than 0.3 % (high velocity regions at far-field of jet). It is at most 2 % (at low velocity regions of the jet) for the second moment statistics, but somewhat higher for the third moments. Fourth (and higher) moments were available, but not deemed reliable because of the limited bandwidth of the LDA bandpass filters which removed the tails necessary to compute them.

Most problematical for these measurements was the mean swirl velocity W for which equation 4.2 reduces to

$$\epsilon^2_{W_N} = \frac{1}{N_{eff}} \frac{\langle w^2\rangle}{W^2}. \tag{4.3}$$

The mean square azimuthal velocity $\langle w^2\rangle$ is about equal to the other turbulence normal stresses (and scales with U_c^2), but the expected value of W drops rapidly with increasing x (as noted in preceding chapters). Therefore, even if great care is taken in aligning the optical system to enable accurate measurement of W, statistical errors greatly complicate its determination.

Note that similar problems occur for the measurement of the radial mean velocity, V, which is also very small. But these were overcome in the same manner as in Hussein et al. [1994]; namely by using the continuity equation in similarity variables to compute V from U (at least in the far jet where similarity was established).

Chapter 5

Results of the Experiment

This chapter contains the experimental results for three experiments, two with swirl at the inlet plane, one without (the conditions in three cases were explained in precious chapter). The results have previously been published as Shiri et al. [2008, 2007a,b]. The paper by Shiri et al. [2008] using laser Doppler anemometry showed that the growth rate enhancement due to swirl (c.f. Gilchrist and Naughton [2005]) does not persist in the far-field of a swirling jet flow with moderate swirl numbers (0.15 and 0.25). The results were consistent with the equilibrium similarity theory of Ewing [1999] in which the mean swirl velocity was argued to decrease downstream as $1/(x - x_o)^2$, while the mean stream-wise velocity decreased as $1/(x - x_o)$. The investigation in Shiri et al. [2007a,b] included all three velocity components of the turbulence quantities at a swirl number of $S = 0.25$, and all moments to third order were obtained (except those involving both the azimuthal and radial components simultaneously). As noted by George [1989] , if there were an effect of the source conditions on the similarity profiles, it is in the second and higher moment profiles where it would be expected to appear. The second and third-order moments are quite close to the earlier non-swirling results; some collapse on top of them almost perfectly, others show a slight difference.

Regardless, the results should be of considerable interest, since many of the quantities measured are those which must be modeled in all second-order closure models. This evaluation is of particular interest since both the mean azimuthal and mean radial velocities were obtained directly, meaning that both continuity and momentum balances were possible. The swirl is shown to have a negligible effect on the overall Reynolds normal and shear stress balances. Finally they lend additional confidence in the non-swirling jet data of Hussein et al. [1994] who used an earlier generation of LDA equipment.

5.1 Exit Velocity Profiles

The exit velocity profiles for the three cases are shown in figure 5.1. The non-swirling jet has a top-hat axial mean velocity profile at the jet exit. But the swirling jet profiles all exhibit profiles in which the axial velocity peaks at the centreline. Also the magnitude of the centreline velocity relative to the cross-sectionally averaged velocity increases with increasing swirl number. Similar axial profiles for jets with swirl have been observed by Gilchrist and Naughton [2005] and Farokhi et al. [1989]. Panda and McLaughlin [1994] also saw this peak and provided an explanation based on vortex tubes becoming spirals.

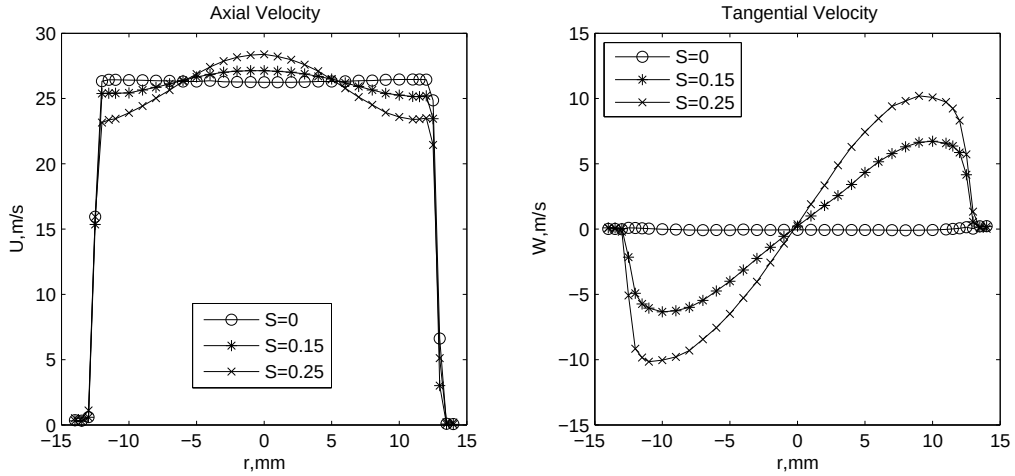

Figure 5.1: Axial and tangential mean-velocity profiles at the jet exit for three different swirl numbers.

The profiles of the azimuthal (or swirl) velocity at the exit, on the other hand, exhibit a simpler behavior. In the core region (about 1/2 of the exit diameter) the swirl velocity for both cases increases nearly linearly with radius; then rolls off smoothly to its maximum value after which it diminishes rapidly to zero at the wall. Clearly the near linear region is close to being in rigid body rotation.

The fact that the exit axial velocity profiles for the two flows differed from the near top-hat of the non-swirling jet means that a simple top-hat scaling with the source exit velocity and diameter is not useful. As noted in the chapter 3 the absence of a simple top-hat profile complicates the scaling of the jet, since its natural length scales are determined by the rates at which mass, momentum and angular momentum are added to the jet at the exit plane. Clearly it is therefore essential to quantify the rates at which mass, momentum and angular momentum were added to the flow, since these are crucial to scaling the data. They are also important for establishing properly the swirl number of each flow.

5.2 Test Cases

A list of the test cases is provided in Table 5.1, where each case has been labeled by its swirl strength, S. The axial and tangential velocities were chosen in order to maintain the same Reynolds number in all three cases: $Re \approx 40,000$. The quantities m_o, M_o and G_o were determined by carrying out their defining integrals (equations 3.13, 3.16 and 3.21). Surveys were made in the following locations downstream ($x/D = 5, 10, 20, 25, 30, 35, 40, 50$) as illustrated in Figure 5.2. In the first set of measurements, the LDA probe was traversed in just a horizontal cross-section of the jet to measure the streamwise and radial velocity components. Then a second set of measurements was performed with the optical probe traversed in both horizontal and vertical directions across the jet cross-section. This method provided all three streamwise, radial and azimuthal velocity components. The second measurement was done just in the locations of $x/D = 28, 30, 32$. Both sets of measurements are reported together below, since there was virtually no difference for the streamwise component.

Table 5.1: Test cases for the present study.

S	$U_{c,0}[m/s]$	$W_{max,0}[m/s]$	$U_*[m/s]$	$D_*[mm]$	M_o	G_o	m_o	S_*
0	26.3	0	25.9	22.7	0.366	0	0.0268	0
0.15	27	6.7	24.8	22.9	0.345	6.75×10^{-4}	0.0260	0.145
0.25	28.4	10	22.9	23.5	0.317	9.66×10^{-4}	0.0252	0.239

5.3 The mean streamwise velocity in the far jet

Figure 5.3 shows the mean axial velocity profiles for all three cases ($S = 0$, 0.15, and 0.25) and the following downstream positions: $x/D_* = 20, 25, 30, 35, 40\ and\ 50$. The mean velocity has been normalized by U_c, its centerline value, and the radial coordinate has been normalized by $\delta_{1/2}$, the jet half-width (determined as described in the next section). In all three cases, the normalized velocities show collapse of the data for all cross sections in the far-field region of the jet. Moreover, there is very little (if any) difference from one set of data to the next. Both of these observations are consistent with the theory presented earlier that the far asymptotic swirling jet should appear to be independent of swirl. The profiles are also in excellent agreement with those reported by Hussein et al. [1994] who used the same facility, before it had been modified for swirl, but at an exit Reynolds number of 100,000. The profiles measured here (see figure 5.4) show slightly higher values of velocity for $r/(x - x_0) > 0.12$, perhaps due to the better LDA hardware (Dantec burst-processor versus the earlier counter). The same differences were also noted recently by Wänström [2009] using PIV.

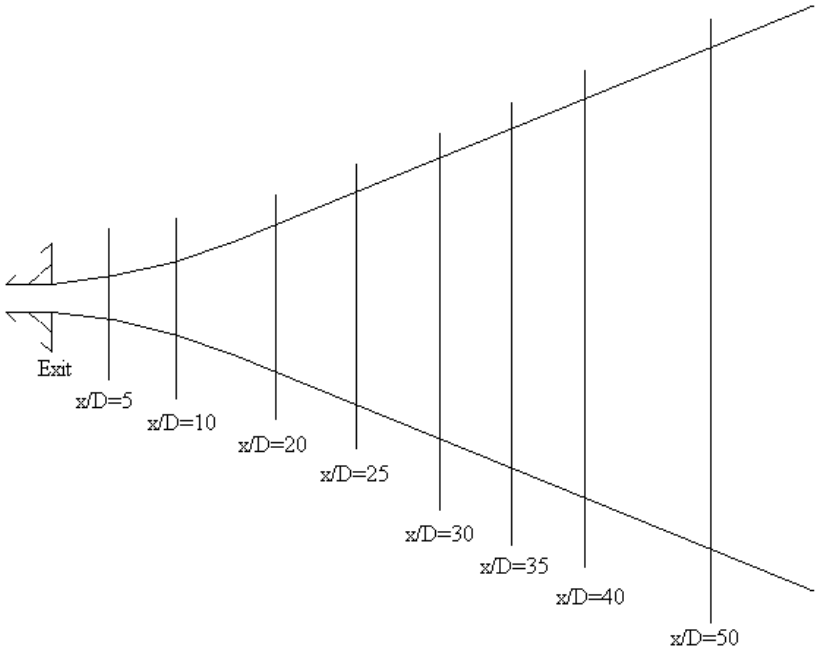

Figure 5.2: Measurement grid for swirling jet experiments.

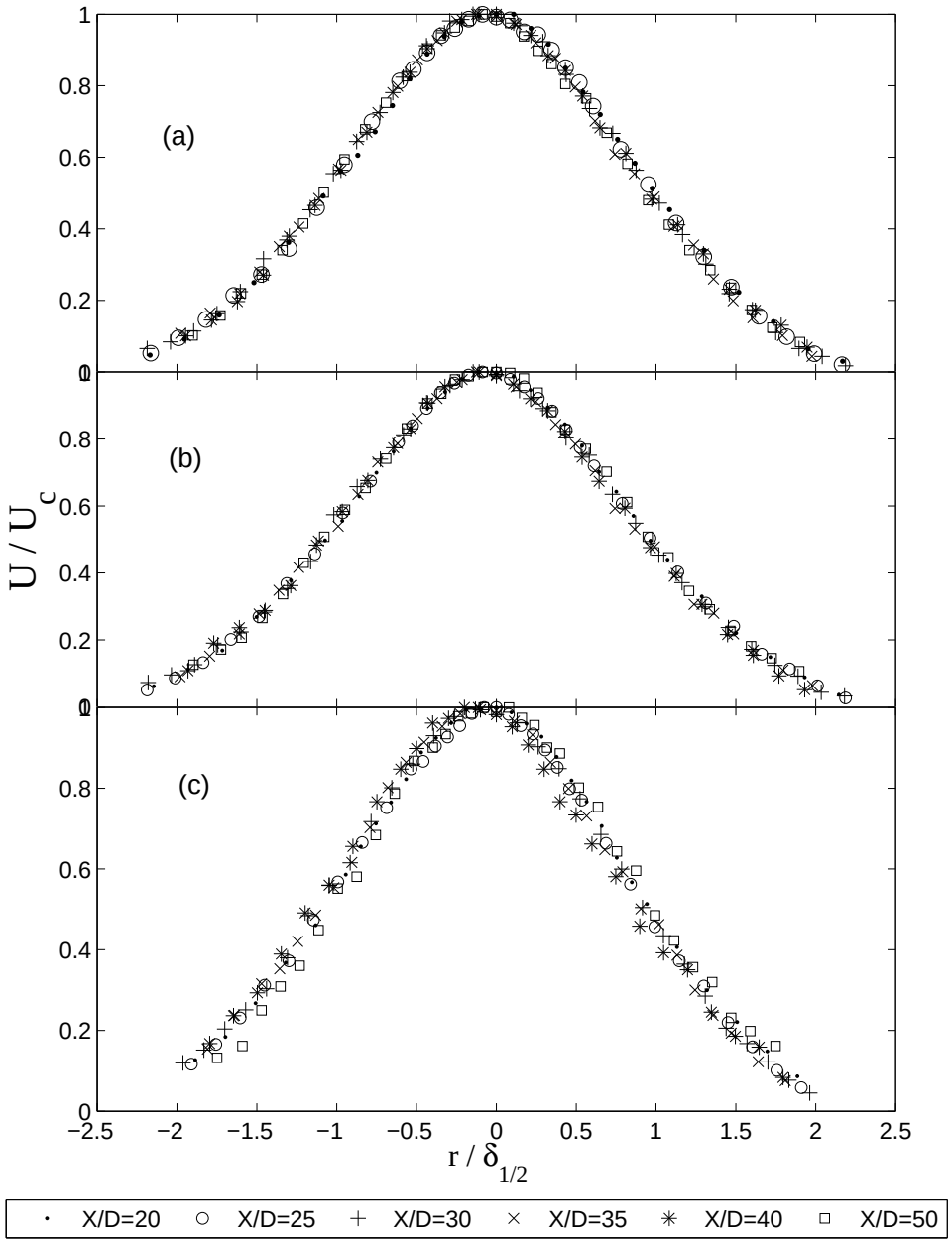

Figure 5.3: Mean streamwise velocity at different axial positions for three different swirl numbers (a) S=0, (b) S=0.15 and (c) S=0.25. The profiles have been normalized by the local mean centerline velocity U_c and the half-width $\delta_{1/2}$.

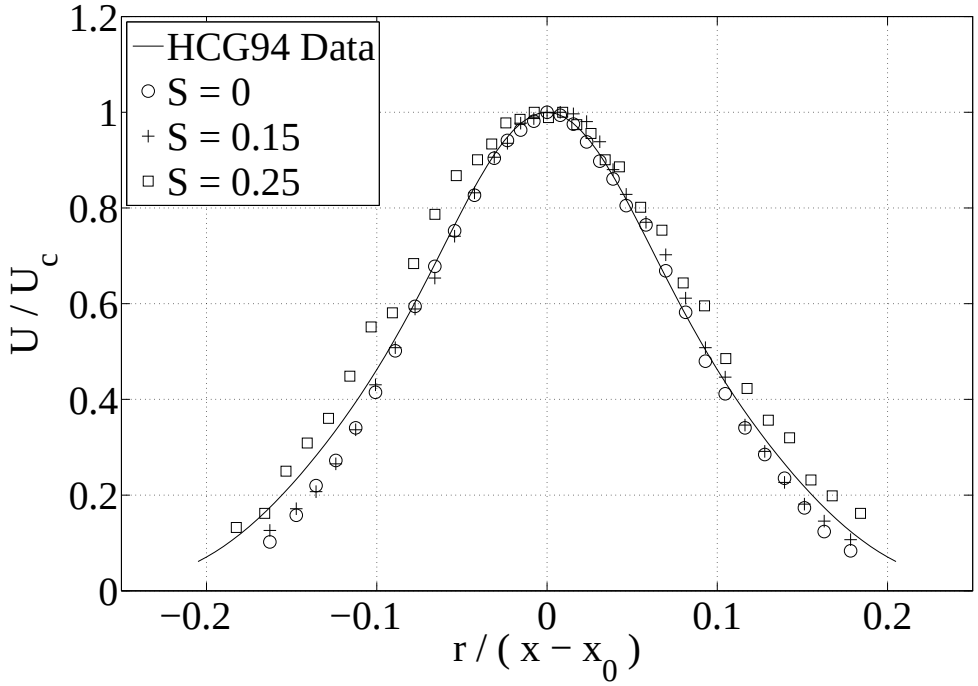

Figure 5.4: Mean streamwise velocity at $x/D = 50$ for three different swirl numbers S=0, S=0.15 and S=0.25 compared with the data presented in Hussein et al. [1994]. The profiles have been normalized by the local mean centerline velocity U_c and the distance from the exit $(x - x_0)$.

5.4 Variation of U_c and $\delta_{1/2}$ with x

The jet velocity half-width is defined as the distance between the centerline and the location where the axial velocity drops to half of the centerline velocity. In order to calculate these values for each curve, the following empirical jet profile was fitted to each profile White [1991]:

$$\frac{U}{U_c} = sech^2\Big(a\frac{r}{x}\Big). \tag{5.1}$$

It is clear from Figure 5.1 that the exit velocity profiles for these swirling jets are not a top-hat profiles, so the centerline velocity at the exit is not representative of the exit flow. Therefore, in order to have a reliable comparison between three different cases, it is necessary to scale the far jet data with the D_* and U_* (defined by equations 3.22 and 3.23 respectively) and summarized in Table 5.1.

The results are shown in Figure 5.5. The solid lines drawn on the figure are regression fits of equation 3.29 with both sides divided by D_*. For all the slope of the curves, A, is 0.093 and the virtual origin is at $x_o = 0.75 - 0.76D_*$. The value of A is very close to the value of $A = 0.094$ in the non-swirling jet of Hussein et al. [1994]. For the same experiment though the virtual origin was at $x_o = 3.5D_*$ ($x_o = 4D$), however, so it is closer to the exit plane for the present experiment. This perhaps reflects the differences in the way the flows were generated, or alternatively simply the inclusion of data for which there was a slight loss in momentum in the earlier experiments which measured farther downstream to $x/D = 100$ (see Appendix 2 of Hussein et al. [1994]). The same regression fit to the $S = 0.25$ case yields 0.093 and -2.9 respectively. This suggests strongly that there is really no statistically significant difference in the

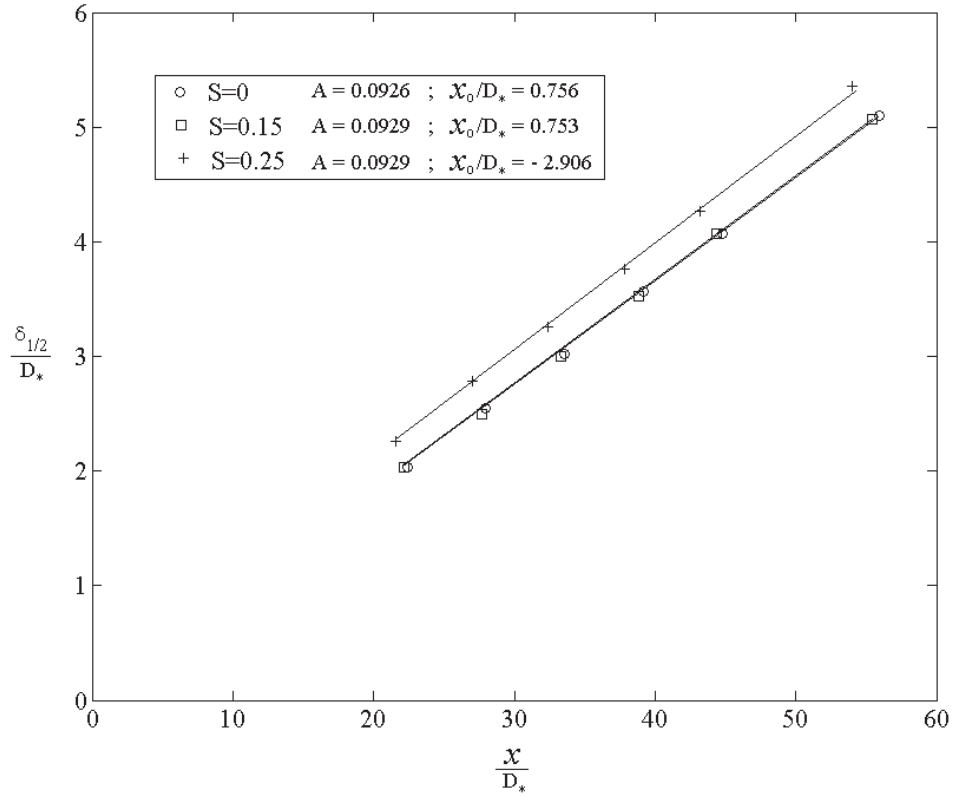

Figure 5.5: Streamwise variation of the velocity profile half-width plotted as $\delta_{1/2}/D_*$ versus x/D_*.

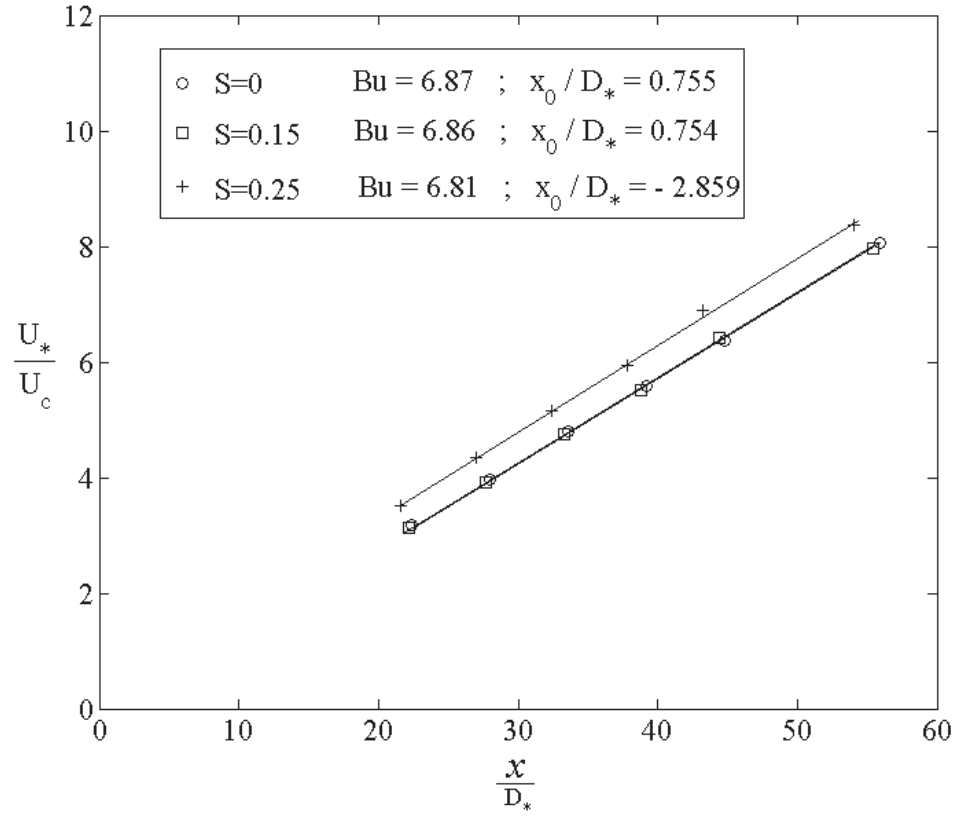

Figure 5.6: Streamwise variation of centerline mean velocity plotted as U_*/U_c versus x/D_*.

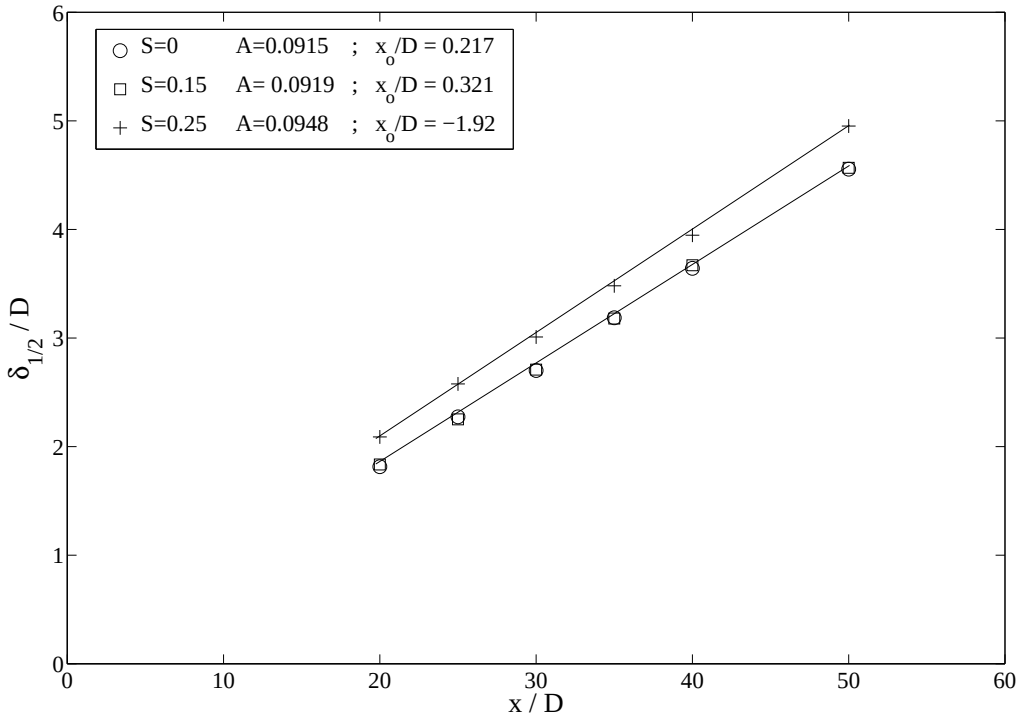

Figure 5.7: Streamwise variation of the velocity profile half-width normalized with D.

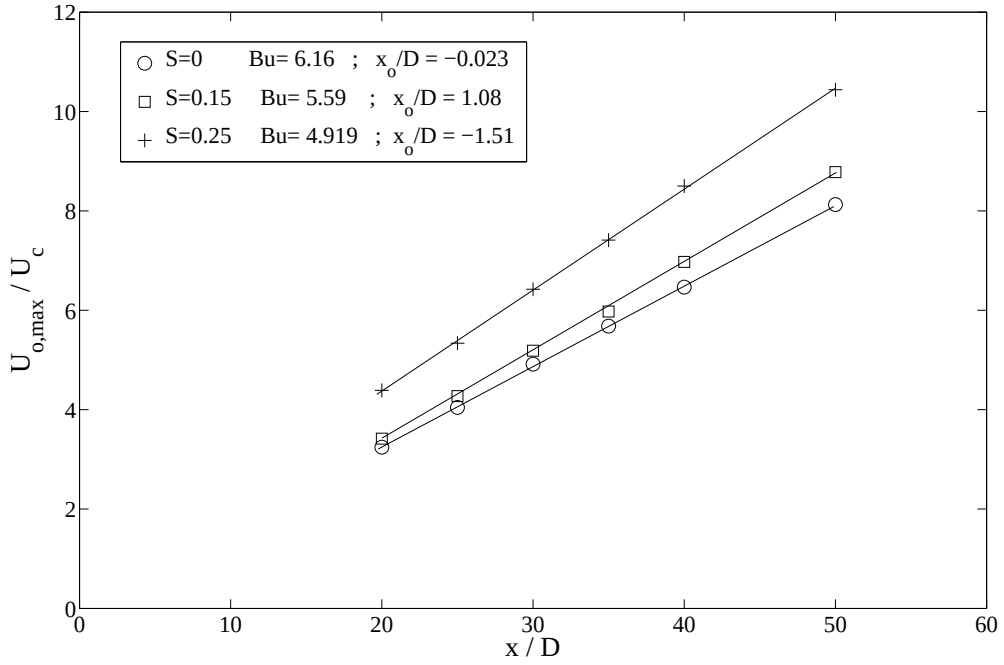

Figure 5.8: Streamwise variation of centerline mean velocity normalized with $U_{o,max}$ and D.

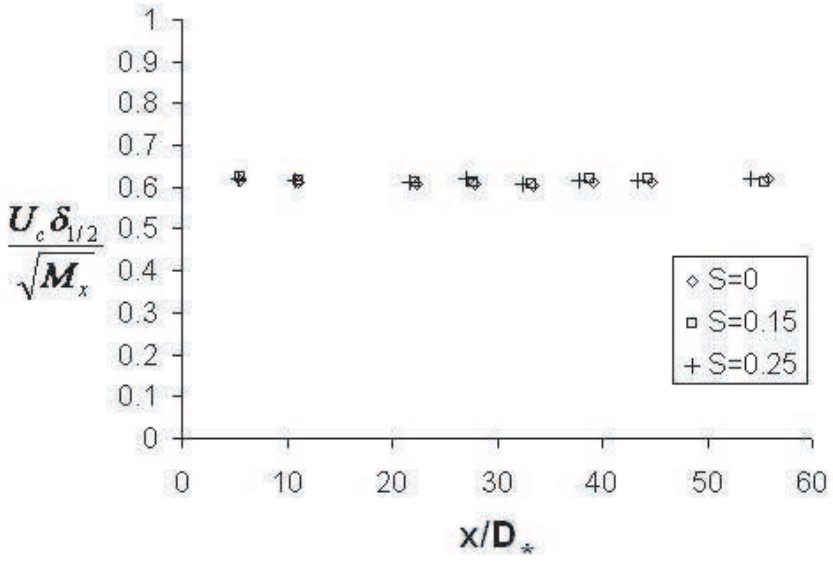

Figure 5.9: Plot of $U_c^2 \delta_{1/2}^2 / M_o$ versus x/D_* for all three swirl numbers.

spreading rate for the three swirl values. There is most certainly, however, a change in virtual origin, which even with the modified curve fit has moved from the zero and low swirl values to $x_o = -2.9 D_*$, which means it is upstream of the exit plane. The fact that there are no differences at all when the flow has low swirl number is consistent with the earlier observations that the swirl number must exceed certain value (between $S = 0.15$ and $S = 0.25$) for any effect to be noticed on the near field, e.g., Gilchrist and Naughton [2005].

The mean streamwise centerline velocity is plotted as a function of downstream location in Figure 5.6 in the region where the jet can be assumed to be self-preserving ($x/D_* > 20$). The solid lines shown are regression fits of equation 3.33. Since the local centreline velocity appears in the denominator of the ordinate, the $1/(x - x_o)$ decay rate is manifested as a straight line in the figure, the slope of which is $1/B_u$. For the $S = 0$ and $S = 0.15$ jets, the values of B_u are nearly identical at 6.87 and 6.86 respectively, and the virtual origins are the same at $x_o/D_* = 0.75$. (Note that the virtual origins are the same as for the curve fits to $\delta_{1/2}$, *as they must be*.) The regression fit to the data for the $S = 0.25$ case yields a slightly smaller value of $B_u = 6.81$ case with a virtual origin of -2.9. Therefore the data as plotted behave according to the expected linear functions of the axial distance. To within the statistical error, there is no change in either the spreading rate or the rate at which the centerline velocity decays, other than the change in virtual origin for the $S = 0.25$ case. These values are slightly higher than then equivalent value from Hussein et al. [1994], which when converted from D_* to D yield B_u = 6.55. This is perhaps due to the slightly higher Reynolds number of the latter, but is within the uncertainty in the integration of the profiles at the exit plane.

The importance of using properly normalized profiles is illustrated in Figures 5.7 and 5.8 from Shiri [2006], which shows the same data normalized in the more traditional manner using the maximum exit velocity and the jet diameter. The effects of the exit profile on the downstream development, especially for the highest swirl number, are very much in evidence, suggesting a significant dependence on exit conditions. This effect vanishes when the data are plotted with proper normalization.

5.4.1 Streamwise momentum integral constraint on mean velocity

Before leaving this section it should be noted that all values of the parameters chosen above satisfy the constraint imposed by the similarity form of the linear momentum conservation expressed by equation 3.30 of the previous chapter. As shown in Figure 5.9, for all three data sets, $A^2 B_u^2 \approx 0.405 \pm 1\%$. This constancy, together with the collapse of the profiles in similarity variables, is a necessary consequence of momentum conservation. Moreover, it confirms that the jet is behaving as a jet in an infinite environment with no co-flow (c.f. Hussein et al. [1994], George [1995]).

5.5 The mean swirl velocity and angular momentum conservation

As noted in the preceding chapter, the measurement of mean azimuthal (or mean swirl) velocity, W, was by far the most difficult part of the experiment. The direct measurements normalized by the centerline mean velocity are shown in Figure 5.10. Because W is almost two orders of magnitude less than the streamwise mean velocity at the locations of interest, even fractions of a degree difference in the alignment of the laser beams introduces significant errors. Also because of the very low value of W compared to $\langle w^2 \rangle$, there is considerable scatter in the results purely because of the statistical error. (In fact the relative statistical error is infinite near the center where $W = 0$).

Nonetheless, by trying to account for the small offset near the origin and fairing curves through points near the local maxima, it was possible to make an estimate of W_{max} for each of the two values of S, and this was invaluable in evaluating the theory. From conservation of angular momentum and equilibrium similarity it was argued in Chapter 3 that W_{max} is described by equation 3.36, and falls off with increasing x as $1/(x - x_o)^2$. Since U_c (described by equation 3.32) falls as only $1/(x - x_o)$, then $U_c/W_{max} \propto (x - x_o)$. Also all of the integrals in similarity variables have constant values (since the normalized profiles are independent of x); hence the values of C (and B_u) should be independent of swirl. It follows immediately that the slope of U_c/W_{max} should be proportional to M_o/G_o; i.e.,

$$\begin{aligned} \frac{U_c}{W_{max}} &= \frac{C}{B_u} \frac{M_o}{G_o} (x - x_o), \\ &= \frac{C}{B_u} S_*^{-1} \left[\frac{(x - x_o)}{D_*} \right]. \end{aligned} \tag{5.2}$$

Thus the higher the swirl number, the farther downstream for the swirl to die off relative to the jet centerline velocity. Alternatively, from the definition of L_* in equation 3.26, it follows immediately that

$$\frac{U_c}{W_{max}} = \frac{B_u}{C} \frac{(x - x_o)}{L_*}. \tag{5.3}$$

Thus the role of L_* as a second length scale is clear: it measures the distance for the swirl mean velocity to die off.

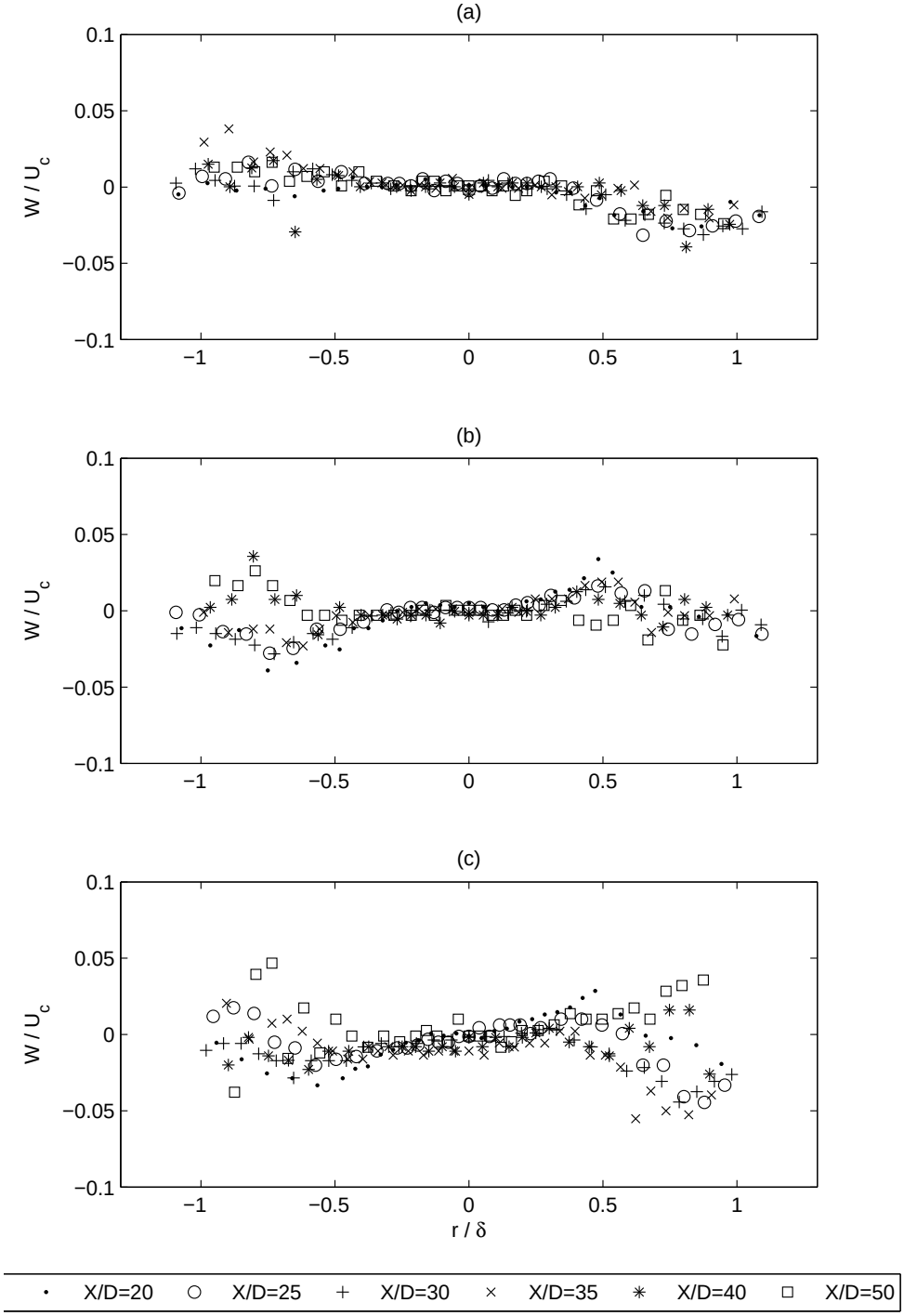

Figure 5.10: Profiles of W/U_c versus $r/\delta_{1/2}$ for $S = 0$, $S = 0.15$ and for $S = 0.25$

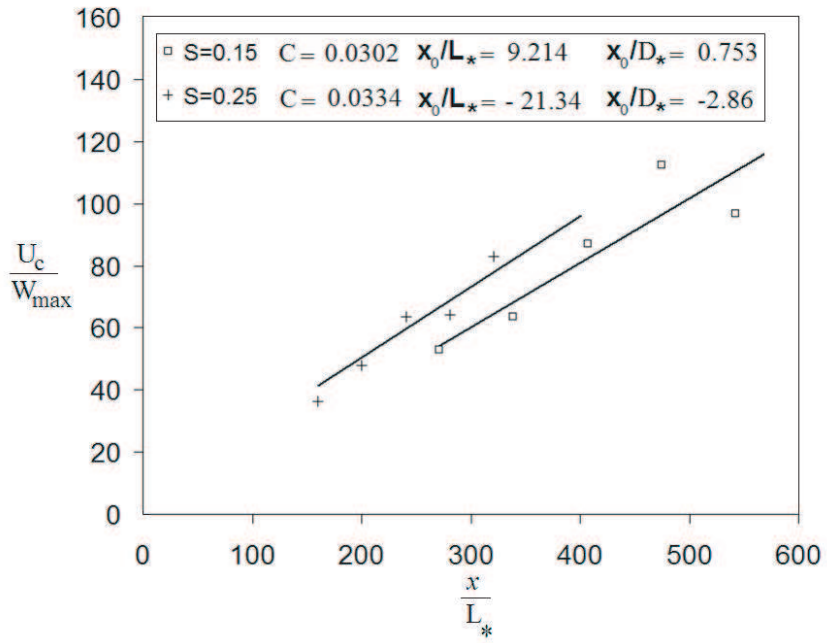

Figure 5.11: U_c/W_{max} versus x/L_* using the same virtual origins as before; i.e, for $S = 0.15$, $x_o = 0.75$ and for $S = 0.25$, $x_o = 2.9$

Figure 5.11 plots U_c/W_{max} versus x/D_*. The fitted lines in the figure use the same virtual origins obtained above for the $S = 0.15$ and 0.25 cases; i.e., $x_o = 0.75$ and -2.9 respectively. From the considerations of the preceding paragraph, the ratio of the slopes of the two plots should be equal to the the ratio of the values of G_o/M_o itself, which is 0.59. The individual slopes are 0.395 and 0.593 respectively so the ratio of which is 0.66. Remarkably, this is well within the experimental error of the expected value of 0.59. Thus in spite of the considerable scatter in the measurement of W and the data presented in Figure 5.11, the overall inferences from them are consistent with Ewing's theory (Ewing [1999]).

5.6 Turbulence higher moments

The investigation included all three velocity components of the turbulence quantities at a swirl number of $S = 0.25$, and all moments to third order were obtained (except those involving both the azimuthal and radial components simultaneously). As noted by George [1989], if there were an effect of the source conditions on the similarity profiles, it is in the second and higher moment profiles where it would be expected to appear. Some of the results are shown in Figures 5.12 and 5.13, together with the earlier measurements of Hussein et al. [1994] in the same jet (but without swirl). The second and third-order moments are quite close to the earlier non-swirling results. Regardless, the results are of considerable interest, since many of the quantities measured are those which must be modeled in all second-order closure models. This evaluation is of particular interest since both the mean azimuthal and mean radial velocities were obtained directly, meaning that both continuity and momentum balances were possible.

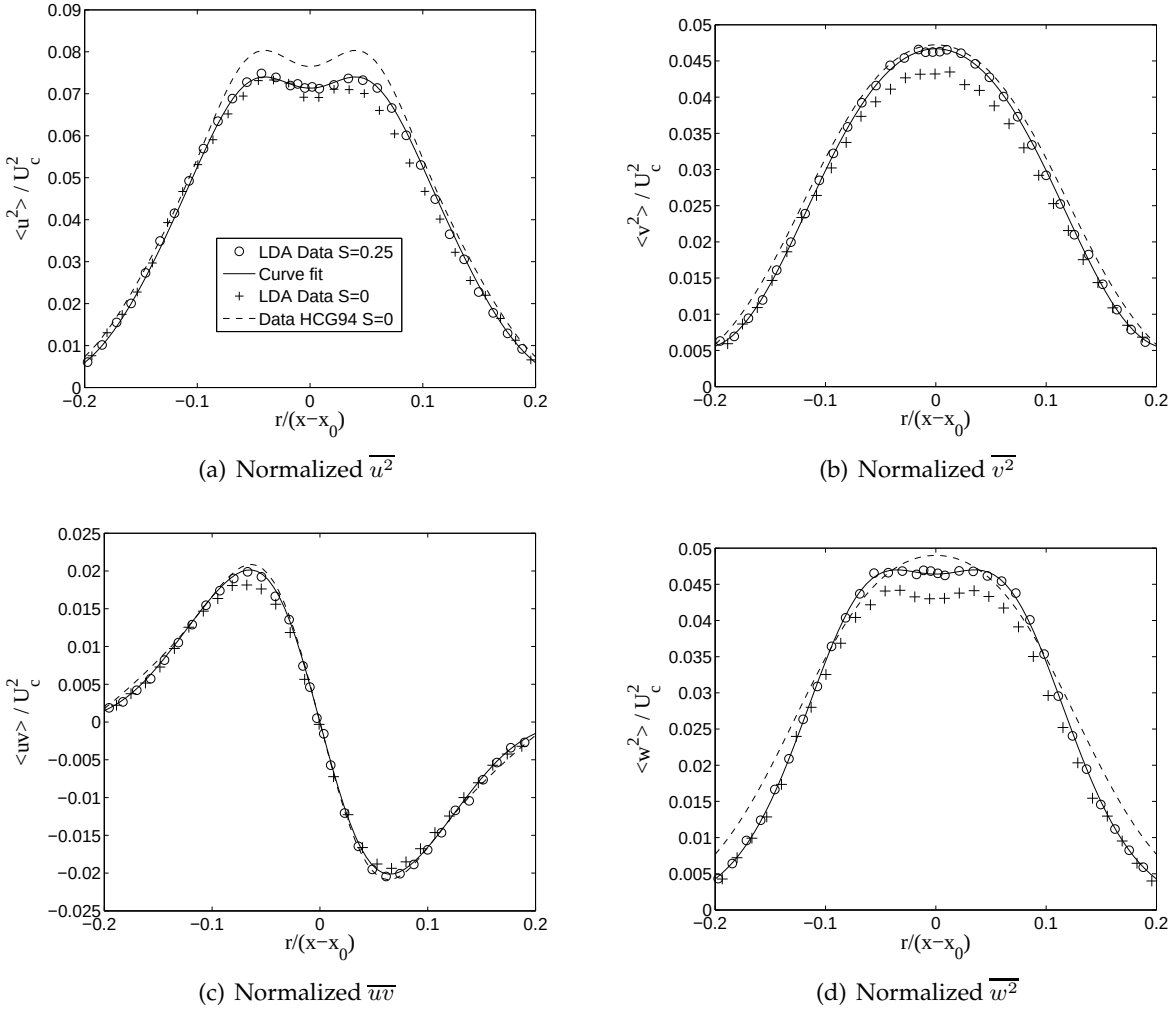

(a) Normalized $\overline{u^2}$

(b) Normalized $\overline{v^2}$

(c) Normalized $\overline{uv}$

(d) Normalized $\overline{w^2}$

Figure 5.12: Second-Order Moments at $x/D = 30$, compared with non-swirling jet data from Hussein et al. [1994].

5.7 Reynolds stresses

The Reynolds stresses $\overline{u^2}, \overline{v^2}, \overline{w^2}$ and $\overline{uv}$ are plotted in figure 5.12. The values are normalized by the square of the centreline velocity at the cross-section and compared with the results from non-swirling jet produced by the same facility with Hussein et al. [1994]. Since only two-component LDA was used, it was not possible to measure the radial-azimuthal correlation, $\overline{vw}$. This is not a serious problem since it should be zero in view of the azimuthal homogeneity. The profiles of all moments measured herein are in excellent agreement with the earlier results, except for a slight decrease in those involving the u-component which are slight lower. The reason for this is not known at this point, but could be related to the different LDA methodologies. On the other hand it is quite possibly related to the higher Reynolds number of the Hussein et al. [1994] experiment (100,000 versus 40,000).

5.7.1 Third-order velocity moments

Third-order moments are plotted in figure 5.13 and compared with the non-swirling data. Curve fits to these data are provided in tables 5.2 and 5.3. As for the second-order moments

Table 5.2: Curve fits for even functions, $f(\eta) = [C_0 + C_2\eta^2 + ...]e^{A\eta^2}; (\eta = r/(x - x_0))$.

-	C_0	C_2	C_4	C_6	A
$\overline{u^2}$	1.587	330.284	−1922.685	878055.498	156.166
$\overline{v^2}$	1.048	53.648	0.066	−	86.364
$\overline{w^2}$	1.032	129.134	−2159.596	52742.686	104.112
$\overline{u^3}$	0.2	146.908	9861.882	−2.579	135.747
$\overline{uv^2}$	−0.172	106.123	−756.518	449688.093	172.189
$\overline{uw^2}$	−0.177	33.640	3474.348	1.342	142.374

Table 5.3: Curve fits for odd functions, $f(\eta) = [C_1 + C_3\eta^3 + ...]e^{A\eta^2}; (\eta = r/(x - x_0))$.

-	C_1	C_3	C_5	C_7	A
$\overline{uv}$	−11.946	−424.067	−34742.577	−1390539.741	173.261
$\overline{u^2v}$	3.418	−2275.911	99175.818	−8126140.636	197.919
$\overline{v^3}$	−3.9411	−488.044	−2.967	−	111.377

above it was not possible using two-component LDA to measure the azimuthal-radial correlations. This is more problematical for the energy balances of the next chapter, especially $\overline{vw^2}$ which can be expected to be of the same order as $\overline{v^3}$. With a single exception, $\overline{uw^2}$, the profiles of all moments measured herein are in excellent agreement with the earlier results, except for (as noted above) a slight decrease in those involving the u-component.

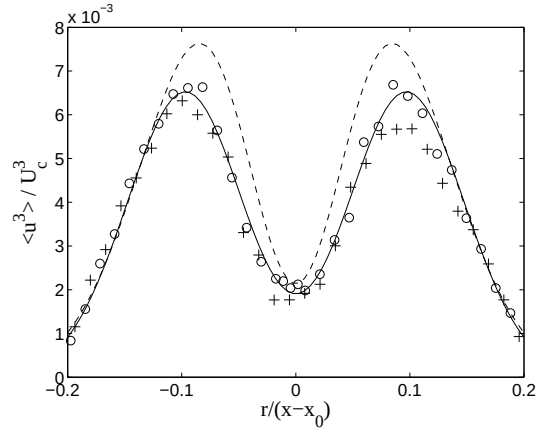

(a) Normalized $\overline{u^3}$

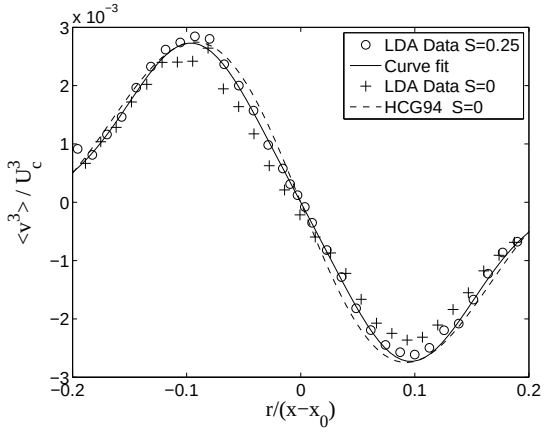

(b) Normalized $\overline{v^3}$

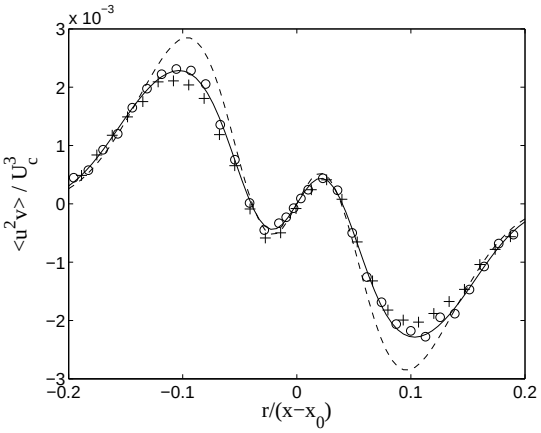

(c) Normalized $\overline{u^2v}$

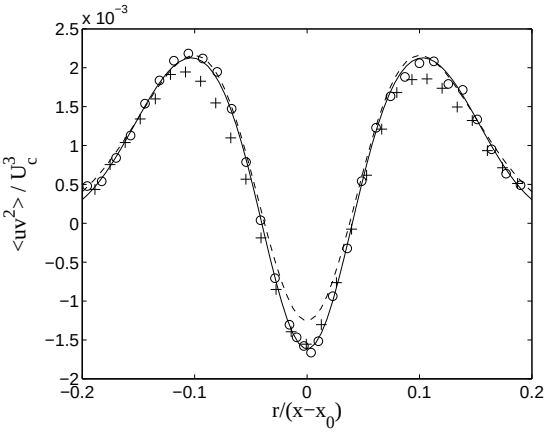

(d) Normalized $\overline{uv^2}$

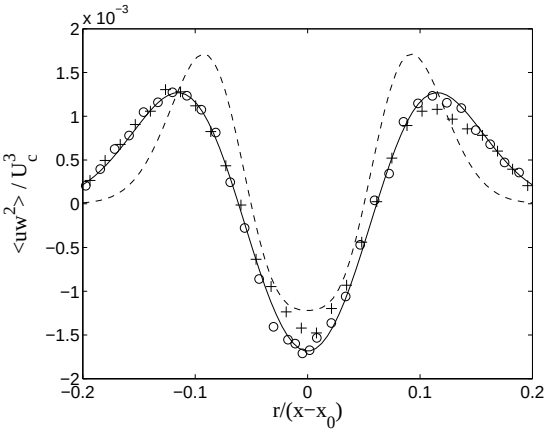

(e) Normalized $\overline{uw^2}$

Figure 5.13: Third-Order Moments at $x/D = 30$, compared with non-swirling jet data from Hussein et al. [1994].

Chapter 6

Summary and Conclusions: Swirling Jet

6.1 Overview of results

The far field of an incompressible swirling jet has been studied using two-dimensional laser Doppler anemometry. Three pairs of symmetric injectors were used to produce weak-to- moderate swirling jets. Velocity profiles of the mean and fluctuating streamwise, radial and azimuthal velocity components were measured in jets with two levels of swirl ($S = 0.15$ and 0.25) at axial locations up to 50 jet exit diameters. The velocity and turbulence intensity profiles, centerline decay, and growth rates for the various swirling jets were compared to those obtained in the same facility without swirl ($S = 0$). The mean velocity and turbulence intensities collapsed to the same profiles when scaled with the jet centerline velocity and half-width. Thus, by contrast with previous observations for the near jet Chigier and Chervinsky [1967], Gilchrist and Naughton [2005], there was no observable effect on the properly scaled far jet for the $S = 0.15$ case. The results were virtually identical to the non-swirling jet. For the $S = 0.25$ case, the only statistically significant effect was a shift in the virtual origin (from $x/D_* = 0.75$ to -2.9), indicating a more rapid initial spread rate.

The recent predictions of equilibrium similarity theory of Ewing [1999] were found to be in excellent agreement with the experimental results. In particular, the mean azimuthal component of velocity falls off as the inverse square of the downstream distance. By contrast, the mean streamwise velocity and turbulence intensities fall off with simply the inverse of the downstream distance. As a consequence the mean azimuthal equation uncouples from the rest, so the asymptotic swirling jet behaves like the non-swirling jet. A second length scale, L_*, defined from the rates at which momentum and angular momentum are added at the source characterizes the distance which is required for the swirl to become negligible.

The present investigation extends the previous study to include all three velocity components of the turbulence quantities at a swirl number of $S = 0.25$. Since only a two-component LDA was available, this was accomplished by making traverses in both the vertical and horizontal directions. All moments to third order were obtained, excepting those involving both the azimuthal and radial components simultaneously.

6.2 Energy Balance and Dissipation

If the pressure-velocity correlations and dissipation were known it would be possible to calculate the other terms by using the turbulence kinetic energy equation:

$$U\frac{\partial k}{\partial x}+V\frac{\partial k}{\partial r}=-\left[\frac{\partial}{\partial x}\left(\frac{1}{\rho}\overline{pu}+\frac{1}{2}\overline{q^2u}-\nu\frac{\partial k}{\partial x}\right)+\frac{1}{r}\frac{\partial}{\partial r}r\left(\frac{1}{\rho}\overline{pv}+\frac{1}{2}\overline{q^2v}-\nu\frac{\partial k}{\partial r}\right)\right] - \left[\overline{uv}\left(\frac{\partial U}{\partial r}+\frac{\partial V}{\partial x}\right)+\overline{u^2}\frac{\partial U}{\partial x}+\overline{v^2}\frac{\partial V}{\partial r}+\overline{w^2}\frac{V}{r}\right]-\epsilon \tag{6.1}$$

In the present experiment we were not able to directly measure the dissipation, therefore, the velocity-pressure correlation terms $\frac{1}{\rho}\overline{pv}$ and $\frac{1}{\rho}\overline{pu}$ in the equation 6.1 could not be inferred directly as in Hussein et al. [1994]. The streamwise gradient of $\overline{pu}/\rho$ can be ignored relative to the radial gradient of $\overline{pv}/\rho$. Also, Hussein et al. [1994] showed from a locally axisymmetric dissipation; that the radial gradient has the same shape as $\overline{q^2v}$, consistent with the estimate of Lumley [1978] that $-\overline{pv}/\rho=(\frac{1}{5})\overline{q^2v}$. Also the coincident moment of tangential and radial velocity components, $\overline{uw}$, was not measured because of the two-component LDA measurement. In the energy balance computation it was assumed that $\overline{vw^2}\equiv\overline{v^3}$. Using this, we are able to calculate the dissipation through kinetic energy equation. The normalized kinetic energy balance is plotted in figure 6.1. The results are virtually indistinguishable from those of Hussein et al. [1994].

The component Reynolds stress equations for the jet are given as below from appendix B:

- $\overline{u^2}$ *Balance:*

$$U\frac{\partial\overline{u^2}}{\partial x}+V\frac{\partial\overline{u^2}}{\partial r}=\left[2\overline{\frac{p}{\rho}\frac{\partial u}{\partial x}}\right]-\left[2\overline{uv}\frac{\partial U}{\partial r}+2\overline{u^2}\frac{\partial U}{\partial x}\right]-\left[\frac{\partial\overline{u^3}}{\partial x}+\frac{\overline{u^2v}}{r}+\frac{\partial\overline{u^2v}}{\partial r}\right]-2\epsilon_{xx} \tag{6.2}$$

- $\overline{v^2}$ *Balance:*

$$U\frac{\partial\overline{v^2}}{\partial x}+V\frac{\partial\overline{v^2}}{\partial r}=\left[2\overline{\frac{p}{\rho}\frac{\partial v}{\partial r}}-\frac{2}{\rho}\frac{\partial\overline{pv}}{\partial r}\right]-\left[2\overline{v^2}\frac{\partial V}{\partial r}+2\overline{uv}\frac{\partial V}{\partial x}\right] - \left[\frac{\overline{v^3}}{r}+\frac{\partial\overline{v^3}}{\partial r}-2\frac{\overline{vw^2}}{r}-4W\frac{\overline{vw}}{r}+\frac{\partial\overline{uv^2}}{\partial x}\right]-2\epsilon_{rr} \tag{6.3}$$

- $\overline{w^2}$ *Balance:*

$$U\frac{\partial\overline{w^2}}{\partial x}+V\frac{\partial\overline{w^2}}{\partial r}=\left[\frac{2}{r}\overline{\frac{p}{\rho}\frac{\partial w}{\partial\theta}}\right]-\left[2\overline{uw}\frac{\partial W}{\partial x}+2\overline{vw}\frac{\partial W}{\partial r}\right] - \left[\frac{\partial\overline{uw2}}{\partial x}+\frac{\partial\overline{vw^2}}{\partial r}+3\frac{\overline{vw^2}}{r}+2\overline{vw}\frac{W}{r}+2\overline{w^2}\frac{V}{r}\right]-2\epsilon_{\theta\theta} \tag{6.4}$$

- $\overline{uv}$ *Balance:*

$$U\frac{\partial\overline{uv}}{\partial x}+V\frac{\partial\overline{uv}}{\partial r}=\left[\overline{\frac{p}{\rho}\left(\frac{\partial v}{\partial x}+\frac{\partial u}{\partial r}\right)}\right]-\left[\overline{uv}\left(\frac{\partial U}{\partial x}+\frac{\partial V}{\partial r}\right)+\overline{v^2}\frac{\partial U}{\partial r}+\overline{u^2}\frac{\partial V}{\partial x}\right] - \left[\frac{\partial\overline{u^2v}}{\partial x}+\frac{\partial\overline{uv^2}}{\partial r}+\frac{\overline{uv^2}}{r}-\frac{\overline{uw^2}}{r}-2\overline{uw}\frac{W}{r}\right]-2\epsilon_{xr} \tag{6.5}$$

The locally axisymmetric estimate is suggested by Hussein et al. [1994] to best represent the dissipation in the jet flow. But because we could not measure the dissipation directly for each Reynolds stress equation, the only possible hypothesis is to assume isotropic dissipation distribution; i.e., $\epsilon_{xx} = \epsilon_{rr} = \epsilon_{\theta\theta} = \epsilon/3$ and $\epsilon_{xr} = \epsilon_{r\theta} = \epsilon_{x\theta} = 0$. The energy balances for Reynolds stresses are plotted in figure 6.2. The values are normalized by cube of the centerline velocity over distance from nozzle. x_0 is the virtual origin of the swirling jet as shown in figure 5.5. The graphs are in a good agreement with the earlier non-swirling jet energy balance of Hussein et al. [1994].

6.3 Conclusions

An investigation of turbulent transport equations in the self-preserving region of a moderate swirling jet flow has shown that the role of different terms in energy balance has not been affected by the additional azimuthal velocity component at the exit of jet. As previously noted by Shiri and George [2008], the mean streamwise velocity for the swirling jet has the same rate of evolution as the non-swirling jet with the same initial condition. The higher-order moments in the swirling jet flow also shows this similarity. The slight differences observed in some moments like $\overline{u^2}$ could be the effect of exit profile which tends to change when azimuthal component is added to the jet, or it could be simply due to differences in the measurement methodology. The quantities measured and calculated in this study are essential for evaluating turbulence closure models.

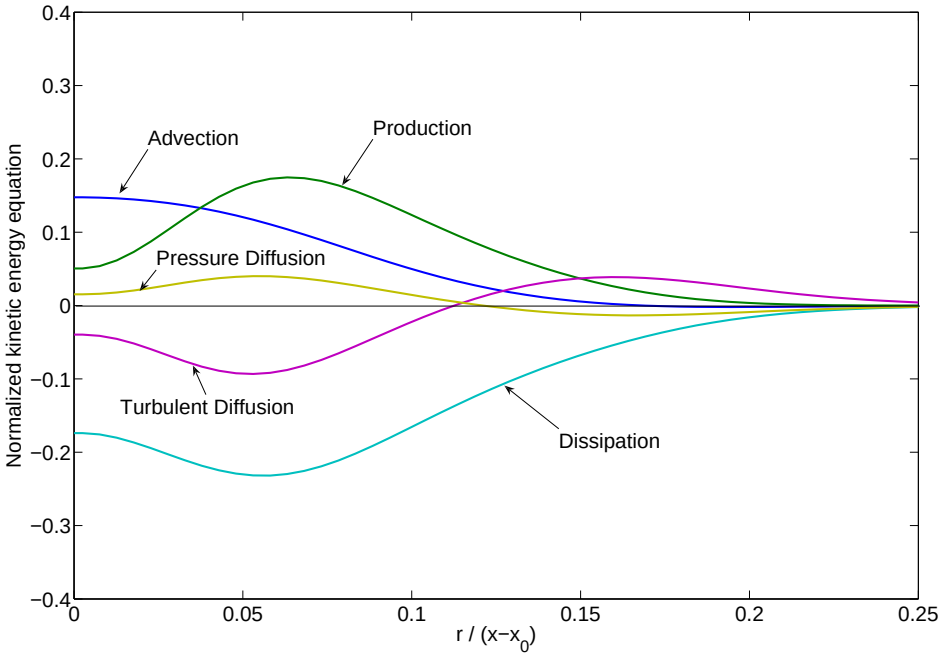

Figure 6.1: Kinetic energy balance normalized by $U_c^3/(x - x_0)$.

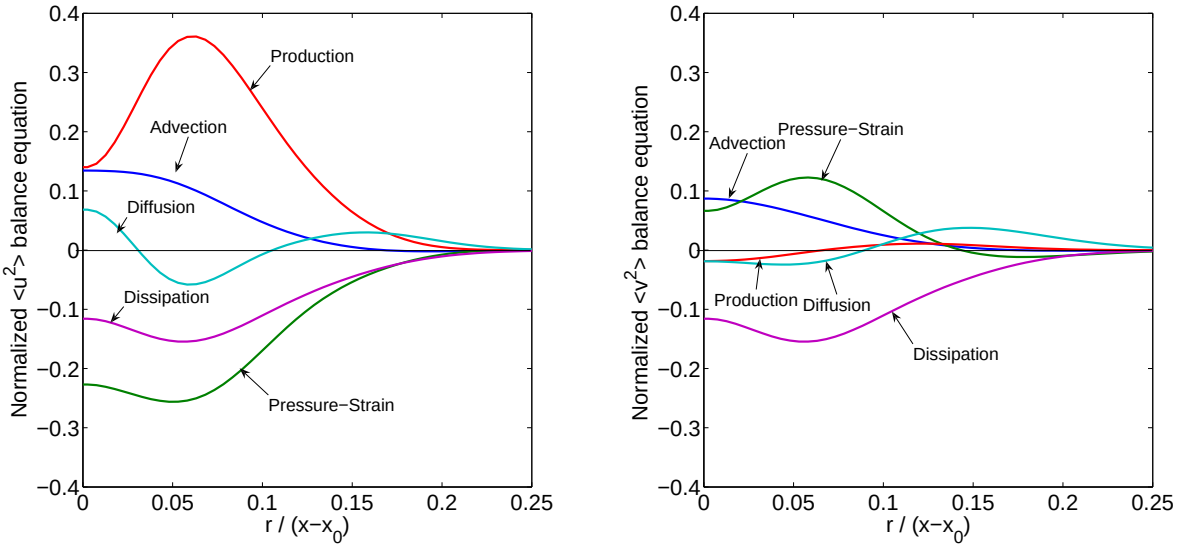

(a) $\overline{u^2}$

(b) $\overline{v^2}$

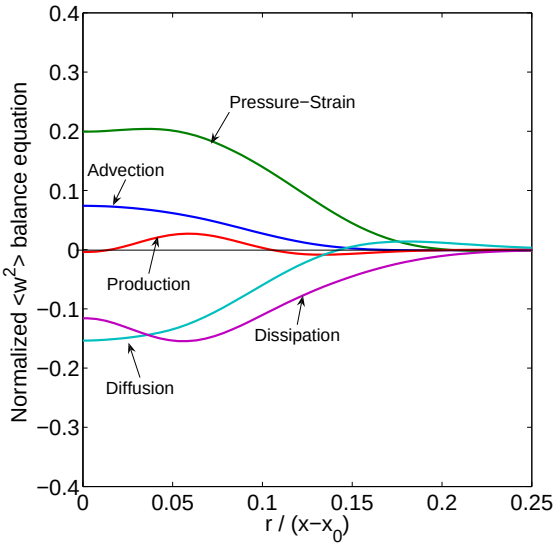

(c) $\overline{w^2}$

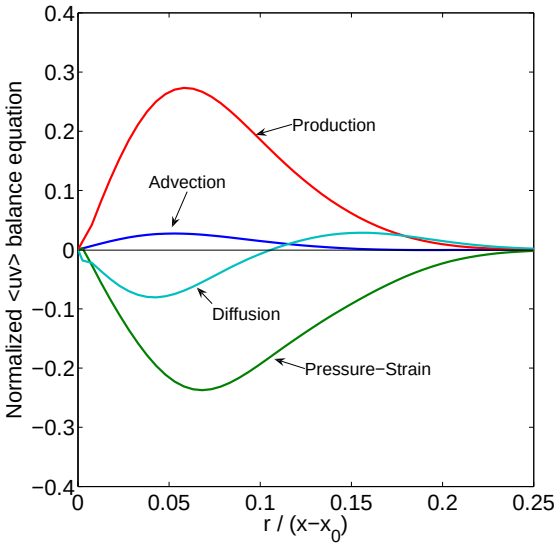

(d) $\overline{uv}$

Figure 6.2: Reynolds stress balance equations normalized by $U_c^3/(x - x_0)$.

Part II

Turbulent Natural Convection Boundary Layer Around Vertical Cylinder

Chapter 7

Introduction

7.1 Heat Transfer

Energy is the source of life and utilization of the energy is both engineering and art. Technology provides for us a wide variety methods to manipulate the energy extracted from natural resources. But they all come with a price, wasting a great deal of energy in the process of gaining a fragment. The major contribution to this loss is unwanted heat transfer. We know how to transfer electrical or mechanical energy without losing much; but in the process of transferring and converting the thermal energy, efficiency is mostly lower.

Heat transfer takes place whenever a temperature difference exists in a medium. It can occur in three different *modes*. *Conduction* is the way that thermal energy passes through a stationary material at the atomic and molecular level. The process is relatively slow, and in solids it is the only method that heat can be exchanged internally. But in fluids, in addition to energy transfer due to conduction, the bulk motion of the fluid plays an important role by moving energy from one place to another. In doing so it can make the temperature gradients larger, thus increasing conduction.

Such a heat transfer mode associated with the motion of fluid is called *convection*. Thermal energy can also be emitted from a solid surface or an opaque fluid with a nonzero temperature to the ambient with different temperature. Therefore the heat transfer through *radiation* is the third mode of energy exchange. In radiation energy is transported by electromagnetic waves and there is no need for a medium in this process.

Controlling the motion of the fluid provides the ability to manipulate the process of convection. Thus having a mobile bulk of material facilitates the design of more efficient systems of heat transfer. But it also adds the complexity of fluid dynamics into the rather simpler nature of heat transfer. The widespread applications of convection and the complexity of the fluid motions makes this mode of heat transfer the most interesting and challenging of all. From industrial applications including power plants, reactors, turbines, heat exchangers and internal combustion engines to the domestic applications like heating and ventilation of the buildings, convection is a primary subject for study by engineers as well as scientists.

Convective heat transfer can be divided into three categories: forced convection, natural (or free) convection, and mixed convection. The density of most fluids varies with temperature. So when the temperature in the bulk of fluid differs from the surrounding environment, buoyancy forces due to the differing gravitational attraction create imbalances in the forces acting

(a)

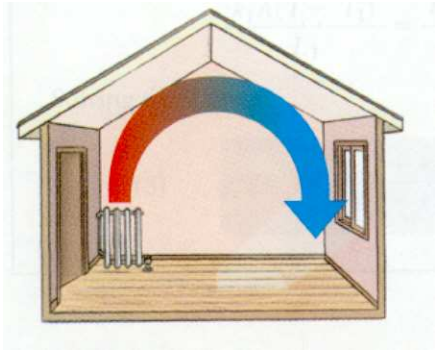

(b)

Figure 7.1: Natural Convection occurs (a) in nature, (b) in buildings.

in different parts of the fluid. These imbalances usually result in motion. Heat transfer due to buoyancy driven flow is called *natural convection*. Natural convection happens whenever there is a temperature gradient in a body of fluid. Although the process of heat transfer improves when flow is caused by external means, such as by a fan, a pump, or atmospheric winds, it is customary to use the term *forced convection* when the effect of buoyancy is negligible in the momentum balance of the flow. *Mixed convection* occurs whenever the motion is a mixture of natural and forced convection. Of all the flows, natural convection flows are among the least well understood. The major focus of this study is to acquire a better understanding of the natural convection next to a vertical surface through an experimental investigation.

7.2 Natural Convection

Natural convection is the most commonly occurring method of convective heat transfer in the world. Even nature controls the environment with it. From the large scale systems like hurricane formation to the the small electrical heat sinks and the simple household radiator[1] (figure 7.1, the presence of this phenomenon can be observed almost everywhere. Although a buoyancy driven flow could be created caused by other sources of density variation in a fluid, like concentration, the ones caused by temperature gradient are more common. The subject is twofold: the fluid dynamics of the natural convection flow and the heat transfer of the fluid. Due to the complex nature of buoyancy dominated flows, the details of both aspects of this phenomenon have never been well understood. This is especially true when the fluid motions are turbulent.

Buoyancy, the driving force for natural convection in fluids, is the result of density differences in the presence of a proper acceleration such as gravity, centripetal force or Coriolis force. As the buoyancy acts on the bulk of the material, it is considered as a body force acting on the fluid to increase (or decrease) the momentum of the flow. The temperature distribution in the flow is the key parameter in both equations governing the motion of the fluid and the energy balance in the flow. Therefore these two equations are coupled together and should be solved simultaneously. To simplify the equations one can use the Boussinesq approximation to limit

[1]Note that the word 'radiator' suggests radiation, but in fact it works primarily by natural convection.

the temperature dependence of the momentum equation into just one linear buoyancy term ($g\beta\Delta T$). We will discuss this assumption in detail in the next chapter.

As we mentioned in chapter 1, the *Grashof number* ($Gr = g\beta\ \Delta T L^3/\nu^2$) plays the same role in natural convection that the *Reynolds number* ($Re = UL/\nu$) plays in the forced flows. The ratio of these two dimensionless numbers is the best indication of the role of buoyancy in the process of heat transfer. Natural convection dominates the flow when the ($Gr/Re^2 \gg 1$); and it can be neglected when ($Gr/Re^2 \ll 1$). Both methods of heat transfer are present (mixed convection) when this ratio is close to unity.

Another parameter of interest for natural convection heat transfer is the *Nusselt* number defined as:

$$Nu \equiv \frac{hL}{\kappa_f} = \left.\frac{\partial T^*}{\partial y^*}\right|_{y^*=0} \tag{7.1}$$

where the $T^* = (T - T_{ref})/\Delta T$ is the temperature normalized by the highest temperature difference in the flow and $y^* = y/L$ is the cross-stream distance normalized by a length scale. It can be considered as the ratio of the convective to conductive heat transfer as the value of it increases in flows with more active convection like a turbulent flow. Through dimensional analysis of the governing equations, it can be shown that the *Nusselt* number also describes the temperature gradient at the surface as a dimensionless number.

The general empirical correlation for heat transfer can be expressed in the form of

$$Nu = f(Re, Gr, Pr) \tag{7.2}$$

where the *Nusselt number* is a function of *Grashof*, *Reynolds* and *Prandtl* numbers (cf. Incropera [2007]). There are very few truly theoretical results saying how these parameters should be related to each other, so most often the relations are determined empirically and expressed as power laws. For forced convection, the role of *Grashof* number is negligible, so the heat transfer law is often expressed as:

$$Nu = C_1\ Re^m Pr^n \tag{7.3}$$

where C_1, m and n have to be determined from experiment. In a pure natural convection flow the *Reynolds* number is replaced by the *Grashof* number, so that the heat transfer law is usually expressed as:

$$Nu = C_2\ Gr^p Pr^q, \tag{7.4}$$

where as before C_2, p and q are determined from experiment.

The *Prandtl* number, Pr, describes the property of the fluid as the dimensionless ratio of momentum diffusivity (kinematic viscosity) to the thermal diffusivity

$$Pr \equiv \frac{\nu}{\alpha} = \frac{C_p\,\mu}{\kappa_f} \tag{7.5}$$

where ν $[m^2/s]$ is the kinematic viscosity, α $[m^2/s]$ is the thermal diffusivity, μ $[Pa\ s]$ is the dynamic viscosity, C_p $[J/(kg.K)]$ is the specific heat at constant pressure and κ_f $[W/(m.K)]$ is the thermal conductivity of the fluid. For a low *Prandtl* number fluid, like liquid metals, heat

conduction is very effective compared to convection: thermal diffusivity is dominant. For a high *Prandtl* number fluid, like oils, convection is very effective in transferring energy, compared to pure conduction: momentum diffusivity is dominant. In air this value is close to one and the *Prandtl* number is usually ignored. In laminar flows, the *Prandtl* number also indicates the relative thickness of the momentum and thermal boundary layers, but this in not true in turbulent flow. In turbulent flow the *Prandtl* number does specify the relative thicknesses of the viscous and conductive sublayers, given respectively by $\eta_u = \nu/u_*$ and $\eta_T = \alpha/u_*$. Here u_* is the skin friction velocity defined as $u_*^2 = \tau_w/\rho$ where τ_w is the wall-shear stress.

Like in the forced flow, natural convection can happen in the presence of solid boundaries (boundary layer flow) or in a unconfined ambient (like in a plume). In this study we are focusing on the flow induced by the natural convection from a vertical surface with the temperature higher than surrounding fluid. The boundary layer flow along this surface defines the heat transfer correlations and the buoyancy force generated by this heat transfer controls the behavior of the flow. So the flow is both cause and consequence of the natural convection heat transfer.

7.3 Turbulent Natural Convection Boundary Layer

One of the major research subjects in the field of heat transfer is the *Turbulent Natural Convection Boundary Layer* (TNCBL) next to a vertical surface. Understanding the nature of buoyancy-driven flow next to a heated vertical surface has long been a challenging area of research in the field of Fluid Dynamics and Heat Transfer. Classical explanations and empirical relations with low level of accuracy can not answer the progressive needs of new technological applications. Efficient domestic heating and ventilation, compact heat sinks in electronic devices, passive control heat transfer in reactors and many other subjects would benefit from a more complete understanding of natural convection heat transfer.

Despite numerous investigations and theoretical studies on the *Turbulent Natural Convection Boundary Layer*, there is a lack of reliable experimental data. Part of the reason for this will be clear from the problems encountered in this investigation. But as a result, numerical analysis and turbulence modeling of the phenomena proceed without realistic guidelines. The usual assumptions and conditions are far from the actual behavior of this flow. Additional considerations on this matter, such as new properties, scaling factors and new theories of boundary layer, are needed. And as will be seen in the next chapter, there is even debate about the basic equations themselves, not just the turbulence models and theories about them.

Turbulence is that characteristic state of a flow in which scalar transport such as heat and mass transfer are enhanced compared to laminar flow sometimes by many orders of magnitude. In the presence of a boundary (like a vertical heated wall) the flow creates a boundary layer along the surface (see figure 7.2) which starts from bottom to the top of the vertical wall. As the flow moves up along the wall, the boundary layer will evolve from a steady, laminar flow into a transition region, and if the wall is high enough it will become a fully turbulent boundary layer. Where this happens is very much in doubt, since for experiments (especially in air) the distances required for this to happen can be quite large, often several meters or more, even for relatively large temperature differences.

Transition of a laminar natural convection boundary layer into a turbulent one depends

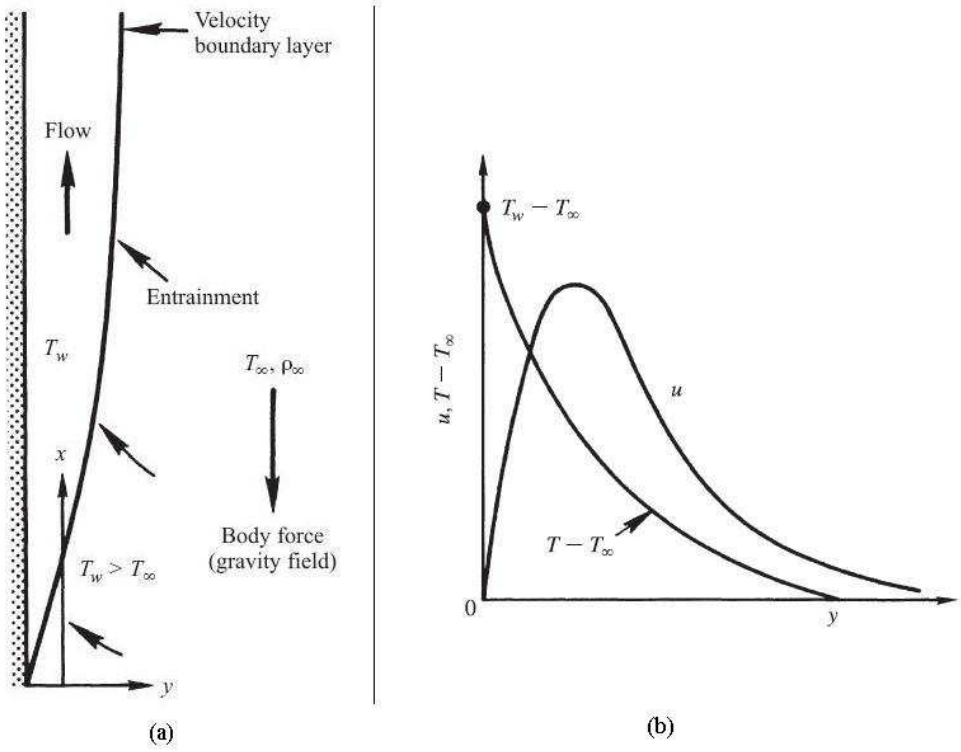

Figure 7.2: (a) Boundary layer created on a vertical hot wall; (b) Velocity and temperature profile in the boundary layer.

on the relative magnitude of the buoyancy and viscous forces in the fluid. The first stages of breakdown of a laminar flow can characterized by a specific point at which the flow can be said to become unstable to infinitesimal disturbances. The dimensionless parameters which define this point of instability in the buoyancy-driven flow are the *Prandtl* number (Pr) and either *Grashhof* number (Gr) or *Rayleigh* number (Ra) given by:

$$Ra_L \equiv Pr\ Gr = \frac{g\beta\Delta T L^3}{\alpha\nu} \tag{7.6}$$

where L is the streamwise length scale.

There have been many studies of instability of natural convection flows next to vertical surfaces. But transition to turbulence occurs much later, and often involves several different types of turbulence precursors which form first. For forced boundary layers there is first the region of non-linear growth, then the formation of turbulent spots, and finally these merge to form a fully turbulent flow. These processes are not very well understood in natural convection flows next to vertical surfaces, but have been the subject of great interest over the past decade or so (c.f. Prudhomme and Le Quere [2007], Pons and Le Quere [2007]). Exactly when the flow can be considered to be turbulent is thus very much in question, and even a question of definition. Thus we depend on empirical correlations, sometimes based on heat transfer data, sometimes on observation of phenomena, sometimes on profiles of mean and fluctuating quantities.

From previous experimental results an approximate criterion for the beginning of turbulence in natural convection next to a vertical flat plate is in the range of *Rayleigh* numbers between 10^8 to 10^{10} (c.f. Gebhart [1973]). The fact that this varies by two orders of magni-

tude illustrates the problem. In the flow used in the experiment described later, $\Delta T \approx 40°K$, $\beta \approx 1/(300°K)$, $g = 9.8m/s^2$, $\alpha \approx 2.9 \times 10^{-5}m^2/s$ and $\nu \approx 2 \times 10^{-5}m^2/s$. Using these, transition by the criterion above can be expected to occur somewhere between a height of $0.6m$ and $2.8m$. This is a huge range, and very much complicates the design of any experiment – and in fact, complicates even deciding what regime one is observing. The flow next to vertical cylinders is even less well-understood.

Different regions of the boundary layer can be recognized where the effect of diffusion or bulk motion of the fluid dominates the heat transfer process. Viscosity enforces a no-slip boundary condition near the surface which slows down the flow velocity, hence the molecular motion plays the important role in this region. Far from the surface, the advection of the bulk fluid motion dominates the thermal energy transfer. Near the wall, however, for the layer of the fluid adjacent to the surface conduction is the only method of heat transfer.

In this study, our intent was to carry out in a well-controlled environment a turbulent natural convection experiment at high *Rayleigh* number($\sim 10^{11}$), and perform detailed measurements of velocity and temperature in the fully developed turbulent natural convection boundary layer next to a heated wall. Because of the difficulties in creating a two dimensional flow, a cylindrical axisymmetric surface (the outer surface of a long pipe) was used instead of a vertical planar wall. There are several reasons for this particular choice of experiment. First of all, it is a flow case which has been studied before with only limited degree of success (Tsuji and Nagano [1988a]). Second, we can measure with sufficient details the complicated near-wall flow to provide new physical insight as well as new experimental information. Third, it is a generic flow case, which means that the obtained results have general validity, Therefore it would be valuable as test case for CFD validation and further development of turbulence models.

7.4 Previous Experimental Investigations

The early attempts to study the natural convection were mainly focused on developing a better understanding of the heat transfer process next to flat surfaces. Theoretical work has been more concerned about the laminar flows, in large part because these were the only ones that could be analyzed using the available mathematical tools. The assumption of similarity in the velocity and temperature enabled exact solutions for the laminar flow by Ostrach [1952] and cited many places (e.g., Incropera [2007]). These kind of solutions formed the basis of the studies of instability by Gebhart and his co-workers (e.g. Gebhart et al. [2003]).

Approaches to turbulent flow, like in laminar flow, were mostly based on dimensional analysis and experiment; i.e., on finding an empirical correlation between the Nusselt number as the dimensionless heat transfer parameter and the Grashof number as the flow specification and Prandtl number as the fluid characteristic. Many empirical relations for different geometries and different ranges of *Rayleigh* number have been collected by Incropera [2007], Gebhart et al. [2003],Arpaci and Larsen [1984] among others. Amongst them the one suggested for a vertical isothermal plate over the entire range of Ra by Churchill and Chu [1975] as below:

$$\overline{Nu_L} = \left(0.825 + \frac{0.387 Ra_L^{1/6}}{\left[1 + (\frac{0.492}{Pr})^{9/16}\right]^{8/27}} \right)^2 \tag{7.7}$$

In the limit of infinite Rayleigh number ($Ra \to \infty$) , $\overline{Nu_L} \to C(Pr)Ra^{1/3}$. The cube-root dependence on Rayleigh number is consistent with many experiments (e.g., Warner and Arpaci [1968], Balaji et al. [2007], Vliet and Liu [1969]). It was also deduced theoretically by George and Capp [1979]. The Prandtl number dependence in this limit, $Pr^{2/3}$, is empirical and based on the experiments of Fujii et al. [1970].

Although most measurements that have been carried out obtained only mean heat transfer rates and mean temperature profiles, one of the first (and few) studies on the velocity and temperature fields of the presumably turbulent natural convection boundary along heated vertical flat plates were performed by Cheesewright [1968]. He used hot-wire anemometry and cold wire resistance thermometery to measure mean velocity and temperature. The platinum wire used for temperature measurement was rather thick ($12.7\mu m$ in diameter and $14mm$ in length), so the instantaneous temperature was not measured. Later on, however, it was shown by Hoogendoorn and Euser [1978] that the energy balance for the boundary layer was not satisfied, and that the most likely error was in the velocity measurements. This was later confirmed and is easy to understand: using hot-wires in flows with large velocity and temperature fluctuations requires a very good separation of these fluctuations, which is extremely difficult to do. Also the turbulence intensities are very high, and hot-wires really don't work very well above about a $30\ \%$ turbulence level due to cross-flow sensitivity and flow reversal on the wires.

The accuracy problem with hot-wires in thermal flows is a consequence of the physics of the method, and therefore can not easily avoided. Another problem with hot-wires is that the velocity magnitudes of buoyancy-driven flows are in the range of less than $1\ m/s$. Therefore the natural convective heat transfer of the wire itself has an effect on the velocity field, plus cross-wire probes suffer a loss of directional sensitivity (Shabbir et al. [1996]). As a result, turbulence data obtained with hot-wires in buoyant flows suffer from large uncertainties, particularly in boundary layers (close to the wall). This also has been seen, for example, in the experimental data of Tsuji and Nagano [1989a]. In spite of this, their experiment is still used as test case for validating turbulence models, since there were (and still are) no other alternatives. The remedy to the problem of uncertainty in the velocity measurement is to replace the hot-wire techniques of previous experiments with one which does not suffer from the same limitations. Laser Doppler anemometry (*LDA*), can in principle, produces highly accurate results, assuming adverse refractive index effects on the beam paths are not significant (c.f., Buchhave et al. [1979]).

There are other problems with the earlier experiments as well. Many of the previous studies of the natural convection boundary layer have been made in flows along vertical plates which attempted to simulate an infinite surface (Cheesewright [1968]; Cheesewright and Ierokiopitis [1982]; Tsuji and Nagano [1988a]; Tsuji and Nagano [1988b]; Tsuji and Nagano [1989b]). In vertical flat plate experiments, it is hard to eliminate the effect of side walls. Attempts to measure the heat transfer correlations of a heated cylinder by Fujii et al. [1970] were more focused on the Prandtl number effect of the heat transfer rather than turbulence properties. Persson and Karlsson [1996] in their work used combination of LDA and resistance thermometer but their measurements were carried out at rather low *Rayleigh* number and they reported large uncertainty in the measurements caused by the confinement of the rig.

Some of the problems encountered by these earlier experiments, were encountered in our experiments as well. Unfortunately there is considerable evidence that the previous researchers may not have been aware of them. Thus any skepticism by us about our own results in the fol-

lowing chapters, should apply also to almost all of the earlier results as well. In fact a useful criterion for looking at all the experiments (old and new) might be this: *If a particular phenomenon was not explicitly and quantitatively ruled out as being a problem, it should probably be viewed as a serious problem.* Unfortunately by this criterion, there seems to be almost nothing that has been done that can be believed, except perhaps heat transfer measurements using electrically heated films where the heat transfer could be known relatively accurately and independently from the temperature field.

Chapter 8

Basic Equations for Natural Convection

This chapter reviews the basic equations for the fluid mechanics and thermodynamics, especially as they apply to natural convection flows in air. Important issues addressed include to what degree such flows can be considered to incompressible, exactly which forms of the ideal gas equations should be used, and the manner in which the various so-called Boussinesq approximations should be applied. It concludes with the Reynolds-averaged equations as they apply to natural convection in air.

8.1 Summary of Basic Equations

For a better understanding of the parameters and equations governing the motion and energy balance in the flow, it is appropriate to collect all the assumption from the beginning. To do so we start with the most general version of the equations and list the constrains and assumptions to simplify them. These equations are the fundamental laws of continuum mechanics.

- **Continuity**

$$\frac{1}{\rho}\frac{D\,\rho}{D\,t} = -\nabla.\vec{\mathbf{v}} \tag{8.1}$$

  for a flow with no sources (or sinks) of mass.

- **Conservation of momentum**

$$\rho\,\frac{D\,\vec{\mathbf{v}}}{D\,t} \;=\; -\;\nabla P \;+\; \nabla.\,\vec{\tau}_{ij} \;+\; \rho\,\vec{g} \tag{8.2}$$

  for a flow with the gravity ($\vec{g}$) as the only body force acting on it.

- **Conservation of internal energy**

$$\rho\,\frac{D\,e}{D\,t} = -P\,(\nabla.\,\vec{\mathbf{v}}\,) + \;\vec{\tau}_{ij}\;:\nabla\vec{\mathbf{v}}\;-\nabla.\,\vec{q} \tag{8.3}$$

  without electromagnetic, chemical and nuclear energy sources.

T	ρ	$\mu \times 10^5$	$\nu \times 10^5$	$\kappa \times 10^2$	$\alpha \times 10^5$	C_p	Pr
$[^\circ C]$	$[kg/m^3]$	$[N.s/m^2]$	$[m^2/s]$	$[W/m.K]$	$[m^2/s]$	$[kJ/kg.K]$	
0	1.29	1.71	1.33	2.41	1.89	1.0065	0.714
20	1.20	1.80	1.50	2.57	2.16	1.0069	0.709
50	1.09	1.95	1.79	2.80	2.59	1.0079	0.704
100	0.95	2.17	2.30	3.17	3.38	1.0113	0.695

Table 8.1: Properties of air at $1atm.$; [White [1994]].

- **Thermodynamic equations of state**

$$\rho = \rho\,(P,T) \tag{8.4}$$
$$e = e\,(\rho,T) \tag{8.5}$$

where in these equations ρ is the density of the fluid, P is the thermodynamic pressure, T is the temperature, $\vec{\mathbf{v}}$ is velocity vector, e is the absolute thermodynamic internal energy, $(\vec{\tau}_{ij} : \nabla\vec{\mathbf{v}})$ is the inner product of viscous stress tensor and velocity gradient tensor and $(\nabla.\,\vec{q})$ is the net heat flow. They represent the instantaneous quantities for a turbulent flow.

The Newton's viscosity law and Fourier's conduction law are two **constitutive equations** which can be applied to a simple viscous fluid without memory like air. For a flow without internal heat generation or combustion and ignoring the radiation, the viscous stress tensor and heat flux can be written as:

$$\tau_{ij} = 2\mu\,[S_{ij} - \frac{1}{3}S_{kk}\delta_{ij}] \tag{8.6}$$
$$q_i = -\kappa\,\frac{\partial T}{\partial x_i} \tag{8.7}$$

where κ is thermal conductivity and symmetric strain rate tensor defined as,

$$S_{ij} = \frac{1}{2}\left[\frac{\partial u_i}{\partial x_j} + \frac{\partial u_j}{\partial x_i}\right] \tag{8.8}$$

Implementing these two equations in the momentum equation 8.2 gives us the Navier-Stokes equation for linear momentum as below:

$$\rho\,\frac{D\,\vec{\mathbf{v}}}{D\,t} = -\,\nabla P + \rho\,\vec{g} + 2\nabla.(\mu\,S_{ij}) - \frac{2}{3}\,\nabla(\mu\,\nabla.\vec{\mathbf{v}}\,) \tag{8.9}$$

The flow which we would like to be interested in would be an incompressible Newtonian flow with nearly constant viscosity. The constant viscosity assumption is popular and practical because it simplifies the momentum equations for analytical purposes. This advantage of a constant viscosity in the equation 8.9 can be easily seen: the two viscous diffusion terms change to:

$$\rho\,\frac{D\,\vec{\mathbf{v}}}{D\,t} = -\,\nabla P + \rho\,\vec{g} + \mu\,\nabla^2\vec{\mathbf{v}} + \frac{1}{3}\,\mu\,\nabla(\nabla.\vec{\mathbf{v}}\,) \tag{8.10}$$

Unfortunately the viscosity of air is a function of temperature and varies around 20% for the temperatures used in this experiment according to the table 8.1. The density of air also

changes almost 20% over the same temperature range. In our experiments the absolute value of the viscous terms are several orders of magnitude smaller than other terms in the momentum equation, except very close to the wall where they dominate. Unfortunately this is also the region where the temperature is varying the most (roughly 90% of the total drop from wall to ambient). Obviously one should be aware of the consequences of the constant viscosity (or thermal diffusivity) assumption in numerical computations as well, at least if comparison is to made to experimental results. The assumption that either is constant becomes problematical when the temperature variation increases rapidly, even over a modest range, as it does very close to the wall in the experiments of interest herein.

The viscous stress tensor, τ_{ij}, is a symmetric tensor for a non-polar continua [Panton [2005]]. We can write any tensor like $\nabla\vec{\mathbf{v}}$ as the summation of a symmetric and an anti-symmetric tensor. The viscous dissipation term ($\vec{\tau}_{ij} : \nabla\vec{\mathbf{v}}$) is just the inner product of τ_{ij} with the symmetric part of the velocity gradient tensor. Thus we can write ($\vec{\tau}_{ij} : \nabla\vec{\mathbf{v}}$) $\equiv$ ($\vec{\tau}_{ij} : S_{ij}$). By using the Newton's viscosity law 8.6, the viscous dissipation term in energy equation 8.3 is simplified to $\mu\,\Phi$, where dissipation function (Φ) defined as:

$$\Phi = 2\left[(S_{ij} : S_{ij}) - \frac{1}{3}(\nabla.\vec{\mathbf{v}})^2\right] \tag{8.11}$$

Viscous dissipation is always positive and produces internal energy by taking from the kinetic energy. Now the internal energy equation, considering equation 8.7, can be written as:

$$\rho\,\frac{D\,e}{D\,t} = -P\,(\nabla.\,\vec{\mathbf{v}}\,) + \nabla.(\kappa\nabla T) + \mu\,\Phi \tag{8.12}$$

Note that for this equation the constant viscosity assumption is not necessary.

8.2 Continuity Equation and Incompressibility

As mentioned before, the general mass conservation (or continuity) equation is expressed by equation 8.1. The term on the left is the rate of density change of a material particle per unit density. As the material particle moves through the fluid, its size and shape may change. It can be shown that right hand side term in the continuity equation has a physical interpretation as the **rate of expansion** of the material region (Panton [2005]):

$$\lim_{V_{MR}\to 0}\frac{1}{V_{MR}}\frac{D\,V_{MR}}{D\,t} = \nabla.\vec{\mathbf{v}} \tag{8.13}$$

The thermodynamical term, *incompressible*, clearly represents liquids since they have negligible rate of expansion, but by contrast, *compressibility* is the nature of gases. So in the fluid mechanics of gases, the main criterion for whether compressibility of the *flow* is important (for the continuity equation) has been whether its velocity, say u, is comparable to the speed of sound, say c; i.e., low *Mach* number, M, where $M = u/c$. That this is problematical for the thermally varying flows of interest herein can easily be seen, as shown below.

For all conditions of interest in our experiments, the air can be assumed to behave as an ideal gas. Thus its equation of state is given by $p = \rho RT$ (or equivalently, $\rho = p/RT$) where R is the gas constant for the particular gas of interest. Taking differentials and applying the chain rule yields immediately:

$$d\rho = \frac{1}{RT}dp - \frac{p}{RT^2}dT \tag{8.14}$$

or

$$d\rho = \frac{\rho}{p}dp - \frac{\rho}{T}dT \tag{8.15}$$

But the isentropic sound speed is defined as $c^2 = \partial p/\partial\rho|_s$. For an ideal gas (with constant thermal properties $c^2 = \gamma p/\rho$ where $\gamma = C_p/C_v$ is the ratio of specific heats. (C_p is the specific heat at constant pressure and C_v is the specific heat at constant volume.) For air $\gamma \sim 1.4$. Substituting into equation 8.15 and dividing by the density yields:

$$\frac{d\rho}{\rho} = \gamma\frac{dp}{\rho c^2} - \frac{\rho}{\rho}\frac{dT}{T} \tag{8.16}$$

This has the following counterpart for moving fluid particles:

$$\frac{1}{\rho}\frac{D\rho}{Dt} = \frac{\gamma}{\rho c^2}\frac{D\,p}{Dt} - \frac{1}{T}\frac{DT}{Dt} \tag{8.17}$$

For low Mach number flows, changes in pressure within the flow are on the order of ρu^2 (i.e., $dp \sim \rho u^2$), where u is typical of changes in flow speed. Thus the first term on the right-hand side of either equation is on the order of the Mach number squared; i.e., $M^2 = (u/c)^2$.

It is usually argued from the above if the *Mach* number is low, then the rate of expansion is effectively zero. But clearly there is another term in equation 8.16 that must also be considered, the temperature term. Whether $d\rho/\rho_o << 1$ depends completely on whether the temperature fluctuations themselves are relatively small (i.e., $dT/T << 1$). For the experiments considered herein, $\Delta T \sim 40°K$ while $T \sim 300°K$. Moreover most of this variation occurs in the very near wall region. Thus the assumptions of incompressibility are quite marginal here and the most one can safely say is that:

$$\frac{1}{\rho}\frac{D\rho}{Dt} \approx -\frac{1}{T}\frac{DT}{Dt} \tag{8.18}$$

As shown below, the non-negligibility of the expansion in thermally varying flows will turn out to be crucial in reconciling the various forms of the internal energy equation. In particular it is this residual thermal variation that switches C_v to C_p, and implies the negligibility of the Dp/Dt term in the corresponding enthalpy equation. This is particularly problematical for numerical analysis of natural convection flows which often assume incompressibility at the outset.

Before leaving this section, it should be noted that incompressibility, even if approximately true does not imply that the density is the same constant value throughout entire flow field. It only implies that if a fluid moves incompressibly then the density of a particular fluid particle remains constant, while the density of adjacent particles can be different. This can be easily seen by substituting zero for the divergence term in equation 8.1 to obtain the following equivalent forms:

$$\frac{D\,\rho}{D\,t} = 0 \qquad \text{or} \qquad \nabla.\vec{\mathbf{v}} = 0, \tag{8.19}$$

and recalling that D/Dt is the derivative following the fluid motion.

8.3 Thermodynamics Relations

Among the thermodynamic relations which can be considered as equation of state, we select those that relate properties like internal energy and density to the temperature. As it is mentioned before, $\rho = \rho\,(P, T)$ and $e = e\,(\rho, T)$ are the best choice for the general form of equation of state in buoyancy driven flows. Taking differentials from the general density equation yields:

$$\frac{d\rho}{\rho} = \beta_T\, dp - \beta\, dT \tag{8.20}$$

where β_T and β are defined by:

$$\beta_T\,(p,T) = \frac{1}{\rho}\left(\frac{\partial \rho}{\partial p}\right)_T; \qquad \text{Isothermal compressibility coefficient} \tag{8.21}$$

$$\beta(p,T) = -\frac{1}{\rho}\left(\frac{\partial \rho}{\partial T}\right)_p; \qquad \text{Thermal expansion coefficient} \tag{8.22}$$

Using cyclic and reciprocity relations for two partial derivatives in equations 8.21 and 8.22, we have:

$$\left(\frac{\partial \rho}{\partial p}\right)_T \cdot \left(\frac{\partial p}{\partial T}\right)_\rho \cdot \left(\frac{\partial T}{\partial \rho}\right)_p = -1 \qquad \Rightarrow \qquad \left(\frac{\partial p}{\partial T}\right)_\rho = \frac{\beta}{\beta_T} \tag{8.23}$$

The isothermal compressibility is defined by change of density due to pressure. In the absence of high convection force (i.e., low Mach number flows), hydrostatic pressure is the main cause for pressure differences. Unless we are dealing with thick flow fields (like the atmospheric boundary layer), the effect of the isothermal compressibility coefficient is much less than the thermal expansion coefficient and therefore negligible [Arpaci and Larsen [1984]].

For ideal gases, β_T and β take particularly simple forms. It follows immediately from the equation of state, $p = \rho RT$, that:

$$\beta = \frac{1}{T} \tag{8.24}$$

$$\beta_T = \frac{1}{p} \tag{8.25}$$

8.4 Equations for internal energy and enthalpy

Differential forms of internal energy equations and enthalpy equation can be found in the thermodynamics textbooks [Cengel and Boles [1998]]:

$$de = C_v\, dT + \rho^{-2}\left(p - T\frac{\partial p}{\partial T}\bigg|_\rho\right) d\rho \tag{8.26}$$

$$dh = C_p\, dT + \rho^{-1}\,(1 - T\beta)\, dp \tag{8.27}$$

where $C_v(\rho, T)$ and $C_p(p, T)$ are the specific heat at constant volume and pressure respectively. They are defined as:

$$C_v(\rho, T) = \left(\frac{\partial e}{\partial T}\right)_\rho \tag{8.28}$$

$$C_p(p, T) = \left(\frac{\partial h}{\partial T}\right)_p \tag{8.29}$$

Defining the enthalpy as $h \equiv e + p/\rho$ leads us to:

$$de = dh - \rho^{-1} dp + \rho^{-2} p \, d\rho \tag{8.30}$$

By substituting equation 8.27 into equation 8.30 and replacing differentials by material derivatives[1] we have:

$$\rho \frac{D\, e}{D\, t} = \rho\, C_p \frac{DT}{D\, t} - \beta T \frac{Dp}{D\, t} + \frac{p}{\rho} \frac{D\, \rho}{D\, t} \tag{8.31}$$

The last term in the equation above can be replaced by $-p\ (\nabla.\vec{v}\ )$ using continuity equation 8.1. Now we can replace the internal energy derivative from equation 8.3 with the one in equation 8.31. Considering the constitutive equations 8.7 and 8.11 for a Newtonian fluid with no radiation and internal heat generation yields:

$$\rho C_p \frac{DT}{D\, t} = \nabla.(\kappa\, \nabla T) + \mu\, \Phi + \beta T \frac{Dp}{D\, t} \tag{8.32}$$

If we do the same thing with the internal energy equation 8.26 and use equation 8.23, we obtain:

$$\rho C_v \frac{DT}{D\, t} = \nabla.(\kappa\, \nabla T) + \mu\, \Phi + \frac{T}{\rho} \left(\frac{\beta}{\beta_T}\right) \frac{D\, \rho}{D\, t} \tag{8.33}$$

Using equations 8.24 and 8.25, these can be rewritten for an ideal gas as follows:

Enthalpy equation (ideal gas)

$$\rho C_p \frac{DT}{D\, t} = \nabla.(\kappa\, \nabla T) + \mu\, \Phi + \frac{Dp}{D\, t} \tag{8.34}$$

Internal energy equation (ideal gas)

$$\rho C_v \frac{DT}{D\, t} = \nabla.(\kappa\, \nabla T) + \mu\, \Phi + (RT) \frac{D\, \rho}{D\, t} \tag{8.35}$$

8.5 A common problem: C_p versus C_v

It is commonly assumed that the appropriate form of the temperature equation (at least for low Mach number flows) for heat transfer analysis is the enthalpy equation, equation 8.34, but with the Dp/Dt term neglected; i.e.,

$$\rho C_p \frac{DT}{D\, t} = \nabla.(\kappa\, \nabla T) + \mu\, \Phi \tag{8.36}$$

It is not immediately obvious why this should be true, especially since the low Mach number argument has been for incompressibility, which when applied to equation 8.35 leads to:

[1] This requires assuming each fluid particle is undergoing a quasi-equilbrium process.

$$\rho C_v \frac{DT}{D\,t} = \nabla.(\kappa\,\nabla T) + \mu\,\Phi \tag{8.37}$$

These are clearly different in that one uses C_p and the other C_v. This is not a problem for liquids (in which they are equal), but it most certainly is for gases where they differ by 30-40% (e.g., for air $\gamma = C_p/C_v = 1.4$).

First notice that there is no fundamental inconsistency between the original equations 8.32 and 8.33. One can easily be derived from the other. So the problem clearly is in our approximations, and in particular the approximation of incompressibility. It was noted above that incompressibility can only be approximate in a thermally varying compressible fluid; in particular, from equation 8.18, $D\rho/Dt \approx -(\rho/T)DT/Dt$. Substituting this into equation 8.35 leads immediately to:

$$\rho C_v \frac{DT}{D\,t} = \nabla.(\kappa\,\nabla T) + \mu\,\Phi - (\rho R)\,\frac{DT}{D\,t} \tag{8.38}$$

But $R = C_p - C_v$. Using this and taking the DT/Dt to the other side lead immediately to equation 8.36 with no other assumptions required. Clearly only the assumption of low Mach number is required, with no corresponding *assumptions* about Dp/Dt. In fact, it can be further deduced that Dp/Dt must also be negligible (relative to $\rho C_p DT/Dt$) since the energy and enthalpy equations must be the same.

For a nearly incompressible flow ($Mach \rightarrow 0$), the viscous dissipation term in equation 8.32 is can also be argued to be negligible for most low Mach number flows. Therefore the temperature equation which will be considered hereafter in this thesis is:

$$\rho C_p \frac{D\,T}{D\,t} = \nabla.(\kappa\,\nabla T) \tag{8.39}$$

Before leaving this section it is worth nothing that there is an interesting dilemma for numerical analysis. Experiments are interrogations of exact solutions of the Navier-Stokes equations, and their analysis must account for the fact that the flow knows it is not quite incompressible (as shown above). This implies that the C_p form of the temperature equation is appropriate. But many CFD attempts begin by imposing strict incompressibility. Clearly for such attempts, C_v is the appropriate choice, not C_p. The difference is quite substantial, and may account for some of the difficulties in handling thermally varying flows numerically.

8.6 Boussinesq Approximations

We are going to make our biggest approximations in this section, so we have to be precise about the type of flow which is of interest. The fluid can be liquid or gas but the density is assumed to vary only with the temperature variation through the flow field. The major characteristic of this type of flow is the buoyancy force acting on the material region of the flow with the density of ρ in a quiescent surrounding environment with reference density ρ_0. The direction of this force is aligned with the direction of body force, which is assumed to be gravity in the case of our interest. The reference density does not have to be constant everywhere, but it should be time-independent. The density deviation from the reference value for our arbitrary material region is:

$$\rho = \rho_0 + \Delta\rho \tag{8.40}$$

By substituting this new definition into the momentum equation 8.2 we have:

$$(\rho_0 + \Delta\rho)\,\frac{D\,\vec{\mathbf{v}}}{D\,t} \;=\; -\;\nabla p \;+\; \nabla.\,\vec{\tau}_{ij} \;+\; (\rho_0 + \Delta\rho)\,\vec{g} \tag{8.41}$$

If we choose our reference point in a place that temperature approaches a uniform value, the convection term in the momentum equation vanishes and equation 8.41 reduces to the hydrostatic equation for the flow at rest:

$$0 \;=\; -\;\nabla p_h \;+\; \rho_0\,\vec{g} \tag{8.42}$$

where p_h is the hydrostatic pressure imposed by gravity. Let's subtract equation 8.42 from 8.41:

$$(\rho_0 + \Delta\rho)\,\frac{D\,\vec{\mathbf{v}}}{D\,t} \;=\; -\;\nabla(p - p_h) \;+\; \nabla.\,\vec{\tau}_{ij} \;+\; \Delta\rho\,\vec{g} \tag{8.43}$$

In the equation 8.43, p is the actual static pressure at any given point and the pressure difference ($p_m = p - p_h$) is the change in pressure that arises through the fluid motion. In an external flow, this pressure difference is negative $p_m < 0$ and is the source of the entrainment of the ambient fluid into the flow. Choosing the correct reference point could be crucial if the flow field is big enough to create a distinctive hydrostatic pressure gradient due to height difference. In some cases the stationary layered regions of the fluid form far from the flow and the reference position has to be considered within the same region.

The first of the so-called **Boussinesq approximation** is to assume flow to behave approximately incompressibly. As noted above this must handled differently for experiments and DNS. The experimentally realized flow knows it is not really quite incompressible, so C_p is the appropriate choice in the thermal energy equation. But incompressible numerical solutions do not, so the appropriate choice is C_v.

The second of the Boussinesq approximations is applied here: when two terms of the equation containing density difference ($\Delta\rho$) are compared. In the convection term at the left hand side of the equation 8.43, the ($\Delta\rho + \rho_0$) approaches to ρ_0 in the limit of small difference compare to reference density; i.e., $\Delta\rho \ll \rho_0$. While on the right hand side, the buoyancy term just depends on $\Delta\rho$. Therefore the momentum equation for a natural convection flow with a small temperature reference (hence small density variation) can be written in a simplified version:

$$\frac{D\,\vec{\mathbf{v}}}{D\,t} \;=\; -\,\frac{1}{\rho_0}\,\nabla(p_m) \;+\; \frac{1}{\rho_0}\,\nabla.\,\vec{\tau}_{ij} \;+\; \frac{\Delta\rho}{\rho_0}\,\vec{g} \tag{8.44}$$

This approximation is a major help, from a theoretical point of view, for understanding the importance of each term and their role in the Navier-stokes equations. But it may not make sense to use it in a numerical computation where there is option to calculate the exact instantaneous density for each point of the flow. Therefore we should be careful to compare the theories with the exact computations or experimental results, since the assumption may not be satisfied.

The **Boussinesq** approximation is summarized in two statements (Spiegel and Veronis [1960]):

- The density change in the flow is purely due to thermal effect, and viscosity and pressure do not play any role.
- The density variations considered to be effective only when it is coupled to the body force(e.g. gravity). In other terms, the density fluctuation is ignored.

These statements are valid when the condition of ($\Delta\rho/\rho_0 \ll 1$) is satisfied. The first statement leads us to a specific case of equation of state for density:

$$\rho^* = \rho^*(T^*) \tag{8.45}$$

where ρ^* and T^* are dimensionless variables of density and temperature defined as:

$$\begin{aligned} \rho^* &= \frac{\rho}{\rho_0}, \\ T^* &= \frac{T - T_0}{T_w - T_0} \end{aligned} \tag{8.46}$$

This function can be expanded as a Taylor series around $T^* = 0$:

$$\rho^* = 1 + \frac{\partial \rho^*}{\partial T^*} T^* \tag{8.47}$$

substituting dimensionless forms of density and temperature into the equation 8.47 leads to:

$$\Delta\rho = \rho - \rho_0 = -\rho_0 \beta_0 (T - T_0) \tag{8.48}$$

Even though we chose $T^* = (T - T_0)/(T_w - T_0)$ as the temperature variable in equation 8.45, the replaced temperature difference in the buoyancy term is $(T - T_0)$. This shows the importance of choosing right reference value for our specific case. Replacing equation 8.48 into the equation 8.44 leads us to:

$$\frac{D\,\vec{\mathbf{v}}}{D\,t} = -\frac{1}{\rho_0} \nabla(p_m) + \frac{1}{\rho_0} \nabla . \vec{\tau}_{ij} - \vec{g}\beta_0 (T - T_0) \tag{8.49}$$

The third type of Boussinesq approximation can be made with regard to what values of density are to be applied for computing fluid properties like kinematic viscosity, ν, and thermal diffusivity, α. In fact, as will be seen in the next chapter, there is no simple answer to this question, and the best choice is determined by what region of the flow is being analyzed.

8.7 Reynolds-Averaged Equations in Cylindrical Coordinates

From this point we use the index notation or expanded form of the equations to simplify the understanding of each term in the equations. The axi-symmetric nature of the flow leads us to use a cylindrical coordinate rather than Cartesian but the assumptions will be implemented in general forms of the equations as long as it is possible.

The momentum equations for cylindrical coordinates with the flow and the gravity vector parallel to the axial direction have been given in the appendix B (equations B.17 - B.20). These equations for a steady state flow without any azimuthal gradient $\frac{\partial}{\partial\theta}$ are mentioned below. The velocity components in axial, radial and tangential coordinate (x, r, θ) are denoted by (u, v, w) respectively. (U, V, W) represent the mean values for velocities in each direction and $\overline{u^2}, \overline{v^2}, \overline{w^2}, \overline{uv}, \overline{uw}$ and $\overline{vw}$ are the Reynolds stresses for the turbulent flow. The mean tangential velocity is assumed negligible due to symmetry of the flow, therefore the term $(-W^2/r)$ is omitted. The azimuthal momentum equation only describes the relation of the tangential velocity correlations ($\overline{uw}$, $\overline{vw}$) and is not used here.

Averaged Continuity Equation:

$$\frac{\partial U}{\partial x} + \frac{1}{r}\frac{\partial (rV)}{\partial r} = 0 \tag{8.50}$$

Averaged Momentum Equation in Axial Direction:

$$U\frac{\partial U}{\partial x}+V\frac{\partial U}{\partial r}=-\frac{1}{\rho}\frac{\partial P}{\partial x}+\frac{\partial}{\partial x}\left(\nu\frac{\partial U}{\partial x}-\overline{u^2}\right)+\frac{1}{r}\frac{\partial}{\partial r}\left(r(\nu\frac{\partial U}{\partial r}-\overline{uv}\,)\right) + g\beta(T-T_0)+\left\{\frac{\partial \nu}{\partial x}.\frac{\partial U}{\partial x}+\frac{1}{r}\,\frac{\partial \nu}{\partial r}.\frac{\partial rV}{\partial x}\right\} \quad (8.51)$$

Averaged Momentum Equation in Radial Direction:

$$U\frac{\partial V}{\partial x}+V\frac{\partial V}{\partial r}=-\frac{1}{\rho}\frac{\partial P}{\partial r}+\frac{\partial}{\partial x}\left(\nu\frac{\partial V}{\partial x}-\overline{uv}\right)+\frac{1}{r}\frac{\partial}{\partial r}\left(r(\nu\frac{\partial V}{\partial r}-\overline{v^2}\,)\right) + \left\{\frac{\partial \nu}{\partial x}.\frac{\partial U}{\partial r}+\frac{\partial \nu}{\partial r}.\frac{\partial V}{\partial r}\right\}-\nu\,\frac{V}{r^2}+\frac{\overline{w^2}}{r} \quad (8.52)$$

The terms inside the curly brackets can be deleted for a constant viscosity flow. Considering equation 8.49 in previous section, the reference values are chosen for density ρ, viscosity ν and thermal expansion coefficient β in equations 8.51 and 8.52. The pressure in the momentum equations is the difference between local static pressure and the hydrostatic pressure as mention in previous section. The hydrostatic pressure is still present in buoyancy term. For the energy equation in cylindrical coordinate the mean temperature value is represented with T and the velocity-temperature correlations are $\overline{ut}$ and $\overline{vt}$.

Energy equation:

$$U\frac{\partial T}{\partial x}+V\frac{\partial T}{\partial r}=\frac{\partial}{\partial x}\left(\alpha\frac{\partial T}{\partial x}-\overline{ut}\right)+\frac{1}{r}\frac{\partial}{\partial r}\left(r\,(\alpha\frac{\partial T}{\partial r}-\overline{vt}\,)\right)+\frac{\nu}{C_p}\,\Phi \quad (8.53)$$

where $\alpha=\kappa/\rho C_p$ is the thermal diffusivity of the fluid. It is obvious that these equations are coupled through the buoyancy term and can not be solved independently. In none of the equations above, for a Newtonian, incompressible flow, is the assumption of constant viscosity and thermal diffusivity is necessary. But, as written, the reference density has been, and it appears in the denominator of both α and ν.

For the type of flow we are interested in, the average values of velocities are very small. Therefore the heat generated through viscus diffusion is negligible compare to the heat transfer due to high temperature differences. Note that in the momentum equations, the viscous dissipation is a characteristic of the turbulent flow and can not be ignored. In the energy equation 8.53, the last term $(\nu/C_p)\,\Phi$ is negligible in the flow of our interest.

Chapter 9

The Natural Convection Boundary Layer Equations

This chapter summarizes the governing equations believed to be relevant to the natural convection experiment next to the vertical heated cylinder performed herein. Originally it was expected that our focus would be on testing the applicability of similarity analysis (e.g., extending and testing the theory of George and Capp [1979], Wosnik and George [1994], etc.) Also it was hoped the measurements could be used for an extensive analysis of the component Reynolds stress and kinetic energy equations. At very least it was expected to be able to establish unambiguously the heat transfer law for the fully-developed turbulent boundary layer next to a heated vertical cylinder. Unfortunately, as will be seen in the subsequent chapters, the experiment appears to have developed a fully developed turbulent boundary layer at only the uppermost measurement point, if even there. This pretty much precludes unequivocal statements about the asymptotic heat transfer law. Moreover, even there the ratio of outer to inner lengths scales will be seen to be too low for any asymptotic theory to be reasonably evaluated. Worse, problems with the temperature measurements (due to the large thermal gradients present) have preoccupied us with more fundamental (even primitive) questions about whether the measurements and our interpretations of them are correct.

Therefore the primary equations of interest herein are not the equations for the turbulence, but for the mean flow itself, none of which seem to have been considered in detail elsewhere (for the axisymmetric flow conditions). Of particular importance are the equations very close to the wall, so we can evaluate the accuracy of the shear stress and heat flux inferences from the measurements of the mean velocity and temperature profiles. To do so we have had to include in the analysis as well the variation of thermal properties in the near wall region. Also in order to even establish the very nature of the flow and whether the near wall inferences make sense, we have had to consider in detail the integral balances and evaluate the role of the stratification of the ambient.

9.1 The Reduced (or Boundary Layer) equations

Equations 8.51 to 8.53, together with the incompressible continuity, equation 8.50 constitute the basic set of equations which govern buoyancy-domintated flows. These contain, however, a number of terms which are relatively small over most of the natural convection boundary layer. A detailed scaling analysis has been carried out in Appendix D, in which it is concluded that the following reduced forms of the averaged equations, together with the incompressible

continuity equation, contain all of the most significant terms:

$$U\frac{\partial U}{\partial x}+V\frac{\partial U}{\partial r} = \frac{1}{r}\frac{\partial}{\partial r}r(\nu\frac{\partial U}{\partial r}-\overline{uv})+g\beta(T-T_\infty) + \left\{\frac{\partial}{\partial x}\left[\overline{v^2}-\overline{u^2}-\int_r^\infty\frac{\overline{w^2}-\overline{v^2}}{r'}dr'\right]\right\} \quad (9.1)$$

$$U\frac{\partial T}{\partial x}+V\frac{\partial T}{\partial r} = \frac{1}{r}\frac{\partial}{\partial r}r\,(\alpha\frac{\partial T}{\partial r}-\overline{vt}\,)+\left\{\frac{\partial}{\partial x}\overline{ut}\right\} \quad (9.2)$$

Note that the streamwise pressure gradient has been eliminated by integrating the radial momentum equation across the flow, which also introduces the $\overline{v^2}$ and $\overline{w^2}$ terms into the streamwise momentum equation. The terms in curly brackets at the end of each are streamwise derivative of terms which are of second order in turbulence intensity relative to the others, so could have also been neglected. But they have been retained for the moment since they can make a contribution to the integrated momentum and energy equations because of the large turbulence intensities in the outermost extremes of the flow. These equations are a consequence of the Boussinesq approximation, where the thermal properties are to be evaluated at the ambient conditions at the same height, x. Slightly different approximations will be used when the near wall equations are considered in section 9.4 below.

Since temperature differences from the ambient value directly affect the momentum equation (through the buoyancy term), it is of interest to rewrite equation 9.2 in terms of $T-T_\infty$. In general, T_∞ is a function of x, since it is virtually impossible to generate a laboratory flow without some stratification. Therefore the most general (and most useful) form of an equation for the temperature difference from the ambient temperature is given by:

$$U\frac{\partial[T-T_\infty]}{\partial x}+V\frac{\partial[T-T_\infty]}{\partial r}=\frac{1}{r}\frac{\partial}{\partial r}r(\alpha\frac{\partial[T-T_\infty]}{\partial r}-\overline{vt}\,)+\left\{\frac{\partial}{\partial x}\overline{ut}\right\}-U\frac{d\,T_\infty}{dx} \quad (9.3)$$

This can readily be converted into a buoyancy equation by simply multiplying by $g\beta$. The last term will be seen to be particularly important when applying the integrated buoyancy equation below to experimental data, since it acts to add or diminish the net buoyancy just like heat addition at the wall, depending upon its sign (c.f., Shabbir and George [1994], Beuther [1980]).

9.2 Momentum and Buoyancy Integral Equations

By using the incompressible continuity equation for the mean flow, equations 9.1 and 9.3 can converted into equations which can be integrated across the entire flow. These can provide particularly useful checks on experimental data (e.g., Shabbir and George [1994], Hussein et al. [1994]), and for wall-bounded flows independent checks on the wall shear stress and heat flux (e.g., George and Castillo [1997], George et al. [2000]).

Momentum integral equation: To develop the integrated momentum equation, first multiply the mean continuity equation by U to obtain:

$$U\frac{\partial U}{\partial x}+\frac{U}{r}\frac{\partial\,(r\,V)}{\partial r}=0 \quad (9.4)$$

Adding this to equation 9.1 and combining terms (using the inverse of the chain-rule for differentiation) yields:

$$\frac{\partial\, U^2}{\partial x} + \frac{1}{r}\frac{\partial\, r\, U\, V}{\partial r} = \frac{1}{r}\frac{\partial}{\partial r} r(\nu\frac{\partial U}{\partial r} - \overline{uv}) + g\beta(T - T_\infty) \\ \left\{ \frac{\partial}{\partial x}\left[\overline{v^2} - \overline{u^2} - \int_r^\infty \frac{\overline{w^2} - \overline{v^2}}{r'} dr' \right] \right\} \quad (9.5)$$

Note that the use of the incompressible continuity equation in this manner might also be questioned in view of the considerations of the previous chapter. But most of the contribution of the convection terms (which are the ones modified by its use) are away from the immediate vicinity of the wall, hence in regions where the flow can be considered truly incompressible since the mean temperature variation is small (less than a percent from the ambient value in the measurements reported subsequently).

Now multiplication by r and integration from the wall to infinity (including integrating the last term by parts) yields the momentum integral equation as:

$$\frac{d}{dx}\int_R^\infty \left[U^2 + \overline{u^2} - \frac{1}{2}(\overline{v^2} + w^2) \right] r dr = -R\frac{\tau_w}{\rho_\infty} \; + \; \int_R^\infty g\beta_\infty [T - T_\infty] r dr \quad (9.6)$$

Note that this is more than just the momentum integral (hence reference to it as the *momentum integral equation*), since it contains all of the terms in the equation, including wall friction, buoyancy and mean pressure gradient. The appearance of ρ_∞ may seem paradoxical, since $\tau_w = \mu_w \partial U/\partial r|_w$. But this seems the most reasonable choice for the following reason: The density occurs in the original equations multiplying the mean convection terms, which are the terms in the integrals. The main contribution to both the integrals come from the region well away the wall where the temperature variation is quite small; hence ρ_∞ is the appropriate choice. By contrast, the wall shear stress occurs, of course, at the wall where the temperature difference is the greatest. Since it is actually the viscosity (not the kinematic viscosity) that determines the wall shear stress (given the velocity gradient at the wall), using the wall value μ_w to determine the wall shear stress there seems the most logical choice. By a similar line of reasoning, the value of β should be chosen at the ambient value, $\beta = 1/T_\infty$, because the primary contribution of the buoyancy integral is over the bulk of the flow, not the wall region. We will use similar considerations below when developing equations for the near wall region.

Buoyancy integral equation: A similar approach using the incompressible continuity equation can be used to develop an integral equation for the vertical heat flux (or equivalently, the buoyancy). First multiply the continuity equation by $T - T_\infty$, then add it to equation 9.3 to obtain:

$$\frac{\partial\, U\, [T - T_\infty]}{\partial x} + \frac{1}{r}\frac{\partial\, r\, V\, [T - T_\infty]}{\partial r} = \frac{1}{r}\frac{\partial}{\partial r} r(\alpha\frac{\partial [T - T_\infty]}{\partial r} - \overline{vt}\,) + \left\{ \frac{\partial}{\partial x}\overline{ut} \right\} - U\frac{d\, T_\infty}{dx} \quad (9.7)$$

Multiplication by r and integration from the wall to infinity yields immediately:

$$\frac{d}{dx}\int_R^\infty (U[T - T_\infty] + \overline{ut}) r dr = R\frac{q_w}{\rho_\infty C_{p\infty}} \; - \; \frac{dT_\infty}{dx}\int_R^\infty U r dr \quad (9.8)$$

The reasoning behind the choice of $C_{p\infty}$ and ρ_∞ is analogous to that used above for the momentum integral equation. Both these properties enter the equation through the mean convection

terms, the principal contribution from which are away from the wall. By contrast q_w is evaluated using the properties at the wall; i.e., $q_w = -\kappa \partial T/\partial r|_w$.

One important question remains: what value of β should be used if converting this to a buoyancy integral balance equation by multiplying it by $g\beta$. By applying the same criterion, wall phenomena should be evaluated at the wall and *vice versa*, the choice should be $\beta = 1/T_\infty$ for the left-hand side and stratification integral; and $\beta = 1/T_w$ for the wall heat flux term. An interesting consequence of this that is the buoyancy balance is slightly different than the energy balance in that relatively less buoyancy is added at the wall for a given heat transfer rate (assuming, of course, that $T_w > T_\infty$).

9.3 The main (or "outer") boundary layer

Following the same scaling approach as George and Capp [1979] for the natural convection boundary layer next to a flat vertical surface, it is straight-forward to show that as the *Rayleigh* (or equivalently, the *Grashof* or H-numbers[1]) increase, the viscous and conduction terms in the equations for the mean flow become increasingly negligible over the entire boundary layer, except very close to the wall.[2] In fact, the higher the *Rayleigh* number, the thinner the region next to the wall (relative to the overall flow) in which viscosity and conductivity are important. As a consequence, at even the modest Rayleigh numbers achieved in the experiments reported herein, over most of the boundary layer the viscous and conduction terms can be ignored. In fact the measure of whether the turbulence is truly fully-developed or not is whether these terms are truly negligible inside the location of the velocity maximum.

Thus the equations (to leading order in turbulence intensities), the so-called *outer flow equations* George and Capp [1979], which govern most of the fully-developed natural convection boundary layer are given by:

$$U\frac{\partial U}{\partial x} + V\frac{\partial U}{\partial r} = -\frac{1}{r}\frac{\partial}{\partial r}(r\,\overline{uv}\,) + g\beta(T - T_\infty) \tag{9.9}$$

$$U\frac{\partial T}{\partial x} + V\frac{\partial T}{\partial r} = -\frac{1}{r}\frac{\partial}{\partial r}(r\,\overline{vt}\,) \tag{9.10}$$

The corresponding outer temperature difference equation (including the stratification term) is:

$$U\frac{\partial [T - T_\infty]}{\partial x} + V\frac{\partial [T - T_\infty]}{\partial r} = -\frac{1}{r}\frac{\partial}{\partial r}(r\,\overline{vt}\,) - U\frac{d\,T_\infty}{dx} \tag{9.11}$$

9.4 The near wall equations

Again using the scaling approach applied by George and Capp [1979], it is straight-forward to show that very close to the wall the mean convection terms (the left-hand side of both of the equations momentum and energy) are negligible. This includes the stratification term in the temperature difference equation as well. Thus close to the wall (which means well inside

[1] The H-number is defined by George and Capp 1979 as $H = GrPr^2$.

[2] It is important to realize that this is never true in the dynamical equations for the fluctuations, since viscosity and conductivity always affect the smallest scales of motion providing the dissipation. The higher the *Rayleigh* number, though, the less the effect of viscosity and conductivity on the turbulence scales producing the Reynolds shear stress and turbulence heat fluxes.

the peak in velocity for the flow considered here), the momentum and thermal equations (to leading order in turbulence intensity) reduce to:

$$0 = \frac{1}{r}\frac{\partial}{\partial r} r(\nu\frac{\partial U}{\partial r} - \overline{uv}) + g\beta(T - T_\infty) \tag{9.12}$$

$$0 = \frac{1}{r}\frac{\partial}{\partial r} r\,(\alpha\frac{\partial T}{\partial r} - \overline{vt}\,) \tag{9.13}$$

It may seem strange to have the ambient temperature difference in the streamwise momentum equation, but recall that it is removing the effect of the ambient static pressure gradient due to gravity acting on the fluid.

George and Capp [1979] integrated the corresponding equations for a flat plate boundary layer. From the temperature integral they identified the existence of a *constant (total) heat flux layer*, and from the momentum integral a *buoyant sublayer*. For the constant heat flux layer, the near wall equations integrated to:

$$-\overline{vt} + \alpha\frac{dT}{dy} = \alpha\frac{dT}{dy}\bigg|_w = -\frac{q_w}{\rho C_p} \tag{9.14}$$

where $q_w = -\kappa dT/dy|_w$ is the wall heat flux. The corresponding *buoyant sublayer* equations were given by:

$$-\overline{uv} + \nu\frac{dU}{dy} + \int_0^y g\beta[T - T_\infty]dy' = \nu\frac{dU}{dy}\bigg|_w = \frac{\tau_w}{\rho} \tag{9.15}$$

The buoyant sublayer was the counterpart of the inertial sublayer (or constant 'total' stress layer) in forced boundary layer flows. It was called the 'buoyant sublayer' because the 'total' stress was clearly not constant, but continuously modified by buoyancy across the layer. The very near wall region for both the thermal and velocity sublayers was easily shown to be characterized by linear profiles starting from the wall, the so-called conductive sublayer and linear viscous sublayer for the velocity.

Examination of equations 9.12 and 9.13 make it immediately clear that **there can be no such regions in the annular boundary layer under consideration.**[3] Consequently the George/Capp analysis is simply not applicable, at least without modification. Nor for that matter is any other analysis or computation valid that is based upon the idea of a constant stress or heat flux layer. In fact it will be shown below that even the familiar (and commonly assumed) linear regions for the very near wall are at best the leading terms in the proper (logarithmic) near-wall solutions.

9.5 Constant heat flux and buoyant sublayers next to a cylinder

In this section we shall shown that the George/Capp ideas can be generalized to apply to even this annular geometry. It will prove to be more convenient later if we use a slightly more general form of the near wall equations in which the Boussinesq approximation is made locally (instead of globally). These more general equations are given by:

[3]This is obviously true for all axisymmetric boundary layer flows, whether natural convection or forced. This does not previously seemed to have been noticed, but it would very much affect the applicability (or lack thereof) of especially wall-function approaches to the turbulence modeling and CFD of such flows.

$$0 = \frac{1}{r}\frac{\partial}{\partial r} r(\mu\frac{\partial U}{\partial r} - \rho\overline{uv}) + g[\rho - \rho_\infty] \tag{9.16}$$

$$0 = \frac{1}{r}\frac{\partial}{\partial r} r\,(\kappa\frac{\partial T}{\partial r} - \rho C_p\overline{vt}\,) \tag{9.17}$$

where ρ and C_p are to be evaluated at the local mean temperature of the flow. Note that the conductivity, k, viscosity μ, have been used instead of their kinematic counterparts, $\nu = \mu/\rho$ and $\alpha = \kappa/(\rho C_p)$. To within these approximations, these equations are a complete description of the near wall region in fully-developed[4] high *Rayleigh* number natural convection boundary layer.

It should be immediately obvious that these equations can both be integrated from the wall to an arbitrary radial location, r, to obtain:

$$r(\mu\frac{\partial U}{\partial r} - \rho\overline{uv}) - g\int_R^r [\rho - \rho_\infty] r' dr' = \mu_w R \left.\frac{\partial U}{\partial r}\right|_w = R\,\tau_w \tag{9.18}$$

$$r\,(k\frac{\partial T}{\partial r} - \rho C_p\overline{vt}\,) = \kappa_w R \left.\frac{\partial T}{\partial r}\right|_w = -R\,q_w \tag{9.19}$$

where the subscript 'w' means evaluation at $r = R$ which is the wall location.

Thus the counterpart to the buoyant sublayer of George and Capp [1979] is one in which the total stress plus buoyancy integral falls off inversely with radius, r; i.e.,

$$\mu\frac{\partial U}{\partial r} - \rho\overline{uv} - \frac{g}{r}\int_R^r [\rho - \rho_\infty] r' dr' = \left(\frac{R}{r}\right)\mu_w \left.\frac{\partial U}{\partial r}\right|_w = \frac{R}{r}\,\tau_w \tag{9.20}$$

And the counterpart to the constant heat flux layer is one in which the total heat flux falls off inversely with radius, r; i.e.,

$$k\frac{\partial T}{\partial r} - \rho C_p\overline{vt} = \left(\frac{R}{r}\right) k_w \left.\frac{\partial T}{\partial r}\right|_w = -\frac{R}{r}\,q_w \tag{9.21}$$

9.5.1 Near wall temperature and heat flux: constant thermal properties

From equation 9.21 it follows immediately that for constant $\alpha = \kappa/\rho C_p$ that:

$$\left[-\langle vt\rangle + \alpha\frac{\partial T}{\partial r}\right] = \left(\frac{R}{r}\right)\left[\alpha\frac{\partial T}{\partial r}\right]_{r=R} \tag{9.22}$$

The mean temperature near the wall: Very close to the wall the turbulence contribution to the heat transfer is negligible, so equation 9.22 reduces to:

$$\alpha\frac{\partial T}{\partial r} \approx \left(\frac{R}{r}\right)\left[\alpha\frac{\partial T}{\partial r}\right]_{r=R} \tag{9.23}$$

This can be integrated directly to obtain:

[4] In fact this begs the question, since a fully-developed boundary layer can be defined to be one for which these near-wall equations apply.

$$T - T_w = R\frac{\partial T}{\partial r}\bigg|_{r=R} \ln(r/R) \tag{9.24}$$

Thus the mean temperature *at the wall* varies logarithmically, instead of the usual linear behavior for plane flows (c.f. George and Capp [1979]). The logarithm can, of course, be expanded around $r = R$ to obtain the usual liner term as the first term in an expansion; i.e., $T - T_w = dT/dr|_w[r - R]$.

There has long been a question about how to scale the near wall temperature (c.f., George and Capp [1979], Wosnik and George [1994], Wosnik [1994]). From equation 9.23 and the linear expansion of equation 9.24 it is clear that the correct choice of a temperature scale and length scale for $T_w - T$ in the near wall region should involve the kinematic heat flux $F_o = q_w/(\rho C_p) = -\alpha dT/dr|_w$ and α (since it occurs explicitly in the original equations). Most importantly, there is no particular argument that can be made (at least at this point) that it should involve $T_w - T_\infty$, $g\beta$, or the wall shear stress, τ_w (or equivalently the friction velocity defined below, u_*). Unfortunately F_o and α are not enough to define a temperature scale from dimensional analysis alone, so the question must remain open for now. The temperature (or buoyancy) integral of equations 9.7 and 9.8, which can be considered to be equations for the heat (or buoyancy) flux, are largely determined at high Rayleigh numbers by the flow well outside the near wall region. This would seem to indicate that the missing parameter in the temperature analysis should come from the flow itself or its boundary conditions. But this would open up all the possibilities above: $T_w - T_\infty$ (since that is driving the overall flow), $g\beta$ (since it occurs in the equations), and τ_w (since as argued below it characterizes the effect of the flow on the wall region). Of these only the latter is non-local, in the sense that it measures the net effect on the boundary layer of all the heat which has been added below. In the data presentation of the next chapter the wall temperature will be normalized using a temperature scale of $F_o/u*$ and a viscous length scale (from the velocity analysis), ν/u_*; but it should be noted that other possibilities would have worked equally well given the ambiguity left by the dimensional analysis.

The turbulent heat flux: Equation 9.22 can be solved for $-\overline{vt}$ to yield an equation for the turbulent heat flux near the wall in terms of the mean temperature. Given the difficulties of measuring anything near a wall, this can be of considerable value to experimentalists. The result is

$$-\overline{vt} = \left(\frac{R}{r}\right)\left[\alpha\frac{\partial T}{\partial r}\right]_{r=R} - \alpha\frac{\partial T}{\partial r} \tag{9.25}$$

As we move away from the wall, the conduction term rapidly vanishes leaving only:

$$-\overline{vt} \to \left(\frac{R}{r}\right)\left[\alpha\frac{\partial T}{\partial r}\right]_{r=R} \equiv -\left(\frac{R}{r}\right)\frac{q_w}{\rho C_p} = -\frac{R}{r}F_o \tag{9.26}$$

Thus this is very unlike the planar problem. There is no constant heat flux layer, only one in which the turbulent heat flux drops off as $1/r$; i.e., $\overline{vt} \to (R/r)F_o$. Clearly this can be expected to be valid only out from the wall until the mean convection terms become important. And this can be true only if the Rayleigh number is high enough for there to exist such a region.

9.5.2 Near wall velocity and Reynolds shear stress: constant thermal properties

Equation 9.20, the momentum equation near the wall, for constant thermal properties can be written in terms of the temperature as:

$$\nu\frac{\partial U}{\partial r} \; - \; \overline{uv} - \frac{g\beta}{r}\int_R^r [T \; - \; T_\infty]\, r' dr' = \left(\frac{R}{r}\right)\nu_w \left.\frac{\partial U}{\partial r}\right|_w = \left(\frac{R}{r}\right)\frac{\tau_w}{\rho} \tag{9.27}$$

Near wall mean velocity: Close to the wall, the Reynolds shear stress is negligible (exactly zero at the wall). Also the mean temperature profile varies logarithmically according to equation 9.24. Thus very close to the wall the equation reduces to:

$$\frac{\partial U}{\partial r} = \left(\frac{R}{r}\right)\left.\frac{\partial U}{\partial r}\right|_w \; + \; \frac{g\beta}{r\,\nu}\int_R^r \left[(T_w \; - \; T_\infty) + R\left.\frac{\partial T}{\partial r}\right|_w \ln(r'/R)\right] r' dr'. \tag{9.28}$$

This can be readily integrated from the wall to obtain:

$$U = R\;\left.\frac{\partial U}{\partial r}\right|_w \ln(r/R) \; + \; \frac{g\beta}{\nu}\left[\frac{(T_w \; - \; T_\infty)}{2}\left((\frac{r^2-R^2}{2}) - R^2\ln(\frac{r}{R})\right)\right.$$
$$\left. + R\left.\frac{\partial T}{\partial r}\right|_w \left(\frac{r^2-2R^2}{4}\ln(\frac{r}{R}) - \frac{r^2-R^2}{2}\right)\right] \tag{9.29}$$

Taylor expansion of the first term in the right hand side of equation 9.29 gives us a linear term proportional to $(r-R)$ times the wall shear stress (which sets the gradient at the wall); i.e. $U = [\tau_w/\mu](r-R)$. As is clear from the momentum integral, this is mostly imposed on the wall by the flow in the main part of the boundary layer (which dominates the momentum integral). This is consistent with the recent reconsideration of the George/Capp theory for parallel walls by Shiri and George [2008]. In the usual manner, a friction velocity can be defined as $\rho u_*^2 = \tau_w/\mu$ and a viscous sublayer length scale as $\eta_w = \nu/u_*$. Then non-dimensionalizing the velocity and distance from the wall with them leads immediately to the familiar near the wall linear profile $U^+ = (r-R)^+$.

The coefficient of the next term in an expansion near the wall depends on both the temperature difference, $T_w - T_\infty$ and the buoyancy flux, $g\;\beta\;dT/dr|_w$. The temperature dependent (or buoyancy)terms can be considered to be analogous to forced pressure gradient boundary layers (or pipe/channel flows) which are also as quadratic, since this term arises from the static pressure gradient due to the density differences.

9.5.3 Temperature near wall: Variable thermal properties

It is straightforward to evaluate the effects of the temperature on the conductivity, viscosity, and density very close to the wall. From equation 9.21 the temperature equation reduces to:

$$0 = \frac{1}{r}\frac{\partial}{\partial r} r\left[\kappa\frac{\partial T}{\partial r} - \rho C_p\overline{vt}\right] \tag{9.30}$$

Integrating from the wall yields:

$$\kappa\, r\frac{\partial T}{\partial r} - \rho C_p\overline{vt} = \kappa_w R\left.\frac{\partial T}{\partial r}\right|_w \tag{9.31}$$

Turbulent heat flux: In the wall region as long as the mean convection terms are negligible, equation 9.31 can be solved to yield the turbulent heat flux as:

$$-\,\rho C_p\overline{vt} = k_w R\left.\frac{\partial T}{\partial r}\right|_w \; - \; k\; r\;\frac{\partial T}{\partial r} \tag{9.32}$$

where ρC_p and k are to be evaluated at the local temperature. For gases this is given to an excellent approximation by the Chapman-Enskog relation: $k/k_w = (T/T_w)^{1/2}$. Direct substitution yields:

$$-\overline{vt} = \frac{1}{\rho C_p}\left\{k_w R\left.\frac{\partial T}{\partial r}\right|_w - k_w\left[\frac{T}{T_w}\right]^{1/2} r\frac{\partial T}{\partial r}\right\} \tag{9.33}$$

To within an excellent approximation the specific heat at constant pressure, C_p is nearly constant over any range of interest, while the density varies inversely with temperature; i.e., $\rho = \rho_w(T_w/T)$. So in terms of the temperature and wall values only, $\overline{vt}$ is given by:

$$-\overline{vt} = \left\{\alpha_w R\left[\frac{T}{T_w}\right]\left.\frac{\partial T}{\partial r}\right|_w - \alpha_w\left[\frac{T}{T_w}\right]^{3/2} r\frac{\partial T}{\partial r}\right\} \tag{9.34}$$

An exact near wall mean temperature with variable conductivity

To a first approximation, we ignore the $\rho C_p\overline{vt}$ near the wall, and very close to the wall write:

$$\frac{\partial T}{\partial r} = \left(\frac{k_w}{k}\right)\frac{R}{r}\left.\frac{\partial T}{\partial r}\right|_w \tag{9.35}$$

The Chapman-Enskog relation for the conductivity variation with temperature is given by:

$$\frac{k}{k_w} = \left[\frac{T}{T_w}\right]^{1/2} \tag{9.36}$$

Substitution yields:

$$\frac{\partial T}{\partial r} = \left[\frac{R}{r}\right]\left[\frac{T_w}{T}\right]^{1/2}\left.\frac{\partial T}{\partial r}\right|_w \tag{9.37}$$

or

$$T^{1/2}\frac{\partial T}{\partial r} = \left[\frac{R}{r}\right]T_w^{1/2}\left.\frac{\partial T}{\partial r}\right|_w \tag{9.38}$$

This can be integrated directly to obtain:

$$T^{3/2} = T_w^{3/2} + \frac{3}{2}RT_w^{1/2}\left.\frac{\partial T}{\partial r}\right|_w \ln(r/R) \tag{9.39}$$

Solving for the temperature itself yields the near wall temperature profile including the near wall variation of the conductivity as:

$$T = \left\{T_w^{3/2} + \frac{3}{2}RT_w^{1/2}\left.\frac{\partial T}{\partial r}\right|_w \ln(r/R)\right\}^{2/3} \tag{9.40}$$

where the second term arises entirely from the thermal variation of the thermal properties.

Taylor expansion of temperature near the wall

It is interesting to Taylor expand the exact solution of equation 9.40 above from $r = R$; i.e.,

$$T - T_w = \left.\frac{\partial T}{\partial r}\right|_w [r - R] + \frac{1}{2}\left.\frac{\partial^2 T}{\partial r^2}\right|_w [r - R]^2 + \cdots \tag{9.41}$$

The first and second derivatives of equation 9.40 are:

$$\frac{\partial T}{\partial r} = \left(\frac{R}{r}\right)\left.\frac{\partial T}{\partial r}\right|_w \left[1 + \frac{3}{2}\frac{R}{T_w}\left.\frac{\partial T}{\partial r}\right|_w \ln r/R\right]^{-1/3} \tag{9.42}$$

$$\begin{aligned}\frac{\partial^2 T}{\partial r^2} = &-\left(\frac{R}{r^2}\right)\left.\frac{\partial T}{\partial r}\right|_w \left[1 + \frac{3}{2}\frac{R}{T_w}\left.\frac{\partial T}{\partial r}\right|_w \ln r/R\right]^{-1/3} \\ &- \frac{1}{2T_w}\left[\left(\frac{R}{r}\right)\left.\frac{\partial T}{\partial r}\right|_w\right]^2 \left[1 + \frac{3}{2}\frac{R}{T_w}\left.\frac{\partial T}{\partial r}\right|_w \ln r/R\right]^{-4/3}\end{aligned} \tag{9.43}$$

Evaluating these at $r = R$ yields:

$$\left.\frac{\partial T}{\partial r}\right|_w = \left.\frac{\partial T}{\partial r}\right|_w \tag{9.44}$$

$$\left.\frac{\partial^2 T}{\partial r^2}\right|_w = -\frac{1}{R}\left.\frac{\partial T}{\partial r}\right|_w - \frac{1}{2T_w}\left[\left.\frac{\partial T}{\partial r}\right|_w\right]^2 \tag{9.45}$$

Thus the very near wall expansion is given by:

$$T - T_w = \left.\frac{\partial T}{\partial r}\right|_w (r - R) - \frac{1}{2}\left\{\frac{1}{R}\left.\frac{\partial T}{\partial r}\right|_w + \frac{1}{2T_w}\left[\left.\frac{\partial T}{\partial r}\right|_w\right]^2\right\}(r - R)^2 \tag{9.46}$$

9.5.4 Velocity and Reynolds shear stress near wall: variable thermal properties

The momentum equation near the wall can be written as:

$$\frac{1}{r}\frac{\partial}{\partial r} r\left[\mu\frac{\partial U}{\partial r} - \rho\overline{uv}\right] + g(\rho - \rho_\infty) = 0 \tag{9.47}$$

We replace $\rho - \rho_\infty$ with the temperature as follows:

$$\rho - \rho_\infty \approx [\rho_w - \rho_\infty] + \left.\frac{\partial \rho}{\partial T}\right|_w [T - T_w] \tag{9.48}$$

The reason for doing this is to be able to use the linear approximation near the wall (which would not be valid if we expanded around T_∞) . In this case: $\partial\rho/\partial T|_w = \rho_w/T_w$. (Note that far from the wall we will use ρ_∞/T_∞ instead, since we want to expand about T_∞ .)

Multiplying by r, then integrating equation 9.47 from the wall (including for the moment the Reynolds shear stress term) yields:

$$r\left[\mu\frac{\partial U}{\partial r} - \rho\overline{uv}\right] + \frac{1}{2}g(\rho_w - \rho_\infty)(r^2 - R^2) + \frac{g\rho_w}{T_w}\left.\frac{\partial T}{\partial r}\right|_w \int_R^r (r' - R)r'dr' = \mu_w R\left.\frac{\partial U}{\partial r}\right|_w \tag{9.49}$$

The Reynolds stress near the wall: Equation 9.49 can be considered to be an equation for the Reynolds shear stress, at least until the mean convection terms become important. This can be quite useful for checking the internal consistency of experimental data. Rewriting it yields:

$$\begin{aligned} -r\rho\overline{uv} &= \left\{\mu_w R \left.\frac{\partial U}{\partial r}\right|_w - \mu r\frac{\partial U}{\partial r}\right\} - \frac{1}{2}g(\rho_w - \rho_\infty)(r^2 - R^2) \\ &\qquad - \frac{g\rho_w}{T_w}\left.\frac{\partial T}{\partial r}\right|_w \int_R^r (r' - R)r'dr' \\ &= \left\{\mu_w R \left.\frac{\partial U}{\partial r}\right|_w - \mu r\frac{\partial U}{\partial r}\right\} - \frac{1}{2}g(\rho_w - \rho_\infty)(r^2 - R^2) \\ &\qquad - \frac{g\rho_w}{6T_w}\left.\frac{\partial T}{\partial r}\right|_w [2r^3 - 3Rr^2 + R^3] \end{aligned} \tag{9.50}$$

or

$$\begin{aligned} -r\overline{uv} &= \left\{\nu_w R \left.\frac{\partial U}{\partial r}\right|_w - \nu r\frac{\partial U}{\partial r}\right\} - \frac{1}{2}g\frac{(\rho_w - \rho_\infty)}{\rho_w}(r^2 - R^2) \\ &\qquad - \frac{g}{6T_w}\left.\frac{\partial T}{\partial r}\right|_w [2r^3 - 3Rr^2 + R^3] \end{aligned} \tag{9.51}$$

By substituting $r = R + y$ for r and the expansion for dU/dy above, it is easy to say that the presence of the buoyancy term introduces a quadratic term in the Reynolds stress. This is quite different from the forced convection problem where the Reynolds stress begins as the cube of the distance from the wall, but consistent with the constant properties solution derived above.

Mean velocity near the wall: Our goal is to integrate equation 9.47 from the wall. The question is, which terms need to be retained to have a consistent expansion. From the above $\langle uv\rangle$ near the wall begins at least quadratically. Therefore in developing the near wall expansion of U there is no point of including quadratic terms or higher, without explicitly dealing with the Reynolds stress. Thus we will concern ourselves with only the linear terms, so we can skip dealing with the Reynolds shear stress explicitly.

Dividing both sides by r and rearranging yields:

$$\begin{aligned} \mu\frac{\partial U}{\partial r} = \mu_w\frac{R}{r}\left.\frac{\partial U}{\partial r}\right|_w - g(\rho_w - \rho_\infty)\frac{(r^2 - R^2)}{2r} \\ + \left\{\langle\rho uv\rangle - \left(\frac{g\rho_w}{T_w}\right)\left.\frac{\partial T}{\partial r}\right|_w \frac{1}{r}\int_R^r (r' - R)r'dr'\right\} \end{aligned} \tag{9.52}$$

We can rearrange the remaining terms as follows:

$$\frac{\partial U}{\partial r} = \left(\frac{\mu_w}{\mu}\right)\frac{R}{r}\left.\frac{\partial U}{\partial r}\right|_w - \frac{g[\rho_w - \rho_\infty](r^2 - R^2)}{2\mu r} \tag{9.53}$$

Using $\mu/\mu_w = (T/T_w)^{1/2}$ this becomes:

$$\frac{\partial U}{\partial r} = \left[\left(\frac{R}{r}\right)\left.\frac{\partial U}{\partial r}\right|_w - \left(\frac{g(\rho_w - \rho_\infty)}{2\mu_w}\right)\frac{(r^2 - R^2)}{r}\right]\left[\frac{T_w}{T}\right]^{1/2} \tag{9.54}$$

Substituting for T using equation 9.46 yields:

$$\frac{\partial U}{\partial r} = \left[\left(\frac{R}{r}\right)\left.\frac{\partial U}{\partial r}\right|_w - \left(\frac{g[\rho_w - \rho_\infty]}{2\mu_w}\right)\frac{(r-R)^2}{r}\right]\left\{1 + \frac{(r-R)}{T_w}\left.\frac{\partial T}{\partial r}\right|_w\right\}^{-1/2} \tag{9.55}$$

The first term in the first brackets on the right-hand-side alone is the term we would obtain if the viscosity were constant everywhere. The second term in the first set of brackets is the contribution of the buoyancy. The second set of brackets on the right-hand-side is the contribution from the thermal variation of the viscosity with temperature.

This result can be arranged to look more like the constant property without buoyancy by factoring out the first time in the first brackets to obtain:

$$\frac{\partial U}{\partial r} = \left(\frac{R}{r}\right)\left.\frac{\partial U}{\partial r}\right|_w \left\{1 - \frac{g[\rho_w - \rho_\infty]}{2\mu_w}\left[R\left.\frac{\partial U}{\partial r}\right|_w\right]^{-1}(r^2 - R^2)\right\}\left\{1 + \frac{(r-R)}{T_w}\left.\frac{\partial T}{\partial r}\right|_w\right\}^{-1/2} \tag{9.56}$$

We can see the role of the variation of the thermal properties more clearly if we apply a binomial expansion to the second term to obtain:

$$\frac{\partial U}{\partial r} = \left(\frac{R}{r}\right)\left.\frac{\partial U}{\partial r}\right|_w \left\{1 - \frac{g[\rho_w - \rho_\infty]}{2\mu_w}\left[R\left.\frac{\partial U}{\partial r}\right|_w\right]^{-1}(r^2 - R^2)\right\}\left\{1 - \frac{(r-R)}{2T_w}\left.\frac{\partial T}{\partial r}\right|_w\right\} \tag{9.57}$$

We will integrate a truncated version of this equation in the next section.

Expansion of the velocity very near the wall

It does not look possible to integrate equation 9.56 analytically, so it will necessary to integrate approximate versions of it. We can end up with a form which looks like its constant viscosity-no buoyancy counterpart in axisymmetric coordinates if we work with the approximate form of equation 9.57.

Expanding equation 9.56 term-by-term yields:

$$\frac{\partial U}{\partial r} \approx \left(\frac{R}{r}\right)\left.\frac{\partial U}{\partial r}\right|_w - \frac{g[\rho_w - \rho_\infty]}{2\mu_w}\left[r - 2R + \frac{R^2}{r}\right] - \frac{R}{2T_w}\left.\frac{\partial T}{\partial r}\right|_w \left.\frac{\partial U}{\partial r}\right|_w \left[1 - \frac{R}{r}\right] \tag{9.58}$$

This can be readily integrated from r to R to yield our very near wall velocity profile as:

$$U \approx R\left.\frac{\partial U}{\partial r}\right|_w \ln(r/R) + \cdots \tag{9.59}$$

9.6 The constant turbulent heat flux layer

If the Rayleigh number is sufficiently high that there exists a region of the flow where the viscous and conduction effects are negligible AND the mean convection terms are also negligible, then (as already noted above) the governing equations for the mean momentum and thermal energy for this region reduce to:

$$-r\overline{vt} = RF_o \tag{9.60}$$

$$-r\overline{uv} = Ru_*^2 - g\beta \int_R^r (T - T_\infty) r' dr' \tag{9.61}$$

It has already been noted above that this implies that in this overlap region (if it exists), $-\overline{vt} = RF_o/r$.

It is clear from these equations that the only part of the boundary conditions imposed on this region without modification is RF_o, since the net shear stress is very much being modified by the buoyancy integral. The only other parameter occurring in the equations at all is the combination $g\beta$. Thus both dT/dr and dU/dr can at most be functions of r, $g\ \beta$ and $R\ F_o$. It follows immediately from the Buckingham Π-theorem that:

$$\frac{dT}{dr} = -K_1 \frac{(R\ F_o)^{2/3}}{(g\ \beta)^{1/3}\ r^2} \tag{9.62}$$

$$= -K_1 \frac{(F_o)}{(g\ \beta\ R)^{1/3}} \frac{R}{r^2} \tag{9.63}$$

$$\frac{dU}{dr} = K_2 \frac{(g\ \beta\ R\ F_o)^{1/3}}{r} \tag{9.64}$$

where $-K_1$ and K_2 are at most constants. (The minus has been included for convenience, as will be seen below.) Note that we have used dT/dr and dU/dr since the arguments would not be valid for U and $T - T_\infty$ without explicitly accounting for the viscous and conduction effects between this overlap region and the wall. In fact, these effects will determine the integration constants.

These can be integrated directly to obtain the mean temperature and mean velocity profiles in the overlap region as:

$$T(r) - T_\infty = \frac{F_o}{(g\ \beta\ R)^{1/3}} \left[K_1 \frac{R}{r} + A(Pr) \right] \tag{9.65}$$

$$U(r) = (g\ \beta\ F_o\ R)^{1/3}\ [K_2\ \ln\ r/R + B(Pr)] \tag{9.66}$$

where the possible Prandtl number dependence of the additive parameters is a consequence of having to integrate from the wall where the reduced set of equations do not apply. (If integrating from infinity instead these would simply be constants.) Clearly, $F_o/(g\beta R)^{1/3}$ is the temperature scale in this overlap region and $(g\beta R F_o)^{1/3}$ is the velocity scale. Note that the logarithmic dependence of the velocity should not be confused with the logarithmic very near wall solution above. These have quite distinctively different origins and very different physics and scaling. In short, at *very* high Rayleigh number *we should expect to find two logarithmic regions* in the mean velocity profile: one at the wall, and another between the wall and the velocity maximum.

If and when such a region should be observed is very much determined by whether the ratio of inner to outer length scales is large enough. And that in turn is determined by whether the Rayleigh number is high enough. As pointed out by Shiri and George [2008] for planar

buoyant flows, experiments and DNS have fallen woefully short in this regard, since the ratio of outer to inner length scales typically varies as $Ra^{*1/3}$ and $Ra^{*1/3} >> 1$ has never yet been achieved. Therefore it has really been impossible to test the theory. For this flow we have already seen that the inner length scale is ν/u_* for the velocity and α/u_* for the temperature. If we in the absence of an obvious alternative follow George and Capp [1979] and choose the outer length scale as δ_U (defined by equation 12.5), then the requirement for this overlap region to exist would be $\delta_U^+ = u_*\delta_U/\nu >> 1$. (This is exactly the requirement for the usual inertial, or log, layer in forced wall-bounded flows). Unfortunately this criterion is not even marginally satisfied for the experiment reported herein, much to our disappointment.

Chapter 10

Design of the Experimental Facility

As previously mentioned in overview chapter, the original test facility was designed, built and used by Persson and Karlsson (Persson [1994]) at Vattenfall Utveckling AB in order to investigate the natural convection boundary layer along a slender vertical cylinder heated by circulating hot water inside. The cylinder was $10cm$ in diameter and $2.2m$ in height, and was placed in the middle of a $1.8m \times 1.8m \times 2.2m$ cubical enclosure. A $5\ cm$ opening at the bottom of the enclosure allowed the cool air with the seeding for laser measurement enters the system. The hot air was discharged at the top of the cubical through an outlet which was supposed to prevent air recirculation inside the system.

They carried out two sets of measurements in the original experimental rig. The first attempt was to measure mean temperature and velocity separately with two components LDA system and a platinum resistance wire. The second attempt in the same measurement setup included simultaneous measurement of the temperature and velocity, including their correlation. The measurement in the first case was made at the height of $1.1\ m$ from the beginning of pipe (corresponding to *Rayleigh* number based on height of $Ra = 7 \times 10^9$), and the second measurement was at a height of $1.5\ m$ (corresponding to $Ra = 1.4 \times 10^{10}$). Both of these values were too low for a fully turbulent boundary layer within the facility, and the height clearly needed to be increased.

Specification	Original Rig	Present Rig
Diameter of heated cylinder	$10\ cm$	$15\ cm$
Size of enclosure	$1.8\ m \times 1.8\ m$	$1.2\ m$ in diameter
Height of the cylinder	$2.2\ m$	$4.5\ m$
Highest measurement section	$1.8\ m$	$4\ m$
Entrance section	$5\ cm$	$12\ cm$
Outlet pipe size	$25\ cm$	$30\ cm$
Maximum working temperature	$\approx 100\ ^\circ C$	$80\ ^\circ C$
Maximum Rayleigh number	1.4×10^{10}	1.7×10^{11}

Table 10.1: Original and Present Test Rig Specifications; (Persson and Karlsson [1996]).

After these preliminary experiments (reported as Persson and Karlsson [1996]), they realized they also needed to make some modifications to the rig in order to ensure a uniform entrance flow. The height of the inner (and outer shell as well) was also doubled in the hopes of producing a Rayleigh number sufficiently high to obtain a fully turbulent natural convec-

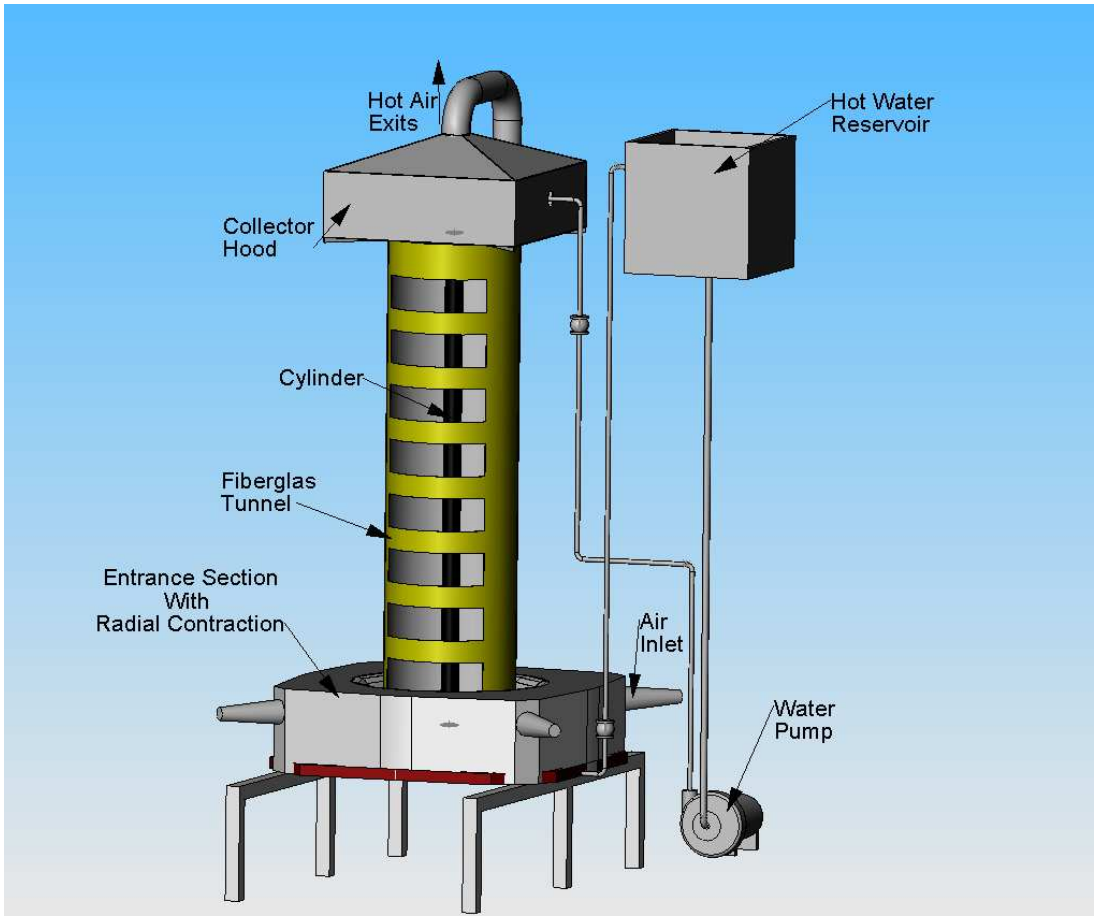

Figure 10.1: Turbulent Natural Convection Boundary Layer Rig Scheme.

tion boundary layer flow. The stratification observed in the enclosure and uncertainty about the inflow uniformity was the motivation to redesign the tunnel with a controlled inlet and outlet. Also in order to have a steady seeding level, a closed loop for the air was necessary. The specifications for the original and modified rigs are summarized in Table 10.1.

The design of a new rig was initiated at Vattenfall AB and some parts of the rig, including the pipe, the fiberglass tunnel and entrance section were built at Vattenfall based on the new design. It was shortly after this that the rig was moved to Chalmers, coincident with the appointment of Rolf I. Karlsson as an Adjunct Professr of Experimental Fluid Dynamics in the fall of 2000. Initial tests on the facility at Chalmers indicated there were still some problems with the entrance flow, so this section was redesigned yet again. The manufacturing of the present section was paid for by and built at Vattenfall. The master thesis work by Axelsson [2003] was a part of this testing/modification process. It took several more years before a place to house the modified facility could be established, but finally in 2005, the *Turbulence Research Lab.* started installation of the new experimental facility.

10.1 Modified Test Rig Outline

The present facility (modified as described above) was installed in a two floor space laboratory with the entrance section in the basement and a portion of the floor above removed to permit

(a) (b)

Figure 10.2: Rig Installation; (a) The Entrance Section and Tunnel, (b) Collector Hood.

the upper part of the facility to extend through it.[1] A schematic of the rig is shown in figure 10.1. A scaffolding was raised around it to allow access for the operator at various levels as can be seen in Figure 10.2. The major modification from the original rig was the height of the test section of the experimental rig. Since the Rayleigh number increases as the cube of the boundary layer length ($Ra \propto L^3$), compared to the temperature difference which affects it only linearly, it is more practical to use a long surface to get larger Rayleigh number. Using a more viscous and dense fluid, like water, had serious drawbacks, especially when measuring with optical methods. The index of refraction in water varies with the temperature fluctuation more than in air, and makes it practically impossible to use laser Doppler anemometry.

Unlike the original facility, a spacious collector section was installed on top of the tunnel to decrease the recirculation of hot air inside the rig and provide a more effective discharge of the air from the test section. Figure 10.2 shows the rig installation (part a) and the collector hood (part b) at the top of the tunnel. The $1.8\ m \times 1.8\ m \times 0.5\ m$ section is connected to the return pipe at the vertex and is separated from the main tunnel by a perforated plate to break down any returning vortices.

A traversing system was designed to reach a vertical traversing span of $4\ m$. The aluminum structure, shown in picture 10.3, provided two horizontal axes of traverse, controlled by the LDA system traversing unit, and the vertical traverse was operated by a manual control. The

[1] This was actually its third location since coming to Chalmers in 2000. The arrangement was not ideal, but was the only possibility given the Department of Applied Mechanics space rent policies which would have taken most of the VR research grant supporting the work.

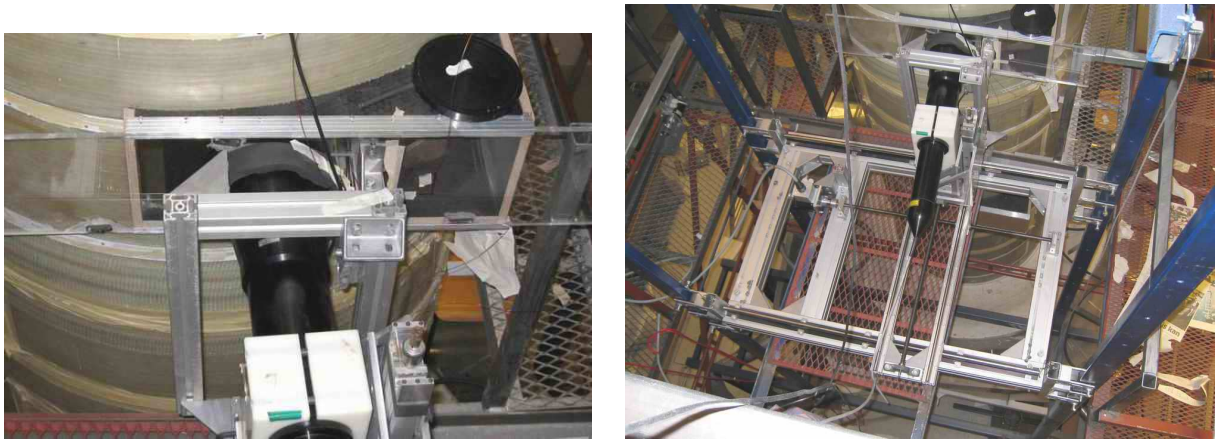

(a) Sliding Window for LDA Lens.

(b) Vertical Traverse.

Figure 10.3: Traverse Structure.

measurements were carried out at three different heights of the pipe from tunnel's floor; $4\ m$, $3\ m$ and $1.5\ m$. At each of these heights, an access window had been cut into the outer shell. Before measuring the laser probe was leveled using four adjustable feet of the traversing table. It unfortunately was not possible to make traverses around the pipe at a given height, so the axisymmetry of the boundary layer flow could only be assumed.

The velocity field was measured using a laser Doppler anemometer operating in back-scatter mode, so that only one optical lens needed to be used for measuring both of the velocity components. The precise positioning and adjustment of the laser measurement volume would have been practically impossible if the laser probe had been traversed outside of the curved window of the tunnel. Therefore a sliding flat window was designed (see figure 10.3) to prevent any laser beam refraction due to surface curvature. The lens was placed inside a circular opening of the slider and the sliding window was moved with the traverse table without touching the lens. The only drawback of this design was that there was a small non-circular section on the tunnel wall at the measurement cross-section. This section was far from the heated wall and did not effect the boundary layer flow. To prevent any geometric imbalance in the axisymmetric design of the rig, the openings of the unused access ports were covered with a dummy fiberglass wall while measuring the other sections of the boundary layer.

10.2 Return Chamber and Seeding Control

As it will be discussed in chapter 11, the choice of velocity measurement method (LDA) worked best with closed loop of air circulating in the system so that uniform seeding of scattering particles could be maintained. For the experiments reported herein, hot air was collected inside the hood and moved into the return chamber without the use of any blower. In other words, the return system also was driven by natural convection. This return chamber was basically a large room enclosing the outer cylinder of dimensions $6\ m \times 4\ m \times 3\ m$. Its function was to gather the returning hot air so that it could be air-conditioned to maintain the temperature and seeding level. Based on the heat transfer rate delivered to the system, a HVAC unit with the cooling capacity of $12,000\ BTU$ was used to cool the returning chamber. To avoid any periodical change in the inflow temperature caused by HVAC controller, the air was circulated inside the chamber using distributed fans. This arrangement produced a constant temperature cooled

air which re-entered the tunnel through inlet section. The fans and air conditioning units were placed far from the exit and entrance of the chamber to eliminate any artificial negative or positive pressure on the system. The size of the chamber was large enough to prevent any closed loop circulation effects. Also the chamber was made of the plastic sheet which was not air-tight so that it did not produce any periodic breathing.

The scattering particles used in LDA measurement were generated by SAFEX fog generator 2010. This device produced a dense white fog by evaporation and condensation of a water-based fog liquid. The quantity of the fog could be adjusted in an automatic switching. The device was turned on and off periodically, but since a change in the fog density over time could produce a bias in the statistical measurement of the velocity, therefore the fog was injected inside the return chamber and mixed using the fans to provide a uniform and constant seeding level in the system.

The seeding particles were selected based on the size and the life time of the particle. The *SAFEX Fog Fluid Extra Clean* produced the water-based oil droplet with the size of $1\mu m$. The estimated response frequency of the seeding particle, suggested by the producer, is $10\ kHz$ and the durability is between the 10 - $30min$ in a confined system. This size of the droplet is also suitable for a low velocity measurement as the drag force should overcome the particle weight. For a estimation of the particle time constant, p_t, we can use the *Stokes* formula presented in Buchhave et al. [1979]:

$$p_t = \frac{d_p^2}{36\ v}(2\frac{\rho_p}{\rho_f} + 1) \tag{10.1}$$

ρ_p and ρ_f are the particle and fluid densities and d is the particle diameter. For the particles in this experiment, this corresponds to $p_t \approx\ 2.5\mu s$, which is much smaller than the time scales of interest.

Selecting a particle size is a compromise between signal amplitude and the particle's ability to follow the flow. Larger particles will increase data rate, but will have a bias toward the accelerating flows, e.g. error in high frequency turbulence measurement. Smaller particles will reduce signal amplitude and data rate, but will follow the flow to higher frequencies. Because the seeding droplets are generated with evaporation and condensation, the temperature in the air differs with the density of the fog. That was the major reason to inject and mix the seeding before conditioning the air flow into the rig.

10.3 Inlet Section Considerations

In the earlier designs, the problem of nonuniform inflow of air at the entrance of the rig led to construction of an axisymmetric inlet section. Axelsson [2003] reported up to 15% deviation from the mean velocity at the perimeter of the original design. The redesign is shown in figure 10.5. An annular contraction with three rows of screens was used to improve the quality of flow and eliminate any possible large scale eddies. Four valves were installed in the connecting pipes before the inlet section to adjust for a uniform inflow. These pipes were fed from the back chamber of the rig with cooled and seeded air. When running the experiment with co-flow, a fan was placed in the connecting pipe with a speed controller to adjust the inflow velocity. Some test run were carried out to observe the effect of co-flow, and even the smallest forced convection had considerable effect on the boundary layer. Therefore this fan was turned off for

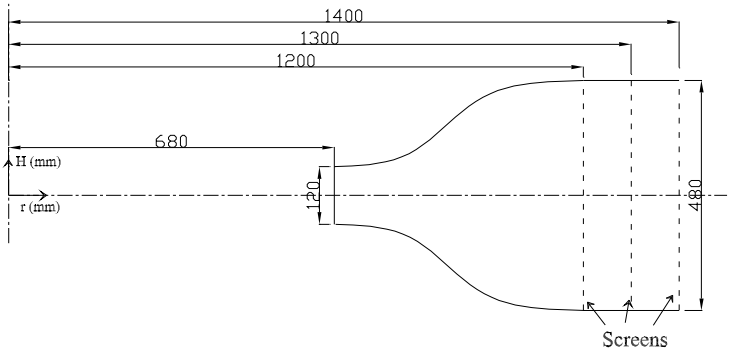

Figure 10.4: Inlet Section Contraction.

all of the experiments reported herein.

Figure 10.4 shows a sketch of the inlet section contraction with the position of the screens behind the contraction. The contraction was made of fiberglass and embedded inside a stainless steel casing to provide the strength to hold the weight of the cylindrical tunnel. The metal casing also acts as the diffuser for the inlet pipes from the side chamber (see figure 10.5). 14 vanes guided the air to enter the rig symmetrically toward the center of tunnel. The tunnel's floor was covered with a flat plexiglass section which the pipe passed through in order to make a distinctive starting point for the vertical surface.

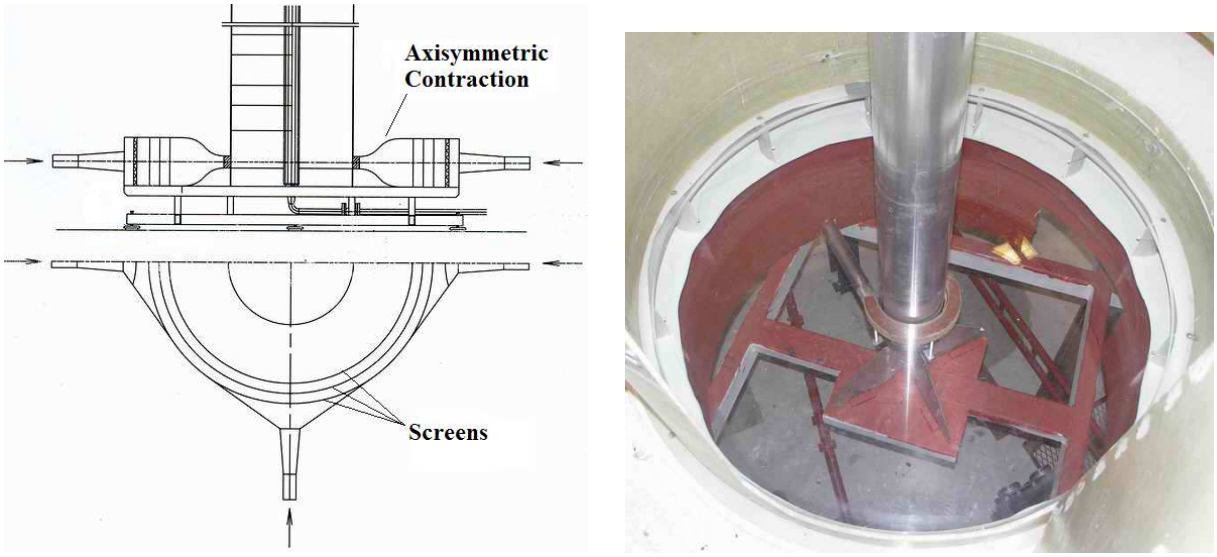

(a) (b)

Figure 10.5: Inlet Section Layout.

10.4 Heating and Cooling of the Test Rig

The system transfers heat to the air from the cylinder's wall in the middle of the tunnel. A water pump, as shown in figure 10.1 circulates hot water through the pipe with a nominal flow rate of $\approx 2\ kg/s$ at a constant temperature. A frequency convertor adjusted the speed of water pump which controlled the water flow rate. This flow rate was chosen to maintain the pipe's outer surface nearly constant, by monitoring the wall temperature difference at the top and bottom of the pipe with thermocouples. The highest preliminary estimation of the heat transfer rate from the cylinder (based on the empirical data on flat surface 7.7) suggested an average value of less than $1kW$. Considering this initial guess, for the given flow rate, the temperature drop in the water (and therefore wall temperature) can be estimated to be less than

$$\Delta T = \frac{q}{\dot{m}\ C_p} = \frac{1000\ [W]}{2\ \left[\frac{kg}{s}\right] \times 4188\ \left[\frac{j}{kg.K}\right]} \approx 0.1^{\circ}C \tag{10.2}$$

This is well below the accuracy of thermocouple measurement method, which made it impossible to cross-check the boundary layer measurement values of heat transfer rate with the actual value of energy provided. This was a significant shortcoming of the experiment, especially given the problems of temperature measurement discussed later.

The measurement was designed to be carried out using an isothermal wall, therefore the circulating hot water inside the pipe had to be kept at a constant temperature. Two heating elements responsible for warming up the reservoir were connected to a controller box (see figure 10.6). The controller was built based on the proportional integral derivative controller (PID controller), which is a control loop feedback mechanism of control. The feedback temperature, measured by a thermocouple type K submerged in the water at the exit section of reservoir, fed the controller as the temperature set point was fixed at $71^{\circ}C$. The diagram 10.7 explains the

(a) (b)

Figure 10.6: Water Heater System; (a) Controller Unit, (b) Reservoir.

controller algorithm.

The PID controller algorithm gives three separate functions of the measured value; the proportional, the integral and derivative values. An error is calculated based on the fixed temperature set point and the feedback temperature from thermocouple. The proportional value determines the response proportional to the current error as $P = K_p e(t)$. The integral value determines the response based on the sum of recent errors; $I = K_i \int e(t)dt$. And the derivative value determines the response based on the rate at which the error has been changing as $D = K_d de/dt$. The weighted sum of these three actions is used to adjust the current via a relay to the power supply of the heating elements so that a steady-state can be achieved according to:

$$V(t) = K_p\, e(t) + K_i \int e(t)dt + K_d \frac{de(t)}{dt} \tag{10.3}$$

where $V(t)$ is the output voltage, K_p is the proportional gain, K_i is the integral gain, K_d is the derivative gain and $e(t)$ is the error (difference between set point and feedback value). The commercial PID controller, purchased from ELFA, was coupled with a three-phase relay to be able to feed the required voltages into the heaters. The heaters were three-phase elements connected in triangle formation, one with a $8\ kW$ output for warm-up stage and a smaller one with the output power of $1\ kW$, to run continuously.[2]

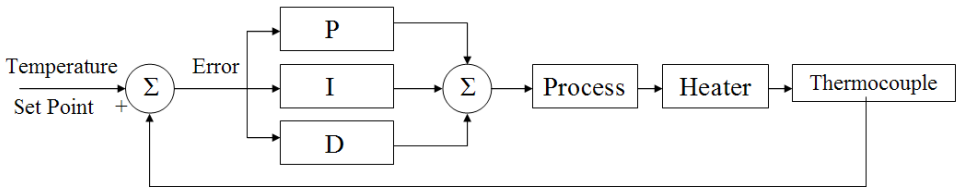

Figure 10.7: Proportional Integral Derivative Controller Diagram.

10.5 Radiation Between the Inner and Outer Cylinders

The arrangement of a two concentric cylindrical surfaces with different temperatures and emissivities immediately allows for radiation heat transfer between these two surfaces. This will not affect the flow (assuming the absorption by the scattering particles and air to be negligible). But it will affect the overall energy balance, i.e., what fraction of the heating provided by the water heater actually goes into the flow itself by conduction at the walls. Therefore it is useful to have an estimate of its value.

By assuming a constant temperature boundary condition on the surfaces we can estimate the net amount of radiation loss from the inner cylinder as (c.f., Incropera [2007]):

$$q_{rad} = \frac{\sigma(2\pi RL)(T_{wi}^4 - T_{wo}^4)}{\frac{1}{\epsilon_i} + \frac{1-\epsilon_o}{\epsilon_o}\left(\frac{R}{R_o}\right)} \tag{10.4}$$

where $\sigma = 5.76 \times 10^{-}8[W/m^2.K^4]$ is Stefan-Boltzmann constant, R & R_o are the radii of the inner and outer cylinders respectively, ϵ_i and ϵ_o are the emissivities of the two surfaces, L is the

[2]The designing and building of these electronic instruments were by Lars Jernquist, whose help and interest throughout the experiment was greatly appreciated.

length of the cylinders, and the surface temperatures are denoted as T_{wi} and T_{wo}.

In order to estimate of how much heat transfers from inner to outer cylinder by radiation, we consider $T_{wi} = 70°C$ $(343°K)$ and $T_{wo} = 22°C$ $(295°K)$ to be the constant surface temperatures. For the inner surface , black paint was used to eliminate the laser reflection, and it has an emissivity of nearly a blackbody ($\epsilon_i \approx 1$). We assume the fiberglass outer surface to have an emissivity of $\epsilon_o \approx 0.8$; (cf. Incropera [2007]). The radii of the inner and outer cylinders were 0.075 m and 0.6 m respectively. Substituting these values in the equation 10.4 gives us the approximate radiation heat transfer rate of $q_{rad} = 165\ W$. Since the estimated energy transfer rate from the inner cylinder was less than $1\ kW$, this is a significant fraction of the overall energy balance for the rig.

10.6 Stability of the Facility

In order to insure that the facility was operating reliably and at stable conditions, the temperatures of the air and pipe wall were monitored continuously at different position. Because the overall air velocity outside of the boundary layer itself was practically negligible, the only parameter to monitor was the mean temperature of the air. A set of thermocouple were positioned at the entrance of the rig, at $4\ m$ height and on the pipe surface and the system started to work at its nominal condition. A measurement of this monitoring from the startup is shown in figure 10.8.

The gradient of the temperature's stratification was also monitored inside the rig, far from the heated cylinder ($r \approx 50\ cm$) at four different heights of $1\ m$, $2\ m$, $3\ m$ and $4\ m$ using thermocouples (see figure 10.8). The value of the temperature difference at each measurement cross-section ($\Delta T = T_w - T_\infty$) was calculated based on the measured value of these thermocouples. The room temperature was also monitored throughout the experiment to document any sudden change in the overall conditions of the measurement.

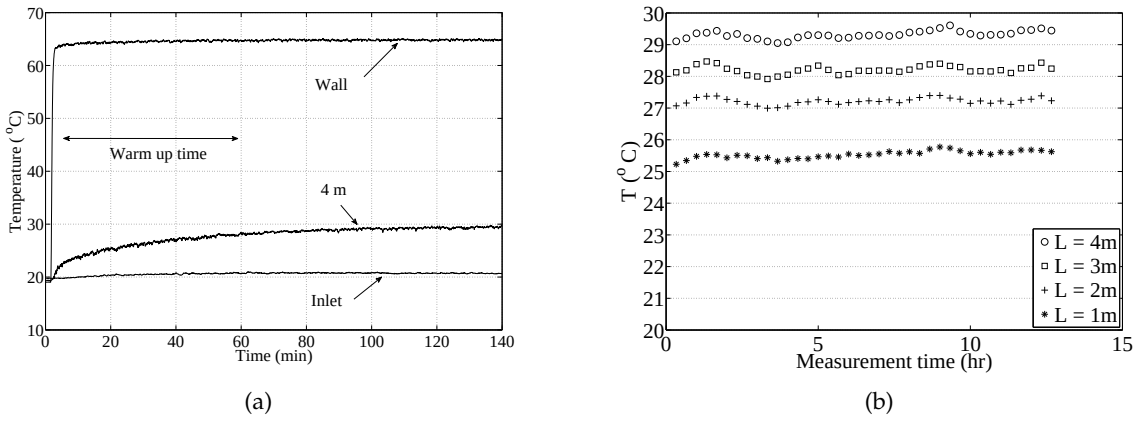

(a) (b)

Figure 10.8: Temperature stability monitoring, (a) at the inlet, surface of the pipe and ambient Air temperature at height $4\ m$, (b) in four different heights during the measurement.

10.7 Accurate Positioning

In the boundary layer velocity measurement with LDA, the measured values should satisfy the no-slip boundary condition. This means that the exact positioning of the probe could be corrected just by shifting the velocity profile along the traversing direction. This is not the case for measuring the temperature with cold-wire, or any other intrusive method. The heat conduction through the prongs or the connecting supports and the error in the measuring of the exact value of wall temperature made it in practice impossible to correct the position based on the temperature curve. Therefore the exact (or at least as accurate as possible) positioning of the temperature measurement probe is essential.

A separate 3-D micrometer traverse system put on top of the probe holder for fine adjustment. the probe holder was a one meter aluminum beam with a NACA profile cross section to prevent vortex generation in the measurement section. Before each attempt at measurement, the laser probe volume was positioned at the wall by traversing the laser beams adjacent to the cylinder surface. The reflection of the laser beams could contaminate the signals from the particles and compromise the measurement. In order to avoid any reflection, the entire surface of the cylinder was painted in black using "Nextel Velvet Coating". The expansion of the structure due to heating and cooling of the system also required readjustment of the wall measurement in every attempt.

The laser probe volume was adjusted relative to the wall by controlling the receiving signal using an oscilloscope. After adjusting the laser, the cold-wire and thin thermocouple were positioned next to the wall by the auxiliary micro-traverse and a microscope connected to a CCD (see figure 10.9). The picture in the monitor of the microscope had an accurate scale to measure the distance of the probe from the wall. The cold-wire could not be positioned exactly in the laser measurement volume because the reflection from the prong affected the LDA measurement. Therefore the cold-wire probe was placed at the closest position ($\approx 150\ \mu m$) above the laser beams' intersection.

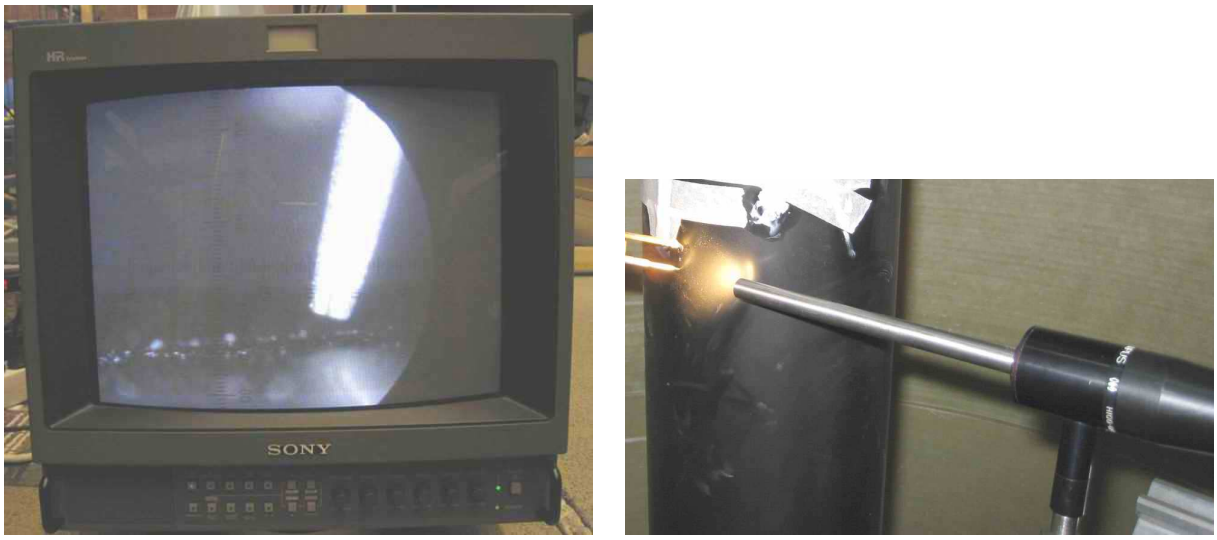

(a) (b)

Figure 10.9: Positioning microscope; (a) Cold-wire on scaled monitor, (b) Lens.

Chapter 11

Measurement Methods and Methodology

This chapter describes the experimental methods used to measure the velocity and temperature in the natural convection boundary layer experimental facility described in previous chapter. Also the details of the criteria for selection of each method, the specifications of the equipment, and the measurement procedure will be explained.

11.1 Introduction

A measurement system consists of four types of elements: sensing, signal-conditioning, signal-processing and data presentation. In order to measure any property of the flow, it first needs to be isolated from the microscopic and macroscopic structure of the medium in order to be measured. This is done by the sensing element which is in the direct contact with the flow and converts the true value of the property to an easy to use output, e.g. voltage, current or frequency. The output represents an estimation of the true value based on the ability of the sensing element to react to changes in the flow property. In this chapter we briefly go through the errors and problems encountered while using the instrumentation and methods of measurement in this natural convection boundary layer experiment.

All of the methods of measurement, as explained in this chapter have limitations regarding the accuracy of the method. At the very first step each measurement method is chosen based on the data specifications required to evaluate the theoretical studies. The instrument used in an actual experiment is always a compromise between the accuracy requirements of the acquired information and the availability of the instrumentation. There is always a drawback compared to the its benefits of using any method or a tool. To interpret and use the results it is important to be aware of as many errors and limitations of them as possible.

The overall goal of this investigation was to measure two components of velocity and temperature simultaneously in the natural convection turbulent boundary layer. The overall condition of the rig also had to be monitored by logging the temperature variation at different positions in the facility. To accomplish this, several main criteria needed to be satisfied in selecting the measurement methods:

- The need to measure with low mean velocity ($< 1m/s$) and high turbulence intensity (over 100%) in parts of the flow.

- The need for a non-intrusive anemometry method as possible to avoid disturbing the flow.
- The need to make velocity measurements very close to a heated wall.
- The need to measure higher moments of turbulence properties accurately, with sufficient frequency response and spatial resolution to avoid significant temporal and spatial filtering.

The "gold standard" for the last requires that the measurement sampling volume should be smaller than half of the Kolmogorov microscale¡ η_K, defined as:

$$\eta_K = \left(\frac{\nu^3}{\epsilon}\right)^{1/4} \tag{11.1}$$

where $\epsilon \equiv u^3/\ell$ is the dissipation of the turbulence in the flow. An almost equivalent criterion is that its largest dimension be smaller that the typical near-wall viscous (or conductive) scale, ν/u_* (or α/u_*) where u_* is the friction velocity. For these experiments both these scales were on the order of $0.3\ mm$.

For the choice of anemometry method, the hot-wire option was ruled out since the heat transfer from the wall and the high temperature gradients make it very difficult to calibrate (or even position) the probe accurately. Also, if we (given a lack of choices) used a temperature probe simultaneously with a hot-wire, the heat generated from the wire can contaminate the flow temperature. Using a cross-wire to measure two components of velocity exacerbates the problem, and also there is a loss of directional sensitivity at low velocities (c.f. Beuther [1980], Shabbir et al. [1996]). There have been some attempts to compensate the deficiencies of this method in measuring low velocity flows close to wall, by using v-shaped hot-wires (see Tsuji and Nagano [1989a]), but since better choices were available with higher accuracy, we did not try this method. Other intrusive methods based on the local pressure difference (e.g. 5-hole probe) did not have the required sensitivity, response time or spatial resolution for this flow; but also have serious problems due to buoyancy induced in them by thermal gradients (c.f., George et al. [1977]).

Particle image velocimetry (PIV) would have very helpful, especially for capturing the unique nature of the large scale motions observed in the flow by eye using smoke, even though implementation close to a surface would have been difficult. But the major reason was lack of availability of a PIV equipment[1] So by default the only optical velocimetry method used in this experiment was laser Doppler anemometry (LDA). LDA is a non-intrusive method with a high spatial resolution ($\sim 50\ \mu m$). It has the disadvantage that the measurements are taken randomly and with a sampling process that is correlated with the flow, thus complicating both statistics and time-resolved measurements. We will discuss this measurement method and the instrumentation in detail later in this chapter.

Two types of temperature measurement were utilized in this experiment. The first consisted of the instantaneous temperature measurements within and across the boundary layer; and the second consisted of the mean temperature of the surrounding (ambient) air and at

[1]The Turbulence Research Laboratory was about the only fluids lab in Sweden that did not have a PIV, in spite of numerous proposals to acquire one. And unlike the Wänström [2009], it was not possible to move this facility to the Danish Technical University to take advantage of their capabilities.

surfaces of the boundaries. Optical thermometry methods are not suitable for temperature profile measurements in a transparent medium such as air. Infra-red and liquid crystal thermography methods can be used for surface temperature (e.g., Arroyo Osso [2009]), but along with other techniques like photoluminescence thermography they suffer from a lack of temporal and spatial resolution. The only method that could measure turbulence fluctuations with good measurement resolution and fast response time was the so-called cold-wire method: a thin resistance wire connected to a constant current circuit. The cold-wire measurements were complemented by mean flow temperature measurements using miniature thermocouples. For monitoring the surface and ambient temperatures throughout the measurement and in many places simultaneously, the most reliable and least expensive choice was standard thermocouples. Both the thermocouple and cold-wire techniques proved to be quite unsatisfactory for the boundary layer measurements. Although it is probably true for most experiments, it is especially true for this one: the results could have been substantially improved had we known at the beginning what we know now, especially about application of these techniques in flows with strong mean temperature gradients.[2]

11.2 Laser Doppler Anemometry

In the experiment we used the laser Doppler anemometry method to measure two components of the velocity. The laser was an argon-ion, *Coherent Innova 90*, capable of producing up to 10 W output in the range of $500\ nm$ wavelength. Using a set of prisms and a Bragg cell, three pairs of the laser beam were generated with the wavelengths of $514.5\ nm$ (green), $488\ nm$ (blue), and dark blue with a smaller wavelength. The two first colors were used in this measurement. The laser beams were carried through a fiber-optic cable into a optical lens which was focused to create the measuring volume. During the measurement the output of the laser cavity was set to 5 W which after passing through the optical sections and the transferring fiber optics, the measured power in each individual beam was approximately 0.035 W. The diameter of the beam entering the optical lens was $2.25\ mm$ and it was expanded using one beam expander with the ratio of 1.96 and a front lens expansion ratio of 1.55. Therefore the diameter of the beam exiting the lens became:

$$Ed = 2.25 \times 1.96 \times 1.55 = 6.8355\ mm$$

The angles between each pair of the beams were measured to be approximately $\beta \approx 10.6°$. Using the beam diameter and the angle between two beams and the focal length of the probe ($f = 600\ mm$), the size of the measurement volume can be calculated as:

$$d_f = \frac{4}{\pi}.\frac{\lambda\sqrt{f^2(1+\tan^2(\beta/2))}}{Ed} \approx 55\mu m \tag{11.2}$$

The fringe spacing can be estimated as:

$$\delta_f = \frac{\lambda}{2.\sin(\beta/2)} \approx 2.7\mu m \tag{11.3}$$

The LDA probe lens was used in a back-scatter mode and was rotated $45°$ around the axis of the lens, therefore each pair of the laser beam were measuring a combination of radial and

[2]Near wall temperature measurements was one of the many parts of this experiment where the absence of the vast measurement experience of Professor Rolf Karlsson was keenly felt.

streamwise velocity components. This arrangement had the advantage of receiving an approximately equal sampling rate in both BSA's, and avoids an optical error bias in the measurement of a particular velocity component. The data were then converted to the actual value of each component using a transformation matrix during the postprocessing. Other information about the measurement setup and the seeding conditions of the flow were presented in chapter10. All data were processed using the residence-time algorithms proposed by Buchhave et al. [1979] and George et al. [1978] (see Velte [2009] for a comprehensive and recent review).

11.3 Acquisition of Simultaneous Data

In order to calculate the temperature-velocity correlations ($\overline{ut}$, $\overline{vt}$), It was necessary to synchronize the data acquisition process of the LDA and cold-wire instruments. As already mentioned, the LDA generates velocity data that is randomly distributed in time, but the cold-wire produces a continuous signal which is evenly sampled in time. To find a temperature sample at very nearly the same time as the burst from the LDA, we need to have the sampling time record of both data sets and match them against each other. Therefore both BSA and Wavebook A/D converter should start sampling at the same time and keep the time with the same clock.

To avoid a gradual shift in the time signals, a circuit was built[3] to provide a high frequency signal ($9.6\ kHz$), as an external clock, for both BSA and Wavebook. The BSA provides a trigger signal when the first burst is detected by photomultiplier. This signal is usually used for synchronization of two BSAs in multi-component LDA measurements. The signal was used as a TTL trigger for the *IO Tech Wavebook* A/D convertor to ensure the simultaneous starting point of measurement in both devices. In every acquisition block, the BSA starts from the beginning to count the number of pulses from the external clock signal and stores the pulse number as arrival time information for every data realization. A schematic of the measurement flowchart is shown in figure 11.1.

As the measurement time interval is set to be constant for BSA, the Wavebook was also set to sample the cold-wire data with the specified frequency for that time interval. The sampling frequency criteria in Wavebook was the constant current circuit cut-off frequency ($3.2\ kHz$). The wavebook starts sampling when the signal from the TTL trigger comes from the BSA. The equal time intervals between temperature samples make it possible to find the arrival time of each sample. Both data sets from BSAs and Wavebook were saved with the information containing arrival time and the value of the property. BSA also saves the transient time of each sample as a weighting function for calculating the statistics of the velocity. Finding the coincident samples is done during the post-processing of the data.

11.4 Thermocouples

In this experiment thermocouples were used in four configurations:

- To measure and monitor at different positions along the surface of heated cylinder.
- To measure and monitor the air temperature at different places inside and outside of the facility.

[3]Designed and built by Lars Järnqvist. *"Trigger to Synchronize CTA with LDA – LJ020408"*

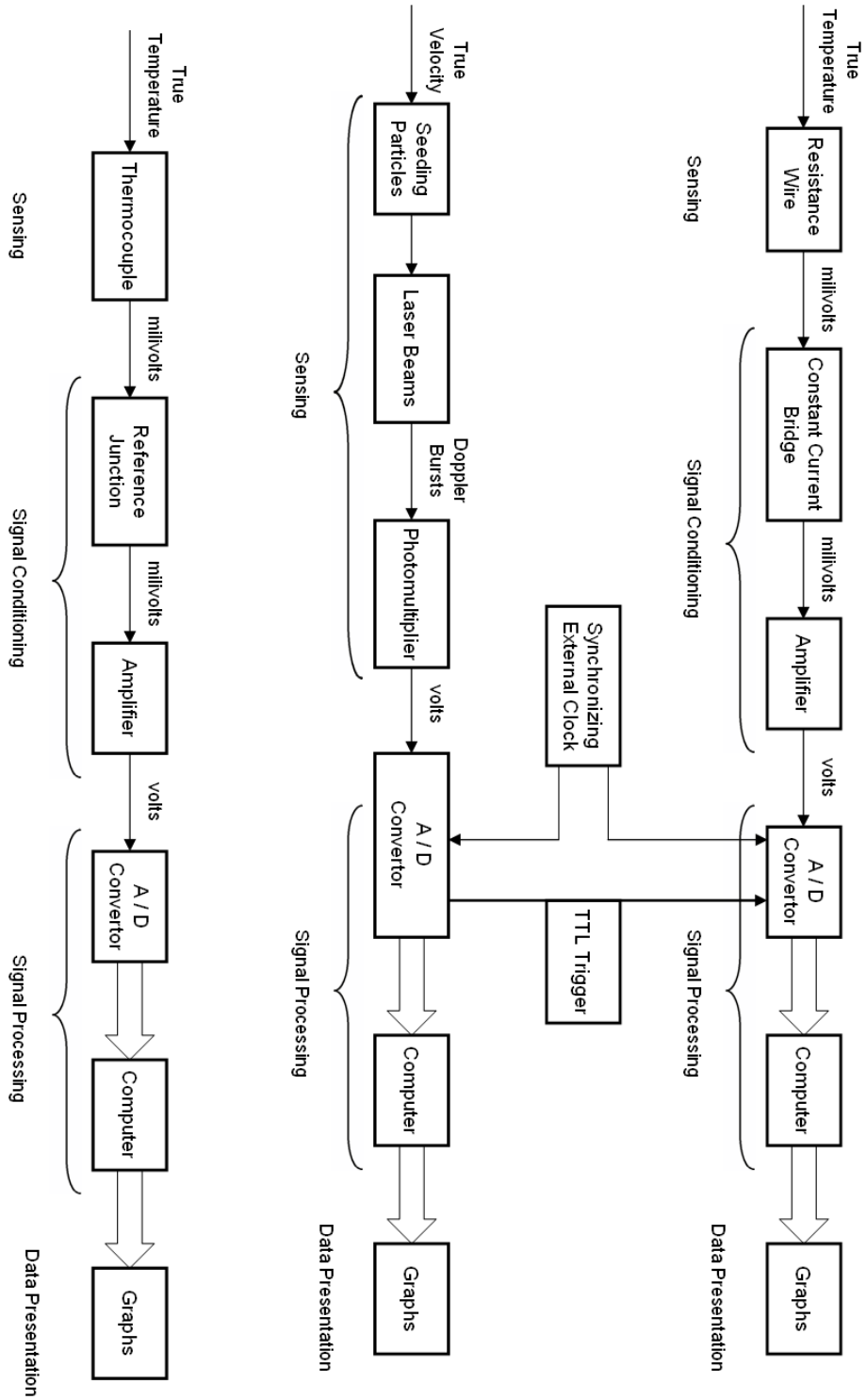

Figure 11.1: Measurement flowchart.

- To measure and monitor the water temperature of the hot water reservoir.
- To provide a zero reference voltage for the other thermocouples.

The thermocouple is by far the most widespread type of temperature sensor in the world. It is relatively inexpensive, robust and straightforward-to-use, and if used correctly, provides quite accurate data. It was T.J. Seebeck in 1821 who discovered that if two dissimilar metals or alloy wires are joined at both ends to form a circuit, an electromotive force (EMF) is produced when there is a temperature difference between the junctions. The two junctions are called the measuring junction and the reference junction. The magnitude of the Seebeck voltage, E_s, depends on the materials of two wires and the temperature difference between the junctions, and is given by:

$$dE_s = S_{A,B} \, .dT \tag{11.4}$$

where $S_{A,B}$, the Seebeck coefficient, is dependent upon the materials of two wires: A and B. Because there are tables for standard thermocouple materials, we can either use the tabulated values for the Seebeck coefficients or calibrate the thermocouple with an accurate temperature measurement device.

All the components of the measuring circuit that are inside the temperature gradient, including the compensating leads and connectors, contribute a separate voltage. To make a circuit that produces the exact voltage correspondent to the temperature at the measuring junction, we should consider these three empirical laws when using a thermocouple circuit:

- The Seebeck voltage is not generated in a single homogenous material, even with a variable cross-section, by applying a temperature gradient. The inhomogeneity can produce such a thermoelectric current.
- The algebraic sum of the thermoelectric currents in a circuit of any number of dissimilar materials is zero as long as all the parts of the circuit is placed in a uniform temperature. Therefore a device for measuring the voltage does not contribute to thermoelectric current generation, regardless of method employed, if the junction is isothermal.
- If two dissimilar metals produce a thermal EMF of E_1 when the junctions are at temperatures T_1 and T_2, and a thermal EMF of E_2 when the junctions are at T_2 and T_3, the EMF generated when the junctions are at T_1 and T_3, will be $E_3 = E_1 + E_2$. Therefore using an extension wire with the same material of the thermocouple wires does not affect the net EMF of the circuit.

The thermocouples used in the experiment for monitoring the temperatures were made of J-type thermocouple wire provided by *Pentronic AB*. The thermocouple wires were made of Iron (+) and Constantan (-) and covered with a resin coating to protect them from short-circuiting. The measuring junction was made by twisting and soldering two wires to protect the junction from rusting or contamination. A thin layer of soldering alloy was applied to the junction so that the overall size of the thermocouple bead did not exceed $1\ mm$ in diameter and $3\ mm$ in length. The length of thermocouple wires were long enough to avoid using any extension cable.

Each thermocouple was coupled with a reference junction in order to create a zero-reference temperature point as shown in figure11.2. Even though the measurement device used in this experiment had a built-in CJC (cold-junction compensation), the use of an ice-bath provided

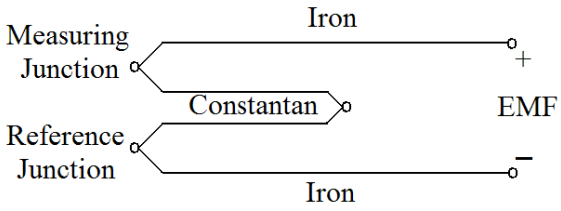

Figure 11.2: Thermocouple circuit configuration with reference junction.

an ideal reference point with less error. Accurate measurement relative to the ambient temperature was especially important since the momentum production by buoyancy was largely due to relatively small temperature differences over most of the flow. The ice bath was made of a $1.5\ \ell it$ water container insulated with Polyurethane foam, filled with crushed ice and water. Following Benedict [2005], a reliable ice-bath was provide with the exact water temperature at melting point, the pieces of crushed ice used were small but not completely smashed. Also the reference junction was placed at a depth of at least $12\ cm$ and far from each side and bottom of the container not less than $2.5\ cm$. The junctions were covered with the silicon based glue to avoid short-circuit between them.

Three sets of National Instrument *NI USB-9211A* were used for the thermocouple measurements. Each one provided 4 channels of 24-bit thermocouple input with a total sampling rate of $12\ sample/s$ and an input voltage span of $\pm 80\ \mu V$. All the modules were placed in a *NI cDAQ-9178* chassis and connected to computer via a USB connection. A LabVIEW code was written to control and log the data acquisition process of the thermocouples.

The thermocouples were calibrated in a hot water bath against a *Pt-100* [4] which was itself calibrated by a providing company recently. Because the thermocouple beads were bare, to avoid short-circuit between the thermocouples they were placed inside a small container filled with a silicon based fluid (DOW CORNING 200 FLUID, polydimethylsiloxane PDMS) and then submerged in the water bath. The calibration curve of each thermocouple in the temperature range between the ambient ($\sim 18°C$) and $80°C$ was used in the computer code to convert the voltage to temperature directly. The position of thermocouples in the rig is shown in figure 11.3.

11.4.1 Fine-Gauge Thermocouple

It was desirable to have an independent measurement of the mean temperature profile of the boundary layer to corroborate the cold-wire thermometry. Several unsheathed fine thermocouple of type K were connected together to measure the temperature difference $(T_w - T)$ directly at different positions across the boundary layer using the arrangement illustrated in figure 11.2. As shown in figure 11.5, the thermocouple and cold-wire probes were positioned on the same traversing setup to measure at approximately the same radial position, but the position of the thermocouple was nearly $1\ cm$ above the cold-wire probe.

The size of the thermocouple wire used in the measurement was $75\ \mu m$, and the size of the thermocouple bead was approximately $100\ \mu m$. The thermocouples were built by the providing company, *OMEGA*, but they were connected and installed in the laboratory. To insulate the

[4] *Pt-100* is a temperature sensor based on measuring the resistance of a platinum element (Platinum Resistance Thermometers, PRT), which the most common type (PT100) has a resistance of 100 Ω at 0 $°C$ and 138.4 Ω at 100° C.

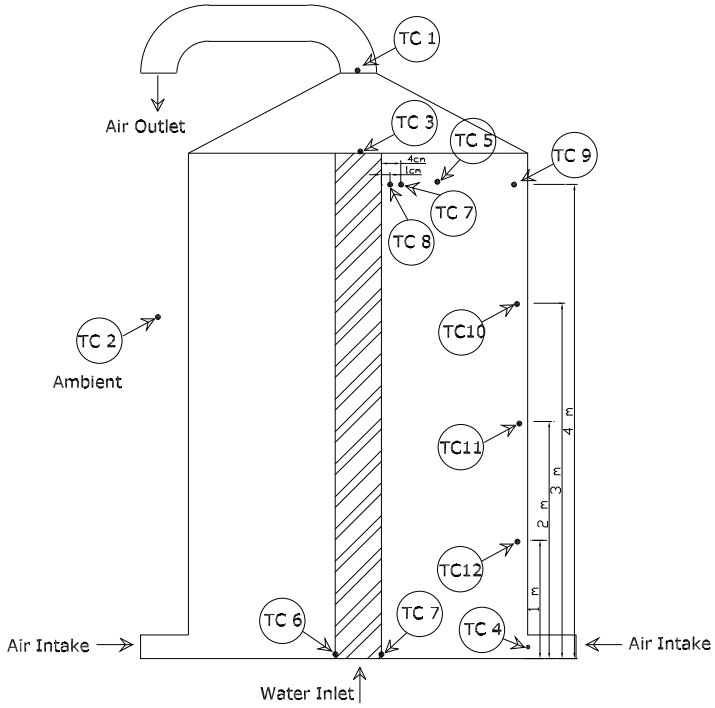

Figure 11.3: Thermocouple positions on the experimental rig.

bare wires they were placed in a plastic shrinking sleeve and a ceramic tube to avoid rupture. One of the junctions was fixed on the cylinder's wall and the other was positioned in air far away in the ambient in order to provide a direct measurement of the temperature difference. This thermocouple setting was not calibrated in the water bath and did not use the zero reference ice bath, because we were just interested in temperature difference between two points. The standard polynomial conversion factor, provided by OMEGA company, was used; i.e.,

$$T = \sum_{i=0}^{9} C_i \, E^i \tag{11.5}$$

To decrease the heat conduction through the thermocouple leads, they were bent 90° approximately $5\ mm$ above the junction. The junction on the wall also placed on the wall approximately $10\ cm$ above the junction and taped to the wall to avoid thermal shunting.

11.4.2 Wall Temperature Using Thermocouples

As shown in figure 11.3, thermocouples number 3 and 6 are measuring the cylinder's wall temperature at the top and bottom of the rig, and the fine-gauge thermocouple is measuring the surface temperature at the same height as the measurement cross-section. In order to have a reliable surface temperature measurement, we should consider some problems when using thermocouples on the surfaces. The thermocouple generates an EMF current based on the temperature of the junction, but the true temperature of the surface might be different than the junction temperature because of the thermal shunting or heat dissipation. We discuss each of these phenomena and suggest our solution for them.

Temperature Range	0 to $500°C$
C_0	0.0
C_1	2.508355×10^{-2}
C_2	7.860106×10^{-2}
C_3	-2.503131×10^{-8}
C_4	8.315270×10^{-10}
C_5	$-1.228034 \times 10^{-14}$
C_6	9.804036×10^{-17}
C_7	$-4.413030 \times 10^{-22}$
C_8	1.057734×10^{-30}
C_9	$-1.052755 \times 10^{-35}$

Table 11.1: Coefficients of the inverse function for thermocouple type K, used in equation 11.5.

Thermal Shunting and Heat Dissipation

Heat is transferred from the surface to the sensor through the thermocouple wires. This phenomenon is known as thermal shunting. The sensor conducts heat away from the hot surface, since the wires are better conductors of heat than the surrounding air. There is a temperature drop in the wall temperature at the point where leads leave the surface. The temperature drop is greatest when the material to be measured has low thermal conductivity. To avoid the problem, the point at which the sensor leaves the surface should be at a suitable distance from the measuring junction (see figure 11.4).

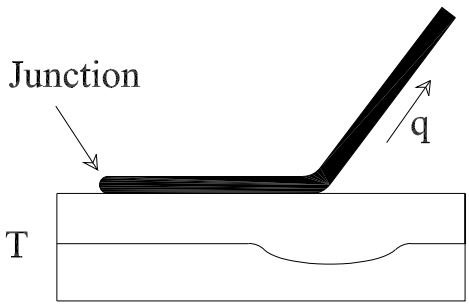

Figure 11.4: Thermal Shunting

Surface versus air contact

Surface-mounted thermocouples also present another problem. If the thermocouple junction is placed on the surface only a fraction of the junction is in direct contact with the surface, and the rest of the sensor responds to the temperature of the surrounding air. To minimize this problem, the maximum possible contact surface should be achieved between the sensor and the surface. We used a thermally conductive silicone paste (*OT-201 OMEGATHERM*) to increase the contact, and also to avoid any direct contact between the surface metal and the bare thermocouple junction. The paste is thermally conductive ($\kappa \simeq 2.307\ W/m.K$) with a high

electrical resistivity ($\rho \simeq 10^{14} ohm.cm$). Also it is critically important that the thermocouple junction made as small as possible, so that it does not upset the heat balance of the surface and so that the temperature gradient within the measurement junction is negligible.

11.5 Cold-Wire Temperature Measurement

To measure the fluctuating fluid temperature, it is customary to use a thin wire operated at a constant current circuit with a low overheat ratio. Such probes are usually called *cold-wires*, because they are cold compared to hot-wire probes in which the wire is heated by the circuit to a much higher temperature than the ambient. The primary limitation on the cold-wire's temporal response is due to its thermal lag, which is in turn related to how much thermal energy is stored in the probe relative to the difference in the rate at which it is being cooled by the flow and heated by its very low current. This is a particular problem at low velocities where the cooling rates can be quite small, as are the temperature differences between probe and environment (since the heating current is low). The only way to get higher frequency response is to make the wire very small. But to minimize end conduction effects, the aspect ratio of the wire must be quite large (typically over 100). So the only solution is to make the diameter of the wire very small. But the lower limit is about one micron diameter, both because of the continuum limit (the frequency response does not improve) and practical manufacturing considerations (smaller wires are very hard to make). Also the smaller the wire, the more likely it is to be broken, so special care must be taken, both in the choice of materials and in the manufacturing.

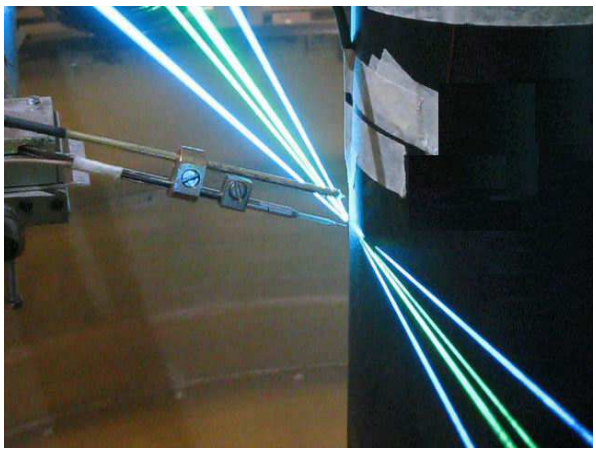

(a)

(b)

Figure 11.5: Cold Wire Setup; (a) Measurement Arrangement, (b) Wire Etching Setup.

11.5.1 Selecting probes

Our first choice was to create our own cold-wire probes using Wollaston wire soldered or welded onto a miniature hot-wire type probe body. Wollaston wire is a very thin platinum wire

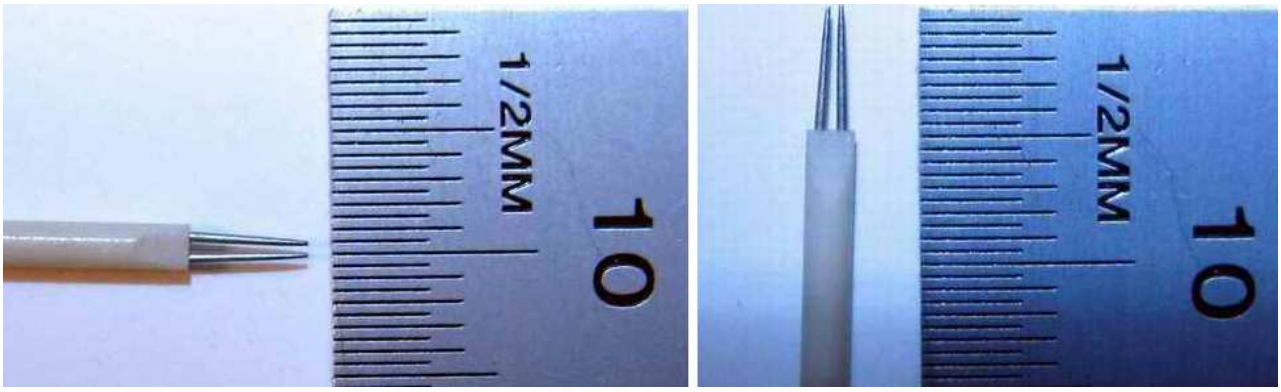

Figure 11.6: The cold-wire probe used for measuring instantaneous temperature.

(less than $1\mu m$) covered by a thick layer of silver (typically $0.025mm$) to protect the platinum wire from rupturing when it is mounted on the prongs. Wollaston wire can be soldered to the prongs or welded using high current spot welder. Either of these methods has its drawbacks. The silver coating does not stick to the tin, therefore a special soldering material is needed. On the other hand, silver is a good electrical conductor, so that when using a spot welding method the high current can create a heat shock on the platinum inside the silver. This can result in a rupture that is not visible until we etch the silver.

After several unsuccessful attempts some probes were made using the etching facility shown in figure 11.5. The soldered Wollaston wire was placed under a buret filled with a solution of acid nitric. The outlet of the buret was small enough to make a continuous stream of acid, approximately $0.5\ mm$ in width. A DC power supply was connected to the probe and running acid was used to facilitate the etching process. The amount of current was adjusted to avoid etching the silver too fast, because sudden removal of the part could rupture the platinum wire. The biggest challenge was to remove the etched wire out of the acid stream without allowing the surface tension of the liquid to break the wire.

It was a long process of trial-and-error, but in the end the quality of the probes we could make with this method was not satisfactory. The $1\ \mu m$ wire was not visible in the microscope available, so the etched area could not be examined to verify the connection between the prong and the platinum wire. Also some contamination of silver coating still remained on the etched section. So we ultimately decided to use a standard $1\ \mu m$ Dantec-Dynamics thermometry platinum wire probe (type 55p31). Figure 11.6 shows the a photograph of the cold-wire probe used in this experiment; the thin wire and supporting prongs. In the standard Dantec wires used in this experiment, the platinum wire is directly welded to the prongs which resembles the configuration shown. The length of the wire was almost $0.4\ mm$ and the total resistance was $50.5\ \Omega$ at room temperature.

These probes, while of small diameter, had the disadvantage that the sensitive length extended all the way to the prongs. The reduction in spatial resolution was not a problem for this experiment, nor was the thermal lag described above. Unfortunately we did not anticipate the substantial reduction in frequency response due to conduction to the prongs. This would not normally have been a problem with such probes. But because they were operating at much lower velocities (with lower convective heat transfer and heating), the relative effects of end losses (steady and unsteady) proved deadly. This problem is discussed in some detail in the

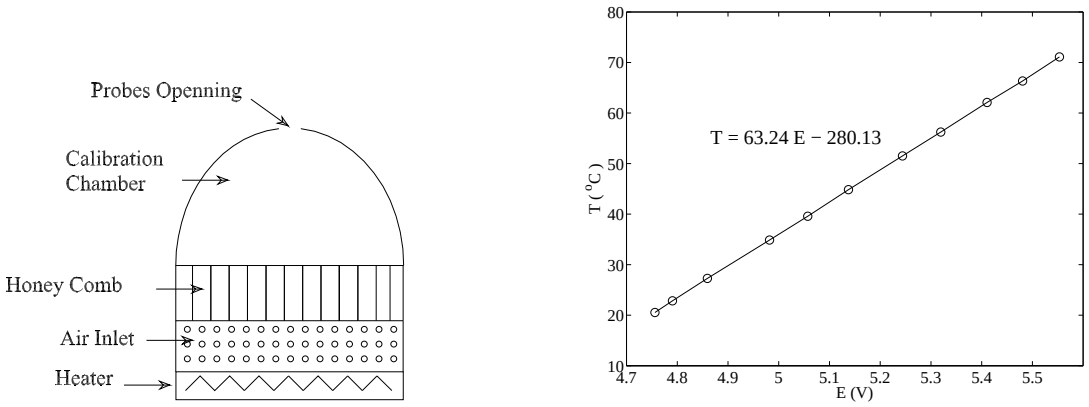

(a) (b)

Figure 11.7: Cold-wire calibration. (a) A schematic of the cold-wire calibration device. (b) A sample of calibration curve measured in the calibration device.

next section.

In order to use the cold-wires for measurement, a constant current of approximately $0.15\ mA$ was passed through the cold-wire probe so that a fluctuating voltage was generated by the varying resistance of the wire due to the temperature fluctuations. A schematic of the constant-current circuit used in this experiment is presented in appendix C. An *IO Tech Wavebook 516* , 16 bits, sample and hold A/D converter was connected to the circuit to sample the continuous voltage signal. The sampling frequency of the cold-wire was set to $3.2\ kHz$ based on the circuit's frequency cut-off and the response time of the wire. An estimation of the wire time response of the wire can be made using equation 11.7. More explanation about the errors in the cold-wire measurement method and the response of a wire will be presented below.

11.5.2 Calibration

In order to calibrate the cold-wire for the range of temperatures in the experiment a device was built using a heater and chamber as shown in figure 11.7. In this device a heater (a hair dryer) connected to an adjustable voltage source was underneath the insulated chamber. For each calibration point, the heater was turned on and off for a short period to heat up the system. The rise in the temperature became stable after a few minutes, at which time the voltage of the cold-wire was recorded against a thermocouple that was placed beside it in the calibration chamber.

As it turns out, our best efforts to calibrate accurately were thwarted when using the cold-wire probes (and thermocouples as well) very close to the wall. The problem, as discussed in detail below, is that operating the probe in a region of strong mean gradient means that the entire probe is not at uniform temperature. At the low velocities and currents near the wall (and everywhere in a laboratory natural convection flow), the fraction of heat loss to the prongs is not insignificant. This affected not only the average temperature along the wire (even at high aspect ratio), but also its frequency response. It is a major short-coming of this experiment that we did not anticipate this problem, nor could we correct for it in a satisfactory manner (at least for the fluctuating part of the temperature).

11.6 Detailed Analysis of Response of Cold-Wires

Cold-wires have traditionally been the choice for the temperature measurement in a turbulent flow. Examples from just natural convection flows include George et al. [1977], Beuther [1980], Shabbir et al. [1996], Shabbir [1987], Shabbir and George [1994]. The primary reason for their popularity is the ability of the thin wire to respond to high frequency temperature fluctuations in the flow. There have been extensive studies to specify the behavior of the wire in the flow (c.f. Bruun [2002] and Perry [1982]). These studies we were well aware of. Unfortunately, until final stages of the experiment, we were not aware of more recent studies focussing on the unique problems that occur when cold-wires are used in strong temperature gradient environments that occur next to surfaces.

11.6.1 Thermal Inertia of Cold-Wire in Uniform Environment

The thermal inertia (due to its finite heat capacity and the finite heat transfer rate to or from it) of the wire *and prongs* prevents it from instantly adjusting to a change in temperature of the fluid around it. If we ignore the heat generated by the small current (typically $\sim 0.1\ mA$) used in the constant current circuit and the radiation from the surrounding surfaces, the only source of this temperature change would be the heat convected from the air and the heat conducted to (or from) connecting prongs. *Here we also assume that the entire wire is placed in an isothermal fluctuating air flow which does not impose any temperature gradient along the wire.* The one dimensional transient thermal energy equation of a material element of the wire is (c.f., Tagawa et al. [2005]):

$$\frac{\partial T}{\partial t} = -\frac{1}{\tau}\left(T(x,t) - T_a(t)\right) + \frac{\kappa_w}{\rho_w\, C_w}\frac{\partial^2 T}{\partial x^2} \tag{11.6}$$

where κ_w, ρ_w and C_w are the thermal conductivity, density and specific heat of the wire respectively. The variable temperature of the ambient fluid is denoted as $T_a(t)$ and $T(x,t)$ is the temperature distribution along the wire. The time constant for wire response is τ which is defined as:

$$\tau = \frac{\rho_w\, C_w\, d_w^2}{4\, Nu\, \kappa_a} \tag{11.7}$$

κ_a is the thermal conductivity of air evaluated at the film temperature. Over a small range of velocity the value of time constant τ can be considered to be approximately constant. In the range of ($0.02 < Re < 0.5$), Collis and Williams [1959] suggested the correlation below for *Nusselt* number estimation:

Material	ρ $[kg/m^3]$	C $[J/kg.K]$	κ $[W/m.K]$
Platinum	21460	133	71.4
Silver	10490	237	427
Alumel	8750	461	29.7
Chromel	8670	444	19.2
Constantan	8922	418	21.6
Tungsten	19250	133	178
Stainless Steel 302	8055	480	15.1

Table 11.2: Physical Properties of Materials Used in Temperature Sensors.; [Benedict [2005]].

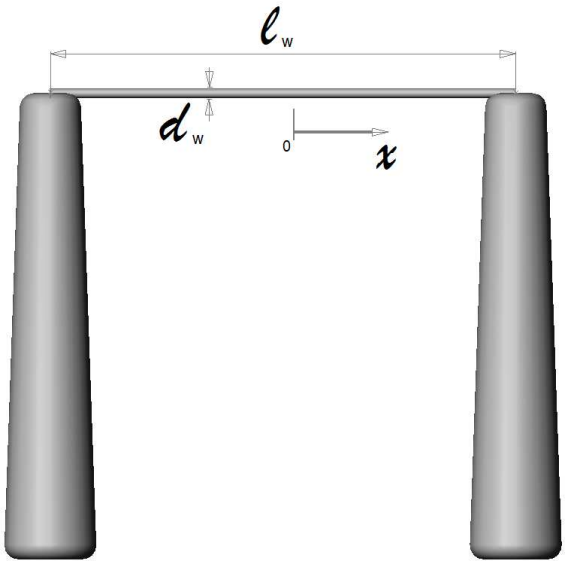

Figure 11.8: Cold-Wire Schematic.

$$Nu = (1.18 + 2Kn - 1.10\ \log_{10} Re)^{-1} \tag{11.8}$$

If we assume a constant molecular mean free path ($\lambda \approx 0.07\mu m$) in atmospheric pressure air, the *Knudsen* number is calculated to be ($Kn = \lambda/d_w = 0.07$) for the $1\mu m$ wire. In the natural convection boundary layer experiment, the mean air velocity does not exceed $0.5m/s$, therefore the *Nusselt* number can be estimated to be $Nu \approx 0.38$. Substituting the values of the table 11.2 for platinum properties, the $1\mu m$ wire time-constant is $\tau \approx 62.6\mu s$.

Therefore the estimated cut-off frequency for the wires used in this experiment based on the equation 11.7 is equal to $f_c = (2\pi\tau)^{-1} \approx 2.5kHz$. This should have been well beyond the estimated highest convected frequency of interest of approximately 1 kHz. Note that this is the classical estimation which is considers only the wire response in a uniform ambient. The effect of the prong conduction has been ignored so far.

11.6.2 Effects of Finite Length

Now we consider a case of finite wire with the length of ℓ_w. Figure 11.8 shows a schematic of a thin wire mounted on two prongs. The boundary conditions for the dynamic response of the equation 11.6 are defined as:

$$x = 0 \qquad : \qquad \frac{\partial T}{\partial x} = 0 \tag{11.9}$$

$$x = \ell_w/2 \quad : \qquad T - T_a(t) = -\tau_p \frac{\partial T}{\partial t} \tag{11.10}$$

This is for the case of uniform instantaneous T_a over the entire prongs and wire. Also in the $x = \ell_w/2$ boundary condition, the temperature at the tip of the prong is assumed to respond to

the fluid temperature only up to the first order (see Tsuji et al. [1992]) by a time constant τ_p.

Using Fourier integral, the equation 11.6 becomes:

$$\frac{\partial^2}{\partial x^2}\,\hat{T}(x,\omega) = \frac{1+j\omega\tau}{\alpha_w\tau}\hat{T}(x,\omega) - \frac{\hat{T}_a(\omega)}{\alpha_w\tau} \tag{11.11}$$

where $\alpha_w = \kappa_w/\rho_w C_w$ is the wire thermal diffusivity, $j = \sqrt{-1}$ and is and the Fourier integrals for fluctuating air temperature and wire response temperature distribution are:

$$T(x,t) = \int_{-\infty}^{\infty} e^{j\omega t}\hat{T}(x,\omega)\,d\omega \tag{11.12}$$

$$T_a(t) = \int_{-\infty}^{\infty} e^{j\omega t}\hat{T}_a(\omega)\,d\omega \tag{11.13}$$

The solution of the differential equation 11.11 is:

$$\hat{T}(x,\omega) = C_1 e^{+\Omega x} + C_2 e^{-\Omega x} + \frac{\hat{T}_a(\omega)}{\alpha_w\tau\Omega^2} \tag{11.14}$$

where C_1 and C_2 are the constants depending on the boundary conditions and Ω is defined as:

$$\Omega = \sqrt{\frac{1+j\omega\tau}{\alpha_w\tau}} \tag{11.15}$$

Imposing the first boundary condition simplifies the equation as $C_1 = C_2$ (symmetry of the wire). If we define the average of wire temperature response over the length of wire as below:

$$\hat{T}_m(\omega) = \frac{1}{\ell_w/2}\int_0^{\ell_w/2}\hat{T}(x,\omega)\,dx \tag{11.16}$$

the frequency response of the wire can be obtained by finding the amplitude-transfer function, as the wire average temperature response to the air temperature fluctuation input:

$$H(\omega) = \frac{\hat{T}_m(\omega)}{\hat{T}_a(\omega)} \tag{11.17}$$

The solution for equation 11.11 based on amplitude transfer function $H(\omega)$ for the prong tip boundary condition 11.10 is given by Paranthoen et al. [1982] as:

$$H(\omega) = \frac{1}{1+j\omega\tau}\left\{1 + 2\frac{\ell_b}{\ell_w}\,\frac{j\omega\tau_p}{1+j\omega\tau_p}\,\frac{1}{\left(\frac{\ell_c}{\ell_b}\right)^2\frac{1}{1+j\omega\tau}-1}\,\tanh\frac{\ell_w}{2\ell_b}\right.$$
$$\left. + \frac{2}{\ell_w(A+jB)}\left[\frac{j\omega(\tau-\tau_p)}{1+j\omega\tau_p} - \frac{j\omega\tau_p}{1+j\omega\tau_p}\,\frac{1}{\left(\frac{\ell_c}{\ell_b}\right)^2\frac{1}{1+j\omega\tau}-1}\right]\tanh(A+jB)\ell_w\right\} \tag{11.18}$$

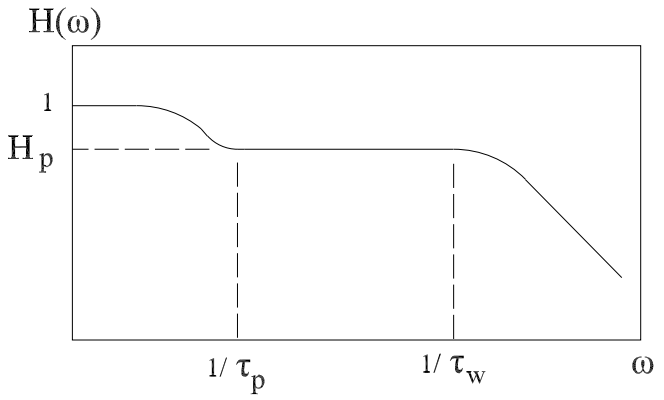

Figure 11.9: Amplitude Transfer Function $H(\omega)$ for a Cold-Wire Probe.

where

$$A = \left(\frac{1}{2\alpha_w \tau}[(1+\omega^2\,\tau^2)^{1/2}+1]\right)^{1/2} \quad ; \quad B = \left(\frac{1}{2\alpha_w \tau}[(1+\omega^2\,\tau^2)^{1/2}-1]\right)^{1/2} \tag{11.19}$$

A typical amplitude transfer function of a cold-wire, shown in figure 11.9, reveals that between the high-frequency cut-off (because of the wire thermal inertia) and the low-frequency attenuation (caused by the heat conduction to the prongs), there is a constant region of frequency response. The approximate value of H_p is suggested by Paranthoen et al. [1982] as:

$$H_p = 1 - 2\,\frac{\ell_c}{\ell_w}\left(\frac{\eta^3-1}{\eta^2-1}\right) \tag{11.20}$$

where $\eta = \ell_b/\ell_c$ and ℓ_c is the cold length given by (see Bruun [2002]):

$$\ell_c = \frac{1}{2}\,d_w\,\left(\frac{\kappa_w}{\kappa_a}\,\frac{1}{Nu}\right)^{1/2} \tag{11.21}$$

ℓ_b is the thickness of the thermal boundary layer on the prong. When the velocity is low, the length of ℓ_b can be appreciable compared to the length of wire ℓ_w. The experiments by Paranthoen et al. [1982] shows a value of $2\ell_b/\ell_w = 0.174$ for the air flow with the the average velocity of $U = 0.5\ m/s$ over a platinum wire of size $2.5\mu m$. This effect made the measured value of H_p becomes approximately equal to 0.66. For higher velocities ($\sim 4m/s$), the transfer function measured by Paranthoen et al. [1982] for a $0.7\mu m$ platinum wire gives a value of $H_p \approx 0.95$ while for a $2.5\mu m$ platinum wire is $H_p \approx 0.81$.

The value above show the importance of the wire size and diameter-to-length ratio of the wire. Unfortunately the wire length used in this experiment was not long enough to completely eliminate the low-frequency attenuation due to unsteady heat transfer to the supports, even though the cut-off frequency of the wire (due to the thermal lag) should be expected to be more than $1\ kHz$.

For the region of measurement with a very low velocity in the natural convection boundary layer, Lecordier et al. [1982] mentions the significant errors involved in temperature measure-

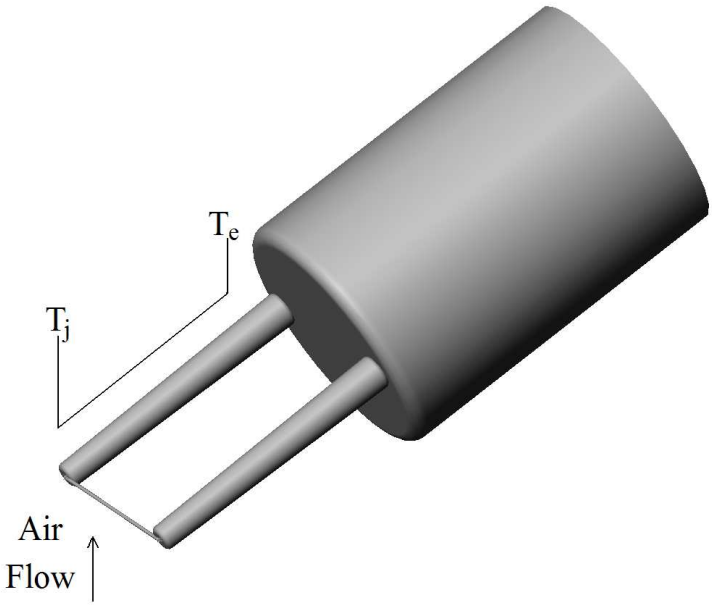

Figure 11.10: Schematic of Cold-Wire Prongs Exposed to a Temperature Gradient.

ment with cold-wires. The lack of any alternative method for measuring fluctuating temperature leave us with a compromise with the accuracy of the results. On the other hand, Tsuji et al. [1992] discusses the influence of the velocity and internal heat generation of the typical cold-wire probe. For a $1\mu m$ platinum wire with a current less than $0.2\ mA$, exposed to a flow velocity less than $1m/s$, the gain varies within 0.1% and the time-averaged temperature difference estimated to be less than $0.1\ ^{\circ}C$.

The cut-off frequency of a resistance wire as shown in equation 11.7 is a function of its diameter, but La Rue et al. [1975] suggests a constant value for wires less than $1\mu m$. Measurements by Tagawa et al. [2005] also shows that the gain in a $0.63\mu m$ platinum wire is close to one for frequencies less than $1kHz$. They suggest using a response compensation for the wires bigger than this size. All these measurements have been carried out in high velocity flows and the effect of very low velocities ($< 1\ m/s$) on the low-frequency response is unknown.

The constant current circuit designed for this experiment had a cut-off frequency of $3kHz$ which samples higher than the fastest response of the wire to temperature fluctuations. To avoid aliasing the Nyquist sampling frequency criterium is considered and the sampling rate of $3kHz$ was chosen in the A/D converter, which is estimated to be more than double the frequency response of the wire.

11.6.3 Prong Temperature Gradient

The equations above were based on the assumption that a uniform temperature fluctuation is applied upon the entire probe. In the boundary layer experiment, the considerable temperature gradient along the prongs (or the thermocouple leads) imposes a new boundary condition in

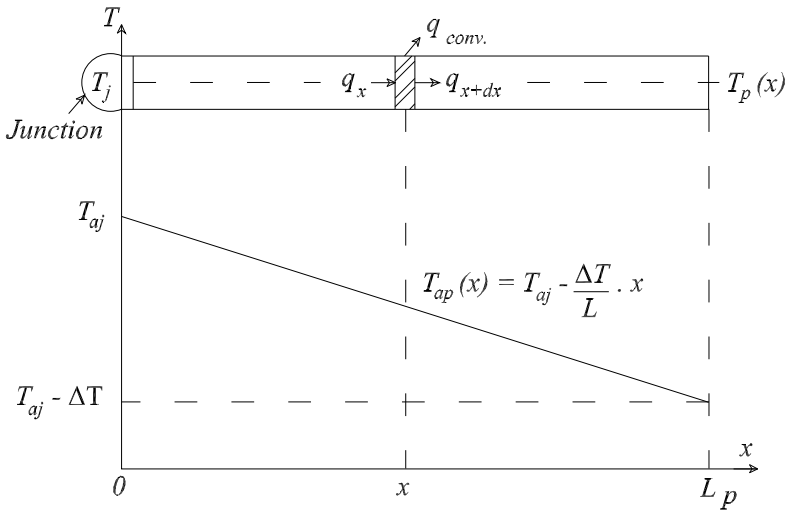

Figure 11.11: Temperature Distribution Along the Prongs.

the energy balance of the measurement probe (see figure 11.10). The new boundary condition (substituting equation 11.10) for the wire becomes:

$$\dot{Q}_{cp}(t) = 2\kappa_w(\frac{\pi d_w^2}{4})\left.\frac{dT}{dx}\right|_{x=\ell_w} \tag{11.22}$$

This heat flux is equal to the heat conducted to the prong through the junction. Now if we assume that there is a approximately linear temperature gradient along the prong (figure 11.11), The steady state energy balance for an element on the prong becomes:

$$\frac{d^2T_p}{dx^2} = \frac{4h_p}{\kappa_p d_p}\left(T_p(x) - T_{ap}(x)\right) \tag{11.23}$$

where $T_p(x)$ is the temperature of the prong, $T_{ap}(x)$ temperature of the air along the prong, d_p is the diameter of the prong (assumed to be constant) and κ_p is the prong thermal conductivity. The linear air temperature sensed by the prong along the length L_p is assumed to be:

$$T_{ap}(x) = T_{aj} - \frac{\Delta T}{L_p}.x \tag{11.24}$$

Changing the variable:

$$\theta(x) = T_p(x) - T_{ap} + \frac{\Delta T}{L_p}.x \tag{11.25}$$

It follows that:

$$\frac{d^2\theta}{dx^2} = m^2\theta \tag{11.26}$$

where:

$$m^2 = \frac{4h_p}{\kappa_p d_p} \tag{11.27}$$

The solution is given by:

$$\theta(x) = C_1 e^{mx} + C_2 e^{-mx} \tag{11.28}$$

Using the initial conditions for this ODE:

$$x = 0 \qquad ; \qquad \theta(0) = T_j - T_{aj} = C_1 + C_2 \tag{11.29}$$

Assuming the other end of the prong to be adiabatic:

$$x = L_p \quad ; \quad \left.\frac{d\theta}{dx}\right|_{x=L_p} = \frac{\Delta T}{L_p} \quad + \left.\frac{dT}{dx}\right|_{x=L_p} \tag{11.30}$$

Using this implies that the solution is given by:

$$C_1 e^{mL_p} - C_2 e^{-mL_p} = Q \tag{11.31}$$

where

$$Q = \frac{1}{m}\left.\frac{dT}{dx}\right|_{x=L_p} + \frac{\Delta T}{mL_p} \tag{11.32}$$

Solving 11.29 and 11.31 for C_1 and C_2 gives us:

$$T_p(x) = T_{aj} - \frac{\Delta T}{L_p}.x + (T_j - T_{aj})\,\frac{\cosh m(L_p - x)}{\cosh mL_p} + Q\frac{\sinh mx}{\cosh mL_p} \tag{11.33}$$

Heat transfer from the junction to the prongs can be computed as:

$$q_{(x=0)} = -2\kappa_p A_p \left.\frac{dT_p(x)}{dx}\right|_{(x=0)} \tag{11.34}$$

This is equal to the averaged heat transferred from the air to the wire and end of the prongs:

$$q_{(x=0)} = q_j = h_w(\pi d_w \ell_w)(T_w - T_{aj}) + 2h_p(\frac{\pi d_p}{4})(T_j - T_{aj}) \tag{11.35}$$

Now consider the time average of the wire temperature to be the same as the junction temperature ($T_w = T_j$), and also that the entire wire senses the air temperature as the junction. By solving equations 11.34 and 11.35, we have:

$$\left.\frac{dT_p(x)}{dx}\right|_{(x=0)} = -\frac{\Delta T}{L_p} - m(T_j - T_{aj})\tanh mL_p + \frac{Qm}{\cosh mL_p} \tag{11.36}$$

We can solve the equations for the temperature difference ($T_j - T_{aj}$):

$$(T_j - T_{aj}) = \frac{(\Delta T/L_p)\cosh mL_p - Q.m}{\left(\dfrac{2h_w d_w \ell_w + h_p d_P^2}{\kappa_p d_p^2}\right)\cosh mL_p - m.\sinh mL_p} \tag{11.37}$$

We can assume an adiabatic boundary condition for $x = L_p$ because heat transfer through the insulated section of the support is much smaller than the bare section; thus:

$$Q \approx \frac{\Delta T}{mL_p} \tag{11.38}$$

Combining equation 11.37 with 11.38 gives us:

$$(T_j - T_{aj}) = -\Psi.\Delta T \tag{11.39}$$

where

$$\Psi = \frac{1 - \cosh mL_p}{L_p \left(\dfrac{2h_w d_w \ell_w + h_p d_P^2}{\kappa_p d_p^2} \right) \cosh mL_p - mL_p . \sinh mL_p} \tag{11.40}$$

Let us put some numbers in this equation by assuming the *Reynolds* numbers for wire and prong to be:

$$Re_w = \frac{U d_w}{\nu} = \frac{0.5(m/s) \times 1(\mu m)}{1.8 \times 10^{-5}(m^2/s)} \cong 0.03 \tag{11.41}$$

$$Re_p = \frac{U d_p}{\nu} = \frac{0.5(m/s) \times 300(\mu m)}{1.8 \times 10^{-5}(m^2/s)} \cong 9 \tag{11.42}$$

By using the relation from Bruun [2002], the *Nusselt* number for the flow around a cylinder, in the ranges $0.01 < Re < 10000$ and $0.71 < Pr < 1000$ is:

$$Nu = 0.42 Pr^{0.2} + 0.57 Pr^{0.33} Re^{0.5} \tag{11.43}$$

For wire the *Nusselt* number is $Nu_w = 0.48$ and for prongs it can be estimated as $Nu_p = 1.91$. Therefore the heat transfer coefficients for the wire and prong become:

$$h_w = \frac{Nu_w K_{air}}{d_w} = \frac{0.48 \times 0.028}{1 \times 10^{-6}} \cong 13440 \quad ; \quad h_p = \frac{Nu_p K_{air}}{d_p} = \frac{1.91 \times 0.028}{300 \times 10^{-6}} \cong 178 \tag{11.44}$$

Looking in the table 11.2, the thermal conductivities of the platinum wire $\kappa_w = 71.4[W/m.K]$ and stainless steel $\kappa_p = 15.1[W/m.K]$ can be used to estimate $m \cong 397$. The effective length of the prongs which is exposed to the temperature difference ΔT is approximately $L_p \approx 4.5mm$. By substituting these values in the equation 11.40, $\Psi = 0.42$. Therefore:

$$(T_j - T_a) = -0.42 \times \Delta T \tag{11.45}$$

The measured temperature difference in the wall region of the boundary layer reaches to $\Delta T = 20^\circ C$ for the length of the prong as $L_p \approx 4.5\ mm$. Using the correction of the equation 11.45, the real air temperature estimated to be $8.4^\circ C$ more than the measured value, which is more than 13% measurement error just because of the heat conduction of the prongs.

A suggested method to decrease this temperature difference is to use a 90° bent prong to keep the prong in an isothermal region. In practice, adjusting any type of probe in the region with considerably large temperature gradient is very difficult and we should be aware of the possible misalignments that leads to the same phenomenon explained above. Unfortunately these problems were realized after the measurement program had been completed.

11.7 Thermocouples in Mean Temperature Gradients

Thermocouples are usually used to measure the mean temperature of the fluid because of their slow response time. They are used for that purpose here as well. The reason they respond so slowly is the finite thermal capacity of the mass of material that forms the junction, which is

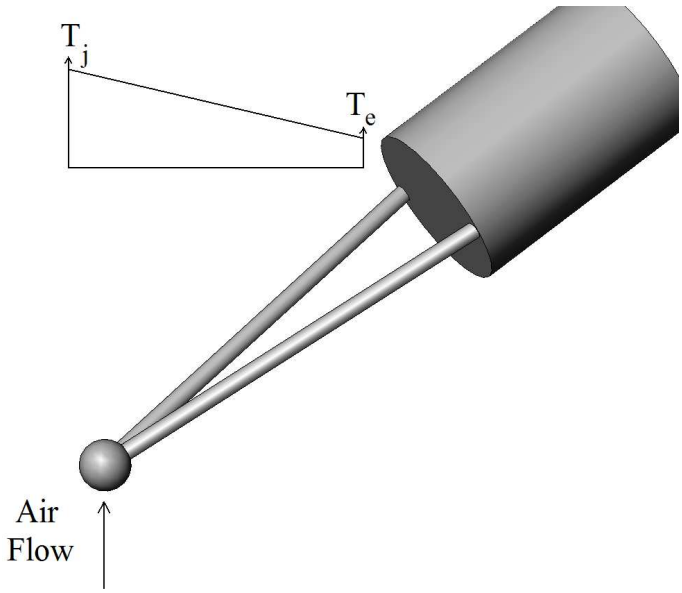

Figure 11.12: Schematic of Thermocouple leads Exposed to a Temperature Gradient.

substantially larger than that of cold wires. Therefore the temporal response of the thermocouples used in this experiment is not of particular interest, especially since their signals are sampled digitally and time-averaged anyway. Also, their spatial resolution is not generally of concern, except very close to the wall where a strong temperature gradient exists.

What turns out to be of great concern (unfortunately mostly in hindsight) is the fact that they too, like the cold wires considered in the preceding section. must of necessity operate in a strong mean temperature gradient near the wall. The problem, simply put, is that conduction through the leads of the thermocouple can cause an error in the measurement. For reducing the thermal shunting and thermal loads, as it mentioned in previous chapter, the leads were connected to the isothermal wall for at least few centimeters. But when using the miniature thermocouples for measuring the mean air temperature profiles we encountered an analogous problem to that posed by the non-uniform temperature on the prongs of the cold-wires. Because the size and physical properties of the thermocouples are different than cold-wire probes, we briefly study this effect on the thermocouple used in the measurement.

The schematic of a thin thermocouple used in the measurement is shown in figure 11.12. We impose the same steady energy balance equation in a temperature gradient region as the cold-wire. Equation 11.33 is still valid, but to impose the boundary condition at the junction, we need to consider the new geometry. The heat transfer from the junction to the leads is:

$$q_{(x=0)} = -2\,\kappa_l\,A_l\,\left.\frac{dT_l(x)}{dx}\right|_{(x=0)} \tag{11.46}$$

where all the parameters with the index "l" refer to the thermocouple lead. The heat conduction is equal to the heat convection from air to the thermocouple bead:

$$q_{(x=0)} = q_j = h_j A_j (T_j - T_{aj}) \tag{11.47}$$

The constant correction factor Ψ for the thermocouple becomes:

$$\Psi = \frac{1 - \cosh mL_l}{L_l \left(\frac{h_j A_j}{2\kappa_l A_l} \right) \cosh mL_l - mL_l . \sinh mL_l} \tag{11.48}$$

We assume a spherical shape of diameter $d_j = 100\mu m$ for the junction of the thermocouple used in the experiment and $d_l \approx 50\mu m$ as the diameter of the lead's cross-section. The surface area of the junction exposed to air is the sphere surface minus the two leads' cross section, therefore the ratio of two surfaces is $A_j/A_l = 14$.

Assuming the *Reynolds* number around the junction to be:

$$Re = \frac{UD_w}{\nu} = \frac{0.5(m/s) \times 100(\mu m)}{1.8 \times 10^{-5}(m^2/s)} \cong 2.7 \tag{11.49}$$

and using the equation 11.43, we have $Nu = 1.235$ for the flow around the junction and $Nu = 0.98$ for the flow around the leads. The heat transfer coefficients for the junction and the leads are:

$$h_j = \frac{Nu_j K_{air}}{d_j} = \frac{1.235 \times 0.028}{100 \times 10^{-6}} \cong 345.8 \quad ; \quad h_l = \frac{Nu_l K_{air}}{d_l} = \frac{0.98 \times 0.028}{50 \times 10^{-6}} \cong 548.8 \tag{11.50}$$

The thermocouple used in the experiment is type *K* which has thermal conductivity of $K_l = 19.2[W/(m.K)]$ for the *Chromel* alloy (90% Nickel - 10% Chromium), and $K_l = 29.7[W/(m.K)]$ for the *Alumel* alloy (95% Nickel - 2% Aluminum - 2% Manganese - 1% Silicon); (see table 11.2. For simplicity we use the average of the thermal conductivity for both leads and the junction. Putting these numbers in the equation 11.27 gives us the value for $m \cong 1325.2$. The effective length of the thermocouple leads which is exposed to the temperature difference ΔT is approximately $L \approx 4mm$. Substituting these into the equation 11.48 gives us:

$$(T_j - T_a) = -0.2 \times \Delta T \tag{11.51}$$

which is 20% error in the temperature measured by thermocouple compare to the actual air temperature. These numbers provide a good estimation of the effect of lead conduction error, but we should be careful about using them directly for correcting the measurement. The most important information in the equation 11.51 is the linear correlation between the error in measurement and the temperature gradient imposed on the leads.

Chapter 12

Results and Discussion

Although some experimental work has been done previously for the boundary layer close to a vertical flat plate, as it was discussed in chapter 7, there is a lack of reliable data for cylindrical surfaces. Therefore the primary goals of this experimental study were three-fold:

- To establish the friction and heat transfer relations appropriate to the natural convection flow next to a heated vertical cylinder at high Rayleigh number.
- To establish the scaling laws (if any) for the inner and outer parts of the boundary layer.
- To measure the turbulence parameters to sufficient accuracy that they can be of benefit for further theoretical and numerical analysis.

As noted in the preceding chapters, there has been considerable lack of knowledge (even confusion) about even what the appropriate governing equations are. And there have also been raised substantial questions about the methodology for temperature measurement, both that employed previously and in this experiment as well. Therefore the first part of this chapter will discuss the mean profile measurements for velocity and temperature, in order to try to glean from them the values of the velocity gradient at the wall and the wall heat flux. These will not only establish the scaling parameters, but will allow an evaluation of exactly what flow conditions actually affected the experiment. Most important of these will be seen to be the stratification, which although slight was very important. Then the turbulence measurements will be presented and discussed.

12.1 Statistical Errors

As mentioned in an earlier chapter, the velocity and temperature measurement were synchronized to produce the correlation of the temperature and velocity, even though one was analog, one was not. To achieve this the measurement times for LDA, cold-wire and all thermocouples were set to a fixed and common length. Each measurement point was sampled for $1000\ s$. The cold-wire was sampled at a fixed sampling rate of $3.2\ kHz$, thus it produced a set of $3,200,000$ samples for each point. The LDA doesn't sample at a fixed rate, but rather relies on the random bursts coming from the particles passing the control volume. Therefore the sampling rate directly depends on the velocity region which is measured. Close to the wall and in the outer part of the boundary layer the velocity is very low, so the data arrival rate is quite low. Near the middle of the boundary layer the sampling rate is higher. For the regions close to the wall evaporation of the particles is probably also important, so we have fewer and smaller particles. This both makes the measurement very difficult and adds to the statistical errors. The outer

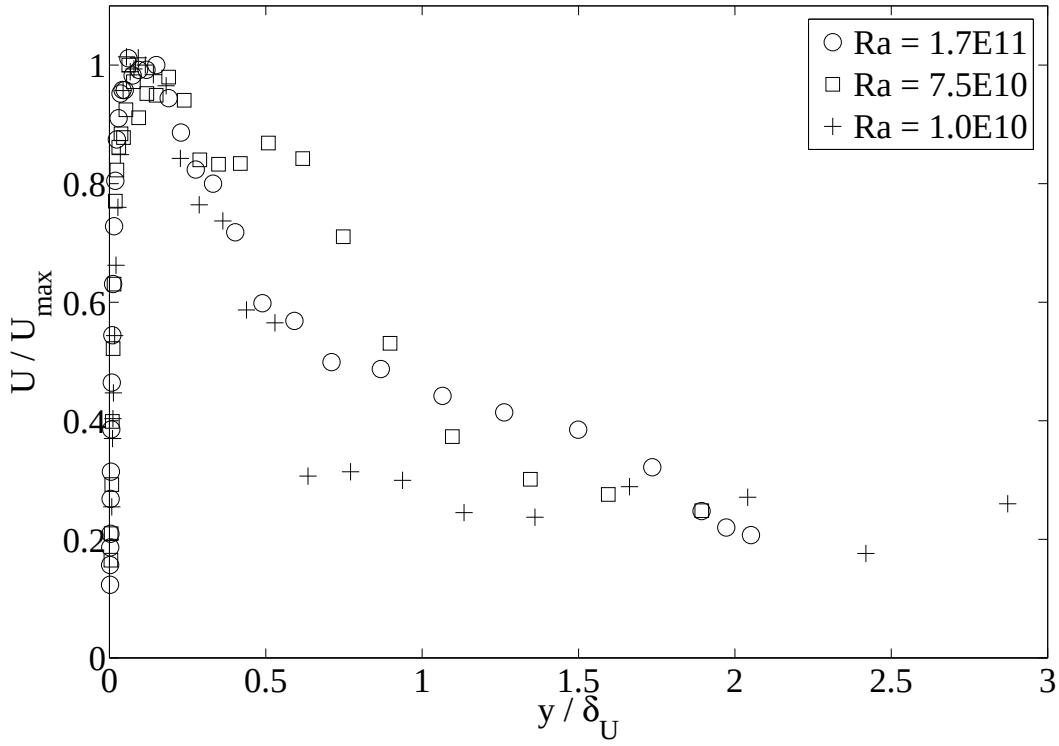

(a) Mean velocity normalized by U_{max} and δ_U.

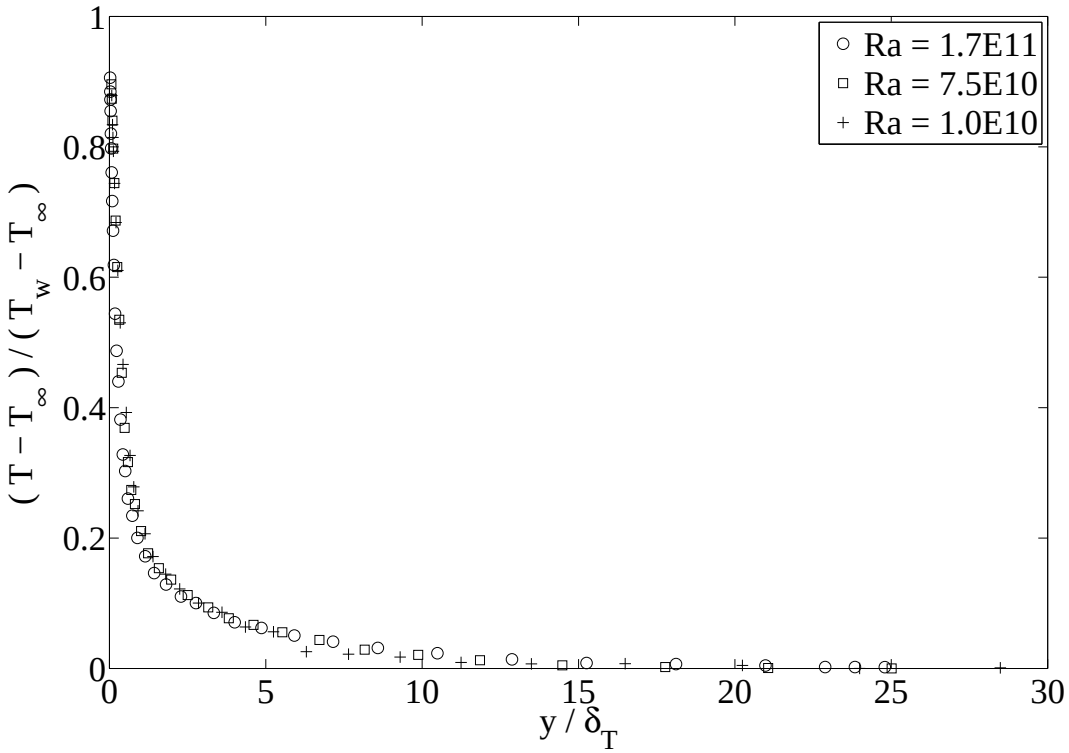

(b) Mean temperature difference normalized by $T_w - T_\infty$ and δ_T.

Figure 12.1: Normalized mean velocity and temperature profiles across the boundary layer at 4 m, 3 m and 1.5 m

region of the boundary layer on the other hand gets a better sampling rate due to entrainment because the particles are added to the flow from outside of the tunnel. The average of the highest sampling rate close to the peak of the velocity was around $200\ Hz$ and the average of the sampling rate close to the wall was close to $50\ Hz$. Note that data rate does not directly enter the statistics, since all moments, including the cross-moments with the temperature sensor, are computed with residence time weighted data. The frequency response of the thermocouples were less than $1\ Hz$ so there was no need to sample them at higher rate. The thermocouples were used only to measure the mean temperatures.

It was estimated from the temperature spectra shown in Appendix E that the integral time scale of the flow might be as long as $1s$. Therefore in spite of the very long data records in time, there were not so many independent realizations as in a forced flow. This could be a part of the reason for the large deviations in the mean velocity profile outside the peak, since the turbulence intensity increases (over 100%) as the mean velocity decreases. The mean temperature profiles are much smoother, in part because they have already been smoothed by their large time constants (already averaged) so their fluctuation level (especially for the thermocouples) is much lower.

The variability of the estimator for the mean velocity can be estimated as (c.f., George et al. [1978]):

$$\varepsilon_U^2 = \frac{2\mathcal{T}_{int}}{T}\,\frac{var(u)}{U^2} \tag{12.1}$$

where $\mathcal{T}_{int}$ is the integral time scale and T is the total measurement time. The flow on average had a turbulence intensity of 50%. Using the $1\ s$ integral time scale estimate, the variability for $1000\ s$ is calculated to be $\varepsilon_U = 2\%$. For the turbulence second moments the variability is given by:

$$\varepsilon_{u^2}^2 = \frac{2\mathcal{T}_{int}}{T}\,\frac{< u'^4 > -(< u'^2 >)^2}{(< u'^2 >)^2} \tag{12.2}$$

Using a Gaussian estimation simplifies this to:

$$\varepsilon_{u^2}^2 = 2 \times \frac{2\mathcal{T}_{int}}{T} \tag{12.3}$$

which gives the estimate for uncertainty of the second moment as $\varepsilon_{u^2} = 6\%$.

The error in measuring the radial velocity component is more problematical because the mean value of the radial velocity is much smaller than the streamwise component, even though the turbulence intensity of the radial velocity is about the same. This increases the relative measurement error substantially for the same measurement time.

12.2 An Overview of the Experimental Results

Figure 12.1 shows the mean velocity and mean temperature data taken at three different heights (1.5m, 3m and 4m) in the natural convection facility described in earlier chapters. The mean temperature profile for the 4 m height has been corrected as described in the next section. They have been normalized in the traditional manner using the integrated velocity and temperature boundary layer thickness, δ_U and δ_T defined by equations 12.4 and 12.5 below:

$$\delta_T = \int_R^\infty \left[\frac{T(y) - T_\infty}{T_w - T_\infty}\right] dy \tag{12.4}$$

and

$$\delta_U = \int_0^\infty \left[\frac{U(y)}{U_{max}}\right] dy \tag{12.5}$$

In spite of the scatter, the plots resemble approximately what we expected for the natural convection boundary layer next to a vertical cylinder.

Figure 12.2 shows the same mean velocity and temperature profiles, but plotted this time in *physical variables*. Tables 12.1 and 12.2 summarize the conditions corresponding to each profile. The first thing to notice about the physical variable plots is that the mean velocity rises rapidly from the wall to its maximum, then rolls off slowly. The peak velocity has increased by a factor of two, while the profile has also broadened by about the same amount. For the profile at $x = 1.5m$, the profile appears to asymptote to a constant value, about $0.06\ m/s$. The profile at $3m$ drops quite differently and it is not so clear whether an asymptote of about $0.08m/s$ has been reached or not. For the highest profile the flow seems to continue to drop from about $r = 70mm$ all the way to the last point shown. It clearly does not reach an asymptote. In fact, measurements taken all the way to the outer cylinder show that it reverses and becomes negative.

By contrast the temperature drops rapidly and monotonically from wall, so fast in fact that almost all of the temperature drop (90 %) occurs with the first $10\ mm$ from the wall. This is well inside the point at which the mean velocity peaks; and in fact, almost all of the velocity profile is outside the peak. Table 12.2 summarizes for the various heights a number of parameters that can be used to characterized the profiles. The values for δ_U and δ_T are from the integration of the profiles shown, but the last one, δ_U, is really not converging by the last point but continuing to increase nearly linearly with radius.

Finally note the temperature difference in the outer region. The temperature at the wall of the heated pipe, T_w, was nearly the same for all experiments at about $70.4°K$, but more importantly had a rms variation during each experiment of approximately $0.02°K$. The second temperature, $T_{lastpoint}$ was the temperature at the last point of traverse with the differential themocouple, one junction of which was affixed to the surface of the heated pipe, and the other traversed to produce the profile shown in the figure. $T_{oppwall}$ was measured with a fixed thermocouple at each height, but about 10 cm away of the outer cylinder, and was also continuously monitored throughout the experiments at all height simultaneously. These measurements had an rms variation of approximately $0.1°K$. These temperature difference, together with the temperature difference, $T_w - T_{lastpoint}$, are summarized in Table 12.1. There is a clear increase in the ambient temperature from one height to the next (Figure 12.3). Also shown in the table are the corresponding values of the Rayleigh and the Nusselt numbers (from section 12.4 below).

It is clear from the above that in spite of our best efforts to create a natural convection boundary layer next to a heated vertical surface at very high Raleigh number, that we have not succeeded. While the flow at the lowest location bears the closest relation to the flow we wished to create, the mass integral even here beyond about $r = 100mm$ starts to increase nearly linearly. In fact it appears that we have created *the developing natural convection flow between differentially heated vertical cylinders*. This is especially evident from the shape of the mean velocity

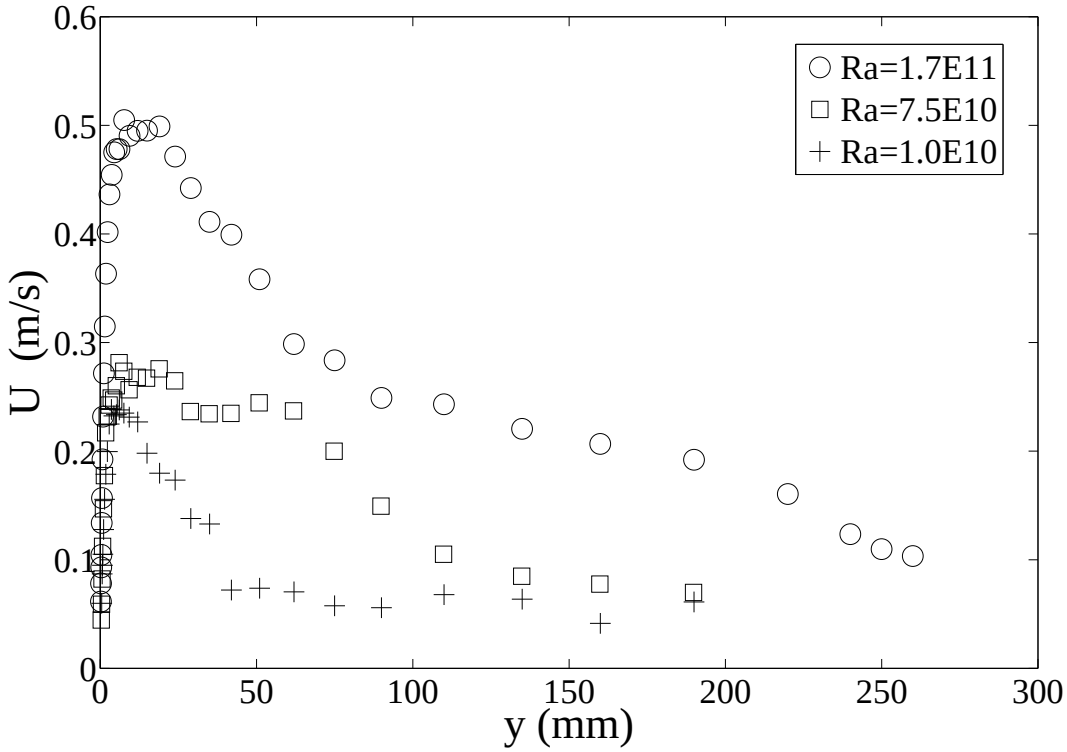

(a) Mean Velocity

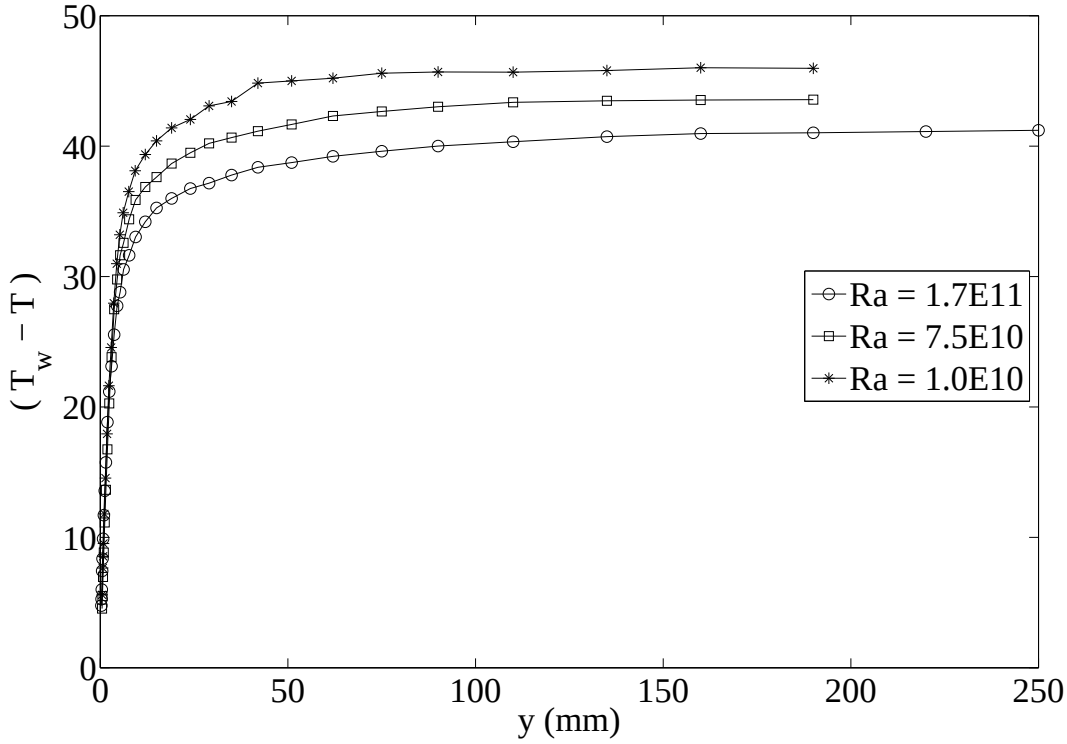

(b) Mean Temperature Difference,

Figure 12.2: Mean velocity and temperature profiles across the boundary layer at 4 m, 3 m and 1.5 m.

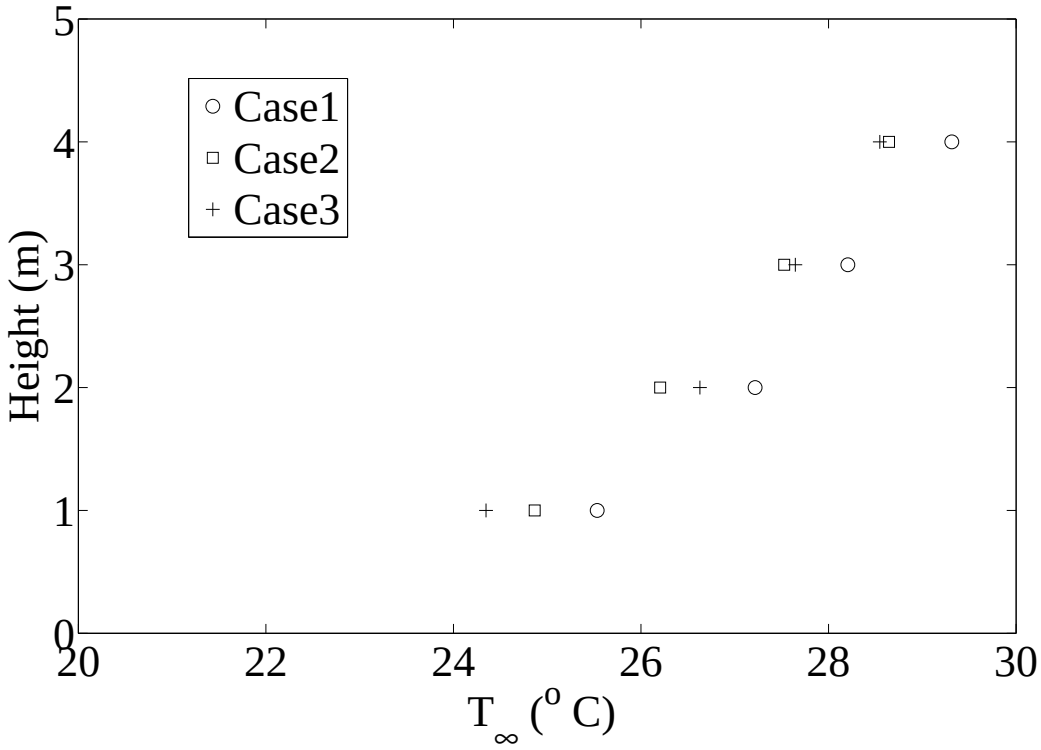

Figure 12.3: Ambient temperature variation with height during measurements at the three different heights.

$Height[m]$	$(T_w - T_\infty)[K]$	$T_w[K]$	$T_{lastpoint}[K]$	$T_{oppwall}[K]$	Ra_x	Nu_x
4	41.2	70.3	29.1	29.2	1.689×10^{11}	1344
3	43.6	70.6	27.1	28.0	7.469×10^{10}	634
1.5	46.0	70.4	24.4	26.1	0.998×10^{10}	302

Table 12.1: Summary of mean temperature data and Rayleigh/Nusselt numbers.

profile at the highest location ($4m$), where the profile continues to drop over the entire range of measurement. This is, of course, quite disappointing for two reasons: first for the obvious reason that we wanted to measure natural convection next to a vertical cylinder; and second because if we had realized it earlier we would have approached the problem differently. Unfortunately it was only realized in the very last stages of this thesis.

In 1990 in a paper entitled "Governing equations, experiments and the experimentalist" George [1989] stated in the abstract:

> ... the most important test of the understanding of any experiment is whether or not the results are consistent with the equations and boundary conditions believed to govern the flow. If they are not, then either the measurements are incorrect, the equations or boundary conditions are wrong, or the experiment performed was not the one believed to have been done.

Height [m]	$\delta_T\ [mm]$	$\delta_U\ [mm]$	$U_{max}\ [m/s]$
$4\ m$	10.5	126.7	0.499
$3\ m$	7.6	100.3	0.28
$1.5\ m$	6.7	66.1	0.235

Table 12.2: Integral Thickness of Velocity and Thermal Boundary Layers and Maximum Velocities.

And from the same author in his lecture notes from the experimental methods course taught many times at the Danish Technical University:

> Every experiment is really three experiments. There is the experiment you set out to do. There is the experiment you thought you did. And then there is the experiment you really did. The challenge is to bring these three into coincidence.

Clearly we did not do the experiment we set out to do. Almost all of the preceding chapters on both theoretical analysis and experimental methodology were motivated by trying to understand what we actually did, from the perspective of the experiment we thought we did. It was our repeated failures to satisfy the integral constraints for a natural convection boundary layer in an infinite environment in particular that brought us to the final realization. Thus without them we would have never come to an understanding of the experiment we actually did, the results of which are presented in the succeeding sections.

12.3 Differential Temperature with Thermocouples

The mean temperature profile at three different heights is shown in figure 12.2 and a more detailed plot for the region close to wall is presented in figure 12.4. The temperature difference values are calculated using the thermoelectric voltage polynomial function provided from thermocouple's technical specification.

The temperature profiles were corrected for the heat transfer through the thermocouple leads as explained in chapter 11. In "Case 1", a 50 micron thermocouple wire was used and the size of the bead was approximately 100 micron. The thermocouple used in the experiment was type *K* and the estimated temperature correction factor given in equation 11.48 was $\Psi = 0.32$, hence:

$$(T_j - T_a) = -0.32 \times \Delta T \tag{12.6}$$

where T_j is the temperature that thermocouple junction senses and T_a is the true air temperature around the junction. ΔT is approximated with the temperature difference between the junction and end of the bare section of the inclined leads (L$\approx 3mm$) in the original temperature profile. All the correction was based on this assumption that because the positioning error was minimized using a scaled microscope (see chapter 10), the only cause for the error in the inner region is due to conduction. We ignore the wall temperature error because the second junction was connected to the wall for at least $10\ cm$ above the measuring position.

As shown in figure 12.5, if we extrapolate the original temperature profile, it gives the temperature difference ($T_w - T \approx 6.2$) at the wall. The corrected estimation for the conduction error passes through ($T_w - T \approx 0$), which is the physical wall boundary condition for the temperature. As the probe traverses outward, the air temperature gradient decreases, hence the

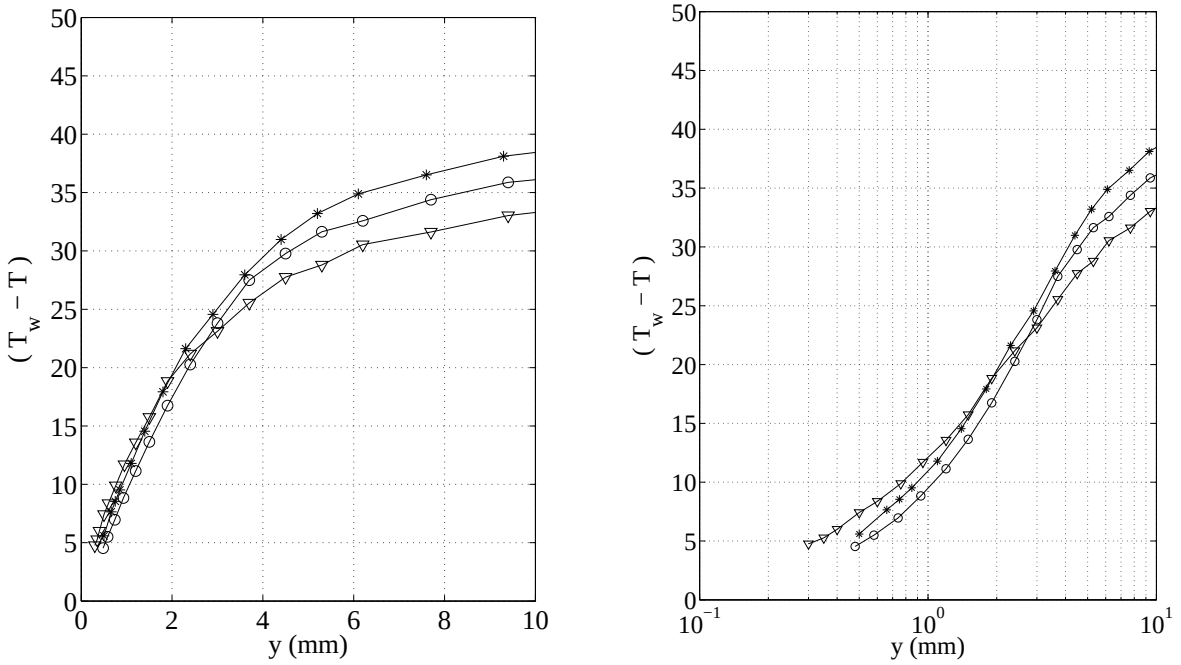

(a) Linear-Linear.

(b) Log-Linear.

Figure 12.4: Close up of the temperature profile 12.2.

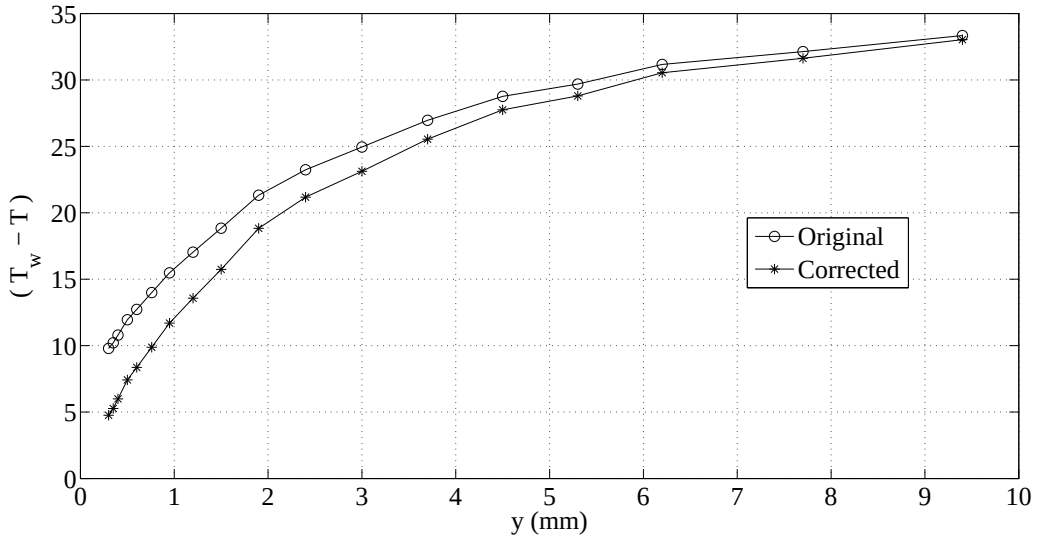

Figure 12.5: Mean temperature profile correction for conduction, Case 1 ; $Ra = 1.7 \times 10^{11}$

conduction error decreases; therefore the correction increases the slope of the curve.

In cases 2 and 3, the thermocouple wire size was $75\ \mu m$ and the leads were bent to form a "L" shape probe and it was placed parallel with the wall to minimize the heat conduction from the junction. For these two cases no temperature correction were done for the conduction error because the profiles satisfied the wall temperature boundary condition. The thermocouple for

all three cases were positioned approximately $1\ cm$ above the cold wire probe and traversed outward together, as it is shown in picture 12.6.

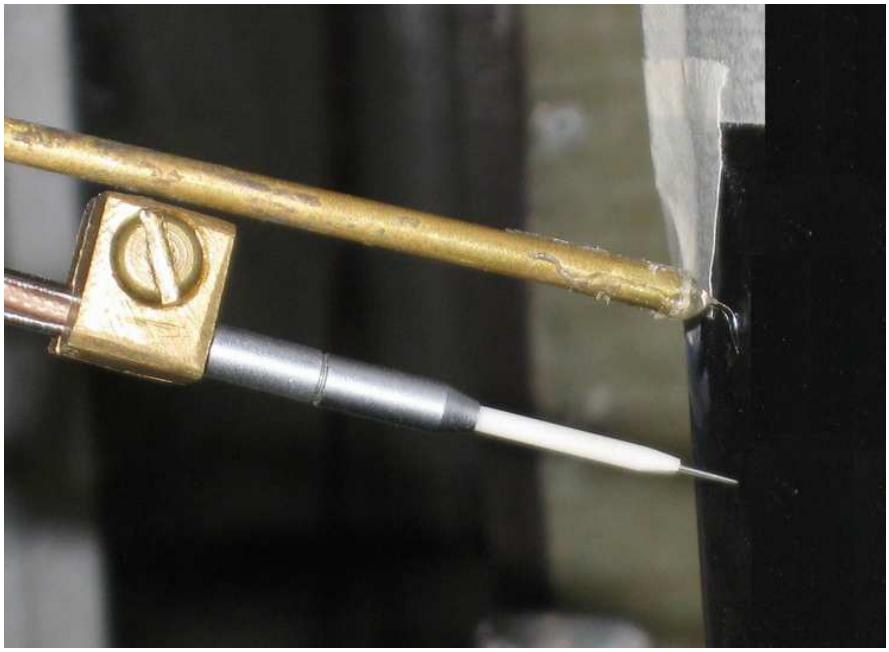

Figure 12.6: Thermocouple and cold-wire positions.

12.4 Determination of Wall Heat Transfer Rate and Wall Shear Stress

The goal of this section is to use the theoretical results of chapter 9, together with the near wall profile measurements to determine the wall heat transfer and wall shear stress. Even though the flow has been shown to not be a reasonable approximation to a natural convection boundary layer in an infinite environment, the near wall equations of the section 9.5 in chapter 9 are still applicable. In particular the scaling laws proposed and the functional form of the mean velocity, mean temperature, turbulence heat flux and Reynolds shear stress should still apply. The difference from a purely natural convection flow in an infinite environment will be in the values of the friction coefficient and heat transfer coefficient defined using the maximum velocity or $T_w - T_\infty$: these should be expected to be different since the near both τ_w and q_w are largely determined by the integral equations over the entire flow.

12.4.1 The near wall results

In section 9.5.1 the following exact solutions were were derived for the velocity and temperature near the wall:

$$U \cong \quad R\,\frac{u_*^2}{\nu}\,\ln(\frac{r}{R}) \tag{12.7}$$

$$T - T_w \cong \quad R\,\frac{F_o}{\alpha}\,\ln(\frac{r}{R}) \tag{12.8}$$

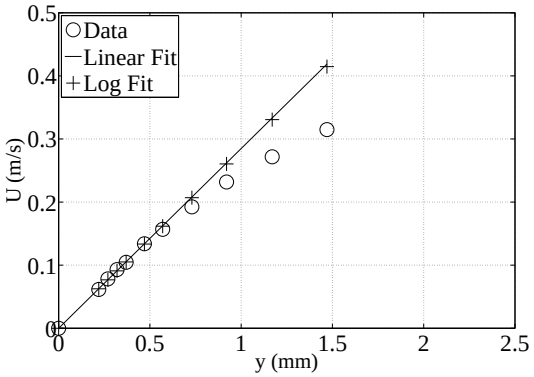

(a) Velocity Curve Fit at Case 1 ($4\ m$)

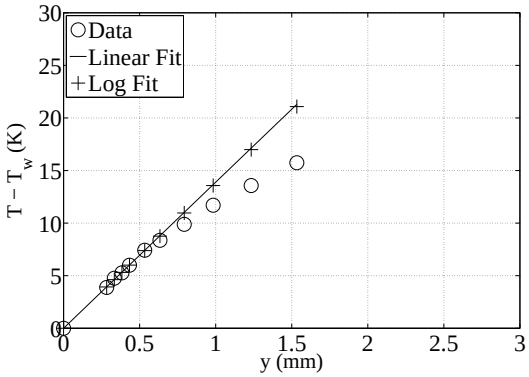

(b) Temperature Curve Fit at Case 1 ($4\ m$)

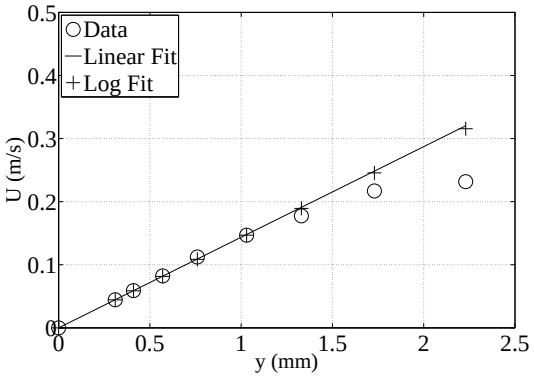

(c) Velocity Curve Fit at Case 2 ($3\ m$)

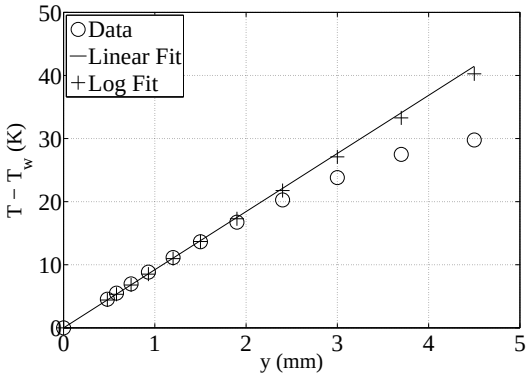

(d) Temperature Curve Fit at Case 2 ($3\ m$)

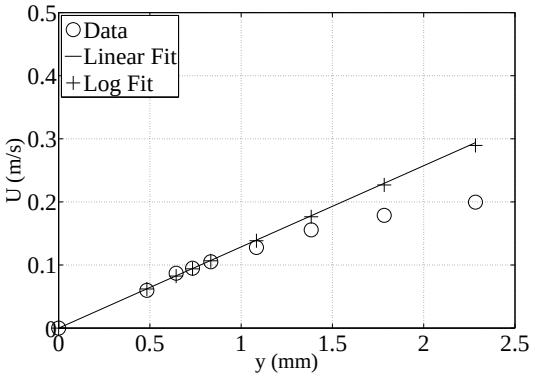

(e) Velocity Curve Fit at Case 3 ($1.5\ m$)

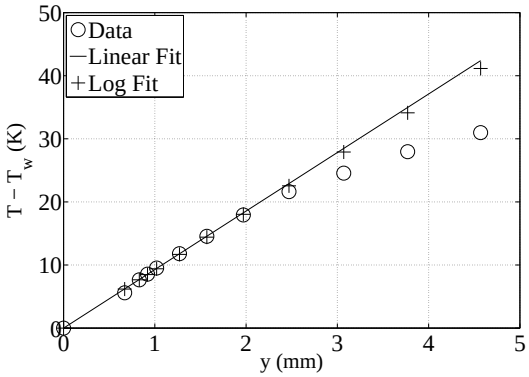

(f) Temperature Curve Fit at Case 3 ($1.5\ m$)

Figure 12.7: Data and curve fits for the velocity and temperature profiles close to the wall. For the curve fit values see table 12.3 .

As also shown in section 9.5.1, these can be expanded to yield as a leading term the more familiar forms of the planar natural convection boundary layer as:

$$U \cong \frac{u_*^2}{\nu} y \tag{12.9}$$

$$T - T_w \cong \frac{F_o}{\alpha} y \tag{12.10}$$

where we have defined $y = r - R$ as the distance from the wall. By fitting either of these to the mean velocity and temperature measured very close to the wall, these can be used to determine the the mean velocity and temperature gradients at the wall. And from them the wall shear stress and wall heat flux can be determined.

The mean temperature and velocity profiles near the wall for the three locations in the experiment are shown in the plots of figure 12.7. Also shown on the plots are the best fit to the logarithmic wall profiles of equations 12.7 and 12.8 which were fitted regressively to the first 4 - 6 points (including $r = R$) of the data. The mean temperature and mean velocity gradients inferred from them, together with the corresponding wall shear stress and Nusselt number are summarized in table 12.3. The thermodynamic and flow properties (ρ, μ, and k) were evaluated at the wall temperature.

height $[m]$	$\frac{dT}{dy}\Big\vert_{wall}$ $[K/m]$	q_w $[W/m^2]$	F_o $[K.m/s]$	$\frac{dU}{dy}\Big\vert_{wall}$ $[s^{-1}]$	τ_w $[kg/m-s^2]$	u_* $[m/s]$	t_* $[K]$
4	13886	385.75	0.39	284.84	0.0056	0.075	5.21
3	9212	255.9	0.259	143.6	0.0028	0.053	4.87
1.5	9276	260.74	0.261	128.7	0.0025	0.050	5.18

Table 12.3: Heat Transfer and Near Wall Velocity Parameters.

Also shown in the plots are the corresponding linear relations of equations 12.9 and 12.10, but using the values of the velocity and temperature gradients determined from the log fits. The gradient values differed slightly (a few percent) when the linear relations were fitted regressively instead. They are almost indistinguishable from their logarithmic counterparts, not too surprising since the values of $y << R$. What is surprising though is that the logarithmic relations do not capture at all the departure of the flow from the linear behavior. Clearly this is a consequence of either the variable viscosity near the wall, or the emergence of the turbulence Reynolds shear stress and turbulence heat flux.

12.5 Near Wall Scaling

A reasonable test for the validity of the wall shear stress and wall heat transfer rates is whether they can be used successfully to collapse data beyond the immediate vicinity of the linear region from which they were determined. As pointed out the chapter 9 it is generally believed that natural convection turbulent boundary layers at high Reynolds (or very very high Raleigh) numbers are characterized by an region of constant total heat flux in which both inner and outer scaling variables should work equally well. In the case of the developing flow measured here,

there is no similarity theory for the outer boundary layer, so there is no definitive way to decide what the outer length scales are. But for the near wall region, all of the scaling proposals of section 9.5 of chapter 9 can be expected to apply, since this region is relatively insensitive to the outer flow (which only manifests itself in q_w and τ_w).

12.5.1 Near Wall Scaling of Velocity Moments

Figure 12.8 shows a plot of the mean velocity profiles for all three heights plotted in inner variables, $U^+ = U/u_*$ and $y^+ = yu_*/\nu$. The value of ν was determined at the wall temperature, and the values used for the viscous length scale, ν/u_*, were $.39mm$, $.37mm$ and $.26mm$ for heights of 1.5 m, 3 m and 4 m respectively. The data collapse quite remarkably for $y^+ < 10$, but it is clear from the progression of the curves that the reason for them diverging is the increasing Rayleigh number. In the fact the point of departure from the highest Rayleigh number curve makes the emergence of the outer convection terms in the average streamwise momentum equation, and hence the outer boundary of the constant heat flux region. The fact the maximum mean velocity occurs at only $y^+ \approx 10 - 20$ makes it clear that in spite of the large facility and high Rayleigh number, from the point of view of the turbulence this is not really a fully-developed turbulence. Therefore there is no reason to expect the constant turbulence heat flux layer solutions of section 9.6 chapter 9 to even be marginally observed, and they are not.

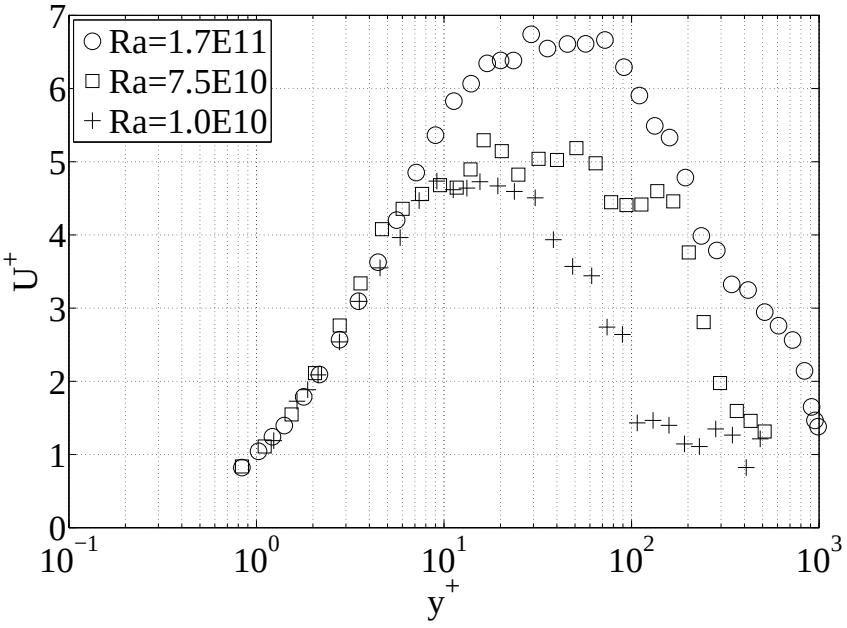

Figure 12.8: Scaled streamwise velocity at three different heights.

Figure 12.9 shows the radial mean velocity component, plotted in the same inner variables. Here the collapse is not as good, most probably because of the extreme difficulties in measuring this component of velocity in any shear flow, much less near the wall. It is interesting to note, however, that V immediately starts from zero and goes negative, as required.

Figures 12.10 through 12.12 plot the three components of the Reynolds stresses measured in this experiment: the normal stresses $\overline{u^2}/u_*^2$ and $\overline{v^2}/u_*^2$, and the Reynolds shear stress $\overline{uv}/u_*^2$. The best collapse is for the radial component $\overline{v^2}$, which collapses over almost the exact range as the

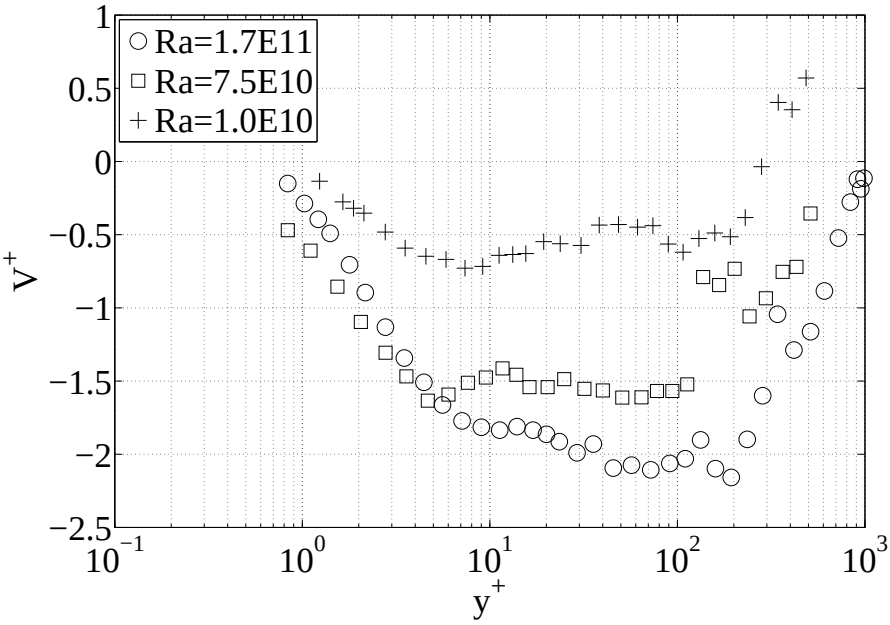

Figure 12.9: Scaled radial velocity in three different cases.

mean streamwise velocity. It would be tempting to interpret the less than perfect collapse of $\overline{u^2}$ as being a consequence of the evolving nature of the outer flow away from a near natural convection boundary layer towards a channel flow between parallel cylinders, particularly since all three moments at 4m show substantial departures from the other two outside of the mean velocity peak. But this would not be consistent with the Reynolds shear stress plot of figure 12.12 in which it is the middle position that deviates for the data closest to the wall. In the plot for $\overline{v^2}$ is the position closest to the wall is slightly away from the others. In fact all three moments have one curve which stands apart very near the wall, and it is the data from a different location for each. Thus it is probably safest to conclude that the differences are most likely due to slight differences in the alignment of the optical system for at least $\overline{v^2}$ and $\overline{uv}$. $\overline{u^2}$ is problematical for all boundary layer measurements at low to modest Reynolds numbers, in large part because of the contribution of the flow from well outside the near wall (e.g., the sloshing by the big eddies, the so-called in-active motions, c.f., Carlier and Stanislas [2005]).

12.5.2 Near Wall Scaling of the Temperature Moments

Figure 12.13 shows the mean temperature profiles measured by thermocouple plotted in inner variables as $(T_w - T)/t_*$ versus yu_*/ν, where $t_* = F_o/u_* = q_w/(\rho C_p u_*)$. (Strictly speaking, yu_*/α should have been used, but since the Prandtl number is nearly independent temperature and near unity the difference is slight, and it makes no difference for the collapse.) The two lowest locations, 1.5 m and 3 m collapse quite nicely *for all distances from the wall*. This is mostly because, as noted in chapter 8, most of the temperature drop occurs in the linear region very close to the wall. Regardless, the overall collapse provides considerable confidence in the validity of the scaling parameters, and especially the wall heat flux determination, at least at these two locations.

The highest location, 4 m, deviates quite noticeably outside of $y^+ > 3$ approximately. Originally we interpreted this to mean that at the lower heights the boundary layer was not fully-

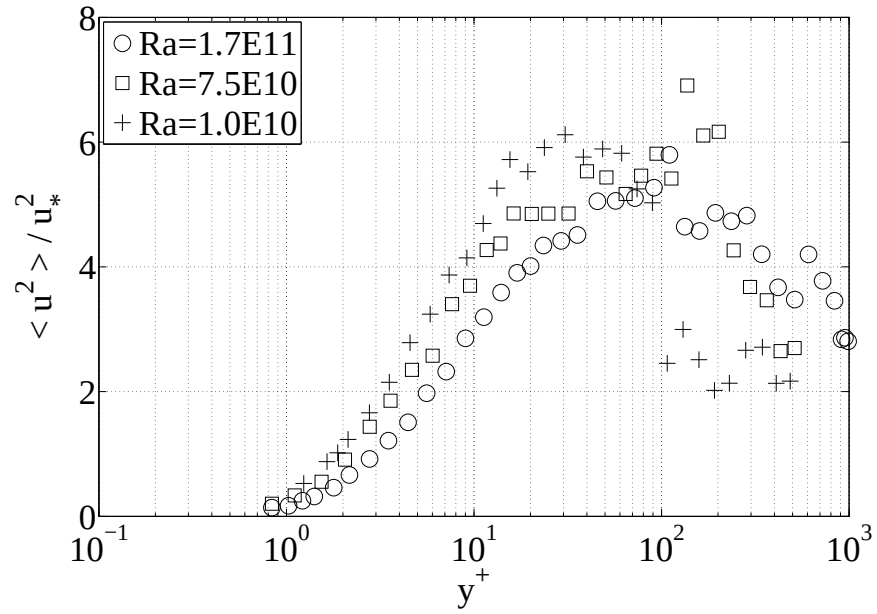

Figure 12.10: Scaled streamwise Reynolds normal stress velocity in three different cases.

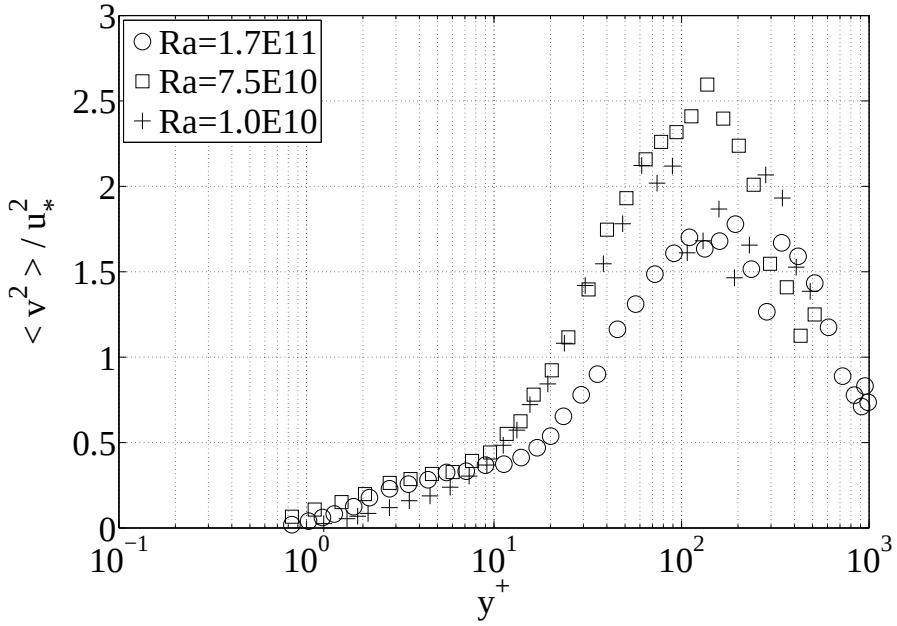

Figure 12.11: Scaled radial Reynolds normal stress velocity in three different cases.

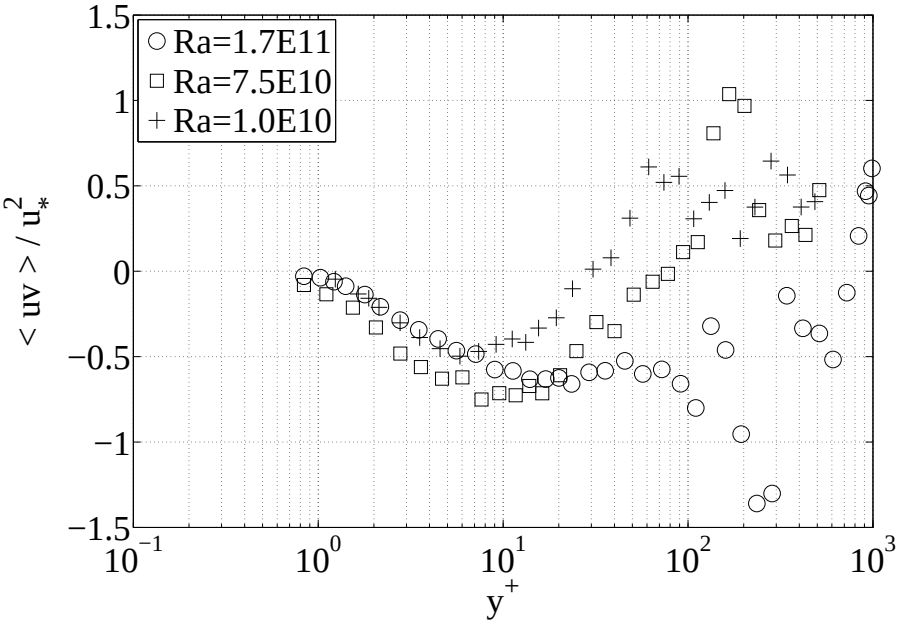

Figure 12.12: Scaled Reynolds shear stress velocity in three different cases.

developed. While that may indeed be true, we now know that in fact the flow has changed its character dramatically with height and is probably moving toward being a channel flow. The interpretation is even more complicated by the difficulties we had in taking the measurements. It was the thermocouple at 4 m which was not bent and therefore had to be corrected for the thermal gradient along the wires. And it was in the region of collapse that the largest corrections were applied. Therefore it is our belief that this profile should be viewed with suspicion. This is particularly problematical since we had hoped to use it to correct the fluctuating temperature measurements at this height.

As mentioned in chapter 11, the temperature was measured simultaneously with a 1 micron platinum resistance wire (cold-wire) and a pair of thin thermocouples, connected differentially to measure the temperature difference ($T_w - T$). Because the cold-wire measurements close to the wall were complicated by the heat conduction along the prongs, it is been impossible (at least to this point) to correct the data in a satisfactory manner. But it should be clear from the analysis of that chapter that unsteady conduction to the prongs of cold-wires operating in low velocity flows is a very serious problem, even in the absence of mean thermal gradients (and even if only a portion of the wire is etched). Therefore we absolutely do not believe the rest of the measurements of the fluctuating moments shown below. Why then are they shown? The reason is to illustrate how good they look, and how easy it might have been to pass them off to an unsuspecting turbulence (especially CFD) community. We were almost fooled!

Figures 12.14 to 12.16 show plots in inner variables of $\overline{t^2}$, $\overline{ut}$, and $\overline{vt}$ respectively. Only measurements from 3 m and 4 m are presented (since the last wire broke while doing the 1.5 m experiment). Note the excellent collapse in the near wall region. It would be very easy to believe these measurements in the absence of a good reason not to. Aside from the esoteric arguments about probe response, our first clue not to believe them came from the near wall theoretical solutions for the turbulence heat flux of section 9.5.1, equations 9.25 and its variable thermal properties counterparts. The exact solutions for $\overline{vt}$ are almost an order of magnitude

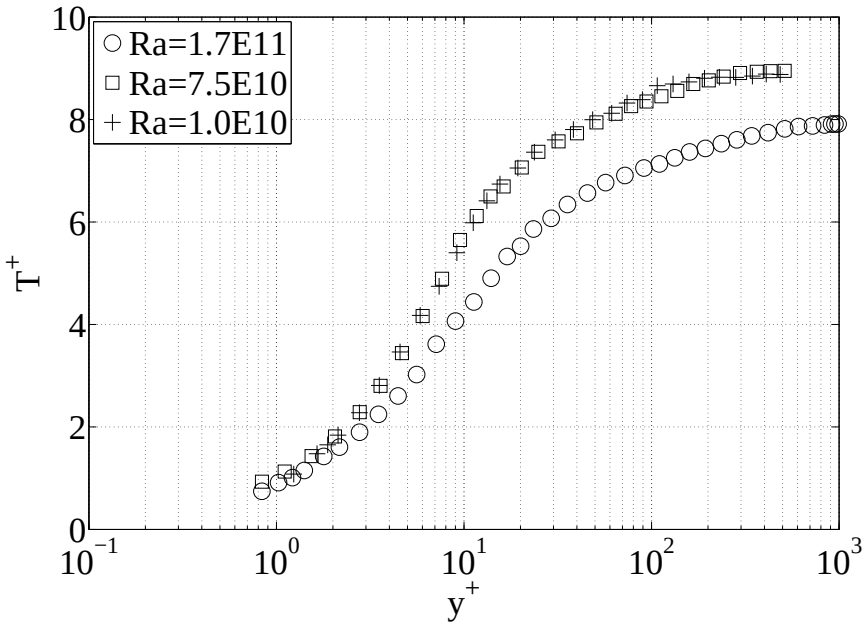

Figure 12.13: Scaled mean temperature at 1.5m, 3m and 4m.

larger near the wall than the measured values shown in figure 12.16! A second clue that something is wrong lies the values of the rms fluctuating temperature itself, which is only about $3 - 4°K$, even in the region where the velocity gradient is quite steep and drops almost $30°$. Interestingly and somewhat surprisingly, the $\overline{ut}/u't'$ coefficient peaks near 0.5 which is not far from the values of 0.6 to 0.7 that have been observed for plumes (e.g., Shabbir and George [1994]). The $\overline{vt}/v't'$ correlations also peak at about -0.07 in the near wall region, which again is not far from that expected. This can both perhaps be explained if this correlation is largely determined by the very large energetic scales which survive the filtering by the end losses. Thus even if $\overline{t^2}$ is substantially diminished by the filtering, its normalized correlations are relatively less attenuated.

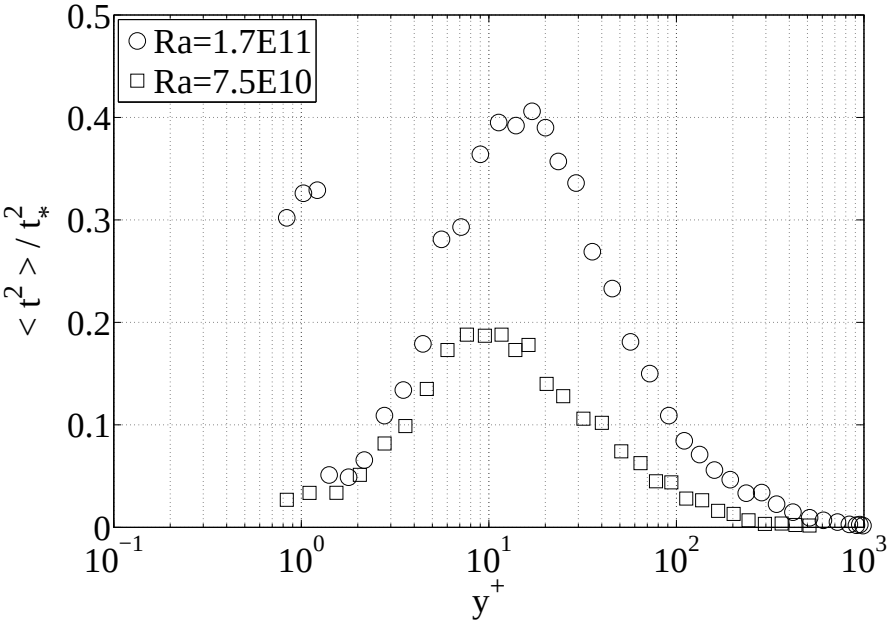

Figure 12.14: Scaled temperature variance at 3 m and 4m.

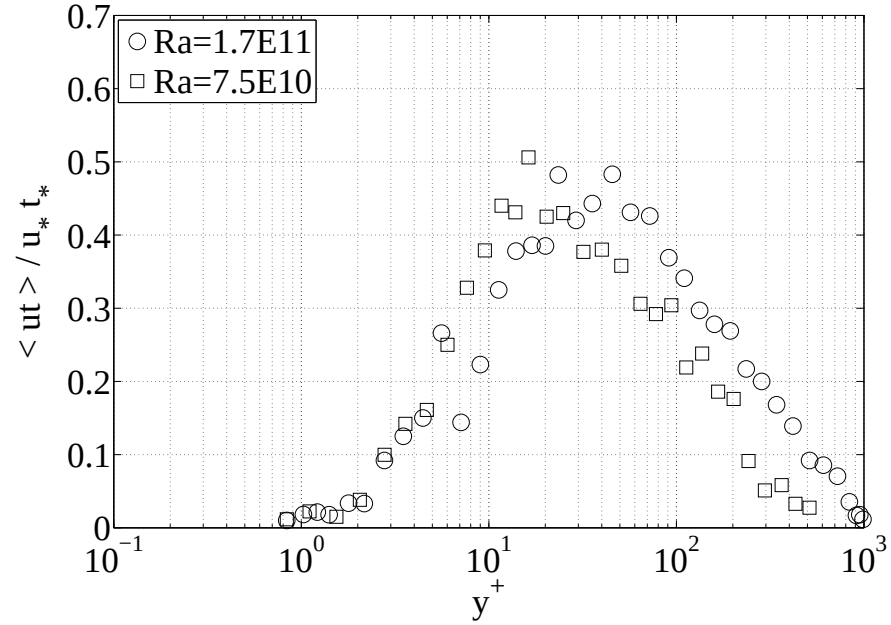

Figure 12.15: Scaled streamwise velocity-temperature correlation at 3 m and 4m.

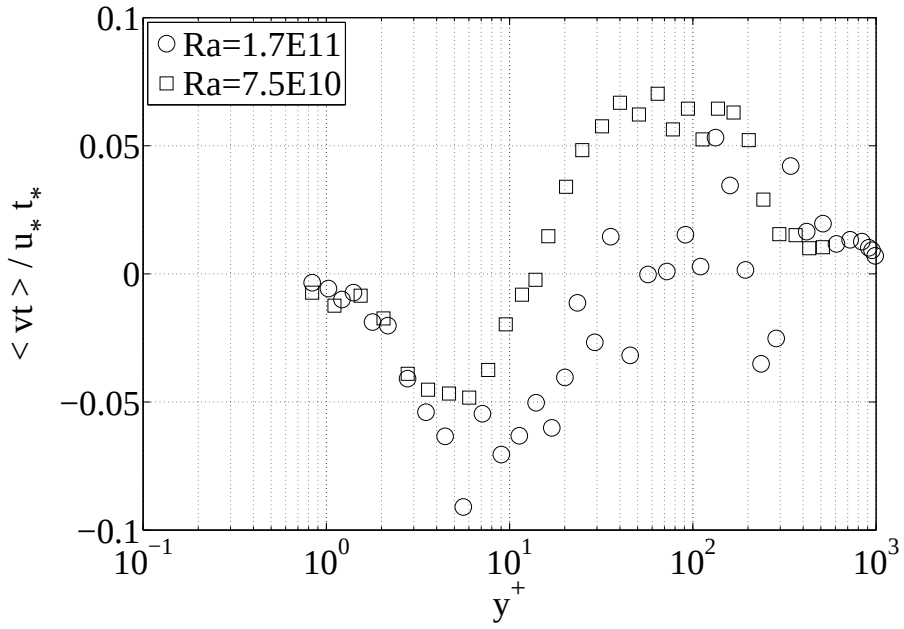

Figure 12.16: Scaled radial velocity-temperature correlation at 3 m and 4m.

Chapter 13

Summary and Conclusions

The temperature and flow fields of what we had hoped would be a turbulent natural convection boundary layer flow along a heated vertical circular cylinder have been experimentally studied using laser Doppler anemometry, cold-wire thermometry and thermocouples. Two velocity components, radial and streamwise, were measured simultaneously with temperature. The results of the experiment were presented, including the mean profiles of the temperature and velocity across the boundary layer at three different heights, representing three Rayleigh numbers of: $Ra = (g\,\beta\,\Delta T\,L^3)/(\nu\alpha) = 1.7\times10^{11},\ 7\times10^{10}$ and 10^{10} . Also the higher order moments and temperature-velocity correlations are given in the turbulent region of the boundary layer.

In fact, it appears that the flow at all locations, but certainly the highest Rayleigh numbers, was not purely a natural convection boundary layer, but one which developing into the thermally-driven flow between two differentially heated walls. This was not anticipated. Nor is it clear how to achieve as high (or higher) Rayleigh numbers in future experiments. The water heater for the heated pipe is already near the boiling point, and also the temperature differences are at the limit of what is reasonable with hot-air while still assuming incompressibility. A much larger outer cylinder would possibly help, but at considerable difficulty in managing and cooling the facility.

Further complicating this study was a problem with experimental methods for measuring temperature, specifically the cold-wire thermometry. The problems encountered with the thermocouples operating in a strong temperature gradient could have been solved had we anticipated the problems, and in fact were solved (by bending the probe so it was parallel to the wall) for the measurements taken afterwards (1.5m and 3m). But the problems with the unsteady heat loss to the ends of the cold-wire do not seem to have a solution, in spite of a straight-forward analysis of them. This caused a substantial reduction in the rms temperature measurement, and a corresponding reduction in the velocity temperature cross-correlations. These were very subtle problems to detect, and became obvious only by applying the near wall Reynolds-averaged equations and noting that the $\overline{vt}$ cross-correlation was much too low.

In part because of our search to understand the measurement, new theory for the boundary layer flow was established for buoyancy driven flow in cylindrical coordinates. Both temperature and velocity in the near wall region in particular have logarithmic solutions instead of the familiar linear ones of planar flows. In practice the differences from linear seemed to be slight, although they did make a slight difference in the estimation of the wall shear stress and wall heat flux. Solutions which included a temperature-dependent near wall viscosity and

conductivity were also included. Perhaps most surprising of all was the recognition of the inconsistency of carrying out numerical computations which assume incompressibility, but use C_p in the thermal energy equation. Clearly either incompressibility must be relaxed (as it is in the real world of experiments) or C_v must be used.

Bibliography

Vedat S. Arpaci and Poul S. Larsen. *Convection Heat Transfer*. Prentice Hall Inc., 1984. ISBN 0-13-172346-4.

Carlos Arroyo Osso. *Aerothermal Investigation of an Intermediate Turbine Duct.* Phd. thesis, Chalmers University of Technology, 2009.

L.U. Axelsson. An investigation of buoyancy-driven turbulent flows. Master's thesis, Chalmers University of Tech., 2003.

C. Balaji, M. Holling, and H. Herwig. Nusselt number correlations for turbulent natural convection flows using asymptotic analysis of the near-wall region. *Transactions of the ASME. Journal of Heat Transfer*, 129(8):1100 – 5, 2007.

R. P. Benedict. *Manual on the use of Thermocouples in Temperature Measurement*. American Society for Testing and Material, STP470B, 2005. ISBN 99-0286040-0.

P.D. Beuther. *Experimental Investigation of the Axisymmetric Turbulent Buoyant Plume.* PhD thesis, State University of NewYork at Buffalo, May 1980.

H. H. Bruun. *Hot-Wire Anemometry*. Oxford Science Publications, 2002. ISBN 0-19-856342-6.

P. Buchhave, W. K. George, and J. L. Lumley. The measurement of turbulence with the laser-doppler anemometer. In Van Dyke, Wehausen, and Lumley, editors, *Annual Review of Fluid Mechanics*, volume 11, pages 443–503. Academic Press, Palo Alto, CA., 1979.

P. Burattini, R.A. Antonia, and L. Danaila. Similarity in the far field of a turbulent round jet. *Physics of The Fluids*, 17(025101), 2005.

J Carlier and M Stanislas. Study of the eddy structure in a turbulent boundary layer using particle image velocimetry. *Journal of Fluid Mechanics*, 535:143–188, 2005.

J.E. Cater and J. Soria. The evolution of round zero-net-mass-flux jets. *Journal of Fluid Mechanics*, 472:167 – 200, 2002.

Yunus A. Cengel and Michael A. Boles. *Thermodynamics, An Engineering Approach*. McGRAW-HILL, 3rd edition, 1998. ISBN 0-07-011927-9.

R. Cheesewright. Turbulent natural convection from a vertical plane surface. *Transactions of the ASME. Series C, Journal of Heat Transfer*, 90(1):1 – 8, 1968.

R. Cheesewright and E. Ierokiopitis. Velocity measurements in a turbulent natural convection boundary layer. pages 305 – 309, Munich, Ger, 1982.

N.A. Chigier and A. Chervinsky. Experimental investigation of swriling vortex motion in jets. *Transaction of the ASME,Journal of Applied Mechanics*, pages 443–451, 1967.

S.W. Churchill and H.H.S. Chu. Correlating equations for laminar and turbulent free convection from a vertical plate. *International Journal of Heat and Mass Transfer*, 18(11):1323 – 9, 1975.

D.C. Collis and M.J. Williams. Two-dimensional convection from heated wires. *Journal of Fluid Mechanics*, 6(357 - 384):357 –, 1959.

A. Craya and M. Darrigol. Turbulent swirling jet. volume 10, 1967.

D. Ewing. Decay of round turbulent jets with swirl. In *Proceedings of the 4th International Symposium on Engineering Turbulence Modeling and Experiments*, Elsevier, 1999.

S. Farokhi, R. Taghavi, and E.J. Rice. Effect of initial swirl distribution on the evolution of a turbulent jet. *Journal of AIAA*, 27(6):700–706, 1989.

T. Fujii, M. Takeuchi, M. Fujii, K. Suzaki, and H. Uehara. Experiments on natural-convection heat transfer from the outer surface of a vertical cylinder to liquids. *International Journal of Heat and Mass Transfer*, 13(5):753 – 87, 1970.

B. Gebhart. Instability, transition, and turbulence in buoyancy-induced flows. *Annual Review of Fluid Mechanics*, 5:213 – 246, 1973.

Benjamin Gebhart, Yogesh Jaluria, Roop L. Mahajan, and Bahgat Sammakia. *Buoyancy Induced Flows and Transport*. Taylor & Francis, 2003.

Jr. George, W.K., R.L. Alpert, and F. Tamanini. Turbulence measurements in an axisymmetric buoyant plume. *International Journal of Heat and Mass Transfer*, 20(11):1145 – 54, 1977.

W. K. George. Burst-mode processing of laser doppler anemometer signals. *Journal of Exp. Thermal and Fluid Science*, 1:48–68, 1988.

W. K. George. Some new ideas for similarity of turbulent shear flows. In Hanjalic and Pereira, editors, *Proc. ICHMT Symposium on Turbulence, Heat and Mass Transfer, Lisbon, Portugal (1994)*. Elsevier, Amsterdam, 1995.

W. K. George, P. D. Beuther, and J. L. Lumley. Processing of random signals. In *Proceedings of the Dynamic Flow Conference, Lygnby, Denmark*, pages 757–800, Denmark, 1978. Dantec.

William K. George and Luciano Castillo. Zero-pressure-gradient turbulent boundary layer. *Applied Mechanics Reviews*, 50(12 pt 1):689 – 729, 1997.

William K. Jr. George and Steven P. Capp. A theory for natural convection turbulent boundary layers next to heated vertical surfaces. *International Journal of Heat and Mass Transfer*, 22(6): 813 – 826, June 1979.

W.K. George. The self-preservation of turbulent flows and its relation to initial conditions and coherent structures. In W.K. George and R. Arndt, editors, *Advances in Turbulence*, pages 39–73. Springer, New York, 1989.

W.K. George. Is there an asymptotic effect of initial and upstream conditions on turbulence? In *Proceedings of ASME 2008 Fluids Engineering Meeting, Freeman Lecture, August 10-14, Jacksonville, Florida*, number FEDSM2008-55362. ASME, 2008.

W.K. George, H. Abrahamsson, J. Eriksson, R.I. Karlsson, L. Lofdahl, and M. Wosnik. A similarity theory for the turbulent plane wall jet without external stream. *Journal of Fluid Mechanics*, 425:367 – 411, 2000.

R.T. Gilchrist and J.W. Naughton. Experimental study of incompressible jets with different inital swril distributions: Mean results. *AIAA Journal*, 43(4):741–751, April 2005.

C.J. Hoogendoorn and H. Euser. Velocity profiles in the turbulent free convection boundary layer. volume II, pages 193 – 7, 1978.

H. J. Hussein, S. P. Capp, , and W. K. George. Velocity measurements in a high-reynolds-number, momentum-conserving, axisymmetric, turbulent jet. *J. Fluid Mech.*, 258:31–75, 1994.

Frank P. Incropera. *Introduction to heat transfer*. Wiley, 2007.

J.C. La Rue, T. Deaton, and C.H. Gibson. Measurement of high-frequency turbulent temperature. *Review of Scientific Instruments*, 46(6), 1975.

J.C. Lecordier, Moreau D., and P. Paranthoen. Prong-wire thermal interaction effect induced harmonics for the thin-wire resistance thermometer. *Journal of Physics E (Scientific Instruments)*, 18(7):571 – 572, 1982.

J.L. Lumley. Computational modeling of turbulent flow. *Advances in Applied Mechanics*, 18: 123–176, 1978.

J. Mi, D.S. Nobes, and G.J. Nathan. Influence of jet exit condition on the passive scalar field of an axisymmetric free jet. *Journal of Fluid Mechanics*, 432:91–125, 2001.

A.S. Monin and A.M. Yaglom. *Statistical Fluid Mechanics: Mechanics of Turbulence*, volume 2. MIT Press, 1975. ISBN 0-262-13098-2.

S. Ostrach. Analysis of laminar free-convection flow and heat transfer about flat plate parallel to direction of generating body force. *National Advisory Committee for Aeronautics, Technical Notes*, page 47, 1952.

N. R. Panchapakesan and J. L. Lumley. Turbulence measurements in axisymmetric jets of air and helium. part 1. air jet. *Journal of Fluid Mechanics*, 246:197 – 223, 1993.

J. Panda and D.K. McLaughlin. Experiments on the instabilities of a swirling jet. *Physics of Fluids*, 6(1):263–276, 1994.

Ronald L. Panton. *Incompressible Flow*. John Wiley & Sons Inc., 3rd edition, 2005. ISBN 13 978-0-471-26122-3.

P. Paranthoen, C. Petit, and J.C. Lecordier. The effect of thermal prong-wire interaction on the response of a cold wire in gaseous flows. *Journal of Fluid Mechanics*, 124:457 – 473, 1982.

A.E. Perry. *Hot-wire Anemometry*. Oxford University Press, 1982. ISBN 0-19-856327-2.

Johan Persson. Simultaneous measurement of velocity and temperature in natural convection boundary layer. Technical report, Vattenfall Utveckling AB., 1994.

N. J. Persson and R. I. Karlsson. Turbulent natural convection around a heated vertical slender cylinder. In *8th Int. Symp. on Applications of Laser Techniques to Fluid Mechanics*, Lisbon, 1996.

M. Pons and P. Le Quere. Modeling natural convection with the work of pressure-forces: a thermodynamic necessity. *International Journal of Numerical Methods for Heat & Fluid Flow*, 17 (3):322 – 32, 2007.

M. Prudhomme and P. Le Quere. Stability of stratified natural convection in a tall vertical annular cavity. *Physics of Fluids*, 19:094106, 2007.

A. Shabbir and W.K. George. Experiments on a round turbulent buoyant plume. *Journal of Fluid Mechanics*, 275:1 – 32, 1994.

A. Shabbir, P.D. Beuther, and W.K. George. X-wire response in turbulent flows of high-intensity turbulence and low mean velocities. *Experimental Thermal and Fluid Science*, 12:52 – 56, 1996.

Aamir Shabbir. *An Experimental Study of an Axisymmetric Turbulent Buoyant Plume and Investigation of Closure Hypotheses.* PhD thesis, State University of NewYork at Buffalo, 1987.

H.J. Sheen, W.J. Chen, Jeng S.Y., and Huang T.L. Correlation of swirl number for a radial-type swirl genarator. *Journal of Experimental Thermal and Fluid Science*, 12:444 – 451, 1996.

A. Shiri. Turbulent shear flow experiments: Design of natural convection rig and lda measurement in swirling jets, 2006.

A. Shiri and W.K. George. Turbulent natural convection in a differentially heated vertical channel. In *Proceedings of ASME Summer Heat Transfer Conference*, number HT2008-56333, 2008.

A. Shiri, W.K. George, and J.W. Naughton. An experimental study of the far-field of incompressible swirling jets. In *36th AIAA Fluid Dynamics Conference and Exhibit, 5 - 8 June 2006, San Francisco, California*, 5 - 8 June 2006.

A. Shiri, W.K. George, and S. Toutiaei. Evaluation of closure hypotheses using recent experimental data on the similarity region of swirling jet flow. In *Proceedings of the 4th Ankara International Aerospace Conference*, Ankara, Turkey, September 10-12, 2007a. AIAC-2007-051.

A. Shiri, S. Toutiaei, and W.K. George. Turbulent flow structure in the similarity region of swirling jet. In *Advances in Turbulence XI, Proceedings of the 11th EUROMECH*, pages 471–473, European Turbulence Conference, Porto, Portugal, June 25-28 2007b. Springer.

A. Shiri, W.K. George, and J.W. Naughton. Experimental study of the far field of incompressible swirling jets. *AIAA Journal*, 46(8):2002–2009, August 2008.

V. Shtern, F. Hussain, and M. Herrada. New features of swirling jets. *Physics of Fluids*, 12(11): 2868 – 2877, 2000.

E.A. Spiegel and G. Veronis. On the boussinesq approximation for a compressible fluid. *Astrophysical Journal*, 131(2):442 – 447, 1960.

M. Tagawa, K. Kato, and Y. Ohta. Response compensation of fine-wire temperature sensors. *Review of Scientific Instruments*, 76(9):94904 – 1, 2005.

H. Tennekes and J.L. Lumley. *A First Course in Turbulence*. MIT Press, 3rd edition, 1974. ISBN 0-262-20019-8.

T. Tsuji and Y. Nagano. Characteristics of a turbulent natural convection boundary layer along a vertical flat plate. *International Journal of Heat and Mass Transfer*, 31(8):1723 – 1734, Aug. 1988a.

T. Tsuji and Y. Nagano. Turbulence measurements in a natural convection boundary layer along a vertical flat plate. *International Journal of Heat and Mass Transfer*, 31(10):2101 – 2111, Oct. 1988b.

T. Tsuji and Y. Nagano. An anemometry technique for turbulence measurements at low velocities. *Experiments in Fluids*, 7(8):547 – 559, 1989a.

T. Tsuji and Y. Nagano. Velocity and temperature measurements in a natural convection boundary layer along a vertical flat plate. *Experimental Thermal and Fluid Science*, 2(2):208 – 215, Apr. 1989b.

T. Tsuji, Y. Nagano, and M. Tagawa. Frequency response and instantaneous temperature profile of cold-wire sensors for fluid temperature fluctuation measurements. *Experiments in Fluids*, 13:171 – 178, 1992.

Clara Marika Velte. *Characterization of Vortex Generator Induced Flow.* Phd thesis, Technical University of Denmark, 2009.

G.C. Vliet and C.K. Liu. An experimental study of turbulent natural convection boundary layers. *Transactions of the ASME. Series C, Journal of Heat Transfer*, 91(4):517 – 31, 1969.

Maja Wänström. *Spatial Decompositions of a Fully-Developed Turbulent Round Jet Sampled with Particle Image Velocimetry.* PhD thesis, Chalmers University of Technology, 2009.

C.Y. Warner and V.S. Arpaci. Experimental investigation of turbulent natural convection in air at low pressure along vertical heated flat plate. *International Journal of Heat and Mass Transfer*, 11(3):397 – 406, 1968.

Frank M. White. *Viscous Fluid Flow*. McGraw-Hill, 2nd edition, 1991. ISBN 0-07-069712-4.

Frank M. White. *Fluid Mechanics*. McGRAW-HILL, 3rd edition, 1994. ISBN 0-07-911695-7.

M. Wosnik. Outline of a new theory for the natural convection turbulent boundary layer next to heated vertical surfaces. Master's thesis, University at Buffalo, June 1994.

M. Wosnik and W. K. George. Another look at the turbulent natural convection boundary layer next to heated vertical surfaces. In *Int. Symp. of Turb. Heat and Mass Transfer*, volume 1, pages 14.5.1 – 14.5.6, 1994.

Appendix A

Details of Measurement Window

The opening for laser probe traverse is shown in figure A.1. The probe tilted $3.5°$ to avoid hitting the wall by one of the beams before the measuring volume approaches to the wall.

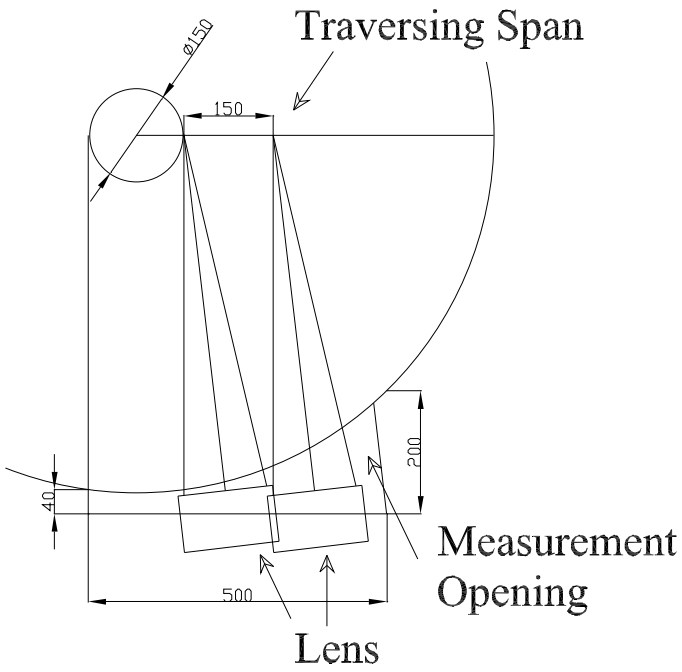

Figure A.1: The schematic for the traversing span in the measurement window.

Appendix B

Momentum Equation in Cylindrical Coordinate

The equations of motion and energy for a Newtonian incompressible flow are given in cylindrical coordinates (x, r, θ) (cf. Panton [2005]). The instantaneous velocity components are $\tilde{v}_x$, $\tilde{v}_r$ and $\tilde{v}_\theta$ respectively in axial, radial and azimuthal directions. Assuming the gravity force acts in axial direction, $\vec{\mathbf{g}} = (-g, 0, 0)$, which also is the main direction of the flow. The flow is assumed to be steady state therefore time variation $(\partial/\partial t)$ terms are omitted.

B.1 Averaged Momentum Equations

Using equation 8.19 we get the continuity equation as below:

Continuity Equation:

$$\nabla.\vec{\mathbf{v}} = \frac{\partial \tilde{v}_x}{\partial x} + \frac{1}{r}\frac{\partial}{\partial r}(r\tilde{v}_r) + \frac{1}{r}\frac{\partial \tilde{v}_\theta}{\partial \theta} = 0 \tag{B.1}$$

Using equation 8.49 we get the momentum equations as below:

Momentum Equation in Axial Direction:

$$\tilde{v}_x\frac{\partial \tilde{v}_x}{\partial x} + \tilde{v}_r\frac{\partial \tilde{v}_x}{\partial r} + \tilde{v}_\theta(\frac{1}{r}\frac{\partial \tilde{v}_x}{\partial \theta}) = -\frac{1}{\rho_o}\frac{\partial \tilde{P}}{\partial x} + \frac{2}{\rho_o}\nabla.(\mu\tilde{S}_x) + g\ \beta\ (\tilde{T} - T_o) \tag{B.2}$$

Momentum Equation in Radial Direction:

$$\tilde{v}_x\frac{\partial \tilde{v}_r}{\partial x} + \tilde{v}_r\frac{\partial \tilde{v}_r}{\partial r} + \tilde{v}_\theta\left(\frac{1}{r}\frac{\partial \tilde{v}_r}{\partial \theta} - \frac{\tilde{v}_\theta}{r}\right) = -\frac{1}{\rho_o}\frac{\partial \tilde{P}}{\partial r} + \frac{2}{\rho_o}\nabla.(\mu\tilde{S}_r) \tag{B.3}$$

Momentum Equation in Tangential Direction:

$$\tilde{v}_x\frac{\partial \tilde{v}_\theta}{\partial x} + \tilde{v}_r\frac{\partial \tilde{v}_\theta}{\partial r} + \tilde{v}_\theta\left(\frac{1}{r}\frac{\partial \tilde{v}_\theta}{\partial \theta} + \frac{\tilde{v}_r}{r}\right) = -\frac{1}{\rho_o}\left(\frac{1}{r}\frac{\partial \tilde{P}}{\partial \theta}\right) + \frac{2}{\rho_o}\nabla.(\mu\tilde{S}_\theta) \tag{B.4}$$

where ρ_o and T_o are the reference density and temperature and the viscous terms are defined as below:

$$2\nabla.(\mu\tilde{S}_x) \equiv 2\frac{\partial}{\partial x}\left(\mu\frac{\partial \tilde{v}_x}{\partial x}\right) + \frac{1}{r}\frac{\partial}{\partial r}\left(r\mu(\frac{\partial \tilde{v}_x}{\partial r} + \frac{\partial \tilde{v}_r}{\partial x})\right) + \frac{1}{r}\frac{\partial}{\partial \theta}\left(\mu(\frac{\partial \tilde{v}_\theta}{\partial x} + \frac{1}{r}\frac{\partial \tilde{v}_x}{\partial \theta})\right) \tag{B.5}$$

$$2\nabla.(\mu\tilde{S}_r) \equiv \frac{\partial}{\partial x}\left(\mu(\frac{\partial\tilde{v}_x}{\partial r}+\frac{\partial\tilde{v}_r}{\partial x})\right)+2\frac{1}{r}\frac{\partial}{\partial r}\left(r\mu\frac{\partial\tilde{v}_r}{\partial r}\right)+\frac{1}{r}\frac{\partial}{\partial\theta}\left(\mu\big(r\frac{\partial}{\partial r}(\frac{\tilde{v}_\theta}{r})+\frac{1}{r}\frac{\partial\tilde{v}_r}{\partial\theta})\right)$$
$$-2\mu\left(\frac{1}{r^2}\frac{\partial\tilde{v}_\theta}{\partial\theta}+\frac{\tilde{v}_r}{r^2}\right) \quad \text{(B.6)}$$

$$2\nabla.(\mu\tilde{S}_\theta) \equiv \frac{\partial}{\partial x}\left(\mu(\frac{\partial\tilde{v}_\theta}{\partial x}+\frac{1}{r}\frac{\partial\tilde{v}_x}{\partial\theta})\right)+\frac{1}{r^2}\frac{\partial}{\partial r}\left(\mu r^2(r\frac{\partial}{\partial r}(\frac{\tilde{v}_\theta}{r})+\frac{1}{r}\frac{\partial\tilde{v}_r}{\partial\theta})\right)$$
$$+\frac{1}{r}\frac{\partial}{\partial\theta}\left(2\mu(\frac{1}{r}\frac{\partial\tilde{v}_\theta}{\partial\theta}+\frac{\tilde{v}_r}{r})\right) \quad \text{(B.7)}$$

The assumption of constant viscosity is practical for swirling jet equations therefore these terms change to $\mu\nabla^2\vec{\mathbf{v}}$. In natural convection equations, the viscosity term should be kept inside the divergence ($\nabla.(\mu\mathbf{S}_{ij})$) as μ varies with the temperature. The density variation effect in non-isothermal flow is limited to the buoyancy term in equation B.2, using the Boussinesq approximation and a reference density ρ_o.

By using *Reynolds decomposition* in equations above, we divide each instantaneous velocity component to its mean and fluctuation part:

Axial Component(x)	:	$\tilde{v}_x = U + u$
Radial Component(r)	:	$\tilde{v}_r = V + v$
Tangential Component(θ)	:	$\tilde{v}_\theta = W + w$
Temperature	:	$\tilde{T} = T + t'$
Pressure	:	$\tilde{P} = P_m + p$

where t and p are the fluctuating temperature and pressure and P_m is the local pressure minus hydrostatic pressure. As long as Boussinesq approximation is used, we avoid decomposing the viscosity(μ) to the mean and fluctuating components because the correlation of viscosity-velocity adds too much complexity into the equations. Now we substitute these terms into the momentum equations and take average:

Averaged Momentum Equation in Axial Direction:

$$U\frac{\partial U}{\partial x}+V\frac{\partial U}{\partial r}+\frac{W}{r}\frac{\partial U}{\partial\theta}=-\frac{1}{\rho_o}\frac{\partial P_m}{\partial x}+\frac{2}{\rho_o}\nabla.(\mu S_x)$$
$$-\left\langle u\frac{\partial u}{\partial x}+v\frac{\partial u}{\partial r}+\frac{w}{r}\frac{\partial u}{\partial\theta}\right\rangle+g\,\beta\,(T-T_o) \quad \text{(B.8)}$$

Averaged Momentum Equation in Radial Direction:

$$U\frac{\partial V}{\partial x}+V\frac{\partial V}{\partial r}+\frac{W}{r}\frac{\partial V}{\partial\theta}-\frac{W^2}{r}=-\frac{1}{\rho_o}\frac{\partial P_m}{\partial r}+\frac{2}{\rho_o}\nabla.(\mu S_r)$$
$$-\left\langle u\frac{\partial v}{\partial x}+v\frac{\partial v}{\partial r}+\frac{w}{r}\frac{\partial v}{\partial\theta}-\frac{w^2}{r}\right\rangle \quad \text{(B.9)}$$

Averaged Momentum Equation in Tangential Direction:

$$U\frac{\partial W}{\partial x}+V\frac{\partial W}{\partial r}+\frac{W}{r}\frac{\partial W}{\partial \theta}+\frac{VW}{r}=-\frac{1}{\rho_o}\left(\frac{1}{r}\frac{\partial P_m}{\partial \theta}\right)+\frac{2}{\rho_o}\nabla.(\mu S_\theta) - \left\langle u\frac{\partial w}{\partial x}+v\frac{\partial w}{\partial r}+\frac{w}{r}\frac{\partial w}{\partial \theta}+\frac{vw}{r}\right\rangle \quad \text{(B.10)}$$

Here we use the sign $<\quad>$ to show the averaged terms in the equations. Using the continuity equation to make the *Reynolds Stresses* involved in the equations yields,

Averaged Continuity Equation:

$$\frac{\partial U}{\partial x}+\frac{1}{r}\frac{\partial (rV)}{\partial r}+\frac{1}{r}\frac{\partial W}{\partial \theta}=0 \quad \text{(B.11)}$$

If we subtract equation B.11 from the decomposed continuity equation, we get:

Fluctuation Continuity Equation:

$$\frac{\partial u}{\partial x}+\frac{1}{r}\frac{\partial (rv)}{\partial r}+\frac{1}{r}\frac{\partial w}{\partial \theta}=0 \quad \text{(B.12)}$$

$$\frac{\partial u}{\partial x}+\frac{1}{r}\frac{\partial (rv)}{\partial r}+\frac{1}{r}\frac{\partial w}{\partial \theta}=0 \quad \xrightarrow{\times u_i} \quad \begin{cases} u\dfrac{\partial u}{\partial x}+\dfrac{u}{r}\dfrac{\partial (rv)}{\partial r}+\dfrac{u}{r}\dfrac{\partial w}{\partial \theta}=0 \\ v\dfrac{\partial u}{\partial x}+\dfrac{v}{r}\dfrac{\partial (rv)}{\partial r}+\dfrac{v}{r}\dfrac{\partial w}{\partial \theta}=0 \\ w\dfrac{\partial u}{\partial x}+\dfrac{w}{r}\dfrac{\partial (rv)}{\partial r}+\dfrac{w}{r}\dfrac{\partial w}{\partial \theta}=0 \end{cases}$$

using chain rule:

$$\Rightarrow \begin{cases} \left(\dfrac{\partial u^2}{\partial x}-u\dfrac{\partial u}{\partial x}\right)+\left(\dfrac{1}{r}\dfrac{\partial (ruv)}{\partial r}-v\dfrac{\partial u}{\partial r}\right)+\left(\dfrac{1}{r}\dfrac{\partial (uw)}{\partial \theta}-\dfrac{w}{r}\dfrac{\partial u}{\partial \theta}\right)=0 \\ \left(\dfrac{\partial (uv)}{\partial x}-u\dfrac{\partial v}{\partial x}\right)+\left(\dfrac{1}{r}\dfrac{\partial (rv^2)}{\partial r}-v\dfrac{\partial v}{\partial r}\right)+\left(\dfrac{1}{r}\dfrac{\partial (vw)}{\partial \theta}-\dfrac{w}{r}\dfrac{\partial v}{\partial \theta}\right)=0 \\ \left(\dfrac{\partial (uw)}{\partial x}-u\dfrac{\partial w}{\partial x}\right)+\left(\dfrac{1}{r}\dfrac{\partial (rvw)}{\partial r}-v\dfrac{\partial w}{\partial r}\right)+\left(\dfrac{1}{r}\dfrac{\partial (w^2)}{\partial \theta}-\dfrac{w}{r}\dfrac{\partial w}{\partial \theta}\right)=0 \end{cases}$$

$$\Rightarrow \begin{cases} u\dfrac{\partial u}{\partial x}+v\dfrac{\partial u}{\partial r}+\dfrac{w}{r}\dfrac{\partial u}{\partial \theta}=\dfrac{\partial u^2}{\partial x}+\dfrac{1}{r}\dfrac{\partial (ruv)}{\partial r}+\dfrac{1}{r}\dfrac{\partial (uw)}{\partial \theta} \\ u\dfrac{\partial v}{\partial x}+v\dfrac{\partial v}{\partial r}+\dfrac{w}{r}\dfrac{\partial v}{\partial \theta}=\dfrac{\partial (uv)}{\partial x}+\dfrac{1}{r}\dfrac{\partial (rv^2)}{\partial r}+\dfrac{1}{r}\dfrac{\partial (vw)}{\partial \theta} \\ u\dfrac{\partial w}{\partial x}+v\dfrac{\partial w}{\partial r}+\dfrac{w}{r}\dfrac{\partial w}{\partial \theta}=\dfrac{\partial (uw)}{\partial x}+\dfrac{1}{r}\dfrac{\partial (rvw)}{\partial r}+\dfrac{1}{r}\dfrac{\partial (w^2)}{\partial \theta} \end{cases} \quad \text{(B.13)}$$

By substituting the averaged fluctuations in equations B.8 to B.10 with the new parameters in equation B.13, we will have *averaged momentum equations* in cylindrical coordinate as:

Averaged Momentum Equation in Axial Direction:

$$U\frac{\partial U}{\partial x}+V\frac{\partial U}{\partial r}+\frac{W}{r}\frac{\partial U}{\partial \theta}=-\frac{1}{\rho_o}\frac{\partial P_m}{\partial x}+\frac{2}{\rho_o}\nabla.(\mu S_x) \\ -\left\langle \frac{\partial u^2}{\partial x}+\frac{\partial (uv)}{\partial r}+\frac{1}{r}\frac{\partial (uw)}{\partial \theta}+\frac{uv}{r}\right\rangle + g\,\beta\,(T-T_{ref}) \quad \text{(B.14)}$$

Averaged Momentum Equation in Radial Direction:

$$U\frac{\partial V}{\partial x}+V\frac{\partial V}{\partial r}+\frac{W}{r}\frac{\partial V}{\partial \theta}-\frac{W^2}{r}=-\frac{1}{\rho_o}\frac{\partial P_m}{\partial r}+\frac{2}{\rho_o}\nabla.(\mu S_r) \\ -\left\langle \frac{\partial (uv)}{\partial x}+\frac{\partial v^2}{\partial r}+\frac{1}{r}\frac{\partial (vw)}{\partial \theta}-\frac{w^2-v^2}{r}\right\rangle \quad \text{(B.15)}$$

Averaged Momentum Equation in Tangential Direction:

$$U\frac{\partial W}{\partial x}+V\frac{\partial W}{\partial r}+\frac{W}{r}\frac{\partial W}{\partial \theta}+\frac{VW}{r}=-\frac{1}{\rho_o}\left(\frac{1}{r}\frac{\partial P_m}{\partial \theta}\right)+\frac{2}{\rho_o}\nabla.(\mu S_\theta) \\ -\left\langle \frac{\partial (uw)}{\partial x}+\frac{\partial (vw)}{\partial r}+\frac{1}{r}\frac{\partial w^2}{\partial \theta}+2\frac{vw}{r}\right\rangle \quad \text{(B.16)}$$

For a statistically homogeneous flow in tangential direction ($\partial/\partial\theta = 0$), the averaged continuity and momentum equations in an incompressible, high *Reynolds number*, turbulent, round jet flow with swirl can be reduced to the equation below:

Averaged Continuity Equation:

$$\frac{\partial U}{\partial x}+\frac{1}{r}\frac{\partial (rV)}{\partial r}=0 \quad \text{(B.17)}$$

Averaged Momentum Equation in Axial Direction:

$$U\frac{\partial U}{\partial x}+V\frac{\partial U}{\partial r}=-\frac{1}{\rho_o}\frac{\partial P_m}{\partial x}+\frac{1}{\rho_o}\left[2\frac{\partial}{\partial x}\left(\mu\frac{\partial U}{\partial x}\right)+\frac{1}{r}\frac{\partial}{\partial r}\left(r\mu(\frac{\partial U}{\partial r}+\frac{\partial V}{\partial x})\right)\right] \\ -\left\langle \frac{\partial u^2}{\partial x}+\frac{\partial (uv)}{\partial r}+\frac{uv}{r}\right\rangle + g\,\beta\,(T-T_{ref}) \quad \text{(B.18)}$$

Averaged Momentum Equation in Radial Direction:

$$U\frac{\partial V}{\partial x}+V\frac{\partial V}{\partial r}-\frac{W^2}{r}=-\frac{1}{\rho_o}\frac{\partial P_m}{\partial r}+\frac{1}{\rho_o}\left[\frac{\partial}{\partial x}\left(\mu(\frac{\partial U}{\partial r}+\frac{\partial V}{\partial x})\right)+2\frac{1}{r}\frac{\partial}{\partial r}\left(r\mu\frac{\partial V}{\partial r}\right)-2\mu\frac{V}{r^2}\right] \\ -\left\langle \frac{\partial (uv)}{\partial x}+\frac{\partial v^2}{\partial r}-\frac{w^2-v^2}{r}\right\rangle \quad \text{(B.19)}$$

Averaged Momentum Equation in Tangential Direction:

$$U\frac{\partial W}{\partial x}+V\frac{\partial W}{\partial r}+\frac{VW}{r}=\frac{1}{\rho_o}\left[\frac{\partial}{\partial x}\left(\mu\frac{\partial W}{\partial x}\right)+\frac{1}{r^2}\frac{\partial}{\partial r}\left(\mu r^3\frac{\partial}{\partial r}(\frac{W}{r})\right)\right] \\ -\left\langle \frac{\partial (uw)}{\partial x}+\frac{\partial (vw)}{\partial r}+2\frac{vw}{r}\right\rangle \quad \text{(B.20)}$$

B.2 Transport Equations For Reynolds Stresses

In order to calculate the transport equations for Reynolds stresses in an incompressible, high-Reynolds number flow, we subtract instantaneous momentum equations (B.2,B.3 and B.4) from averaged momentum equations (B.8, B.9 and B.10):

$$U\frac{\partial u}{\partial x}+V\frac{\partial u}{\partial r}+\frac{W}{r}\frac{\partial u}{\partial \theta}=-\frac{1}{\rho_o}\frac{\partial p}{\partial x}+\frac{2}{\rho_o}\nabla.(\mu s'_x)-\left\{u\frac{\partial U}{\partial x}+v\frac{\partial U}{\partial r}+\frac{w}{r}\frac{\partial U}{\partial \theta}\right\}$$
$$-\left\{\left(u\frac{\partial u}{\partial x}+v\frac{\partial u}{\partial r}+\frac{w}{r}\frac{\partial u}{\partial \theta}\right)-\left\langle u\frac{\partial u}{\partial x}+v\frac{\partial u}{\partial r}+\frac{w}{r}\frac{\partial u}{\partial \theta}\right\rangle\right\}+g\beta t' \quad \text{(B.21)}$$

$$U\frac{\partial v}{\partial x}+V\frac{\partial v}{\partial r}+\frac{W}{r}\frac{\partial v}{\partial \theta}-W\frac{w}{r}=-\frac{1}{\rho_o}\frac{\partial p}{\partial r}+\frac{2}{\rho_o}\nabla.(\mu s'_r)-\left\{u\frac{\partial V}{\partial x}+v\frac{\partial V}{\partial r}+\frac{w}{r}\frac{\partial V}{\partial \theta}-w\frac{W}{r}\right\}$$
$$-\left\{\left(u\frac{\partial v}{\partial x}+v\frac{\partial v}{\partial r}+\frac{w}{r}\frac{\partial v}{\partial \theta}-\frac{w^2}{r}\right)-\left\langle u\frac{\partial v}{\partial x}+v\frac{\partial v}{\partial r}+\frac{w}{r}\frac{\partial v}{\partial \theta}-\frac{w^2}{r}\right\rangle\right\} \quad \text{(B.22)}$$

$$U\frac{\partial w}{\partial x}+V\frac{\partial w}{\partial r}+\frac{W}{r}\frac{\partial w}{\partial \theta}+V\frac{w}{r}=-\frac{1}{\rho_o}\left(\frac{1}{r}\frac{\partial p}{\partial \theta}\right)+\frac{2}{\rho_o}\nabla.(\mu s'_\theta)-\left\{u\frac{\partial W}{\partial x}+v\frac{\partial W}{\partial r}+\frac{w}{r}\frac{\partial W}{\partial \theta}+v\frac{W}{r}\right\}$$
$$-\left\{\left(u\frac{\partial w}{\partial x}+v\frac{\partial w}{\partial r}+\frac{w}{r}\frac{\partial w}{\partial \theta}+\frac{vw}{r}\right)-\left\langle u\frac{\partial w}{\partial x}+v\frac{\partial w}{\partial r}+\frac{w}{r}\frac{\partial w}{\partial \theta}+\frac{vw}{r}\right\rangle\right\} \quad \text{(B.23)}$$

where t' and s' are the fluctuating terms. To create *Reynolds Stress Equations* we multiply each equation above with a fluctuating component, then taking average and adding combination of two equations. Using the continuity equation simplifies some terms:

- Avg ($u\times$ Eqn B.21) + Avg ($u\times$ Eqn B.21)

$$U\frac{\partial\overline{u^2}}{\partial x}+V\frac{\partial\overline{u^2}}{\partial r}+\frac{W}{r}\frac{\partial\overline{u^2}}{\partial \theta} = -\frac{2}{\rho_o}\left\{\frac{\partial\overline{pu}}{\partial x}-<p\frac{\partial u}{\partial x}>\right\}+\frac{2}{\rho_o}<2u\nabla.(\mu s'_x)>$$
$$-2\left\{\overline{u^2}\frac{\partial U}{\partial x}+\overline{uv}\frac{\partial U}{\partial r}+\frac{\overline{uw}}{r}\frac{\partial U}{\partial \theta}\right\}-\left\{\frac{\partial\overline{u^3}}{\partial x}+\frac{1}{r}\frac{\partial\, r\overline{u^2v}}{\partial r}+\frac{1}{r}\frac{\partial u^2w}{\partial \theta}\right\}+2g\beta\overline{ut'} \quad \text{(B.24)}$$

- Avg($v\times$ Eeq.B.22) + Avg($v\times$ Eqn.B.22)

$$U\frac{\partial\overline{v^2}}{\partial x}+V\frac{\partial\overline{v^2}}{\partial r}+\frac{W}{r}\frac{\partial\overline{v^2}}{\partial \theta}-2W\frac{\overline{vw}}{r} = -\frac{2}{\rho_o}\left\{\frac{\partial\overline{pv}}{\partial r}-<p\frac{\partial v}{\partial r}>\right\}+\frac{2}{\rho_o}<2v\nabla.(\mu s'_r)>$$
$$-2\left\{\overline{uv}\frac{\partial V}{\partial x}+\overline{v^2}\frac{\partial V}{\partial r}+\frac{\overline{vw}}{r}\frac{\partial V}{\partial \theta}-\overline{vw}\frac{W}{r}\right\}-\left\{\frac{\partial\overline{uv^2}}{\partial x}+\frac{1}{r}\frac{\partial\, r\overline{v^3}}{\partial r}+\frac{1}{r}\frac{\partial\overline{v^2w}}{\partial\,\theta}-2\frac{\overline{vw^2}}{r}\right\} \quad \text{(B.25)}$$

- Avg($w\times$ Eeq.B.23) + Avg($w\times$ Eqn.B.23)

$$U\frac{\partial\overline{w^2}}{\partial x}+V\frac{\partial\overline{w^2}}{\partial r}+\frac{W}{r}\frac{\partial\overline{w^2}}{\partial\theta}+2V\frac{\overline{w^2}}{r}=-\frac{2}{r\,\rho_o}\left\{\frac{\partial\overline{pw}}{\partial\theta}-<p\frac{\partial w}{\partial\theta}>\right\}+\frac{2}{\rho_o}<2w\nabla.(\mu s'_\theta)>$$
$$-2\left\{\overline{uw}\frac{\partial W}{\partial x}+\overline{vw}\frac{\partial W}{\partial r}+\frac{\overline{w^2}}{r}\frac{\partial W}{\partial\theta}+\overline{vw}\frac{W}{r}\right\}-\left\{\frac{\partial\overline{uw^2}}{\partial x}+\frac{1}{r}\frac{\partial r\overline{vw^2}}{\partial r}+\frac{1}{r}\frac{\partial\overline{w^3}}{\partial\theta}+2\frac{\overline{vw^2}}{r}\right\} \tag{B.26}$$

- Avg($v\times$ Eeq.B.21) + Avg($u\times$ Eqn.B.22)

$$U\frac{\partial\overline{uv}}{\partial x}+V\frac{\partial\overline{uv}}{\partial r}+\frac{W}{r}\frac{\partial\overline{uv}}{\partial\theta}-W\frac{\overline{uw}}{r}\;=\;-\frac{1}{\rho_o}\left\{\frac{\partial\overline{pv}}{\partial x}+\frac{\partial\overline{pu}}{\partial r}\right\}$$
$$+\frac{1}{\rho_o}\left\{<p\frac{\partial v}{\partial x}>+<p\frac{\partial u}{\partial r}>\right\}+\frac{2}{\rho_o}\left\{<v\nabla.(\mu s'_x)>+<u\nabla.(\mu s'_r)>\right\}$$
$$-\left\{\overline{uv}\frac{\partial U}{\partial x}+\overline{v^2}\frac{\partial U}{\partial r}+\frac{\overline{vw}}{r}\frac{\partial U}{\partial\theta}+\overline{u^2}\frac{\partial V}{\partial x}+\overline{uv}\frac{\partial V}{\partial r}+\frac{\overline{uw}}{r}\frac{\partial V}{\partial\theta}-\overline{uw}\frac{W}{r}\right\}$$
$$-\left\{\frac{\partial\overline{u^2v}}{\partial x}+\frac{1}{r}\frac{\partial r\,\overline{uv^2}}{\partial r}+\frac{1}{r}\frac{\partial uvw}{\partial\theta}-\frac{\overline{uw^2}}{r}\right\}+g\beta\overline{vt'} \tag{B.27}$$

- Avg($w\times$ Eeq.B.21) + Avg($u\times$ Eqn.B.23)

$$U\frac{\partial\overline{uw}}{\partial x}+V\frac{\partial\overline{uw}}{\partial r}+\frac{W}{r}\frac{\partial\overline{uw}}{\partial\theta}+V\frac{\overline{uw}}{r}\;=\;-\frac{1}{\rho_o}\left\{\frac{\partial\overline{pw}}{\partial x}+\frac{1}{r}\frac{\partial\overline{pu}}{\partial\theta}\right\}$$
$$+\frac{1}{\rho_o}\left\{<p\frac{\partial w}{\partial x}>+\frac{1}{r}<p\frac{\partial u}{\partial\theta}>\right\}+\frac{2}{\rho_o}\left\{<w\nabla.(\mu s'_x)>+<u\nabla.(\mu s'_\theta)>\right\}$$
$$-\left\{\overline{uw}\frac{\partial U}{\partial x}+\overline{vw}\frac{\partial U}{\partial r}+\frac{\overline{w^2}}{r}\frac{\partial U}{\partial\theta}+\overline{u^2}\frac{\partial W}{\partial x}+\overline{uv}\frac{\partial W}{\partial r}+\frac{\overline{uw}}{r}\frac{\partial W}{\partial\theta}+\overline{uv}\frac{W}{r}\right\}$$
$$-\left\{\frac{\partial\overline{u^2w}}{\partial x}+\frac{1}{r}\frac{\partial r\,\overline{uvw}}{\partial r}+\frac{1}{r}\frac{\partial uw^2}{\partial\theta}+\frac{\overline{uvw}}{r}\right\}+g\beta\overline{wt'} \tag{B.28}$$

- Avg($w\times$ Eeq.B.22) + Avg($v\times$ Eqn.B.23)

$$U\frac{\partial\overline{vw}}{\partial x}+V\frac{\partial\overline{vw}}{\partial r}+\frac{W}{r}\frac{\partial\overline{vw}}{\partial\theta}-W\frac{\overline{w^2}}{r}+V\frac{\overline{vw}}{r}\;=\;-\frac{1}{\rho_o}\left\{\frac{\partial\overline{pw}}{\partial r}+\frac{1}{r}\frac{\partial\overline{pv}}{\partial\theta}\right\}$$
$$+\frac{1}{\rho_o}\left\{<p\frac{\partial w}{\partial r}>+\frac{1}{r}<p\frac{\partial v}{\partial\theta}>\right\}+\frac{2}{\rho_o}\left\{<v\nabla.(\mu s'_\theta)>+<w\nabla.(\mu s'_r)>\right\}$$
$$-\left\{\overline{uw}\frac{\partial V}{\partial x}+\overline{vw}\frac{\partial V}{\partial r}+\frac{\overline{w^2}}{r}\frac{\partial V}{\partial\theta}+\overline{uv}\frac{\partial W}{\partial x}+\overline{v^2}\frac{\partial W}{\partial r}+\frac{\overline{vw}}{r}\frac{\partial W}{\partial\theta}+(\overline{v^2}-\overline{w^2})\frac{W}{r}\right\}$$
$$-\left\{\frac{\partial\overline{uvw}}{\partial x}+\frac{1}{r}\frac{\partial r\,\overline{v^2w}}{\partial r}+\frac{1}{r}\frac{\partial vw^2}{\partial\theta}+\frac{\overline{v^2w}}{r}-\frac{\overline{w^3}}{r}\right\} \tag{B.29}$$

The equation for the turbulence kinetic energy in cylindrical coordinate can be obtained directly from the normal Reynolds stress equations by adding them and defining k, the average fluctuating kinetic energy per unit mass, as:

$$k \equiv \frac{1}{2}\overline{q^2} = \frac{1}{2}[\overline{u^2}+\overline{v^2}+\overline{w^2}] \tag{B.30}$$

The incompressibility condition (B.1) is used to eliminate the pressure-strain rate term.

Turbulence kinetic energy equation:

$$\begin{aligned}
&U\frac{\partial k}{\partial x}+V\frac{\partial k}{\partial r}+\frac{W}{r}\frac{\partial k}{\partial \theta}-W\frac{\overline{vw}}{r}+V\frac{\overline{w^2}}{r} = \\
&-\frac{1}{\rho_o}\left\{\frac{\partial \overline{pu}}{\partial x}+\frac{1}{r}\frac{\partial (r\overline{pv})}{\partial r}+\frac{1}{r}\frac{\partial \overline{pw}}{\partial \theta}\right\} - \frac{1}{2}\left\{\frac{\partial \overline{uq^2}}{\partial x}+\frac{1}{r}\frac{\partial (r\overline{vq^2})}{\partial r}+\frac{1}{r}\frac{\partial \overline{wq^2}}{\partial \theta}\right\}+\frac{2}{\rho_o}\nabla.\mu<\vec{\mathbf{v}}s_{ij}> \\
&-\left\{\overline{u^2}\frac{\partial U}{\partial x}+\overline{uv}\frac{\partial U}{\partial r}+\frac{\overline{uw}}{r}\frac{\partial U}{\partial \theta}+\overline{uv}\frac{\partial V}{\partial x}+\overline{v^2}\frac{\partial V}{\partial r}+\frac{\overline{vw}}{r}\frac{\partial V}{\partial \theta}+\overline{uw}\frac{\partial W}{\partial x}+\overline{vw}\frac{\partial W}{\partial r}+\frac{\overline{w^2}}{r}\frac{\partial W}{\partial \theta}\right\} \\
&\qquad -\frac{2}{\rho_o}\mu<\overline{s_{ij}s_{ij}}> \quad + \quad g\beta\overline{ut'}
\end{aligned} \tag{B.31}$$

In this equation we split the viscous term into the turbulence transport (or divergence) term and dissipation term as below:

- **Transport of kinetic energy due to viscous stresses:**

$$\begin{aligned}
\frac{2}{\rho_o}\nabla.\mu<\vec{\mathbf{v}}s_{ij}> \equiv & \frac{\partial}{\partial x}\frac{\mu}{\rho_o}\left\{\frac{\partial k}{\partial x}+\frac{\partial \overline{u^2}}{\partial x}+\frac{1}{r}\frac{\partial r\overline{uv}}{\partial r}+\frac{1}{r}\frac{\partial \overline{uw}}{\partial \theta}\right\} \\
&+\frac{1}{r}\frac{\partial}{\partial r}\frac{\mu}{\rho_o}r\left\{\frac{\partial k}{\partial r}+\frac{\partial \overline{uv}}{\partial x}+\frac{1}{r}\frac{\partial r\overline{v^2}}{\partial r}+\frac{1}{r}\frac{\partial \overline{vw}}{\partial \theta}-\frac{\overline{w^2}}{r}\right\} \\
&+\frac{1}{r}\frac{\partial}{\partial \theta}\frac{\mu}{\rho_o}\left\{\frac{\partial k}{\partial \theta}+\frac{\partial \overline{uw}}{\partial x}+\frac{1}{r}\frac{\partial r\overline{vw}}{\partial r}+\frac{1}{r}\frac{\partial \overline{w^2}}{\partial \theta}+\frac{\overline{vw}}{r}\right\}
\end{aligned} \tag{B.32}$$

- **Rate of dissipation of turbulence kinetic energy:**

$$\begin{aligned}
-\epsilon \equiv -\frac{2}{\rho_o}\mu<\overline{s_{ij}s_{ij}}> = -\frac{\mu}{\rho_o}\Bigg\langle & 2\left(\frac{\partial u}{\partial x}\right)^2+2\left(\frac{\partial v}{\partial r}\right)^2-2\frac{v^2}{r^2}+2\left(\frac{1}{r}\frac{\partial w}{\partial \theta}\right)^2 \\
&\left(\frac{\partial v}{\partial x}+\frac{\partial u}{\partial r}\right)^2+\left(\frac{1}{r}\frac{\partial v}{\partial \theta}+r\frac{\partial}{\partial r}(\frac{w}{r})\right)^2+\left(\frac{\partial w}{\partial x}+\frac{1}{r}\frac{\partial u}{\partial \theta}\right)^2\Bigg\rangle
\end{aligned} \tag{B.33}$$

B.3 Averaged Energy Equation

General energy equation in cylindrical coordinate for a steady state incompressible flow is calculated using equation 8.32 in chapter 8 as below. We also neglect the density change due to pressure changes since the flows we are interested in are subsonic flows.

Energy equation

$$\rho_o C_p \left(\tilde{v}_x \frac{\partial \tilde{T}}{\partial x} + \tilde{v}_r \frac{\partial \tilde{T}}{\partial r} + \frac{1}{r} \tilde{v}_\theta \frac{\partial \tilde{T}}{\partial \theta} \right) \; = \; \nabla.(\kappa \, \nabla \tilde{T}) \; + \; \mu \, \tilde{\Phi} \tag{B.34}$$

The Laplacian operator and dissipation function are defined as:

$$\nabla.(\kappa \, \nabla \tilde{T}) = \frac{\partial}{\partial x} \left(\kappa \frac{\partial \tilde{T}}{\partial x} \right) + \frac{1}{r} \frac{\partial}{\partial r} \left(\kappa r \frac{\partial \tilde{T}}{\partial r} \right) + \frac{1}{r^2} \frac{\partial}{\partial \theta} \left(\kappa \frac{\partial \tilde{T}}{\partial \theta} \right) \tag{B.35}$$

$$\begin{aligned} \tilde{\Phi} \; = \; 2 \left(\frac{\partial \tilde{v}_r}{\partial r} \right)^2 \; + \; \frac{2}{r^2} \left(\frac{\partial \tilde{v}_\theta}{\partial \theta} + \tilde{v}_r \right)^2 \; + \; 2 \left(\frac{\partial \tilde{v}_x}{\partial x} \right)^2 + \left(\frac{\partial \tilde{v}_\theta}{\partial r} - \frac{\tilde{v}_\theta}{r} + \frac{1}{r} \, \frac{\partial \tilde{v}_r}{\partial \theta} \right)^2 \\ + \; \left(\frac{1}{r} \, \frac{\partial \tilde{v}_x}{\partial \theta} + \frac{\partial \tilde{v}_\theta}{\partial x} \right)^2 + \left(\frac{\partial \tilde{v}_r}{\partial x} + \frac{\partial \tilde{v}_x}{\partial r} \right)^2 \; + \; \frac{2}{3} \; (\nabla.\vec{\mathbf{v}} \,)^2 \end{aligned} \tag{B.36}$$

All the fluid properties in this equation are depend on the temperature fluctuation. To perform a numerical computation, one should consider calculating the correlation of fluctuating viscosity, thermal conductivity and specific heat with respect to the local velocity and temperature. In this study we are just performing the Reynolds decomposition on velocity and temperature and pressure as in the momentum equations. Low velocity in the flow ($M << 1$) helps us to neglect the heat generation due to viscous dissipation and omit the last term of the energy equation.

Averaged Energy equation

$$\begin{aligned} U \frac{\partial T}{\partial x} + V \frac{\partial T}{\partial r} + \frac{W}{r} \frac{\partial T}{\partial \theta} \; = \; \frac{\partial}{\partial x} \left(\alpha \frac{\partial T}{\partial x} - \overline{ut'} \right) + \frac{1}{r} \frac{\partial}{\partial r} \left(\alpha r \frac{\partial T}{\partial r} - r \, \overline{vt'} \right) \\ + \frac{1}{r^2} \frac{\partial}{\partial \theta} \left(\alpha \frac{\partial \tilde{T}}{\partial \theta} - r \, \overline{wt'} \right) \end{aligned} \tag{B.37}$$

The equation governing the transport of the temperature fluctuation can be derived, similar to the Reynolds stress equations, by subtracting the mean energy equation B.37 from the instantaneous energy equation B.34, then multiplying with the fluctuating temperature (t') and averaging them. The result will be:

Mean square fluctuating temperature equation

$$\begin{aligned} U \frac{\partial \overline{t'^2}}{\partial x} + V \frac{\partial \overline{t'^2}}{\partial r} + \frac{W}{r} \frac{\partial \overline{t'^2}}{\partial \theta} \; = \; \frac{\partial}{\partial x} \left(\alpha \frac{\partial \overline{t'^2}}{\partial x} - \overline{ut'^2} \right) + \frac{1}{r} \frac{\partial}{\partial r} \left(\alpha r \frac{\partial \overline{t'^2}}{\partial r} - r \, \overline{vt'^2} \right) \\ + \frac{1}{r^2} \frac{\partial}{\partial \theta} \left(\alpha \frac{\partial \overline{t'^2}}{\partial \theta} - r \, \overline{wt'^2} \right) - 2 \left\{ \overline{ut'} \frac{\partial T}{\partial x} + \overline{vt'} \frac{\partial T}{\partial r} + \frac{\overline{wt'}}{r} \frac{\partial T}{\partial \theta} \right\} \\ - 2\alpha \left\{ < \left(\frac{\partial t'}{\partial x} \right)^2 > + < \left(\frac{\partial t'}{\partial r} \right)^2 > + \frac{1}{r^2} < \left(\frac{\partial t'}{\partial \theta} \right)^2 > \right\} \end{aligned} \tag{B.38}$$

Appendix C

Description of Electronic Circuits

The electronic circuits for the temperature measurement were designed and built by Lars Jernqvist, who was formerly the electronics technician for the Department of Thermo Fluids. He has now retired, but continues to help out, and has been of special value to this project.

Figure C.1 shows the schematic for the constant current circuit used for the cold-wire temperature measurements. A small current (approx. 0.1 mA) passes through the thin platinum wire and the output is the amplified voltage ($\times 500$) that is fed to WaveBook A/D convertor. The changes in wire resistance are directly proportional to changes by the wire's temperature according to the relation:

$$R = R_o + \alpha_R R_o (T - T_o). \tag{C.1}$$

where R_o is the wire resistance at the reference temperature, T_o. So the fluctuating output voltage is linearly proportional to the wire temperature when the current is constant. R_o and α_R (or $\alpha_R R_o$) can be obtained by calibration as described in Chapter 11.

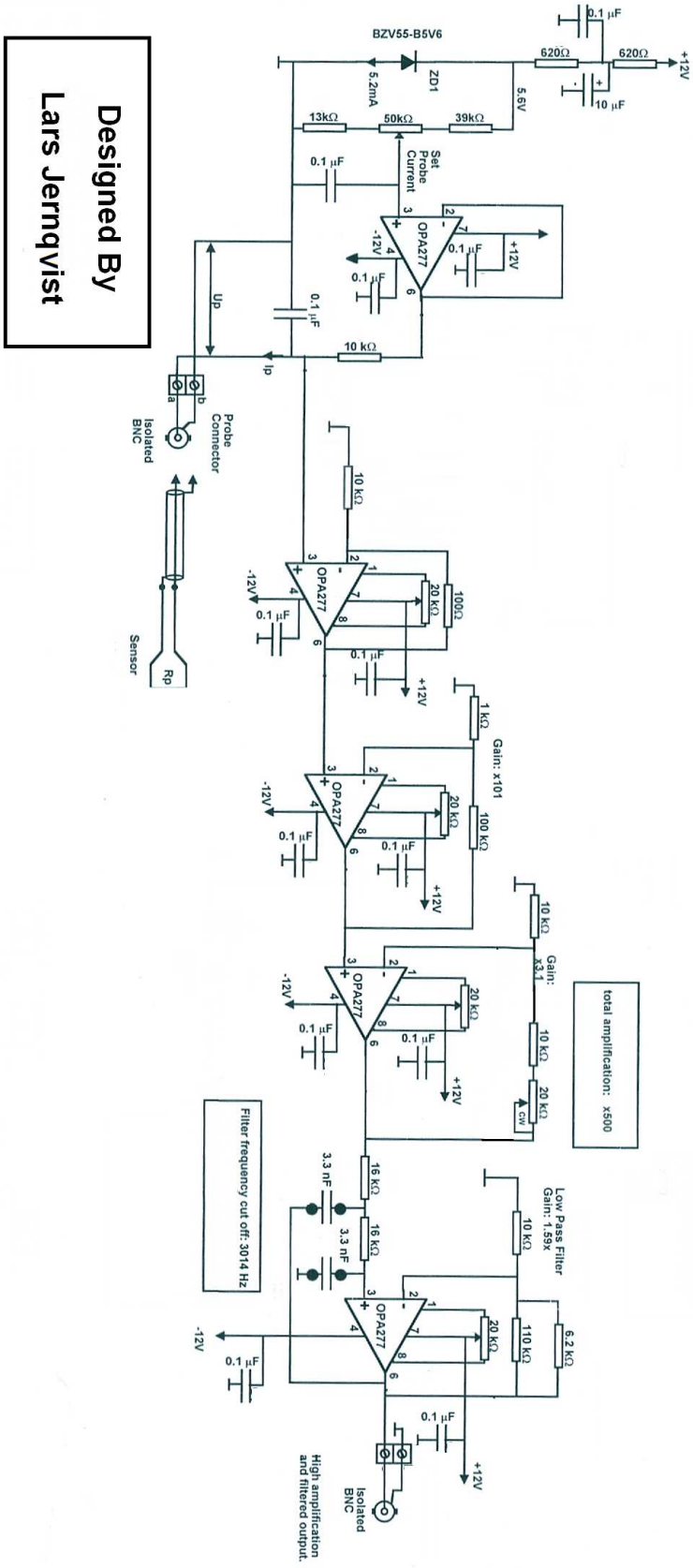

Figure C.1: Constant Current Circuit for Cold-wire.

Appendix D

Scaling Analysis of The Governing Equations

D.0.1 Scaling of the Momentum Equations

An order of magnitude analysis have been applied to the governing equations in order to reduce the terms involved in describing the axisymmetric natural convection boundary layer flow. As the flow adjacent to the wall induced by the buoyancy, the boundary layer generated due to presence of the wall grows. The observations from the experiments suggest that both thermal and velocity boundary layers thickness are smaller than the streamwise length scale of the flow. Therefore the assumption of the thin boundary layer ($\partial/\partial x \ll \partial/\partial r$) is applicable. As in forced boundary layer flow, the streamwise and cross-stream (radial direction) length scales are considered L and δ respectively, where $L \gg \delta$. The velocity and temperature scales as also defined as below:

$$\begin{array}{cccccc} & & & U & \sim & U_s \\ & & & T & \sim & T_s \\ \overline{u^2}, & \overline{v^2}, & \overline{w^2}, & \overline{uv} & \sim & \overline{u_s^2} \\ & & & \overline{ut}, & \overline{vt} & \sim & \overline{u_s t_s} \end{array} \tag{D.1}$$

where U_s is the mean velocity scale in axial direction and T_s is the mean temperature scale. $\overline{u_s^2}$ and $\overline{u_s t_s}$ are also scales for Reynolds stresses and velocity-temperature correlations respectively. The derivatives in the equations are scaled as below:

$$\frac{\partial}{\partial x} \sim \frac{1}{L} \quad ; \quad \frac{\partial}{\partial r} \sim \frac{1}{\delta} \tag{D.2}$$

Substituting in the continuity equation 8.50 we find the mean radial velocity scale as:

$$V_s \sim U_s \frac{\delta}{L} \tag{D.3}$$

Each term in the axial momentum equation 8.51 is represented by its respective scale as below:

$$\begin{array}{ccccccccccccc} U\dfrac{\partial U}{\partial x} & + & V\dfrac{\partial U}{\partial r} & = & -\dfrac{1}{\rho}\dfrac{\partial P}{\partial x} & + & \nu\left(\dfrac{\partial^2 U}{\partial x^2} + \dfrac{\partial^2 U}{\partial r^2} + \dfrac{1}{r}\dfrac{\partial U}{\partial r}\right) & - & \dfrac{\partial \overline{u^2}}{\partial x} & - & \dfrac{\partial \overline{uv}}{\partial r} & - & \dfrac{\overline{uv}}{r} + g\beta(T - T_0) \\ U_s\dfrac{U_s}{L} & & (U_s\dfrac{\delta}{L})\dfrac{U_s}{\delta} & = & ? & & \nu\left(\dfrac{U_s}{L^2} \quad \dfrac{U_s}{\delta^2} \quad \dfrac{1}{\delta}\dfrac{U_s}{\delta}\right) & & \dfrac{u_s^2}{L} & & \dfrac{u_s^2}{\delta} & & \dfrac{u_s^2}{\delta} \quad ? \end{array} \tag{D.4}$$

The same thing is done for the radial momentum equation 8.52:

$$U\frac{\partial V}{\partial x} \quad + \quad V\frac{\partial V}{\partial r} \quad = \quad -\frac{1}{\rho}\frac{\partial P}{\partial r} + \nu\left(\frac{\partial^2 V}{\partial x^2} + \frac{\partial^2 V}{\partial r^2} + \frac{1}{r}\frac{\partial V}{\partial r} - \frac{V}{r^2}\right) - \frac{\partial \overline{uv}}{\partial x} - \frac{\partial \overline{v^2}}{\partial r} - \frac{\overline{v^2}}{r} + \frac{\overline{w^2}}{r}$$

$$U_s\frac{(U_s\delta/L)}{L} \quad (U_s\delta/L)\frac{(U_s\delta/L)}{\delta} \;=\; ? \quad \nu\left(\frac{(U_s\delta/L)}{L^2} \quad \frac{(U_s\delta/L)}{\delta^2} \quad \frac{1}{\delta}\frac{(U_s\delta/L)}{\delta}\right) \quad \frac{u_s^2}{L} \quad \frac{u_s^2}{\delta} \quad \frac{u_s^2}{\delta} \quad \frac{u_s^2}{\delta} \tag{D.5}$$

Note that we took the viscosity out of derivative because we just want to estimate the scale of each term, otherwise this is not a constant viscosity assumption. The order of magnitude of the scalar parameter terms in the equation of motion is unknown for now. To keep the convection terms in the streamwise equation, they should have the order of one in the scaling equation so we divide all terms of two equations by U_s^2/L:

$$1 \quad 1 \quad = \quad ? \quad \left(\frac{1}{Re_L} \quad \frac{L^2}{\delta^2}\frac{1}{Re_L} \quad \frac{L^2}{\delta^2}\frac{1}{Re_L}\right) \quad \frac{u_s^2}{U_s^2} \quad \frac{L}{\delta}\frac{u_s^2}{U_s^2} \quad \frac{L}{\delta}\frac{u_s^2}{U_s^2} \quad ? \tag{D.6}$$

And for the radial momentum equation:

$$\frac{\delta}{L} \quad \frac{\delta}{L} \quad = \quad ? \quad \left(\frac{1}{Re_L}\frac{\delta}{L} \quad \frac{L^2}{\delta^2}\frac{1}{Re_L}\frac{\delta}{L} \quad \frac{L^2}{\delta^2}\frac{1}{Re_L}\frac{\delta}{L} \quad \frac{L^2}{\delta^2}\frac{1}{Re_L}\frac{\delta}{L}\right)$$
$$\frac{u_s^2}{U_s^2} \quad \frac{L}{\delta}\frac{u_s^2}{U_s^2} \quad \frac{L}{\delta}\frac{u_s^2}{U_s^2} \quad \frac{L}{\delta}\frac{u_s^2}{U_s^2} \tag{D.7}$$

where boundary layer Reynolds number defined as:

$$Re_L = \frac{U_s L}{\nu}$$

Now we have to decide which term with the same order of magnitude as 1 to be kept in the equations. In a highly turbulent flow, the condition of $\delta/L < u_s^2/U_s^2$ is acceptable. This means that in equation D.7 the left hand side terms are smaller than the Reynolds stress terms on the right hand side, specially $\partial(\overline{v^2})/\partial r$. If the Reynolds number is considered sufficiently large, the viscous terms are become negligible too. The other term to balance the surviving Reynolds stress gradient has to be the pressure term. Thus the simplified radial momentum equation becomes:

$$0 \quad = \quad -\frac{1}{\rho}\frac{\partial P}{\partial r} - \frac{\partial \overline{v^2}}{\partial r} - \frac{\overline{v^2} - \overline{w^2}}{r} \tag{D.8}$$

$$U\frac{\partial U}{\partial x} + V\frac{\partial U}{\partial r} = -\frac{1}{\rho}\frac{\partial P}{\partial x} + \frac{\partial}{\partial x}\left(\nu\frac{\partial U}{\partial x} - \overline{u^2}\right) + \frac{1}{r}\frac{\partial}{\partial r}\left(r(\nu\frac{\partial U}{\partial r} - \overline{uv}\,)\right) + g\beta(T - T_0) \tag{D.9}$$

Integrating the equation D.8 from r to ∞ yields to:

$$-\frac{1}{\rho}(p - p_\infty) = \overline{v^2} + \int_r^\infty \frac{\overline{v^2} - \overline{w^2}}{r}\, dr \tag{D.10}$$

where p_∞ is the constant hydrostatic ambient pressure at the specific height. For turbulent boundary layer flows the equation D.10 shows that the pressure inside the boundary layer is controlled by the ambient pressure field and the radial Reynolds stress term plays a major role to decrease the pressure with in the boundary layer. This slight cross-stream pressure gradient is responsible for the entrainment of ambient fluid.

Equation D.8 highlighted the important terms in the radial momentum equation and the pressure equation in the flow. Now we can substitute the pressure term in the streamwise momentum equation by taking derivative of equation D.10 with respect to x:

$$-\frac{1}{\rho}\frac{\partial p}{\partial x} = \frac{\partial \overline{v^2}}{\partial x} + \int_r^\infty \frac{1}{r}\left(\frac{\partial \overline{v^2}}{\partial x} - \frac{\partial \overline{w^2}}{\partial x}\right) dr \tag{D.11}$$

The streamwise pressure gradient in the equation D.9 can be replaced by the right hand side of the equation D.11. As we expressed each term of axial momentum equation in the defined velocity and length scales before, the new replaced terms containing $\partial\overline{v^2}/\partial x$ and $\partial\overline{w^2}/\partial x$ are scaled as u_s^2/U_s^2 which is smaller than the radial gradient of the Reynolds stresses in the axial momentum equation by a factor of L/δ. In equation D.9, considering the scaling equation of D.6, all the streamwise gradients are smaller than the radial gradient counterparts, hence we can ignore them. The magnitude of the buoyancy term can not be determined and it should be kept because it is the term responsible for momentum insertion into the flow. By assuming sufficiently large Reynolds number, the viscous terms in the right hand side of the equation also become negligible, but we keep the radial gradient viscous term to have at least one viscous term in the equation. To have a turbulence term, ($\partial r\ \overline{uv}/\partial r$) must stay in the equation, as we require ($L/\delta \gg 1$).

The reduced streamwise momentum equation to the first order becomes:

$$U\frac{\partial U}{\partial x} + V\frac{\partial U}{\partial r} = \frac{1}{r}\frac{\partial}{\partial r}\left(r(\nu\frac{\partial U}{\partial r} - \overline{uv}\ )\right) + g\beta(T - T_0) \tag{D.12}$$

This is the equation that we work with from now on, but we also remember that the other terms are contributing into the equation very little and they are not deleted.

D.0.2 Scaling of the Energy Equations

Finally we scale the energy equation 8.53 with the velocity and length scales as before and the temperature as T_s. Substituting the scaling parameters in the energy equation and normalizing them by convective terms weight (U_sT_s/L), gives the following orders of magnitude for each term:

$$\begin{aligned} U\frac{\partial T}{\partial x} + V\frac{\partial T}{\partial r} &= \frac{\partial}{\partial x}\left(\alpha\frac{\partial T}{\partial x} - \overline{ut}\right) + \frac{1}{r}\frac{\partial}{\partial r}\left(r\ (\alpha\frac{\partial T}{\partial r} - \overline{vt}\ )\right) + \frac{\nu}{C_p}\,\Phi \\ 1 \quad 1 &= \frac{1}{Pe} \quad \frac{u_st_s}{U_sT_s} \quad \frac{1}{Pe}\left(\frac{L}{\delta}\right)^2 \quad \frac{u_st_s}{U_sT_s}\left(\frac{L}{\delta}\right) \quad \frac{1}{ReC_p}\frac{L^2}{T_s}\Phi \end{aligned} \tag{D.13}$$

Where Pe is the Peclet number and defined as:

$$Pe = \frac{U_sL}{\alpha} \tag{D.14}$$

It is obvious that in the right hand side of the equation, the radial gradient terms are L/δ times bigger than the axial gradients, therefore the streamwise conduction term is considerably smaller than the radial component. The viscus dissipation term is also less important in energy equation since the fluid velocity in natural convection flow is slow and the heat generated by viscosity is negligible. Both velocity-temperature correlation terms ($\overline{ut}$ & $\overline{vt}$) are kept for the energy balance integral across the boundary layer. Hence the reduced energy equation to first order becomes:

$$U\frac{\partial T}{\partial x}+V\frac{\partial T}{\partial r}=\frac{1}{r}\frac{\partial}{\partial r}\left(r\,(\alpha\frac{\partial T}{\partial r}-\overline{vt}\,)\right)+\frac{\partial\overline{ut}}{\partial x} \tag{D.15}$$

Appendix E

Correlations of the Instantaneous Data

E.1 Temperature Spectra

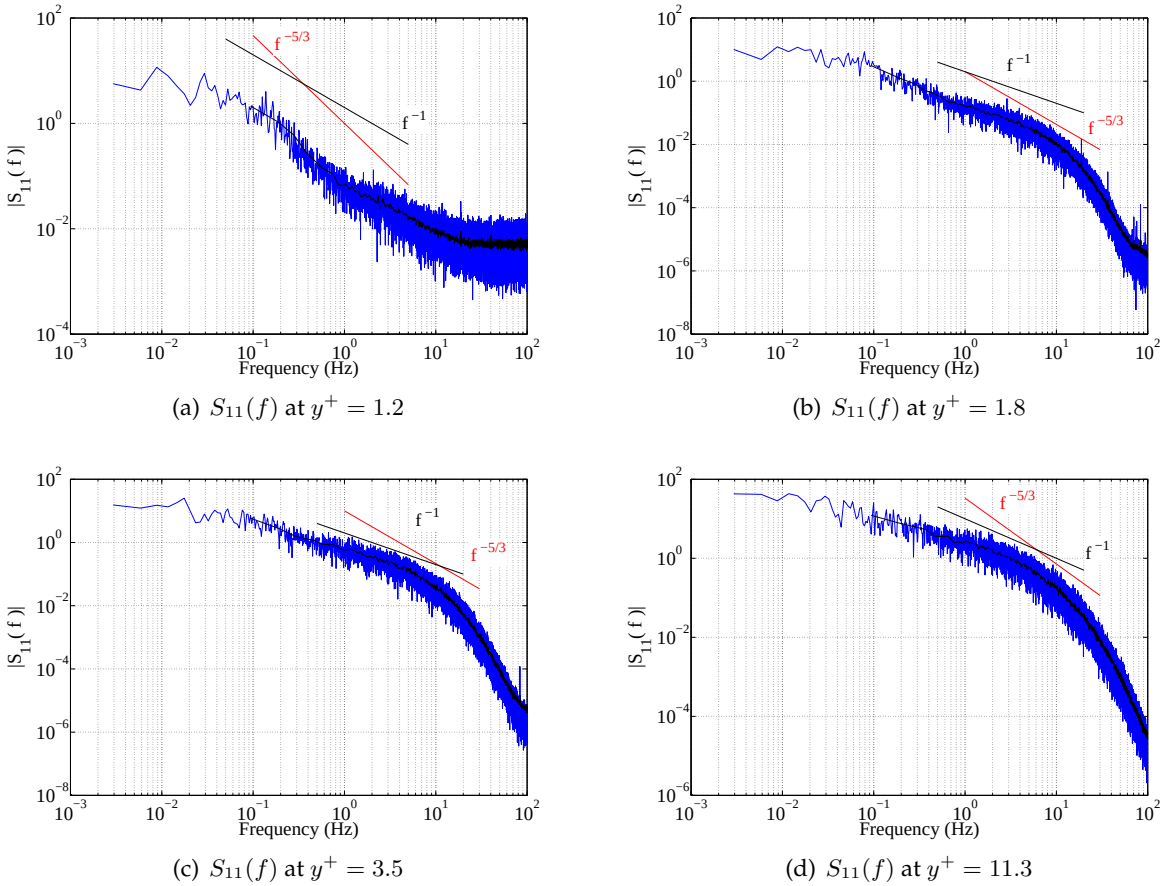

(a) $S_{11}(f)$ at $y^+ = 1.2$

(b) $S_{11}(f)$ at $y^+ = 1.8$

(c) $S_{11}(f)$ at $y^+ = 3.5$

(d) $S_{11}(f)$ at $y^+ = 11.3$

Figure E.1: Instantaneous temperature spectrum in different radial distances from wall, case 1, $4\ m$.

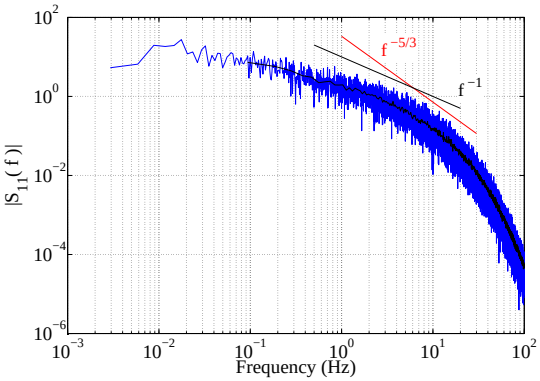

(a) $S_{11}(f)$ at $y^+ = 35.6$

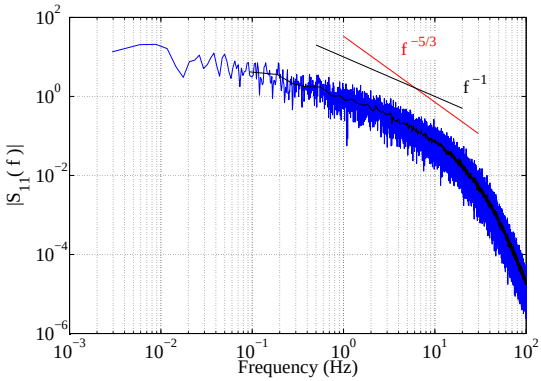

(b) $S_{11}(f)$ at $y^+ = 72$

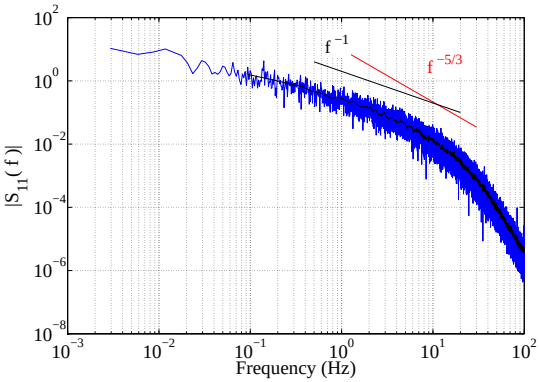

(c) $S_{11}(f)$ at $y^+ = 1943$

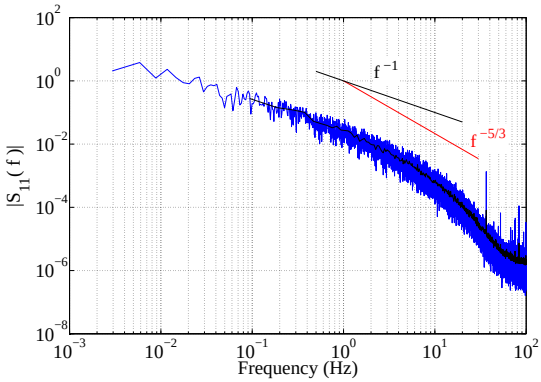

(d) $S_{11}(f)$ at $y^+ = 608$

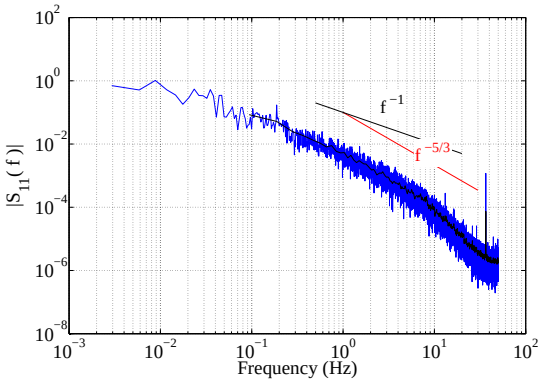

(e) $S_{11}(f)$ at $y^+ = 950$

Figure E.2: Instantaneous temperature spectrum in different radial distances from wall, case 1, $4\ m$.(continue)

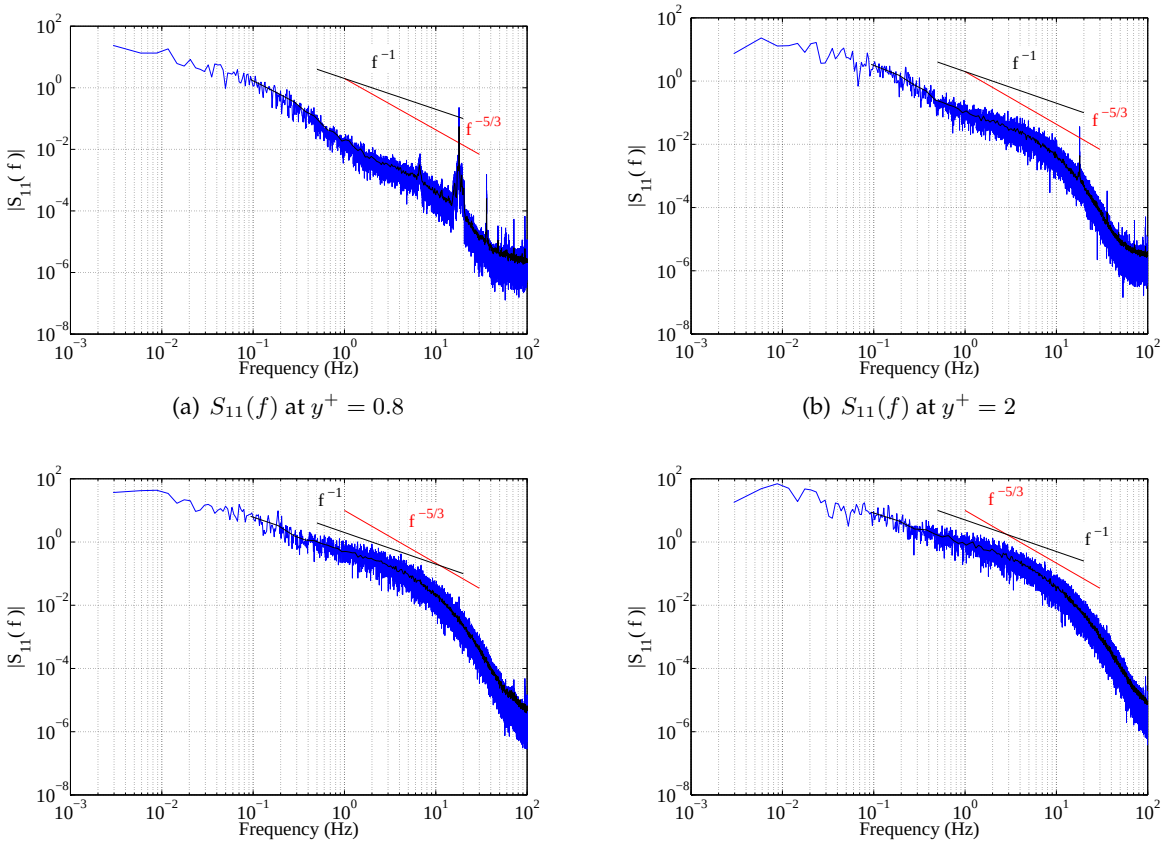

(a) $S_{11}(f)$ at $y^+ = 0.8$

(b) $S_{11}(f)$ at $y^+ = 2$

(c) $S_{11}(f)$ at $y^+ = 4.7$

(d) $S_{11}(f)$ at $y^+ = 9.5$

Figure E.3: Instantaneous temperature spectrum in different radial distances from wall, case 2, 3 m.

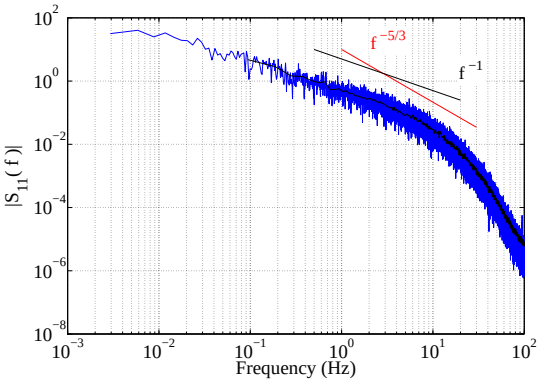

(a) $S_{11}(f)$ at $y^+ = 32$

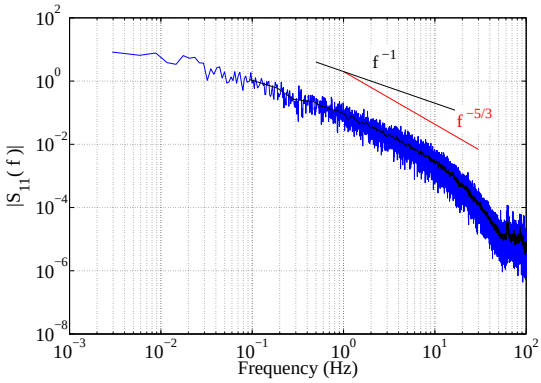

(b) $S_{11}(f)$ at $y^+ = 137$

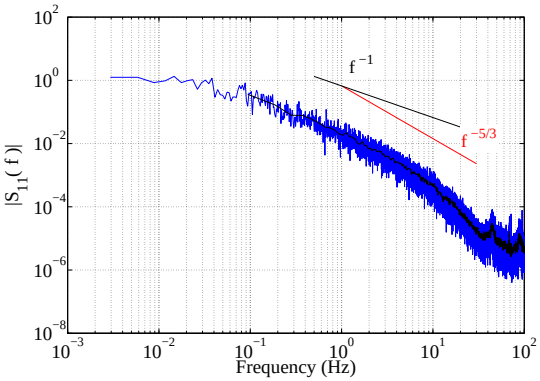

(c) $S_{11}(f)$ at $y^+ = 242$

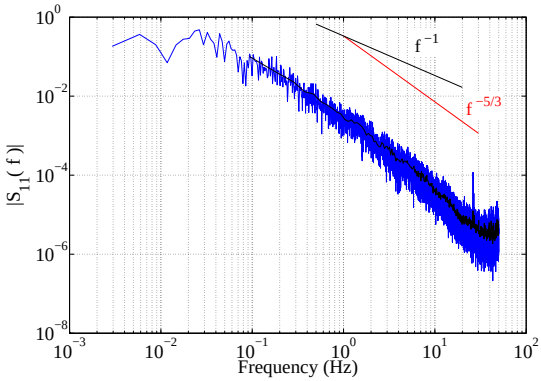

(d) $S_{11}(f)$ at $y^+ = 512$

Figure E.4: Instantaneous temperature spectrum in different radial distances from wall, case 2, 3 m.(continue)

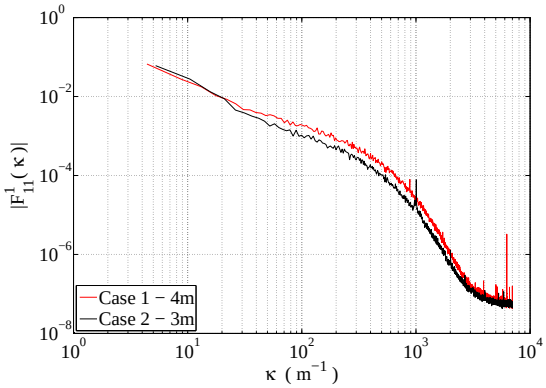

(a) $F^1_{11}(\kappa)$ at $y^+ = 2$

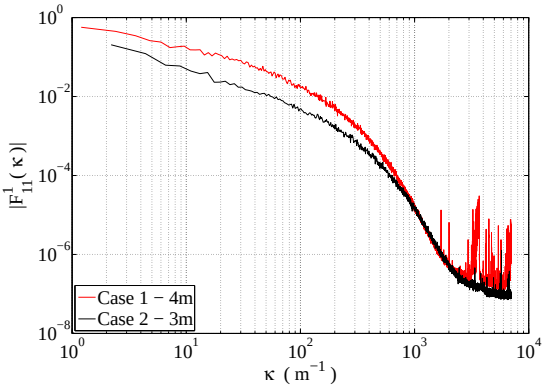

(b) $F^1_{11}(\kappa)$ at $y^+ = 35$

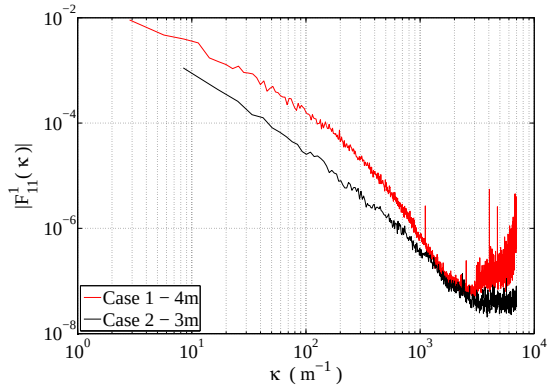

(c) $F^1_{11}(\kappa)$ at $y^+ = 600$

Figure E.5: Comparison of the instantaneous temperature wavenumber spectra in the same normalized radial distances from wall for two cases of $4\ m$ and $3\ m$.

E.2 Cross-correlations of Temperature-Velocity Signal

Table E.1: Cross-Correlation values in positive side, for $case1$ ($4m$ height).

Position	$R_{<ut>}$ $(\tau = 0)$	$R_{<ut>}$ peak	PTL† (ms)	$R_{<vt>}$ $(\tau = 0)$	$R_{<vt>}$ peak	PTL (ms)
$y^+ = 1.4$	0.005	–	–	−0.0017	–	–
$y^+ = 2$	0.0132	0.0182	44	−0.0074	−0.00894	39.7
$y^+ = 3.8$	0.0493	0.0579	32.5	−0.0213	−0.02354	30.2
$y^+ = 12$	0.1287	0.18192	50.4	−0.0248	−0.0377	66.7
$y^+ = 37.5$	0.1711	0.1784	25.4	0.0056	0.0111	15
$y^+ = 75.7$	0.1639	0.1640	2.6	0.00066	0.0116	24.4
$y^+ = 203$	0.1043	–	–	0.00053	−0.01136	153
$y^+ = 637$	0.0331	–	–	0.0045	–	–
$y^+ = 996$	0.0067	–	–	0.0035	–	–

† Peak Time Lag

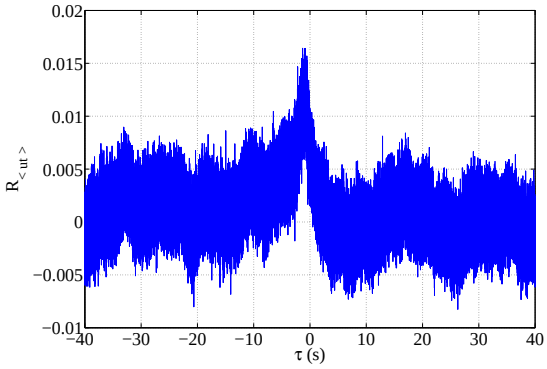

(a) $R_{<ut>}$ at $y^+ = 1.4$

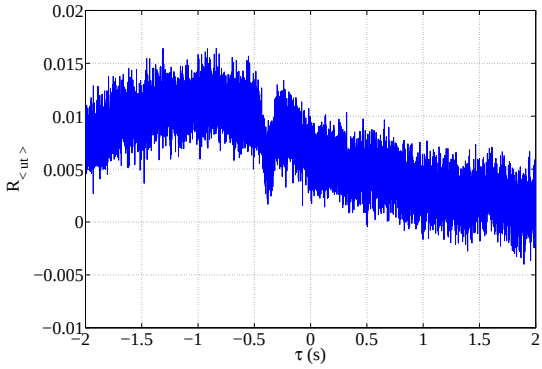

(b) $R_{<ut>}$ at $y^+ = 1.4$ (close up)

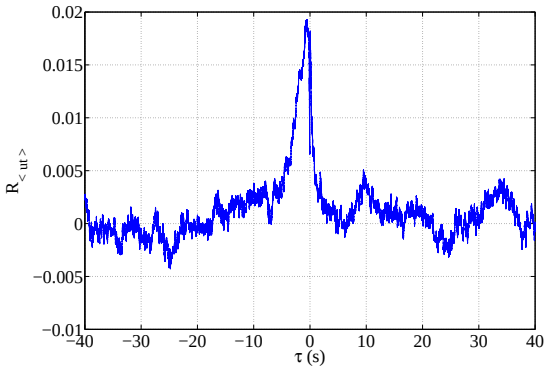

(c) $R_{<ut>}$ at $y^+ = 2$

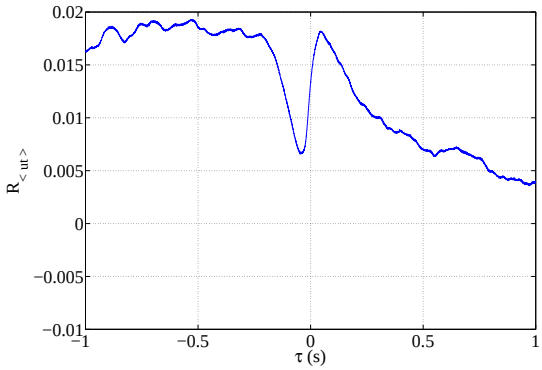

(d) $R_{<ut>}$ at $y^+ = 2$ (close up)

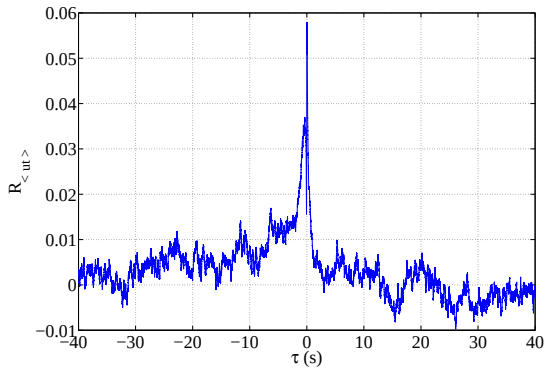

(e) $R_{<ut>}$ at $y^+ = 3.8$

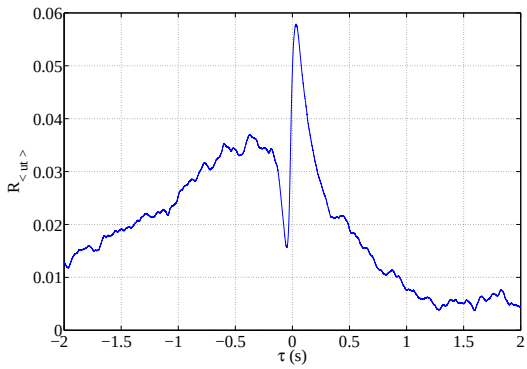

(f) $R_{<ut>}$ at $y^+ = 3.8$ (close up)

Figure E.6: Cross-correlation of streamwise velocity and temperature $R_{<ut>}$ in different radial positions for case 1 ($4m$ height).

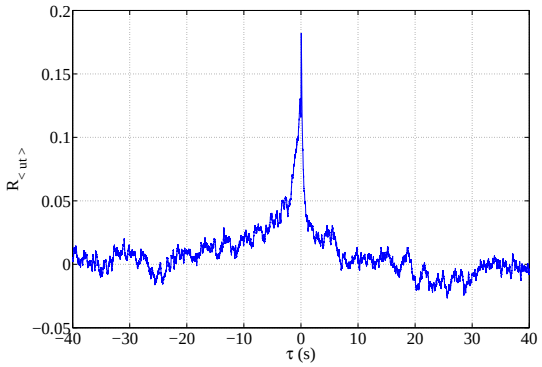

(a) $R_{<ut>}$ at $y^+ = 12$

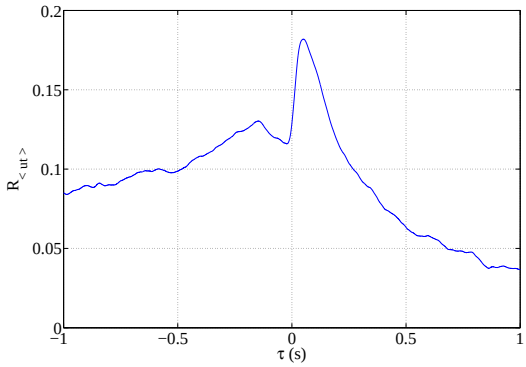

(b) $R_{<ut>}$ at $y^+ = 12$ (close up)

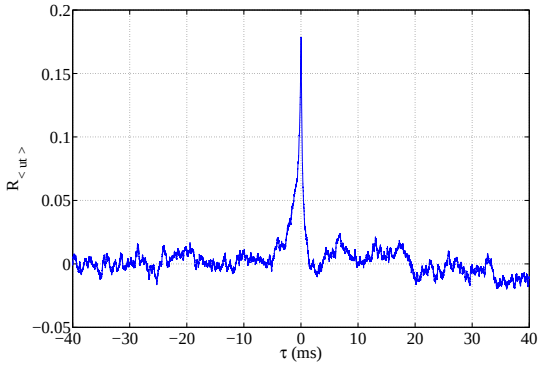

(c) $R_{<ut>}$ at $y^+ = 37.5$

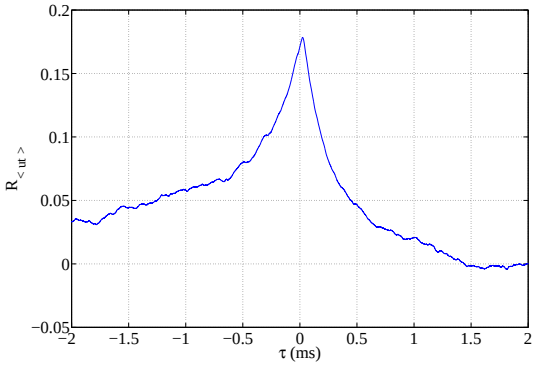

(d) $R_{<ut>}$ at $y^+ = 37.5$ (close up)

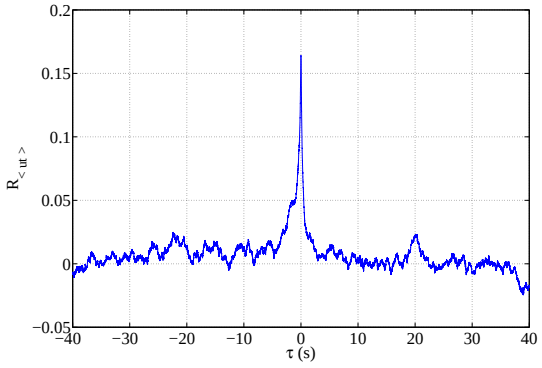

(e) $R_{<ut>}$ at $y^+ = 75.7$

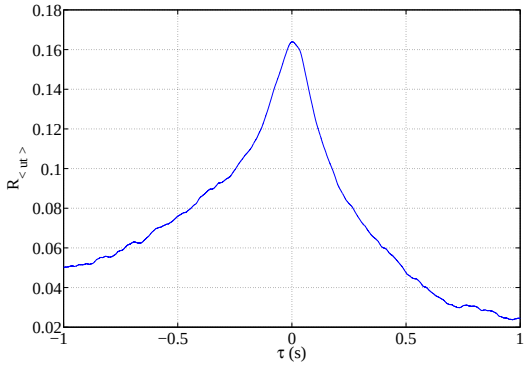

(f) $R_{<ut>}$ at $y^+ = 75.7$ (close up)

Figure E.7: Cross-correlation of streamwise velocity and temperature $R_{<ut>}$ in different radial positions for case 1 ($4m$ height). continue

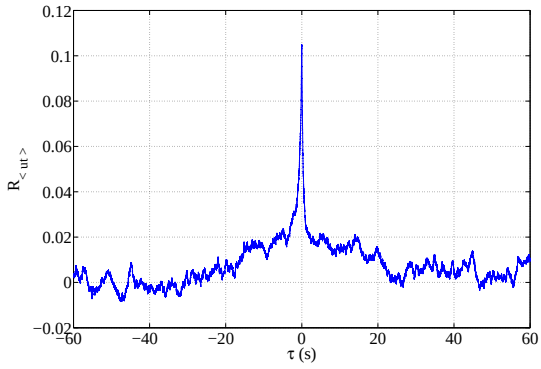

(a) $R_{<ut>}$ at $y^+ = 203$

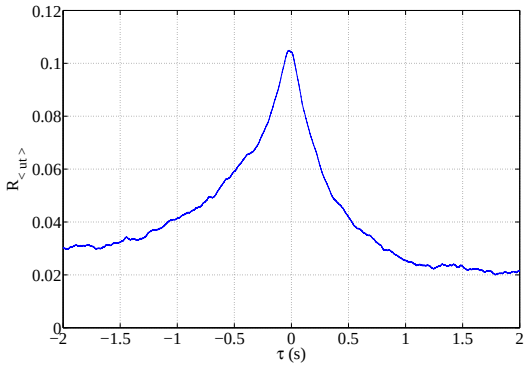

(b) $R_{<ut>}$ at $y^+ = 203$ (close up)

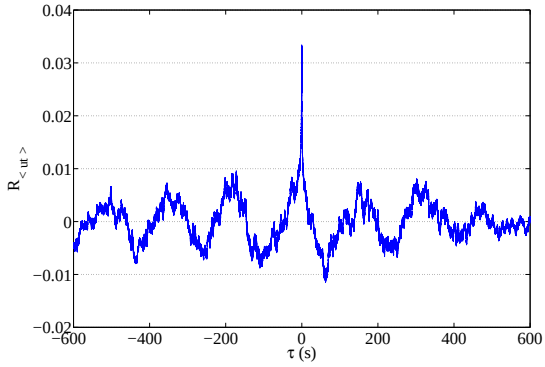

(c) $R_{<ut>}$ at $y^+ = 637$

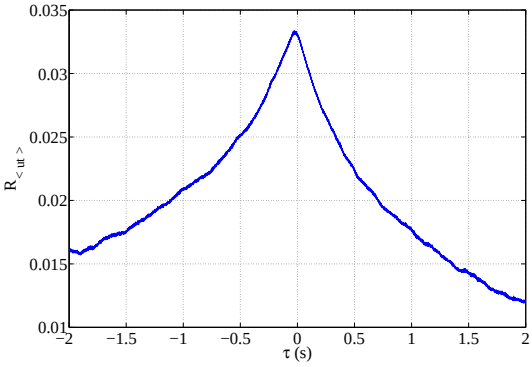

(d) $R_{<ut>}$ at $y^+ = 637$ (close up)

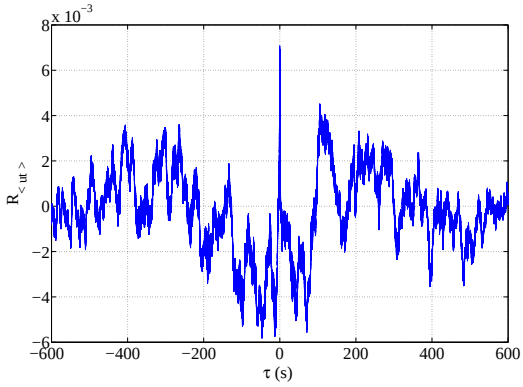

(e) $R_{<ut>}$ at $y^+ = 996$

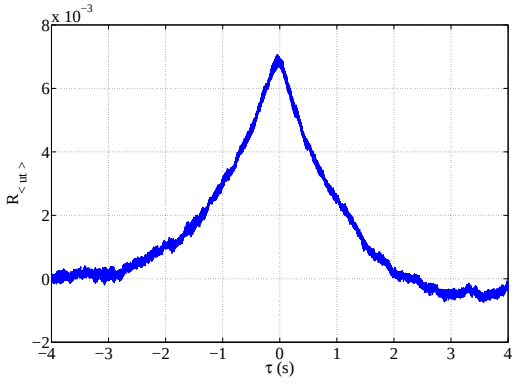

(f) $R_{<ut>}$ at $y^+ = 996$ (close up)

Figure E.8: Cross-correlation of streamwise velocity and temperature $R_{<ut>}$ in different radial positions for case 1 ($4m$ height). continue

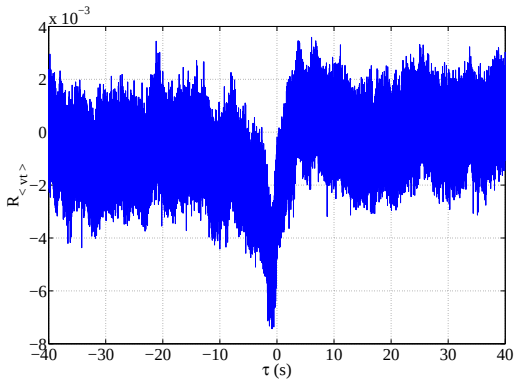

(a) $R_{<vt>}$ at $y^+ = 1.4$

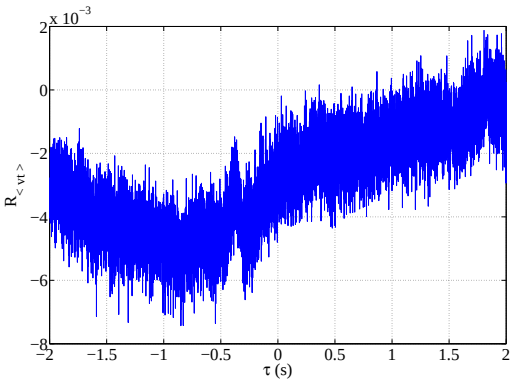

(b) $R_{<vt>}$ at $y^+ = 1.4$ (close up)

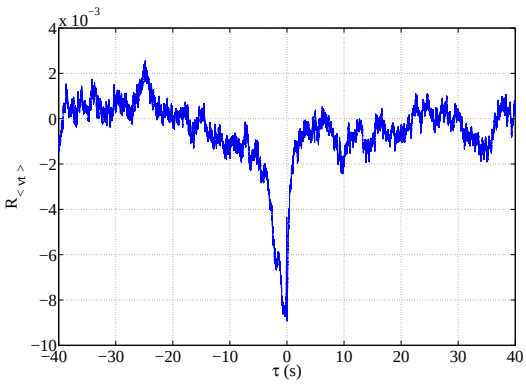

(c) $R_{<vt>}$ at $y^+ = 2$

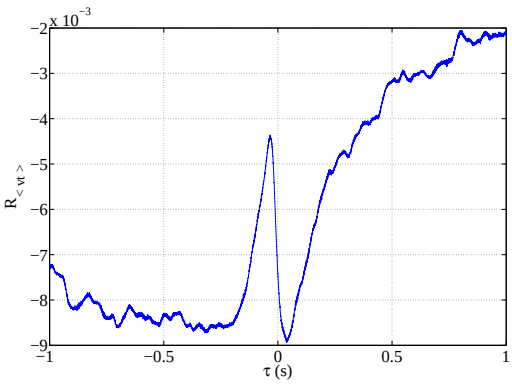

(d) $R_{<vt>}$ at $y^+ = 2$ (close up)

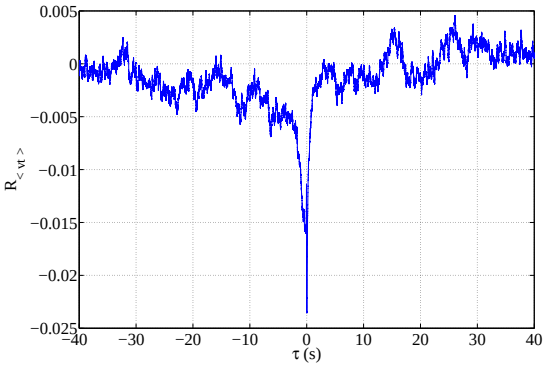

(e) $R_{<vt>}$ at $y^+ = 3.8$

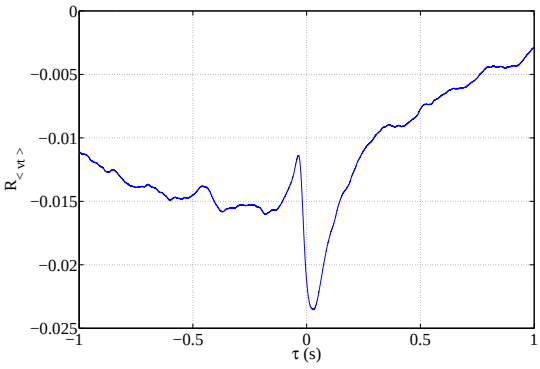

(f) $R_{<vt>}$ at $y^+ = 3.8$ (close up)

Figure E.9: Cross-correlation of radial velocity and temperature $R_{<vt>}$ in different radial positions for case 1 ($4m$ height).

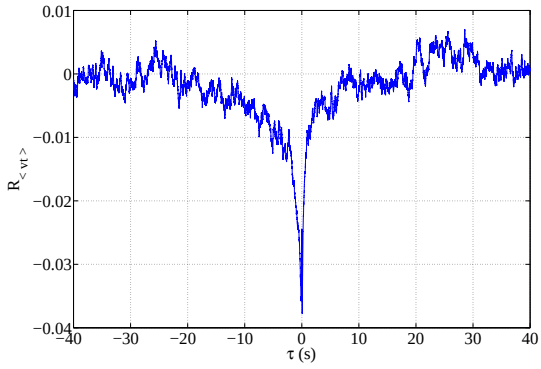

(a) $R_{<vt>}$ at $y^+ = 12$

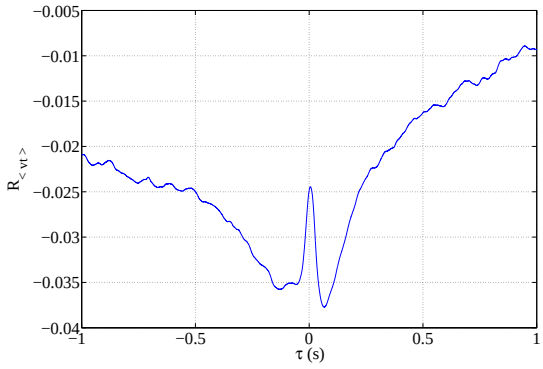

(b) $R_{<vt>}$ at $y^+ = 12$ (close up)

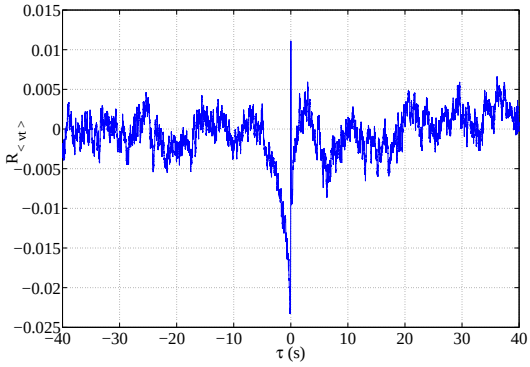

(c) $R_{<vt>}$ at $y^+ = 37.5$

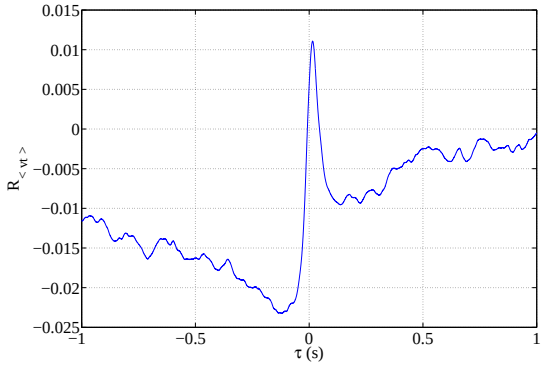

(d) $R_{<vt>}$ at $y^+ = 37.5$ (close up)

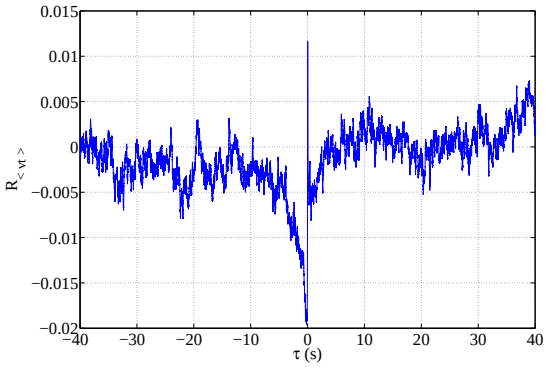

(e) $R_{<vt>}$ at $y^+ = 75.7$

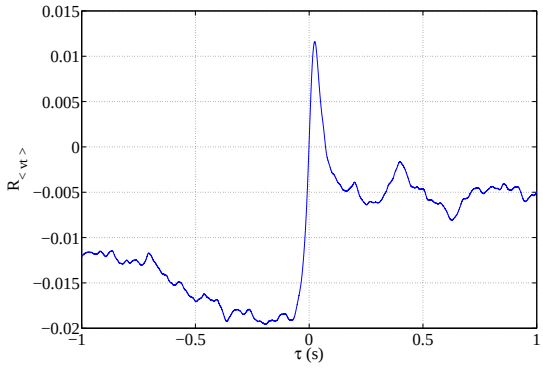

(f) $R_{<vt>}$ at $y^+ = 75.7$ (close up)

Figure E.10: Cross-correlation of radial velocity and temperature $R_{<vt>}$ in different radial positions for case 1 ($4m$ height). continue

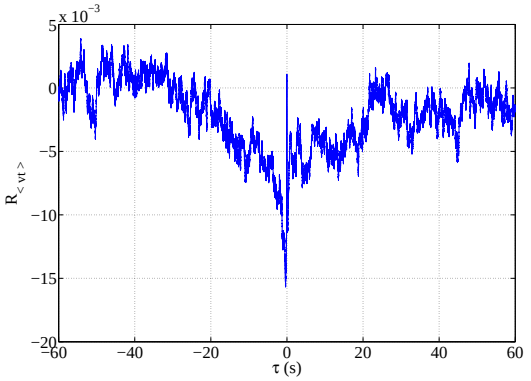

(a) $R_{<vt>}$ at $y^+ = 203$

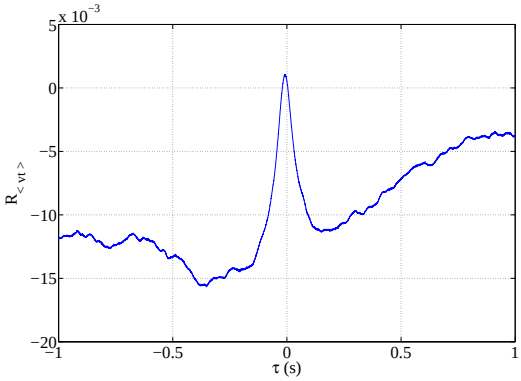

(b) $R_{<vt>}$ at $y^+ = 203$ (close up)

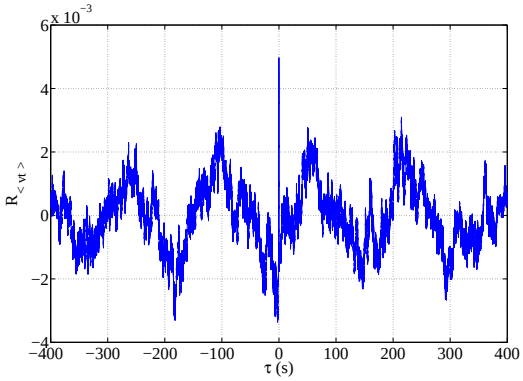

(c) $R_{<vt>}$ at $y^+ = 637$

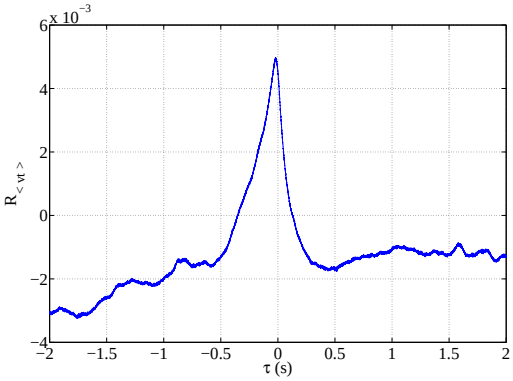

(d) $R_{<vt>}$ at $y^+ = 637$ (close up)

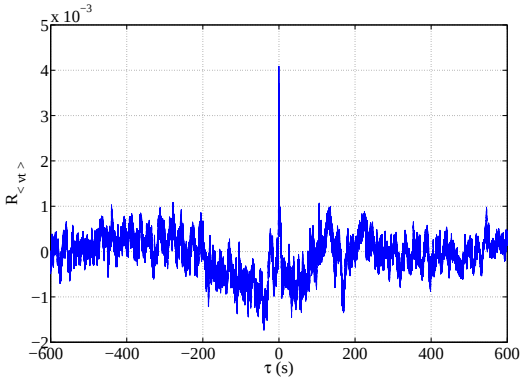

(e) $R_{<vt>}$ at $y^+ = 996$

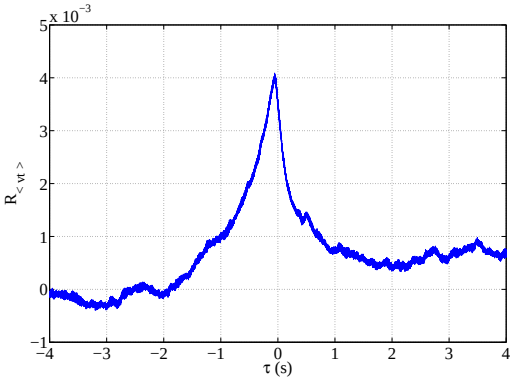

(f) $R_{<vt>}$ at $y^+ = 996$ (close up)

Figure E.11: Cross-correlation of radial velocity and temperature $R_{<vt>}$ in different radial positions for case 1 ($4m$ height). continue